Subsurface modification in Si induced by nanosecond laser irradiation

Lachlan A. Smillie

A thesis submitted for the degree of
Doctor of Philosophy
The Australian National University

August, 2019

Declaration

This thesis is an account of research undertaken between March 2013 and August 2019 at Department of Electronic Materials Engineering, Research School of Physics and Engineering, College of Science, The Australian National University, Canberra, Australia.

Except where acknowledged in the customary manner, the material presented in this thesis is, to the best of my knowledge, original and has not been submitted in whole or part for a degree in any university.

Lachlan A. Smillie
August, 2019

Acknowledgements

I would like to begin by thanking my supervisors, Jim Williams, Jodie Bradby and Andrei Rode, whose guidance was critical to the success of the project. I'd also like to thank them for allowing me the freedom to explore my own ideas and approaches to the project, but also supporting me when I encountered challenges. I would additionally particularly like to thank Jim for his contributions in the effort to explain the results in this thesis, his extensive knowledge was often pivotal in directing the discussion in a productive direction. Jodie's contributions to creating a supportive and friendly group are also noteworthy, as is her encouragement in involvement in matters beyond the project, such as scientific outreach. On a more technical note, I'd like to think Jodie for getting me started with TEM, which as my primary characterisation technique, was of great significance to the project.

Similarly, I am thankful for Bianca Haberl's who helped me get started with FIB, one of the primary sample preparation methods in the project. Aruni Fonseka helped me to learn the basics of tripod polishing, which became the other primary sample preparation method of my project, and so I thank her for that.

Throughout the project I have had a number of collaborators, the most important of whom is Paul Verburg from the University of Twente. Paul was instrumental in developing the laser irradiation process and producing the samples that most of the thesis is based upon. I'd also like to thank Paul for helping to organise my trip to the University of Twente and hosting me while I was visiting. I also appreciate his education on the laser process, which I did not understand well at the time. Additionally, I would like to thank Guido Knippels and Juergen Betz from ALSI, who were instrumental in starting the collaboration that led to my project. They were also the other source of samples examined in the project.

From Boston I would like to thank Mike Aziz at the Harvard University for hosting me during a visit. I'd also like to thank Mike for helping to connect me with Alain Karma and Longhai Lai at Northeastern University. Discussions with them were critical in understanding the finer points of the solidification process. During my visit to Harvard University David Pastor looked out for me on a day to day basis and I'd I thank him for that. At the Harvard Center for Nanoscale Systems Austin Akey helped me get access to the facilities, but also was a great source of conversation on all matters of electron microscopy, FIB and atom probe tomography. I'd also like to thank Jules Gardener for performing the EELS measurements at the Center for Nanoscale System. It is notable that she gave the work first priority to ensure the measurements were collected before I left after the system had been down for an extended period during my visit.

I have Amelia Liu at Monash University to thank for pointing me in the right direction for the analysis of the EELS results. Amelia has also been something of a mentor for me ever since my undergraduate studies at Monash University and so I appreciate her for that as well.

I'd also like to thank Dougal Mcculloch, the staff and students of the RMIT Microscopy and Microanalysis Facility. They allowed me access and provided support for some of my more ambitious FIB and electron microscopy undertakings.

At ANU I have Felipe Kremer and Lily Li to thank for, respectively, keeping the TEMs and FIB operating and providing support when needed. I'd also like to thank the facilities that look

after the instruments, the ANU Centre for Advanced Microscopy and the ANU branch of the Australian National Fabrication Facility.

Within the Department of Electronic Material Engineering Julie Arnold, the departmental administrator, deserves thanks and a great deal of respect. It is undoubtable that Julie keeps the department running. She is also an excellent point of contact when battling university bureaucracy.

My officemates, Tuan Thien Tran and Wenjie Yang, were a great source of comradery through our trials and tribulations of completing a PhD. I'd also like to thank the other members of my group for their companionship: Leonardus Bimo Bayu Aji, Toby Hendy, Xingshuo Huang, Shao Qi Lim, Kiran Mangalampalli, Christian Notthoff, Chris Tanner, Thomas Shiell, Clara Teniswood and Sherman Wong.

Finally, I'd like to thank my family (Annabelle Duncan, Bob Smillie and Nicola Smillie), my friends and my partner (Larissa Huston). Their support was immeasurable and no doubt ensured I enjoyed the good and worked through the bad parts of the years of my PhD candidature.

Abstract

Semiconductor devices are pivotal to modern technology. These devices are batch produced on wafers which must be diced for use. Conventionally, dicing involves destroying the material between each chip, dictating a minimum spacing between modifications. It follows that eliminating this material loss will allow more chips to be created per wafer. This thesis examines subsurface modifications that form part of a dicing process with no material loss.

Subsurface modifications can be induced by focussed pulsed laser irradiation when the photon energy is near or below the material's bandgap. Intensity dependent absorption is used to selectively modify the region near focus. This technique is useful both for technological applications and scientific investigation of material properties and laser-material interaction. This thesis examines columnar modifications created subsurface in Si wafers due to melting induced by nanosecond pulsed laser irradiation. The wafer dicing technique uses rows of closely spaced modifications that can preferentially guide crack propagation over the natural cleavage planes when the sample is cleaved.

The modifications themselves are poorly characterised and it is this deficiency that this thesis seeks to address. The work examines both isolated modifications, where the laser-matter interaction can be probed, and closely spaced modifications, which can provide insight into the dicing process. Additionally, modifications created under several different laser conditions are investigated and contrasted. Transmission electron microscopy is used to examine both the short and long axis of the modifications. Scanning electron microscopy and Raman microspectroscopy are also used.

Detailed examination of the short axis of the modifications reveals a range of morphological features such as a variety of crystalline defects and Si allotropes. These features can be explained by extending upon the literature of one-dimensional pulsed laser melting experiments into two-dimensions and conditions of higher cooling rates. Rapid, accelerating solidification occurs along multiple crystal orientations and propagates inwards from the melt periphery while simultaneously transitioning through several rate-dependent regimes of solidification behaviour.

Examining the long axis allows the solidification process to be understood in three-dimensions. Here, variations observed in the short axis morphology are related to the dependence of melt geometry and thermal gradients on the position along the long axis of the modifications.

Solidification is also subject to perturbations, often density related. These originate in the densification of Si as it melts, which in a subsurface volume drives the formation of voids. During solidification the voids are partially, but incompletely refilled. The material displaced by the remanent voids is largely concentrated in the final regions of the modified volume to solidify, creating compressive strain. However, there are also crystallites of high density Si allotropes. These allotropes form if pockets of high density melt lack room to expand during solidification. Interestingly, although these allotropes have been observed in near-static near-equilibrium pressure loading techniques (diamond anvil cell or nanoindentation loading), the pathway by which the Si allotropes form must clearly differ in this work. It is also noteworthy that the manifestation of the density-dependent morphological features, for example the number, size and position of voids, is highly dependent on the size of the modifications, and duration of the laser pulse used to create them.

The modifications were also found to contain many microcracks after solidification. During cleaving this removes the need to nucleate cracks. Instead, many cracks propagate simultaneously before joining together, completing the dicing process. However, portions of cracks are often bypassed by the cleaving path, potentially compromising the semiconductor chip strength.

Thus, this thesis has rectified the deficiency in knowledge of the modification morphology. In doing so, new solidification and high pressure related behaviour has been observed. Collectively, this information should serve as the basis to improve the dicing technique in the future.

Contents

List of Figures

List of Tables

List of Abbreviations

Phases of Silicon

a-Si	Amorphous Si
β-Sn-Si	Si with the same structure as β-Sn
bc8-Si	Body Centred Cubic Si, 8 atoms per unit cell
dc-Si	Diamond Cubic Si
r8-Si	Rhombohedral Si, 8 atoms per unit cell

Equipment and Techniques

ADF	Annular Dark Field
AEM	Analytical Electron Microscopy
BF	Bright Field
CBED	Convergent Beam Electron Diffraction
DF	Dark Field
EELS	Electron Energy Loss Spectroscopy
FIB	Focussed Ion Beam
HAADF	High Angle Annular Dark Field
IR	Infrared
NA	Numerical Aperture
NBED	Nano Beam Electron Diffraction
PLM	Pulse Laser Melting
SAD	Selected Area Diffraction
SADP	Selected Area Diffraction Pattern
SEM	Scanning Electron Microscopy
STEM	Scanning Transmission Electron Microscopy
TEM	Transmission Electron Microscopy

Institutions

ALSI	Advanced Laser Separation International
ANU	Australian National University

Chapter 1

Introduction

The fabrication of integrated circuit devices is a huge industry which continues to grow and diversify even now, 70 years after the first transistor was created. As such, the commercial demands to improve economics and performance have driven significant research and development. This development has most clearly been oriented towards transistor miniaturisation, allowing either for more powerful chips, or for chip miniaturisation. One of the benefits of chip miniaturisation is that more chips can be produced on each silicon (Si) wafer. As the costs associated with producing chips are largely fixed on a per wafer basis, producing more chips on each wafer is highly economically advantageous. However, having produced many integrated circuits containing millions of devices on a single wafer, the wafer much be diced before each chip can be put to use.

Conventional wafer dicing methods, such as with a wafering blade* or making use of laser ablation, involve the destruction of material in between each chip. The destroyed material is known as the kerf-loss. There is also the potential to damage the chips during dicing, and so a sizeable gap is required between each chip as it is fabricated. The gap is known as the street. This process is illustrated in Fig. 1.1.

Given the existence of kerf-loss and the street, it follows that as chips are miniaturised, an

*circular blade coated in diamonds or SiC

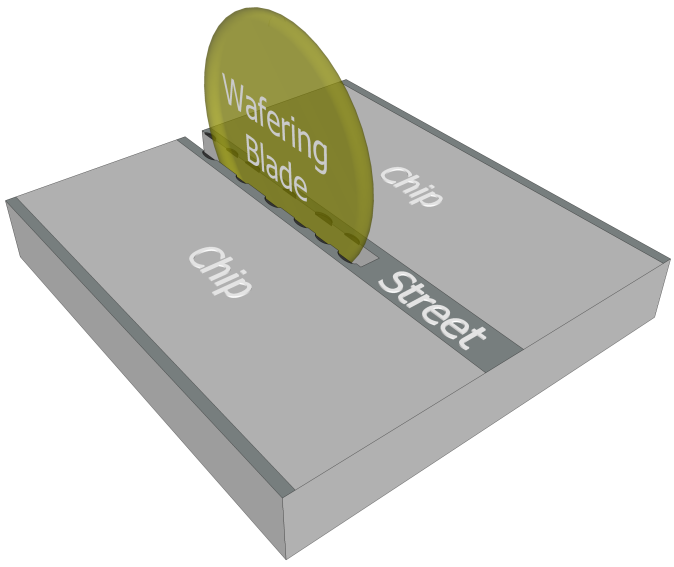

Figure 1.1: Illustration of the conventional dicing process using a wafering blade to destroy material (the kerf) between chips. This requires a gap (street) to prevent damage to the chips.

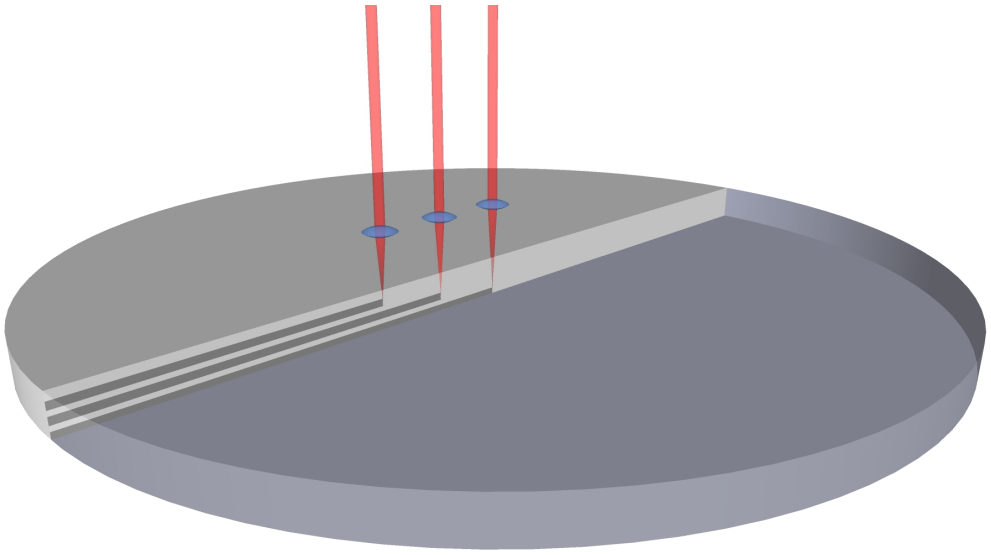

Figure 1.2: Illustration of the subsurface laser modification process showing three focussed lasers creating three layers of modifications over the thickness of the wafer on the intended dicing plane.

increasing proportion of each wafer is allocated to streets, rather than to chips themselves. It would therefore be commercially desirable to minimise the size of the streets so that more chips can be produced on each wafer. Ideally, the kerf-loss would be eliminated, allowing the street width to be drastically reduced. One avenue of interest is to dice the material by cleaving, where the material is fractured without any destruction of the adjacent material. However, in Si the natural cleavage planes are {111} planes.[1] From a fabrication perspective this is highly limiting. Additionally, cleaving along natural cleavage planes isn't sufficiently controlled for commercial application.

The topic of this thesis concerns a method of laser-induced modification-controlled cleaving that has already undergone limited commercialisation. This method is based on a nanosecond regime laser pulse train aimed subsurface in Si. The repetition of the laser is used to produce multiple structural modifications that fill a subsurface plane (perhaps with multiple passes at different depths, depending on the thickness of the wafer). If the wafer is subsequently cleaved, the resultant modifications will act as points of weakness that preferentially guide crack propagation along the plane of modifications, rather than the natural cleavage planes. The laser process is illustrated in Fig. 1.2.

The nanosecond laser pulse system has a number of other advantageous characteristics including:

- Limited damage (perhaps negligible after optimisation) on the cleaved surface allowing for a reduction in street width.
- No need for either water cooling, nor post dicing cleaning, unlike conventional methods.
- Easy integration into conventional wafer handling processes.

As evidence of some of these advantages, a commercialised version of this system has already been shown to be useful for the production of small chips such as microelectromechanical systems.[2]

However, while this method is already in use, the resultant modifications have not been well studied and are not currently well understood. Further improvements are thus likely,

once this deficiency is addressed. This deficiency was recognised by one company that was developing a version of this technique, Advanced Laser Separation International (ASLI), which initiated a collaboration with the University of Twente and the Australian National University (ANU). The intention was for the University of Twente team to focus on understanding the laser absorption process, while efforts at ANU were to focus on understanding the modification morphology. Indeed, the latter is the topic of this thesis. This arrangement was such that ANU would be supplied samples for characterisation by both ALSI, and the University of Twente. Unfortunately, ALSI were bought out and redirected early in the project's timeline. This placed some constraints on the experimental approach, but thankfully both groups had already supplied samples sufficient to complete this project.

This thesis aims to understand the morphology of modifications which are produced under several different, but related, laser conditions. Some insight into the coupling of modifications and the wafer dicing process will also be presented. Due to the unusual conditions created within the laser modified region, this work is also of scientific interest for understanding solidification processes, as well as various Si properties.

This chapter will present a basic introduction to the physics involved with light interacting with Si. It will begin by introducing the electronic band structure of Si, which leads onto the mechanisms of absorbing laser energy. Then selective subsurface absorption will be discussed with some examples of how it is used. Finally, the literature relevant to laser-induced subsurface modification for Si wafer dicing purposes will be considered, both for prior work directly in this field, and relevant work for laser-induced surface modifications.

Once the literature has been covered, a brief overview of the structure of the thesis will be provided.

1.1 Electronic band structure

To understand the morphology of subsurface laser-induced modifications requires an understanding of how the energy from a laser can be deposited subsurface in a bulk material. This first requires an understanding of the electronic band structure of the target material, Si in this thesis. The band structure for Si is shown in Fig. 1.3. The specific details are not of significance to this work, with the exception that there is a wave vector, k, or equivalently a momentum, p, mismatch between the conduction band minimum and the valence band maximum. This makes Si an indirect band gap semiconductor.

1.2 Energy absorption

The physics of energy absorption from intense laser light will be considered in this section. One route is lattice absorption. In Si this process is only possible with infrared (IR) photons, with wavelengths of approximately 6 μm or longer.[4–6] This is of relevance to this thesis only in that lattice absorption limits the parameter space available for subsurface absorption.

Alternatively, and of greater relevance to this thesis, the electronic system can absorb the photons. This involves a photon(s) hitting an electron, which absorbs all the photon(s) energy and momentum. This is only directly possible if, within the material, there is an unoccupied state which can accommodate the change in energy and momentum relative to the electron's original state. With the finite bandgap of Si, this means photons with energy below the bandgap can not be efficiently absorbed under low photon intensity conditions.

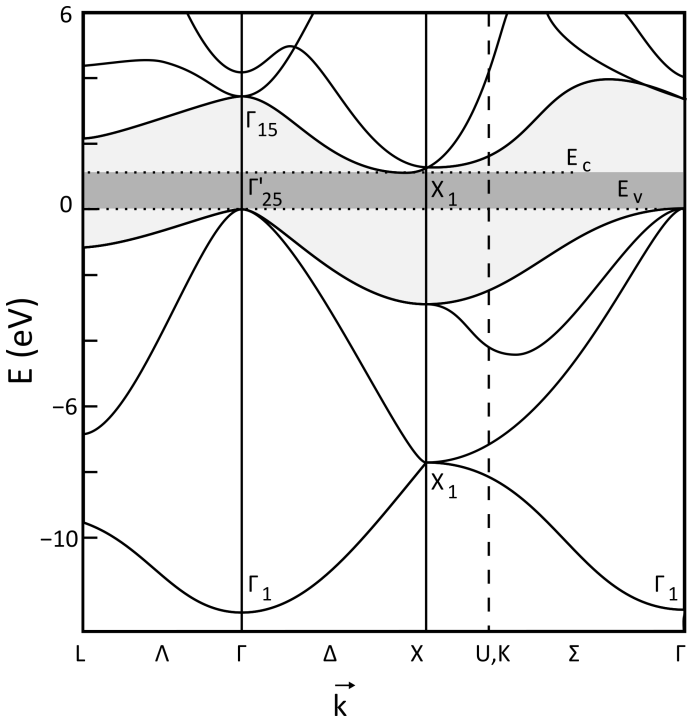

Figure 1.3: The band structure of Si where the grey region is the size of the band gap and the dark grey region is the smallest gap between the valence and conduction bands. Note that these are at different k positions as Si is an indirect bandgap semiconductor. Adapted from[3].

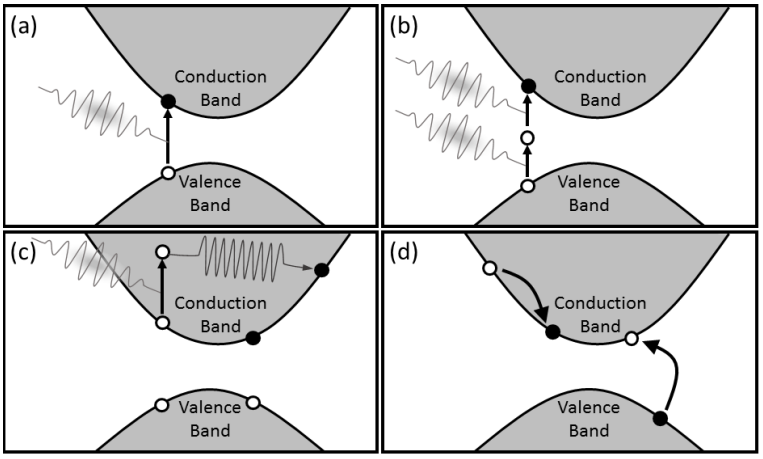

Figure 1.4: Photon absorption by the electronic system can occur by (a) single photon inter-band absorption, (b) multiphoton inter-band absorption (two-photon absorption is shown), (c) free carrier absorption and (d) impact ionisation. The schematic shows the band structure of a direct bandgap semiconductor. Adapted from[7].

The various allowed electron transitions that can occur when light is absorbed can be categorised into: inter-band single photon absorption, inter-band multiphoton absorption, free carrier absorption and impact ionisation.[7] These are shown schematically in Fig. 1.4. The absorption processes may also be categorised as linear or nonlinear. Nonlinear processes are typically orders of magnitude weaker than linear processes and have nonlinear dependence on the light intensity.

Excitation of the electronic system drives the material away from equilibrium conditions. This occurs both by driving the free carrier distributions away from the natural Fermi-Dirac distribution, and by driving the free carrier distribution independently of the lattice.[7] Because the electronic system and lattice can be excited at different levels it is common to consider the electron temperature separately to the lattice temperature using two-temperature models. The material returns to equilibrium conditions by several thermalisation and carrier removal processes, which are notably slower than the absorption process.[7]

With sufficient laser power, the material responds to the laser excitation with structural changes. At one extreme the preceding processes do little more than heat the material, with the heat being redistributed through the material. With sufficient heating a thermally-induced phase transition may occur. At the other extreme, excitation of the electronic system may be so significant so as to induce non-thermal structural changes before any significant thermalisation can occur.[7–9] A wide range of other structural effects are possible between these two extremes, the specifics of which are, in part, material and time dependent.

1.3 Selective subsurface absorption

From the previous sections it is possible to understand how laser energy is absorbed and the fundamental physics of how the material responds. The next matters to consider are the strategies that may be used to produce subsurface modifications. These strategies must clearly require selective subsurface absorption, without significant surface absorption.

The simplest route to achieve subsurface modification is to use a material system with two layers, one that is transparent to the laser, and one that is not. As such, absorption may be induced at the interface between the materials. This is the method used by Rapp et al. for modifications in Si induced on a femtosecond timescale.[10,11] In that work, the short laser timeframe and subsurface confinement was capable of producing extreme conditions not readily reached by conventional experimental techniques. It was reported that several new crystal phases of Si were produced and observed as a consequence.

An approach with more relevance to the work of this thesis is to utilise light with a wavelength that the material is largely transparent to, but with the light focussed subsurface. This creates a strong intensity gradient as the light approaches the focal point, allowing appreciable intensity-dependent absorption near focus. The implied constraints on this approach are that the laser wavelength must be long enough so as not to be efficiently absorbed by single photon absorption elsewhere in the sample, but short enough so as not to be absorbed by lattice absorption. This approach is commonly used in insulators.[12–14]

Subsurface modifications made under these, and similar conditions, can be tailored to changes in the refractive index, where demonstrated applications include; data storage[15], waveguides[16], gratings[17], lenses[18] and even for decorative purposes[19]. Non-optical applications are also possible, including strengthened glass[20] as well as for basic scientific investigations such as to investigate materials under extreme conditions[21–23].

The practicalities of producing subsurface modifications are somewhat less straightforward than simply selecting the appropriate wavelength and focussing the laser. For subsurface modi-

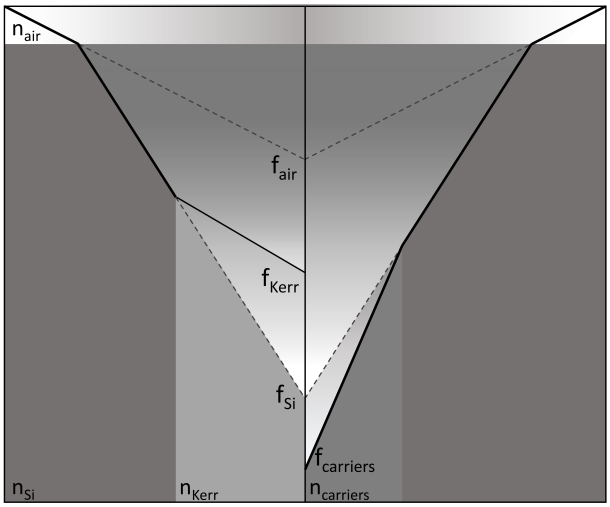

Figure 1.5: Focussing and defocussing effects during intense laser irradiation. The refractive index of the target material (n_{Si}) causes defocussing (f_{Si}). Near focus the optical Kerr effect can increase the refractive index (n_{Kerr}), causing self focussing (f_{Kerr}). Heating of the lattice has a similar effect. Excitation of free carriers decreases the refractive index ($n_{carriers}$), causing a defocussing effect ($f_{carriers}$).

fications, the refractive index is an important property. The laser will typically be focussed to form a convergent beam that first propagates through air. This light then refracts as it enters the material such that its convergence angle changes. A useful way to consider this is with the numerical aperture (NA) of the optics used to focus the light, in conjunction with Snell's law.

$$NA = n_m \sin(\theta_m) = n_t \sin(\theta_t) \tag{1.1}$$

where n is the refractive index, θ is the convergence semiangle, m is the initial medium of propagation, generally air where $n_{air} \approx 1$, and t is the target material. Although there are exceptions, the refractive index of the target material is typically larger than that of the initial medium. As such, the convergence angle of light propagating through the target material will be smaller than in the initial medium. This is illustrated for air and Si in Fig. 1.5, where f_{air} is the focal point without considering defocussing by the Si, and f_{Si} is the focal point accounting for defocussing. Significantly, the smaller convergence angle within the Si implies that intensity dependent absorption becomes less confined than it might otherwise be assumed.

Additionally, the optical properties within the material may change over the course of the laser irradiation. One cause of changing optical properties is the Kerr effect, which relates the refractive index of a material to any applied electric field.[24] As light itself has an electric field, when sufficiently strong it can induce a tangible change in the refractive index, this is a special case known as the optical Kerr effect.[25] This is described in the equation below where n_0 is the linear refractive index, n_2 is the non-linear refractive index and I is the intensity.

$$n = n_0 + n_2 I \tag{1.2}$$

As n_2 is typically small and positive, the optical Kerr effect will increase the refractive index and cause self focussing.[23] A simplified example of the geometry is shown in Fig. 1.5, with focus shifted to f_{Kerr}.

The refractive index is also sensitive to lattice temperature. Hence, if the laser exposure is long enough for thermalisation, changes in the refractive index follow. In Si the refractive

index increases with temperature, and thus, much like the optical Kerr effect, can result in self focussing.[26]

The refractive index is also sensitive to changes induced by excitation of the electronic system. In Si this excitation leads to an increased density of free carriers, which is known to reduce the refractive index.[27] The geometry is otherwise similar to the optical Kerr effect, but the reduced refractive index instead produces a defocussing effect. This is shown in Fig. 1.5 with a focus shift to $f_{carriers}$. An interesting consequence is, when combined with the optical Kerr effect, it is possible to induce an alternating self focusing, defocussing condition which leads to filamentation in certain materials.[28]

Having considered a number of mechanisms that change the refractive index, it is pertinent to note the Kramers-Kronig relations, which state that refractive index and absorption are inherently linked.[24,29] So the previous mechanisms not only cause changes in focus, but also the efficiency of light absorption.

The strategies employed to induce subsurface modifications relevant to this work rely on enhanced absorption induced by the initial irradiation of the laser pulse. Absorption is initiated by a relatively inefficient intensity dependent process, which quickly leads to optical breakdown/thermal runaway and efficient absorption.

Clearly controlled subsurface modification is a complex field requiring a good quantitative understanding of the physics and material properties of these processes. Indeed, understanding and modelling the optical physics in Si was the focus of the work by Verburg et al. (the collaborators for this project from the University of Twente). The outcome of the Verburg et al. work will be presented in the following section, which should now be qualitatively understandable as a result of the discussion thus far.

1.4 Inducing modifications in Si for wafer dicing

For the purposes of wafer dicing, it is necessary to utilise an intensity dependent strategy to induced subsurface modification. This defines a number of constraints on the laser parameters, of which the most consequential are discussed. The first constraint of note is that the parameter space is bounded by efficient linear absorption for photon energies above the band gap ($E = 1.11\ eV$, $\lambda = 1170\ nm$) and lattice absorption for small photon energies ($E \approx 0.207\ eV$, $\lambda \approx 6000\ nm$).[†]

The second constraint is pulse energy, which must be large enough to induce significant heating at focus, but not so large that significant intensity-dependent absorption occurs away from the target area.

The third constraint is pulse duration. This is interrelated with pulse energy; it must be long enough so that efficient intensity-dependent absorption occurs only near focus, but not so long that heat is conducted away before appreciable heating at focus occurs.

For wafer dicing, conditions that produce relatively large modifications in a single pulse are of interest. With this final constraint, this outcome has only been demonstrably met in Si with nanosecond regime pulses.[30,31] Indeed, a number of previous attempts to produce sizeable subsurface modifications with shorter laser pulses have been made. These have either failed outright[32–34], or produced near surface modifications[35].

The nanosecond pulse regime raises an important point; in this regime the energy is easily transferred to the lattice over the pulse duration[7] and thus, the modification should be caused

[†]These are approximate limits only. Subsurface modifications are routinely produced in Si with a $\sim 1064\ nm$ wavelength. The indirect nature of the Si bandgap prevents efficient absorption even with a photon that has more energy than the bandgap.

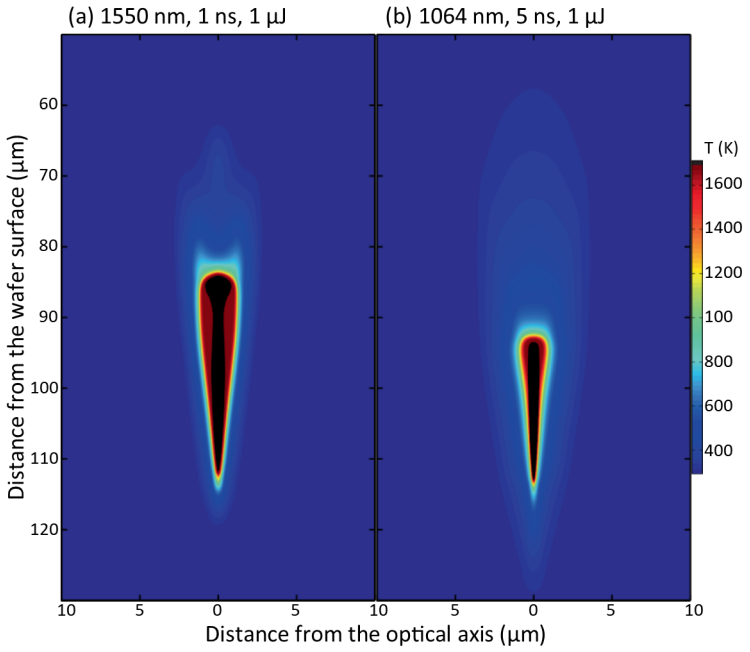

Figure 1.6: Simulation results for the maximum lattice temperature reached in (a) the sub-bandgap regime and (b) the near-bandgap regime. The black area exceeds the melting point of Si. The laser is incident from the top of the figure. Adapted from [31].

by thermal melting. Indeed, previous work has shown modifications to be melting-induced both for surface modifications [36–38], and subsurface modifications [30,31,34].

Considering now specific strategies, Verburg et al. have shown that modifications may be induced in the sub-bandgap regime (with photons less energetic than the bandgap, which requires multiphoton absorption to initiate appreciable heating) using both simulations and experiments. [30,31] Perhaps surprisingly to one not familiar with the field, it has also been shown that the near-bandgap regime (with a photon energy near that of the bandgap) can also induced subsurface modifications. This has again been shown with both simulations and experiments. [31,34,39–44]

The key physical processes that occur for both strategies will now be presented based upon the work of Verburg et al. [30,31,34,44,45] This is the most detailed and comprehensive work in this area and won't be comprehensibly covered here. Thus, reading the listed publications is recommended if further details are desired.

1.4.1 Simulation findings

Verburg's simulations were performed with a comprehensive two-temperature model that tracked free carrier density based on single photon interband absorption, two photon absorption, free carrier absorption, impact ionisation and Auger recombination. It also considered the dependence on temperature, carrier density and similar parameters on conductivity, latent heat, absorption coefficients and refractive index. However the model did have some limitations; some high temperature inputs are based on extrapolated data, it did not fully account for liquid behaviour, nor did it attempt to cover solidification. [31,44]

Verburg's work primarily considered a 0.7 NA focussing objective aimed 100 μm subsurface where spherical aberrations were corrected. In the sub-band gap laser regime a laser pulse with a 1550 nm wavelength, 1 ns pulse duration, and 1 μJ pulse energy was simulated. In this regime absorption was initially dominated by a two-photon process. This led to an in-

crease in free carrier densities and in turn, increased free carrier absorption and then impact ionisation.[30,31] After sufficient heating, the band gap would shrink sufficiently for single-photon interband absorption.[30,31,46]

For the near-bandgap laser regime, a laser pulse with a 1064 nm wavelength, 5 ns pulse duration and 1 μJ pulse energy was the focus of simulated results. In this regime absorption was initiated predominantly due to inefficient single-photon interband absorption.[‡] As with the sub-bandgap regime, the initial absorption leads to more efficient absorption subsequently.[31,44]

For either strategy, a small molten volume was suggested to form during the initial stages of the irradiation. Increased absorption efficiency allowed absorption to be less confined near focus. Instead absorption shifted closer to the laser source, at the periphery of the laser excited region. Over the duration of the laser pulse absorption continually migrated along the laser path. As such, for a prolonged laser pulse it was suggested to be possible to grow the molten region into a rod/columnar shape 10s of μm long. This is somewhat more elongated than the initial absorption volume and is limited mostly by the beam diameter being larger further from focus.[30,31] This elongation was considered desirable for dicing as it allowed the dicing plane to be populated with modified material, which improves dicing performance.[31]

The simulations showed that the sub-bandgap laser process was more efficient, creating longer modifications at a given energy (within the 0.5 $\mu J - 4$ μJ test range). This is because the near-bandgap laser process has:[31]

- Higher energy losses due to absorption away from focus.
- Greater defocussing due to free carriers
- For longer pulses, heat diffusion away from the irradiated region becomes significant.

It should also be noted that the model suggests that peak temperatures may be self-limiting and that they do not greatly exceed the melting temperature. This is because the previously discussed migration of efficient absorption up the modification towards the source shields the melt from further heating.[31]

In Fig. 1.6 an example of the simulation results are shown both for sub-bandgap and near-bandgap conditions. The black region is where temperatures exceed the melting temperature of Si.

1.4.2 Experimental findings

As well as modelling the interaction, Verburg et al. also conducted experimental work to validate the model, optimise dicing and characterise the modifications to some extent. This work was based on producing modifications using parameters similar to those in the simulations.

For the sub-bandgap regime, a 1549 nm wavelength, 3.5 ns pulse duration laser was used. Pulse energy was varied between 0.4 μJ and 4 μJ.[31,45] In the near-bandgap regime the results from $\sim$ 1061 nm modifications were most relevant. Pulse duration and energy was varied between $2 - 460$ ns and $0.5 - 4$ μJ respectively.[31,34]

From a validation perspective, the simulated melt geometry was compared against the observed modification size as viewed on a cleaved surface. This showed a good correlation across the tested parameter range, reinforcing both the validity of the model and the assumption that modifications are melting-induced.[31,34,44]

[‡]Two-photon absorption is still possible in the near-bandgap regime, but it is negligible for the conditions that most experimental modifications are produced in.

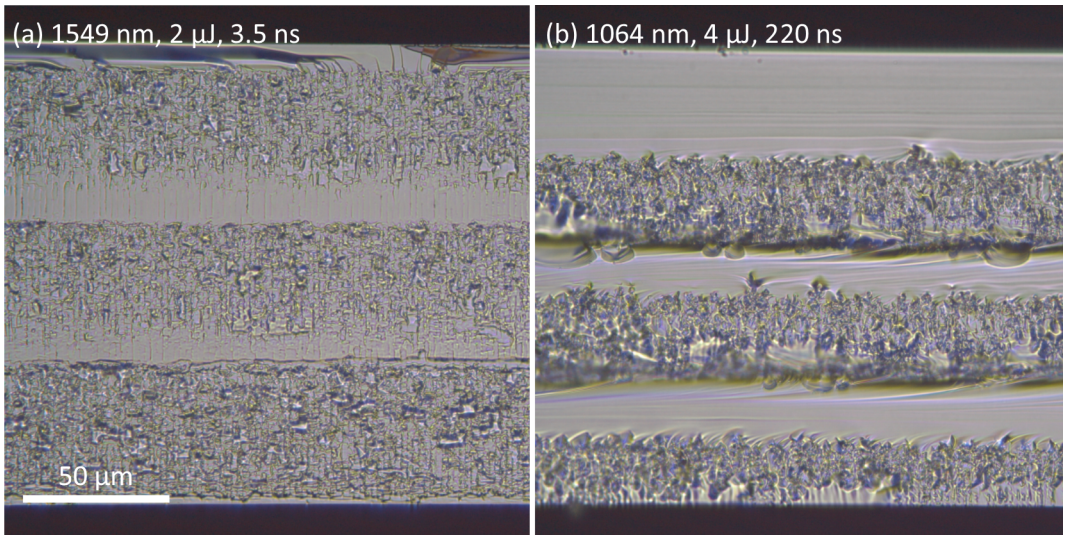

Figure 1.7: Optical microscopy images, at the same scale, of cleaved surfaces after laser irradiation in two of the conditions relevant to this thesis, (a) for sub-bandgap modifications and (b) for near-bandgap modifications. Each surface consists of three layers of modifications, with each modification separated by 2 μm. The laser is incident from the top of the image, being focussed on the bottom of each layer of modifications. The bottom layer must be induced first, and the top layer last.

From a dicing perspective a more complete coverage of the target plane was advantageous. Transverse separation of $2-3$ μm performed well while 4 μm was sufficient to guide crack propagation in general, but not to ensure that the crack always remained on the target plane.[31] In certain conditions cracks between modifications were visible in IR microscopy before dicing. These were said to have reduced the required dicing force, but also were likely to degrade the cleaved surface strength.[31,45]

In Fig. 1.7 (a) an example of a cleaved surface is shown. In this case three layers of modifications were produced in the sub-bandgap regime, specifically with a 1549 nm wavelength, 3.5 ns pulse duration, 2 μJ pulse energy and 2 μm transverse spacing. These conditions match one of the conditions examined in this thesis. Examining this surface with SEM (shown in Chapter 3, Fig. 3.1), small pits were found and these were suggested to be voids.[30,31,45]

1.4.3 Other findings in the literature

ALSI

The collaborators at ALSI independently optimised a near-bandgap laser regime for wafer dicing purposes, the results of which will be examined in Chapter 9. As a commercial company, publication of the results was not a priority for the company. The information that follows is provided by personal correspondence.[47]

The modifications were created with a laser of 1064 nm wavelength, 220 ns pulse duration and 4 μJ pulse energy. These conditions are extremely similar to conditions that Verburg et al. investigated with both modelling and experiments and the modification dimensions are well correlated.

Good cleaving performance was again achieved with three layers of modifications over the thickness of the wafer and with a 2 μm traverse spacing between modifications. This surface is shown in Fig. 1.7 (b). Closer examination with SEM (shown in Chapter 9, Fig. 9.1) again revealed pits that were thought to be voids.

Hamamtsu Photonics and Osaka University

The majority of the published literature concerning subsurface modifications for wafer dicing is the product of a collaboration principally consisting of Hamamtsu Photonics and Osaka University. All of this work concerns a near-bandgap process.

The experimental parameters were a 3.75 μm transverse distance between modifications produced with a 1064 nm wavelength laser, 150 ns pulse duration and $4-6.5$ μJ pulse energy.[39,42,48] Thus, in comparison with previous literature conditions, a larger transverse distance and higher pulse energy are the principle differences. Examination of the modifications on the cleaved surface suggest that they are slightly larger than those produced by ALSI.[41,48] Pits, again suggested to be voids were observed. These voids were suggested to be melting-induced as Si shrinks when it melts.[49]

Accompanying the experimental results were simulation of the laser irradiation process using a single-temperature model. This suggested that temperatures well in excess of melting were reached[50,51], sometimes even well in excess of the boiling point of Si.[39,41,42] Based on this modelling, the modification morphology was said to be the combined result of melting and a thermal shockwave.[39,41,42,50,51] It is noteworthy that this more simplistic model differs greatly to the model used by Verburg et al. The explanation for the modification morphology also differs. This raises one of the questions this thesis intends to answer, can the morphology of the subsurface modifications be explained by melting and solidification alone, or are thermal shockwaves of relevance?

Multipass approach

Another dicing approach that is of some relevance concerned modifications intended to dice a multilayer microelectromechanical system, specifically Si on glass. This approach used a 1064 nm laser wavelength, 10 ns pulse duration and 0.7 NA focusing optics. Pulse energy was varied such that multiphoton absorption could be used to induce modifications in glass, and a near-bandgap process was used in Si.[43]

Subsequently, a second pass with a CO_2 laser was used to induce thermal stress and complete the dicing process without the application of an external macroscopic stress.[43]

It is clear that that thermal stresses can be used to propagate cracks, and so another matter that this thesis intends to investigate is whether thermal stresses contribute to the dicing behaviour of the subsurface modifications.

1.5 Surface pulsed laser melting

It should now be evident that although production of subsurface modifications suitable for wafer dicing is adequately understood, the understanding of the modifications is limited to identifying particular features and characterising these features outside of the context of a complete understanding of the morphology.

However, further insight can be gained by considering the modification of Si under similar conditions for surface laser pulses, which is very well understood. This regime was explored thoroughly as it is of interest for hyperdoping, that is doping far above equilibrium doping limits using ion implantation, which would damage the implanted region. Pulse Laser Melting (PLM) with long picoseconds to short nanosecond laser pulses was used to melt passed this damage, then rapidly solidify the material via liquid phase epitaxy. Performed correctly, this allowed the damage from ion implantation to be repaired, while providing insufficient time for the dopants to segregate.[52–54]

This work showed that solidification speed and crystal quality has a crystal orientation dependence,[55] and that both the melting and solidification in simple planar cases could be accurately modelled.[52,56] As the solid liquid epitaxy interface velocity increases, solidification transitions from perfect crystallisation, to defective crystallisation, to amorphous solidification.[55] This topic will be reviewed in more depth in Chapter 4.

1.6 Surface laser modification of Si with femtosecond lasers

For completeness, the femtosecond laser regime for surface modification of Si will also be considered. This regime has many parallels with subsurface, nanosecond regime modifications in Si. However, these parallels are largely superficial, and are raised here mostly to acknowledge that fact.

This regime is of interest as it provides a method to improve the optical properties of devices. This is achieved by hyperdoping using an alternative path to PLM, and as an avenue for texturing of the surface.[57–59]

With femtosecond timescale laser pulses, absorption by the electronic system occurs entirely before energy is transferred to the lattice.[7] An implication of this is that the ablation thresholds can easily be reached, which is known to lead to surface texturing.[60,61]

During each pulse, material is ablated, a thin melt layer is formed, followed by solidification and condensation of ablation products. Thus, any dopants present in the processing atmosphere can be captured and incorporated into the material well above equilibrium limits.[62]

Interestingly, the process can also result in the formation of high density crystalline allotropes of Si. These are created below melt depth and are thought to be the product of shockwaves. These in turn are created due to the sudden heating of the lattice as energy is transferred from the electronic system.[63,64] As will be shown in Chapter 6, similar phases can be formed in the nanosecond regime subsurface modifications discussed in this work.

1.7 Thesis objectives and outline

The principal objective of this thesis is to determine the nature and clarify the origin of the morphology of the subsurface modifications. In particular, the thesis will clarify whether melting, boiling and thermal shockwaves contribute to the sample morphology. A secondary objective is to explore the link between the morphology and dicing with the ultimate aim of using this knowledge to improve dicing performance.

This investigation will largely focus on modifications created in the sub-bandgap regime, which are well optimised for dicing due to their large size. The modification morphology is composed of many interrelated features. To that end, Chapter 3 will present an overview of most of these features so as to provide context to subsequent chapters which will consider individual features. Chapters 4-6 will examine modifications produced in isolation, so that only the morphology related to the laser irradiation process can be examined. Chapter 7 will examine the influence of close spacing of the modifications and cleaving the sample has on modification morphology. Chapters 8-9 will examine and contrast modifications created under different laser conditions.

Chapter 2 - Experimental

In this chapter the characterisation techniques used in this thesis will first be described. The laser conditions used to produce the modifications will follow, and then the sample preparation

process will be detailed.

Chapter 3 - Overview of the modifications

In this chapter an overview of the sub-bandgap regime modifications will be provided. In providing an overview, this chapter aims to provide the necessary context for subsequent chapters which investigate specific morphological features of the modifications. Additionally, this chapter will consider aspects of experimental analysis that will remain relevant for the entire thesis.

Chapter 4 - The morphology of short axis cross-sections

In this chapter the morphology visible in short axis cross-sections of sub-bandgap regime modifications will be explained based on a two-dimensional solidification process that draws upon the one-dimensional melting and solidification process relevant to PLM.

Chapter 5 - The morphology of long axis cross-sections

In this chapter the morphology visible in long axis cross-sections of sub-bandgap regime modifications will be explained by extending the two-dimensional explanation from the previous chapter into three dimensions.

Chapter 6 - The role of density

In addition to solidification-induced morphology, some morphological features must consider variation in density. In this chapter the origin and evolution of voids during the laser pulse is explored. Subsequently regions of elevated density are investigated.

Chapter 7 - Closely spaced modifications

In this chapter the influence of placing modifications close together, as used for dicing, and the dicing process itself are explored for sub-bandgap regime modifications.

Chapter 8 - Low energy modifications

In this chapter modifications produced in the sub-bandgap regime, but with a greatly reduced laser pulse energy are investigated. The results will be contrasted with the higher energy modifications and will show that most aspects are either the equivalent, or the differences are explainable based on the inherent differences between the laser conditions.

Chapter 9 - Near-bandgap modifications

In this chapter the sub-bandgap regime modifications will be contrasted with near-bandgap regime modifications. Most of the morphology is again either equivalent, or the differences are explainable based on the inherent differences between the laser conditions.

Chapter 10 - Summary, conclusions and future work

In the final chapter the nature of the subsurface modifications will be summarised, conclusions stated and future work based on questions raised during this thesis will be proposed.

Chapter 2

Experimental

In this chapter the experimental approach used to characterise the modifications will be introduced. This approach was subject to a number of key constraints, the most important of which was the small proportion of each sample that is actually modified. It follows that precision techniques must be used to examine only the modified material. Sample preparation must be similarly precise. Complicating this endeavour is the deep subsurface, difficult to observe nature of the modifications. Sample preparation constituted the single greatest challenge of this work.

Sample preparation is specific to each of the various characterisation methods. As such, this chapter will consider the characterisation techniques first, so as to provide context as to why particular sample preparation approaches are chosen. One particular type of sample, cleaved samples, are exceptional in that their sample preparation is straightforward. These samples, on average, split the modifications in half and leave them exposed on the cleaved surface for easy access. However, the resulting surface is sufficiently rough that there are severe restrictions on the information that can usefully be extracted during characterisation.

2.1 Characterisation

In this thesis the modifications were characterised principally by transmission electron microscopy (TEM) and Raman microspectroscopy. IR microscopy, visual light microscopy and scanning electron microscopy (SEM) were also used both to characterise the samples and guide sample preparation.

Sample preparation also made use of focused ion beam (FIB) milling. As the physics of a FIB has a great deal in common with that of an SEM, the underlying physics of both will be presented together.

2.1.1 IR microscopy

Si is opaque to visual light, but transparent to portions of the IR spectrum. As such, transmission IR microscopy allows for the examination of the modifications. This technique may be understood on the same basis as transmitted visual light microscopy.

The use of IR light does, however, limit the achievable resolution in comparison with visual light. This can be appreciated by considering the Rayleigh criterion which relates the minimum resolvable distance, δ, between two features to the wavelength, λ, and the NA:

$$\delta = \frac{0.61\lambda}{\sin(\theta)} = \frac{0.61\lambda}{NA} \tag{2.1}$$

Using, for example, the wavelength corresponding to the bandgap of Si, and a NA of 0.7 results in a resolvable detail of 1020 nm. This is comparable to the diameter of the modifications and so

in this work, under most circumstances, the resolvable detail with IR microscopy was insufficient to observe any features of the modifications. Nevertheless, this does allow the location of the modifications to be determined which was used mostly to guide sample preparation. In contrast, our collaborators were able to make use of IR microscopy to observe some major features such as the presence of large cracks.[45] These features are thought to be absent or negligible in the modifications used in this work.

Equipment

The instrument used was a Motic BA310TMET-T compound microscope. The IR light was produced using a halogen light source. A 100 nm thick Si wafer was used as a long pass filter to remove the visual light component. For detection a CMOS based microscope camera without the IR filter ordinarily attached to such a sensor was used.

2.1.2 Visual light microscopy

Visual light microscopy was used in this work to image the topography of cleaved samples.Various features corresponding to the modifications were observable on this surface.

The large NA needed to resolve smaller details also implies an extremely shallow depth of field. Given the roughness of the cleaved surface, this often meant the entire region of interest could not simultaneously be in focus. In part these limitations can be overcome with SEM. Visual light microscopy was used to screen samples before SEM.

2.1.3 SEM and FIB

Microscopy using electrons has several advantageous characteristics compared with light microscopy. As an electron has both mass and charge, it is strongly interacting, allowing the electron to be accelerated to high energies and hence short wavelengths.[65] The relativistic equation for the De Broglie wavelength is provided below where; h is the Planck's constant, m_0 is the rest mass of the electron, E is the energy and c is the speed of light.

$$\lambda = \frac{h}{\left(2m_0E\left[1+\frac{E}{2m_0c^2}\right]\right)^{1/2}} \tag{2.2}$$

In an SEM energies of $1-30$ keV are typically used, which correspond to a wavelength of $0.039-0.007$ nm respectively. Clearly the resolution of an electron microscope will drastically surpass that of an optical microscope. However, the lenses used for electrons are based on magnetic or electrostatic fields and suffer from significant chromatic and spherical aberrations. These aberrations can be minimised by truncating the incident beam using an aperture such that only the central portion is used. This reduces the effective NA, but counter intuitively improves resolution. A consequence of this is that the depth of fields in electron microscopes are comparatively deep. Thus, despite the poor quality of the lenses, an SEM can surpass both the resolution and depth of field limitations that visual light microscopy has.[65]

Imaging itself is achieved by focusing the incident beam into a small probe on the sample, and raster scanning the probe. Sequentially, at each point on the scan, a signal is collected to form an image. A variety of signals are produced as the incident electrons interact with the sample. In this work only the secondary electrons are of relevance. These are generated as the incident electrons ionise atoms within the material. Secondary electrons escape only

from a small, near surface volume, making them highly sensitive to topography, and the images intuitively understandable on that basis.

In this work secondary electron SEM imaging is used to examine the cleaved surfaces, as well as to check for features during sample preparation using the FIB. In FIB samples the modifications do not appreciably differ when imaged in SEM and only voids or cracks are observable, assuming they are present.

With the basics of SEM established, several practical constraints must be mentioned. Conventional SEMs require clean, non-volatile and electrically ground samples. Insufficient grounding can lead to charge build up, which may both deflect electrons, and thus distort the image, as well as potentially damaging the sample. Si, when suitably mounted would generally be considered to satisfy these requirements. Suitable mounting, in this work, was generally achieved by attaching the sample to an Al stub using Ag paste.

At a superficial level, a FIB is very similar to an SEM with the exception that the FIB uses high energy ions. Typically Ga^+ ions with an energy of $1 - 30\ keV$ are used. These can produce similar sorts of signals, and thus images, to high energy electrons. However, minor technical differences can be advantageous in highlighting different characteristics of the sample. So, from a characterisation perspective, FIBs have their own specific merits.[66]

The increased mass of an ion relative to an electron also allows for the displacement of atoms in the target material. This will cause damage or amorphisation of a thin surface layer of material. More usefully, it can also sputter atoms from the surface, which serves as a mechanism for highly precise milling, which is the principle use of FIBs in this work.[66] It was used to mill thin sections for TEM examination, the procedures and geometry of which are provided below.

Equipment

In this work SEM and FIB were performed on dual beam instruments.* The majority of the work was performed with an FEI Helios 600 NanoLab in the Canberra branch of the Australian National Fabrication Facility in the ANU. Some work was also conducted on an FEI Scios at the RMIT Microscopy and Microanalysis Facility. The latter was largely used for the initial milling of the long axis cross-sections of the modifications, and for preparing samples for electron energy loss spectroscopy (EELS), both of which will be discussed below.

2.1.4 TEM

In TEM, as with SEM, a sample is probed with high energy electrons, typically $60 - 300\ keV$. By making the sample sufficiently thin, it is possible for electrons to either pass right through the sample unaffected, or to be forward scattered. The thickness required depends upon the material and the specifics of the signal of interest, but is generally stated to be less than $100\ nm$. The electrons that forward scatter may be categorised by whether they scatter inelastically or elastically. They may also be categorised by whether they remain coherent.

Incoherent inelastically scattered electrons definitionally have changed energy (typically lost energy), for example due to ionisation of an atom within the sample. This will be discussed in greater depth in the EELS section.

Coherent elastic scattering is largely the result of diffraction.[65] It is assumed that the reader is familiar with diffraction within a material, but briefly, diffraction occurs when Bragg's law is satisfied (subject to certain selection rules), the formula for which is shown here:

*Instruments with both an electron beam and an ion beam. In these instruments the electron and ion columns are displaced by a 52° angle to each other.

$$2d\sin(\theta) = n\lambda \tag{2.3}$$

where d is the interplanar distance, θ is the scattering angle and n is an integer.

A useful tool for considering which crystalline planes satisfy Bragg's law is the Ewald sphere construction. When the sphere cuts through reciprocal lattice points Bragg conditions are satisfied. However, in thin TEM samples the Bragg conditions are relaxed and the reciprocal lattice points expand into rods parallel to the thin axis of the sample. The rods may intersect the Ewald sphere even if Bragg conditions aren't perfectly met. Diffraction can be a significant scattering process in crystalline samples, and one that varies depending on crystal orientation.[65]

Incoherent elastic scattering is largely associated with Rutherford scattering. Again, the reader is assumed to be familiar with this topic, but it will be emphasised this has a dependence on the atomic mass of the atom(s) off which the electron scattered. It will also increase with sample thickness.[65]

Each form of scattering has a different scattering angle dependence. Unscattered electrons are transmitted directly through with no deviation. Inelastically scattered electrons generally undergo minimal deflection and are, thus, almost parallel with unscattered electrons. Coherent elastic scattering is predominant at small angles. Incoherent elastically scattered electrons dominant at larger angles. It should be emphasised that these generalisations breakdown if multiple scattering events occur for each electron, in which case diffuse scattering is said to occur.[65]

All these scattered components can be focussed to create a scatter pattern on which the central feature is a spot from unscattered and inelastically scattered electrons, often called the direct beam. Surrounding this are diffraction spots or rings, from crystalline or amorphous material respectively. As the diffraction component is the dominant feature, the scatter patterns are commonly known as diffraction patterns. These patterns contain a great deal of useful information, but it is also possible to create images from the pattern. The contrast of the resulting images can broadly be divided into three categories; mass thickness contrast (from incoherent elastic scattering and perhaps diffuse scattering), diffraction contrast, and phase contrast (from the interference between coherently scattered components).[65] The exact manner in which the image is created, and the prevalence of each source of contrast is a product of the specific experimental technique. As TEMs are enormously powerful and flexible instruments, a wide range of techniques are possible. In this section the most important techniques to this work and the subtleties therein will be introduced. However, it is by no means comprehensive. For further information a range of textbooks are available.[65,67,68]

Conventional TEM

The key components of a conventional TEM consist of an electron gun, the condenser lens system, the objective lens system, the project lens systems and an electron detection system. A slightly more detailed diagram is provided in Fig. 2.1. The sample sits within the objective lens system, and a region of the sample is illuminated by (ideally) a parallel beam of electrons. Below the sample, a diffraction pattern is formed at the back focal plane of the objective lens; while an image is formed at the image plane. By controlling the strength of a post sample lens in the projector system (the intermediate lens), it is possible to project either of these down to the detection system below.[65] A ray diagram demonstrating this is shown in Fig. 2.2.

It is also possible to make use of apertures to manipulate the resultant image or diffraction pattern. An aperture inserted on the image plane restricts the region of the sample from which electrons are able to contribute to the projected diffraction pattern. For this reason, the resultant pattern is called a selected area diffraction pattern (SADP) and the aperture is a selected area

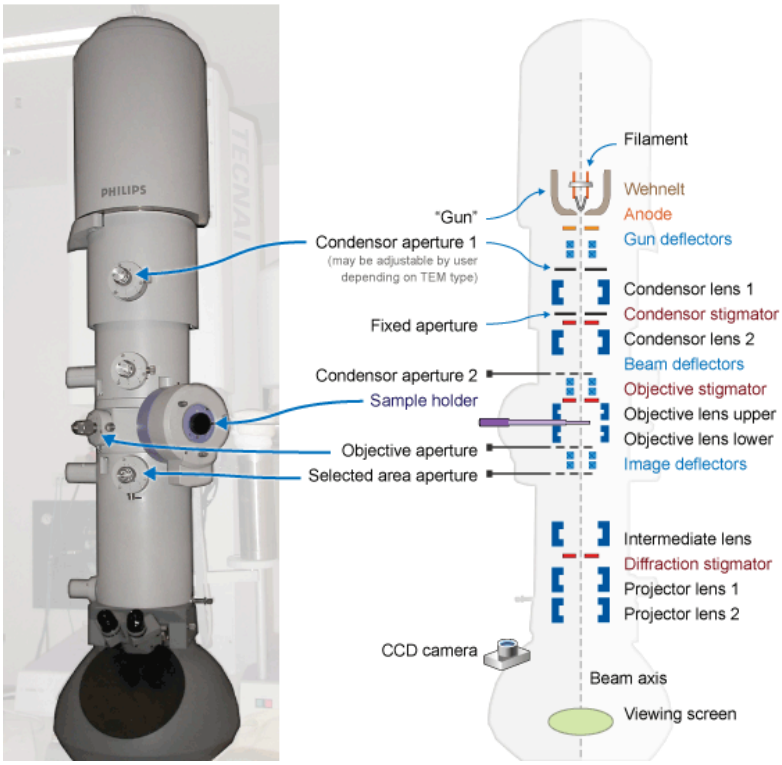

Figure 2.1: A schematic diagram of the optical components of a TEM. Adapted from[69].

diffraction (SAD) aperture.[65] Alternatively, an aperture inserted in the back focal plane will restrict the electrons that contribute to the projected image. This aperture is called an objective aperture.[65] Again, both cases are shown in Fig. 2.2.

Several special classes of images can be created using the objective aperture. Placing the aperture to admit only the direct beam results in a bright field (BF) image. Such an image is bright except for where the material is strongly diffracting, or there is significant mass thickness contrast. Alternatively, the aperture maybe placed over a diffracted beam, in which case the image is dark except for where the material is strongly diffracting. This is called a dark field (DF) image.[65] These imaging modes are controlling diffraction contrast (although mass thickness contrast and phase contrast may still be present).

Recall that diffraction contrast is also dependent on the crystal orientation. It follows that tilting the sample is a further mechanism to control diffraction contrast. The sample can be tilted such that the incident beam is parallel to a low index crystal direction. This condition allows many different lattice planes to satisfy Bragg conditions, leading to many diffraction spots, and a so-called zone axis (ZA) diffraction pattern. Any image created under such conditions will have many different components contributing to the overall contrast. As such a ZA image is rich in details, but relatively difficult to analyse. Instead, the sample can be tilted to specific conditions where only one Bragg condition is strongly excited. With the addition to the direct beam, this means there are only two spots in the diffraction pattern, and this is called a two-beam condition. This condition is often desirable as it implies that (ideally) all diffraction contrast can be associated with only a single Bragg condition. This can clearly simplify analysis as well as allowing for specific crystallographic information to be extracted.[65] Previously it was stated that some deviation from Bragg conditions was acceptable for electron diffraction in TEM. Thus, in reality, other Bragg reflections do tend to be weakly excited in a two-beam condition, which allows for another style of imaging. By placing an objective aperture over one of these very

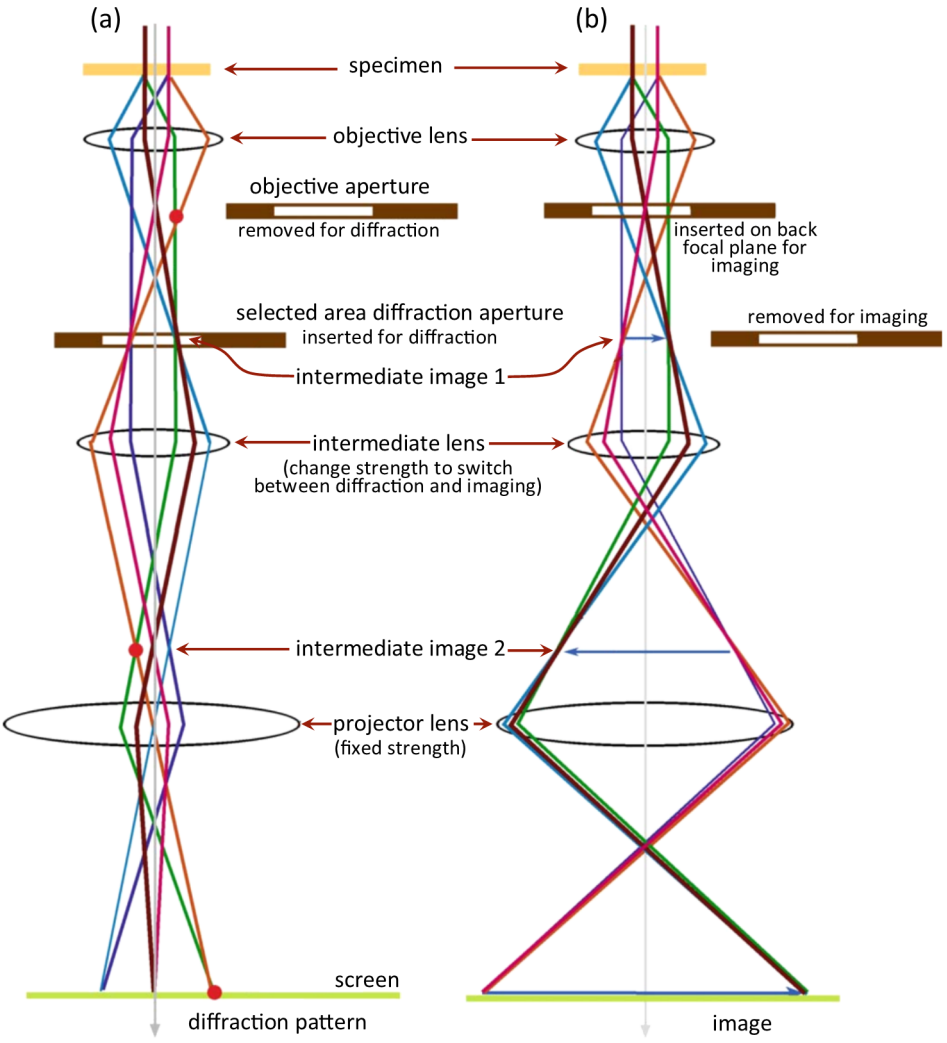

Figure 2.2: A schematic ray diagram of the imaging system in a TEM in two basic operating modes. In (a) the intermediate lens is focused on the back focal plane and projects a diffraction pattern down the column. In (b) the intermediate lens is focussed on the first intermediate image and projects a magnified image down the column. Image adapted from[65].

weakly excited reflections, a weak-beam image can be created. These have drastically lower intensity, but afford more precise, higher resolution imaging of features.[65]

One final diffraction contrast feature must be discussed. Real samples, particularly when thinned to electron transparency, tend to bend somewhat. As such the sample tends to bend in and out of Bragg conditions, resulting in alternating bright and dark regions in images, this is known as bend contrast.[65] In general, these are regarded as an artefact, although they can provide some qualitative feedback as to the stress and strain within the sample. On-ZA images are most sensitive to this, thus, tilting slightly off-ZA allows for major features to remain diffracting, but greatly reduces bend contrast.

Phase contrast

Instead of selecting a single spot from the diffraction pattern to create an image, a larger objective aperture may be used to admit both the direct beam, as well as several diffracted beams. This minimises diffraction contrast, but allows for interference between multiple beams with different phase, and thus phase contrast. When performed on-ZA, this phase contrast allows images with lattice level resolution to be produced. So called high resolution imaging. This is a powerful method to examine crystalline defects and other small features.[65] The modifications examined in this work are not examined at this detail.

Phase contrast can also be produced under other conditions which are of relevance to this work. One such case is the formation of thickness fringes. Recall that in thin samples, the Bragg conditions are relaxed due to the expansion of reciprocal lattice points into rods. If the sample thickness varies there are two surfaces that aren't parallel, and thus, the expansion occurs in two directions. It follows that Bragg conditions can be met by both rods, and these spots may interfere with each other, creating phase contrast.[65] TEM samples in this work are relatively planar, but inclined internal features (that do occur in this work) can produce a similar effect.

A second phase contrast condition of relevance to this work is created by stacking faults[70], twinning[71] and the 9R structure[72]. These are crystal defects, that in Si can be considered as thin platelets of hexagonal crystal within the diamond cubic lattice. Thus, the cross-section may be considered as two wedges of ordinary Si separated by the hexagonal crystal. This can again lead to phase contrast in a similar manner to the previous example. In Si, stacking faults, twins and the 9R structure are favoured on {111} planes. These are also readily observed in diffraction patterns where additional spots form at one third increments of the {111} spots. No attempt is made to specifically distinguish between these defects in this work. The term 'twinning-like defect' will be used to refer to all these structures collectively.

Finally, if viewed out of focus, voids and cracks can produce a particular form of phase contrast known as Fresnel fringes.[65] This technique is therefore useful to find the voids and cracks which are present within the modifications examined in this thesis.

Convergent beam electron diffraction and nanobeam electron diffraction

Whereas conventional TEM is conducted with parallel illumination of the sample, convergent beam diffraction (CBED) uses a convergent beam. This can easily be achieved with some simple changes to the condenser lens system. In such a condition, diffracted electrons are no longer brought to a sharp focus, but rather form discs. From the discs, it is possible to extract much more precise data than from conventional SADP, and thus this technique is of interest for quantitative measurements.[65] Another characteristic of interest is that CBED forms a small probe, allowing information to be collected from a smaller area than is generally possible from a SADP. This characteristic is of interest for characterising crystallites smaller than can be

selected with a SAD aperture; a matter that is sometimes of relevance to this work. However, as it produces discs, small diffraction spots are easily missed.[65]

A similar, but alternative approach to CBED is nanobeam electron diffraction (NBED). As with CBED, the condenser lens system is used to produce a convergent beam, but in this case optimised to be much closer to parallel while still probing a very small area.[65] Because this is much more difficult to set up, and the resultant diffraction patterns are generally of a lower quality than SADPs, NBED results will not be presented in this thesis. However, they were used in this work and were sometimes critical in identifying the individual components in the analysis of conventional SADPs, which will be presented.

Scanning transmission electron microscopy

Scanning Tranmission Electron Microscopy (STEM) is something of a hybrid between conventional SEM and TEM. As with SEM, CBED and NBED a convergent beam is used to form a probe on the sample, and as with SEM this beam is raster scanned over the sample (but kept parallel to the optic axis).

As with TEM the forward scattered signals are of principle interest. For imaging, the central spot of unscattered and inelastically scatted electrons can be collected with a BF detector. An objective aperture may also be used to boost the contrast in BF STEM images. STEMs are also fitted with an annulus detector that collects electrons scattered only at higher angles. The angular range collected can then be varied with the camera length, that is by changing the parameters of the projector lens system. As such, it is possible to collect signal from multiple diffraction spots at smaller angles, or incoherent elastically scattered electrons at high angles. These are, respectively, annular dark field (ADF) or high angle annular dark field (HAADF) images. These differ significantly, ADF images contain a great deal of diffraction contrast, whereas HAADF images are strongly dependent on mass thickness contrast, and can thus differentiate areas based on the atomic mass of the constituent elements.[65] HAADF imaging capability has no strong parallel in conventional TEM, at least for strongly diffracting crystalline samples, and thus, is a useful mode which is capitalised on in this work. Some care is needed when using HAADF however, as electron channelling can drastically change the contrast, leading to misleading results.

Several other characteristics are worth noting in STEM. As a convergent beam is used, the images are less susceptible to minor changes in Bragg conditions. They are therefore less susceptible to bend contrast. Furthermore, as they form a probe on the sample, chromatic aberration in thick samples is less detrimental to image resolution.[65] Finally, the scanning probe nature of the STEM is well suited to analytical electron microscopy (AEM). AEM is based on the collection of a spectrum at the probe's location. By raster scanning the probe, a four-dimensional (or larger) data set can be created, which in the electron microscopy community is called a spectrum image.

Electron energy loss spectroscopy

As incident electrons interact with the sample, they may inelastically scatter. Electron energy loss spectroscopy (EELS) measures the energy of electrons in the direct beam that have lost energy due to these interactions. The EELS spectrum may be divided into three segments: zero-loss, low-loss and core-loss. Electrons that have not lost energy contribute to the zero-loss region. Those that lose energy due to interactions with outer shell electrons of the sample contribute to the low-loss region of the spectrum. Electrons that interact with inner-shell electrons of the sample contribute to core-loss portion of the spectrum.[73,74]

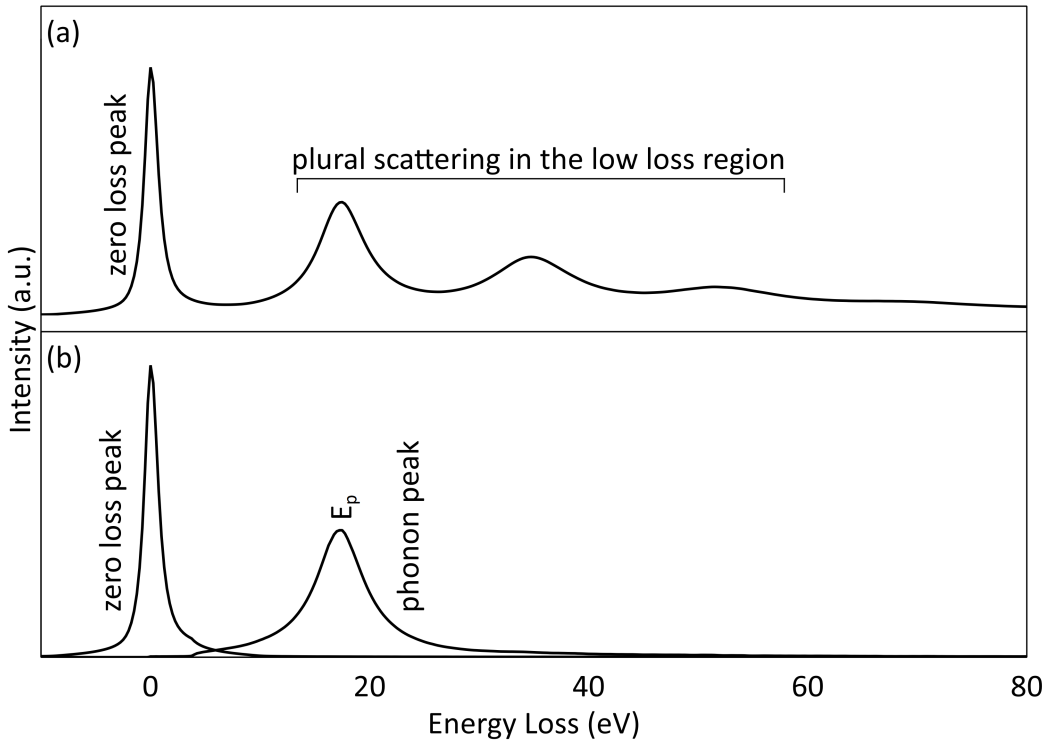

Figure 2.3: An example EELS spectrum as recorded in a-Si, (a), where the zero loss peak is labelled and the low loss region consists of multiple peaks due to plural scattering. In (b) a Fourier-Log deconvolution eliminates the plural scattering effects and separates the zero loss and low loss regions.

In this work EELS is used to measure the density of amorphous Si (a-Si), which makes use of the low-loss region of the spectrum. An example of the zero and low loss region in a-Si is presented in Fig. 2.3. The principle component of the low-loss region is electrons that have lost energy due to interactions with plasmons within the sample. In (a) multiple peaks are visible due to plural scattering. A Fourier-Log deconvolution may be used to remove the effects of plural scattering and deconvolute the zero loss peak from the low loss peak. The outcome of this process is shown in (b).

The plasmon energy, E_p, may be expressed as[73]:

$$E_p = \hbar \left(\frac{n_e e^2}{\varepsilon_0 m_e^*} \right)^{1/2} \tag{2.4}$$

where n_e is the valance electron density, ε_0 is the vacuum dielectric function and m_e^* is the electron effective mass, e is the electron charge and $\hbar$ is the reduced Planck's constant. The (longitudinal) effective electron mass is known for dc-Si to be 0.98 times electron mass.[75] Theoretical calculations show that a-Si has an equivalent effective electron mass, and so this value is used in this work.[76]

The valance electron density can be related to the mass density, ρ_0, assuming each Si atom contributes four valance electrons[77]:

$$n_e = \rho_0 \frac{4N_A}{M_{Si}} \tag{2.5}$$

where N_A is the Avogadro constant and M_{Si} is the atomic mass of Si. Combining Equation 2.4 and Equation 2.5 yields:

$$\rho_0 = E_p^2 \frac{\varepsilon_0 M_{Si} m_e^*}{4\hbar^2 N_A e^2} \tag{2.6}$$

Thus allowing the density of the a-Si to be determined from the plasmon energy.

Equipment

The majority of the TEM characterisation was conducted using two microscopes located at the Centre for Advanced Microscopy at the ANU; a Philips CM300 conventional TEM operating at 300 keV and a Jeol JEM-2100F at 200 keV for both conventional and STEM work.

EELS was conducted at the Harvard University Centre for Nanoscale Systems using a Jeol JEM-ARM200F cold FEG system operating in at 200 keV in STEM mode and with a Gatan Image Filter (GIF) EELS system.

Some work was also conducted at a variety of other microscopes, generally due to availability rather than any technical requirement. Again at the Centre for Advanced Microscopy a Hitachi 7100 operating at 125 keV was used for conventional TEM work. At Harvard University a Jeol JEM-2010F operating at 200 keV was used for conventional TEM work. Finally, at the RMIT Microscopy and Microanalysis Facility a Jeol JEM-2010 operating at 200 kV was used for conventional TEM and a Jeol JEM-2100F operating at either 80 keV or 200 keV was used for both conventional TEM and STEM work.

2.1.5 Raman microspectroscopy

Light incident on a material may scatter off electrons by absorption then emission via a virtual energy state. This primarily occurs via elastic Rayleigh scattering, but can also occur inelastically via Raman scattering, a process 5-6 orders of magnitude weaker than Rayleigh scattering. Energy transfer occurs due to interaction with vibrational energy states, i.e. due to phonons, and may result in a loss of energy, or gain of energy by the photon. These cases are known as Stokes and anti-Stokes scattering respectively.[78] A simple energy diagram of these three cases is shown in Fig. 2.4.

Raman scattering is subject to selection rules which require a change of polarizability with respect to the vibrational mode. In crystals, only specific phonon modes can satisfy these requirements, which in turn leads to well defined Raman transitions. As the properties of the crystal changes, so too does the Raman scattering. At one extreme is amorphous materials, where phonon modes are no longer well defined and broad brands of transitions are possible. Metals are not polarizable, and hence are Raman inactive.[78,79]

Spectroscopy of Raman scattered photons serves both to fingerprint non-metallic materials, and also provides a route to characterise vibrational properties (and hence local bonding arrangements) of these material. In this work it is the fingerprinting capability that is primarily of interest, allowing different phases of Si to be identified. Raman spectroscopy was also used to examine strain, which is known to change the vibrational properties and in turn the phonon energy. This is most readily examined using the shift in the $\sim 520\ cm^{-1}$ spectral peak of diamond cubic Si (dc-Si).[80,81]

A Renishaw Raman spectrometer was used to perform microspectroscopy of the Strokes scattered photons. This involved illuminating the sample with laser light focussed through an 0.85 NA objective lens, then collecting the scattered light through the same objective lens. After filtering out the Rayleigh component, the Raman component was dispersed with a grating onto a CCD sensor to be recorded. Motorisation of the sample stage further allowed for maps of Raman spectra to be collected, analogous to the spectrum images in electron microscopy. The lateral

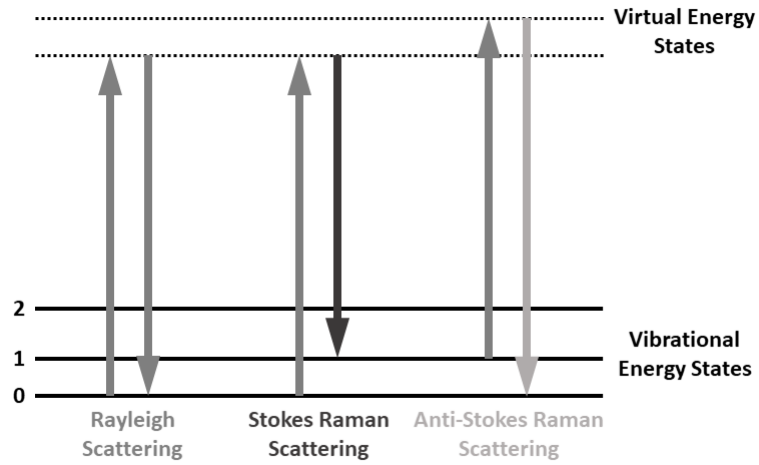

Figure 2.4: Schematic of the transitions in energy states for Rayleigh scattering, Stokes Raman scattering and anti-Stokes scattering.

resolution of said maps was determined by the spot size, d, for which the Rayleigh criterion may again be referenced, this time in its spot size form:

$$d = \frac{1.22\lambda}{\sin(\theta)} = \frac{1.22\lambda}{NA} \tag{2.7}$$

The Raman signal is also dependent on the depth from which signal is collected, a parameter that is less easily defined than spot size as it is additionally dependent on the morphology itself. However, longer wavelengths have a larger interaction depth, which could be tested as the system was fitted with a 532 nm, a 633 nm and a 785 nm laser. The 633 nm laser was found to have the best compromise of resolution and penetration depth. The 532 nm laser was also used in some cases, but appeared to have insufficient penetration to fully sample all the modified material.

Finally, it should be noted that as intense lasers are used to probe the material, it is possible to induce heating and even damage during Raman spectroscopy. Laser power can be reduced, but this must be balanced against increased acquisition time.

2.2 Laser processing

As previously stated, samples for this work were supplied by our collaborators at the University of Twente and at ALSI. Both used the same type of 160 μm thick (100) Si wafers with moderate boron doping and a resistivity of 10.3 $\Omega \cdot cm$.

2.2.1 Laser conditions

Samples prepared in the sub-bandgap process used a MWTechnologies MOPA-LF-1550 laser with a wavelength of 1549 nm and a pulse duration of 3.5 ns FWHM. The laser output was positively skewed with time.

For focussing a Leica 11 101 666 IR objective with a 0.7 NA was used. This is cover corrected for 100 μm of Si in which case the laser had a M^2 beam quality of 1.1 and a theoretical e^{-2} spot size of 2.37 μm. However, modifications examined in this work were not aimed at this depth and, additionally, a thin quartz window was used to protect the objective in case of accidental ablation.

The majority of the work presented in this thesis is based on modifications produced with a 2 μJ on sample pulse energy. This pulse energy was selected as a being suitable for wafer dicing, and thus serving a 'standard' condition. A comparison is also made with 0.6 μJ pulses, which are slightly above the threshold for observable modifications using IR microscopy. These will be termed 'low energy modifications'.

A further comparison is made with 'near-bandgap' modifications produced by ALSI. For this, a 1064 nm laser, with a 220 ns pulse duration and a 4 μJ pulse energy were used.

2.2.2 Sample geometry

To distinguish between the morphology corresponding to isolated modifications, closely spaced interacting modifications, and modifications after cleaving, a set of samples were made for each condition. These each had a unique sample geometry.

Isolated modifications were produced in a single row with a 20 μm transverse spacing, sufficient to prevent interactions between the modifications and accidental dicing of the sample. Closely spaced modifications were produced with a 2 μm transverse spacing as is used for dicing, but only a single segmented row was produced. That is, over a 50 μm transverse spacing, 25 modifications were produced, followed by a 150 μm gap before the next set of modifications. This is sufficient to prevent accidental dicing of the sample, but allowed the interaction between closely spaced modifications to be examined. In both these cases a second set of modifications were produced on a plane 50 μm separated from the target plane. The second plane of modifications was then cleaved. The cleaved surface served as a starting point of further sample preparation to access the target modifications. For the cleaved samples a 2 μm transverse spacing was used between modifications, and three rows of modifications were used over the depth of the wafer. A schematic of each case is shown in Fig. 2.5.

Only the standard, sub-bandgap, modifications were produced in all three geometries. The low energy modifications are produced in isolation, while the near-bandgap modifications were produced only under cleaving conditions. The terminology introduced here will be maintained throughout the thesis.

2.3 Sample preparation

For sample preparation a distinction between examining the short axis and the long axis of the columnar modification is warranted. Both were examined in this work, as shown schematically in Fig. 2.9, and slightly different approaches were needed to prepare samples for each.

A distinction can also be made between samples with subsurface modifications, and those that have been cleaved. The latter required no preparation other than mounting for optical, SEM and Raman examination. For TEM sample preparation was required, but this was relatively trivial and was essentially a subset of the process for subsurface modifications.

Subsurface modifications can not be usefully examined optically or by SEM. It follows that the objective was to prepare the samples for TEM and Raman examination with guidance from IR microscopy. In both cases, the initial step was to remove the $\sim$ 50 μm of excess material between the cleaved surface, and the plane of modifications. For TEM, the modifications were sectioned. All successful sectioning was performed using a FIB. FIB sectioning was either performed directly from polished sample using the ex-situ lift out approach, or produced as H-bar samples. These will be detailed further below, but initially the key distinction is that these require a slightly different polishing process.

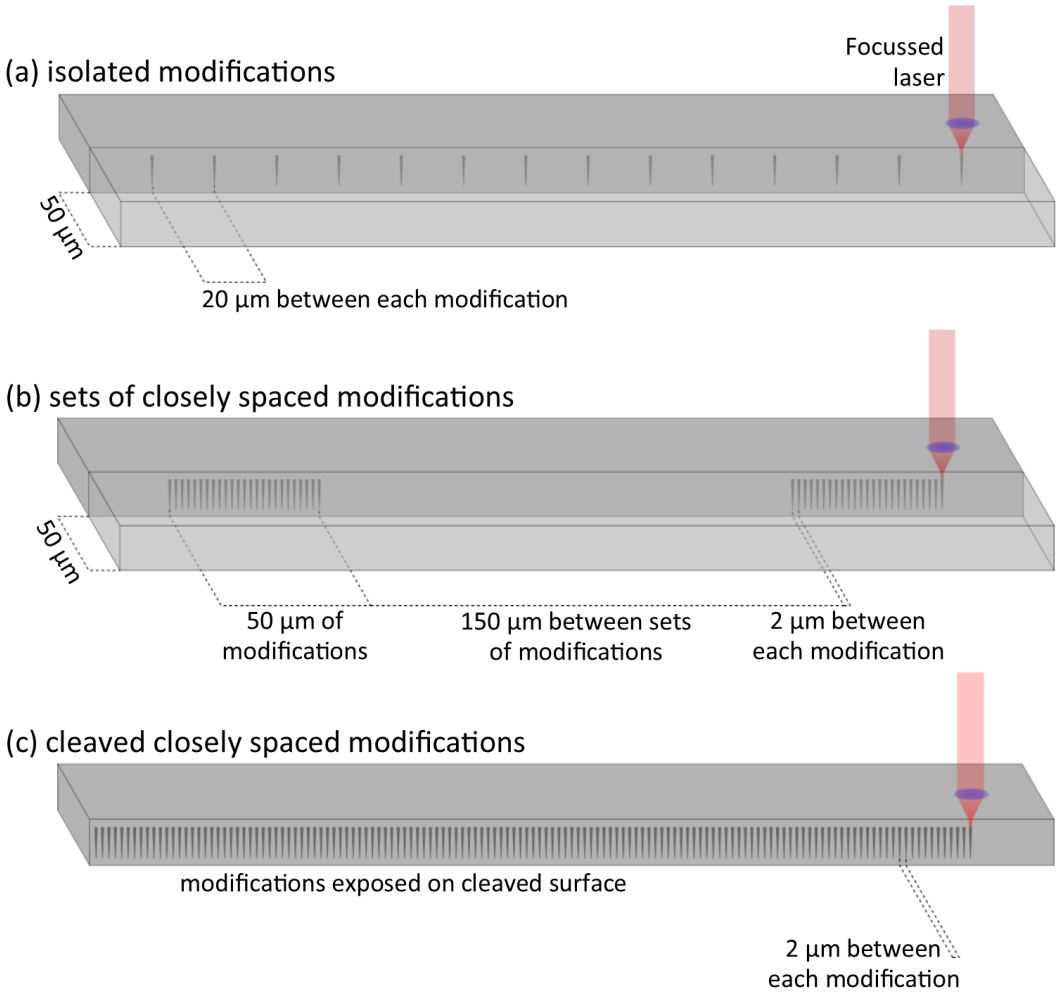

Figure 2.5: Schematics of the three sample geometries used in this work. Isolated modifications, (a), were produced 50 μm from a sample edge and with 20 μm between each modification. Closely spaced but uncleaved modifications, (b), were produced with a 2 μm spacing as used for dicing, but in sets of only 25 modifications with a 150 μm between each set to prevent accidental dicing. The deliberately cleaved samples, (c), had continuous rows of modifications each separated by 2 μm.

2.3.1 Tripod polishing

The tripod polishing process (also known as wedge polishing) uses a system with three points of contact with the polishing medium, the sample and two legs connected to micrometres. It is possible to precisely control alignment of the sample by adjusting the micrometres. Tripod polishing was used in this work to remove most of the $\sim 50\ \mu m$ of material between the cleaved surface and the target modifications. Alignment was cross-checked against the initial cleaved surface, the side walls of the sample, and the modifications as viewed in IR. The polishing medium was diamond lapping films and the final grit was $0.1\ \mu m$. This approach results in a very flat surface with minimal polishing damage.

For Raman spectroscopy the objective was to polish such that the modifications would be as close to the surface as possible, without introducing surface damage. This damage would generally occur as the modifications began to intersect the surface. With a deliberate slight misalignment of the tripod polishing system, surface damage on the modifications nearest the surface would leave those modifications that were slightly deeper subsurface in an excellent state for Raman examination. This approach left the long axis of the modification coplanar with, but slightly below the surface. Thus, Raman spectroscopy would examine the long axis of the modification, as shown schematically in Fig. 2.9.

For TEM, the same basic approach was taken as for Raman spectroscopy sampples, but the target was to leave the modifications slightly further subsurface. For short axis cross-sections, a target of $\sim 1\ \mu m$ from the surface to the periphery of the sample was desired. For the long axis samples the target was $10 - 15\ \mu m$. This distance was judged using IR microscopy. Given the practical and resolution limitations of the IR microscope, such precision was not always achieved. Indeed, several examples are presented in this thesis where a portion of the modification was polished off.

Further polishing steps were required for H-bar samples which were used for long axis cross-sections and some short axis cross-sections. In the former case the samples were polished from the opposite side such that the modifications were $10 - 15\ \mu m$ subsurface from either side. The resultant sample was thus $20 - 30\ \mu m$ thick in one-dimension, $160\ \mu m$ thick in another, and $3\ mm$ wide. It should be appreciated that these samples were inherently far more delicate than normal TEM samples as they were thin in two-dimensions, not one, and were filled with modifications intended to break Si.

H-bars intended to examine the morphology of the short axis required thinning perpendicular to the initial polishing direction so the sample would be perhaps $30\ \mu m \times 2\ mm \times 3\ mm$. In this case the sample is thin only in one-dimension. However, this approach was used for closely spaced modifications, which were even more fragile than isolated modifications.

Samples prepared in the H-bar style were glued to a TEM half grid which was subsequently used for handling the sample.

2.3.2 FIB milling

FIB milling was used to prepare the TEM cross-sections with both the ex-situ liftout technique and the H-bar technique.

ex-situ liftout

The ex-situ liftout process was performed on both polished and cleaved samples to prepare short axis cross-sections. For polished samples a reference point is needed so the cross-section could be created to overlap the modifications, which are not visible in SEM/FIB. This was

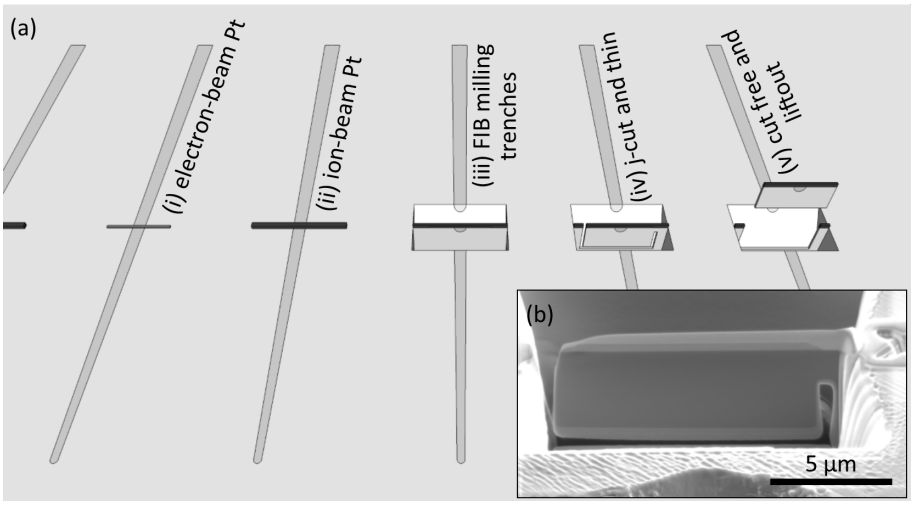

Figure 2.6: The FIB ex-situ liftout technique shown schematically, (a), involves depositing a protective layer of Pt first using the electron-beam, (i). A thicker Pt layer is deposited with the ion-beam, (ii). Trenches are milled either side of the indented cross-section, (iii). The cross-section is mostly cut free with a j-cut, (iv). The sample in then thinned before finally being cut free, (v). A glass needle on a micromanipulator is used ex-situ to remove the cross-section and place it on a TEM grid. In a sample imaged with SEM the modifications are not visible as shown (b).

achieved by examination of the modification's location using IR microscopy relative to a piece of contamination or damage that could be identified in the SEM. Once a region of interest was determined, a relatively standard milling process followed. Initially a protective Pt layer was deposited at any position desired along the modifications length.[†] Next, triangular trenches were dug either side of the region of interest using a high beam current and 30 keV beam. A j-cut is then performed to mostly cut the cross-section free. The cross-section was then thinned at glancing angles and with incrementally decreasing beam current and voltage. Finally, the sample is cut free. This process is illustrated schematically in Fig. 2.6 (a). Although shown in the schematic, the modifications are not visible in SEM as shown in (b).

After cutting free, the cross-section is manoeuvred ex-situ using a micromanipulator controlling a drawn glass needle. The needle attracts the cross-section electrostatically. It is then placed on a TEM grid with a carbon film, which the cross-section adheres to.

H-bar

The H-bar process first requires that a thin sample be attached to a TEM half grid. The region of interest was again protected with Pt, and again material was milled from either side. In this case much more material was removed so that a path was available for electrons in the TEM. A schematic of a H-bar sample is shown in Fig. 2.7 (a). An SEM image of short axis cross-sections in an H-bar sample is shown in (b).

The H-bar process is an older and less popular FIB based sample preparation method, presumably in part because it requires more initial preparation than the modern alternative. It nevertheless has several advantages which are of relevance to its use in this work. The first advantage is that for samples that have been mechanically thinned before being placed in the FIB, less FIB milling is required. Given the high costs of FIB work, this is a not inconsequential

[†]Pt is first deposited using a precursor gas that is cracked by the electron beam. Once a basic level of protection is achieved the deposition is instead performed with the more efficient ion beam.

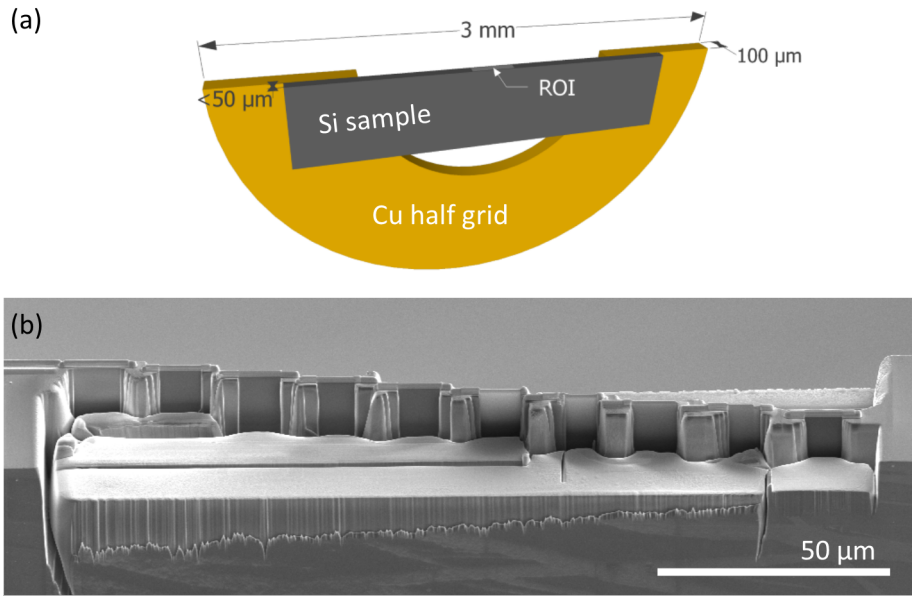

Figure 2.7: A schematic of an H-bar sample, (a). The sample is first mechanically thinned, then mounted on a Cu TEM half grid for subsequent milling in the FIB. An SEM image of the ROI of an H-bar sample with 10 short axis cross-sections is shown in (b).

advantage. However, because of the fragility of the samples in this work, they were left too thick to fully realise this advantage. A second advantage is that the sample can be returned to the FIB for further thinning, unlike ex-situ liftout samples. This advantage was capitalised on in this work, particularly for the long axis modifications where thinning was a highly iterative process. A third advantage is that the thin sections never directly require handling, and furthermore, can be left better supported by the surrounding thick material. They are thus less prone to breaking. Finally, a valuable characteristic for this work is that cross-sections do not get moved relative to the bulk. It is thus easier, and more precise to cross-correlate the position of adjacent modifications. This was critical for long axis cross-sectioning. Specifically, this was achieved by creating angled short axis cross-sections at several depths along a modification. By imaging the modification in STEM mode, combined with extremely careful measurement of the geometry, it was possible to precisely mill the long axis of adjacent modifications. In practice, this wasn't always perfect, but it was always sufficient to provide useful information.

In Fig. 2.8 the result of FIB milling an H-bar sample for long axis cross-sections is shown. Also visible are the angled short axis cross-sections used to help align the cross-sectioning of the adjacent modifications.

It should be noted that the long axis of standard modifications were approximately 50 μm long. Thus, the electron transparent region needed to be approximately 5 $\mu m \times 60$ μm. This is far larger than normal TEM samples and it was not possible to thin such a large area to a thickness that would typically be considered ideal for TEM. Short axis cross-section could be thinned to ~ 100 nm but rarely were as it was neither necessary and may have affected the stability of certain phase transformed regions.

As special note for the sample examined by EELS. This sample was prepared as a short axis H-bar. As EELS is a highly sensitive analytical technique, it was deemed necessary to reduce the thickness of the surface damage layer. To that end a Fischione 1040 NanoMill was used for a final mill. This is essentially a low voltage Ar FIB that produces a thinner damage layer compared with a Ga FIB.

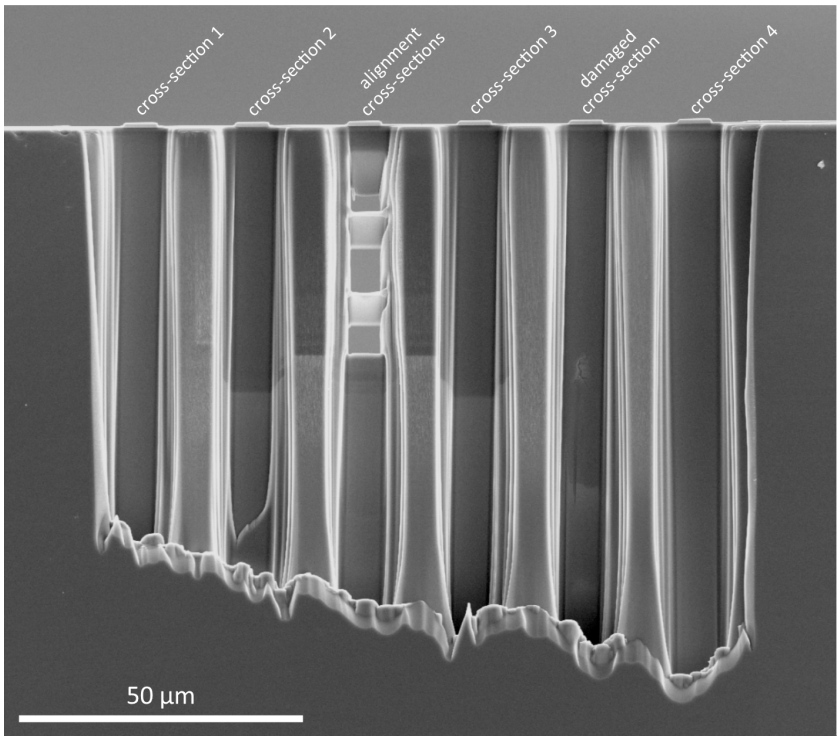

Figure 2.8: An SEM image of long axis cross-sections prepared in an H-bar sample. Alignment cross-sections were created on one modification to guide the final thinning of the adjacent modifications. One cross-section is damaged due to the sample degrading once thinned.

2.4 Modification summary

To conclude the experimental section a summary of the samples examined and the sample preparation performed on them is given below in Table 2.4. Figure 2.9 illustrates the perspectives of Raman spectroscopy, TEM on long axis cross-sections and TEM on short axis cross-sections.

Table 2.1: Summary of the samples, their geometry and the preparation processes that have been used.

	Sub-bandgap (1549 nm, 3.5 ns)				Near-bandgap (1064 nm, 220 ns)
	Standard 2 μJ			Low energy 0.6 μJ	Standard 4 μJ
Geometry	Isolated	Closely spaced	Cleaved	Isolated	Cleaved
Raman	✓	✓		✓	✓
Short axis liftout	✓	✓	✓		✓
Short axis H-bar	✓	✓		✓	
Long axis H-bar	✓			✓	

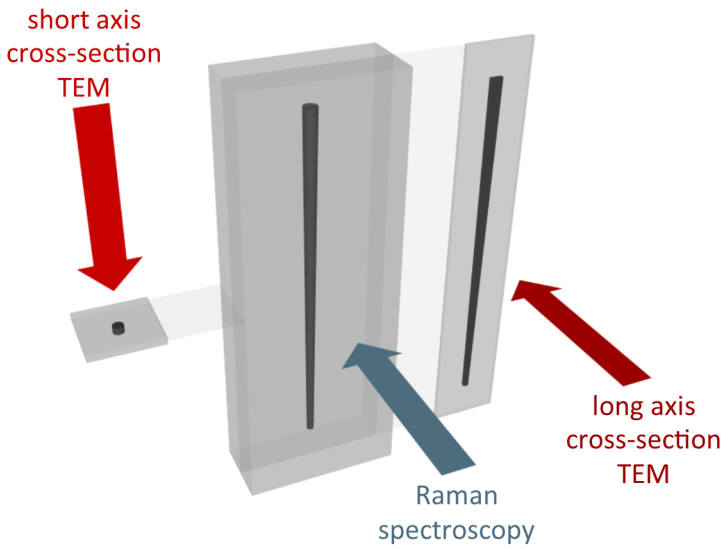

Figure 2.9: An illustration of the perspective of the key experimental techniques.

Chapter 3

Overview of the modifications

The morphology of the laser-induced modifications consists of many interrelated structural features. It is therefore difficult to investigate the individual features without knowledge of their wider context. This chapter intends to provide an overview of the various structural features in order to provide that context for subsequent chapters. It will do so with results from standard modifications produced in Si with the sub-bandgap regime laser process. Where possible isolated modifications will be used.

A second aim of this chapter is to present results from each of the main experimental techniques to demonstrate which structural features they are suitable for investigating. In doing so many of the subtleties involved in analysing these results will be discussed. This is particularly important in TEM where there are many sources of image contrast, some of which may obscure features of interest.

A third aim of this chapter is to establish the terminology that will be utilised throughout this work.

3.1 Experimental

In this chapter standard modifications induced in the sub-bandgap laser regime with a 1549 nm, 3.5 ns, 2 μJ laser pulse are examined. The SEM results come from a sample where the modifications were closely spaced (2 μm) and the sample cleaved, allowing for certain long axis features to be directly examined. Results from Raman microspectroscopy and TEM make use of isolated modifications, where the spacing (20 μm) prevents the interaction between adjacent modifications.

Sample preparation for Raman microspectroscopy involved polishing such that the long axis of the modifications was just subsurface (< 1 μm). For TEM, long axis cross-sections were prepared by FIB milling of H-bar samples. The short axis cross-section was prepared by FIB milling and ex-situ liftout. These procedures were previously introduced in Chapter 2 and shown in Fig. 2.6 and Fig. 2.8.

Raman results were collected as maps using the 532 nm laser for strain measurements and the 633 nm laser for phase identification. TEM results were all collected under conventional TEM conditions.

3.2 Morphology on a cleaved surface

In this work SEM was principally used to examine the surface topography visible after samples were cleaved. This surface consisted of three layers of modifications, of which the middle layer is presented in Fig. 3.1. In this image the length of the modifications runs vertically. Their

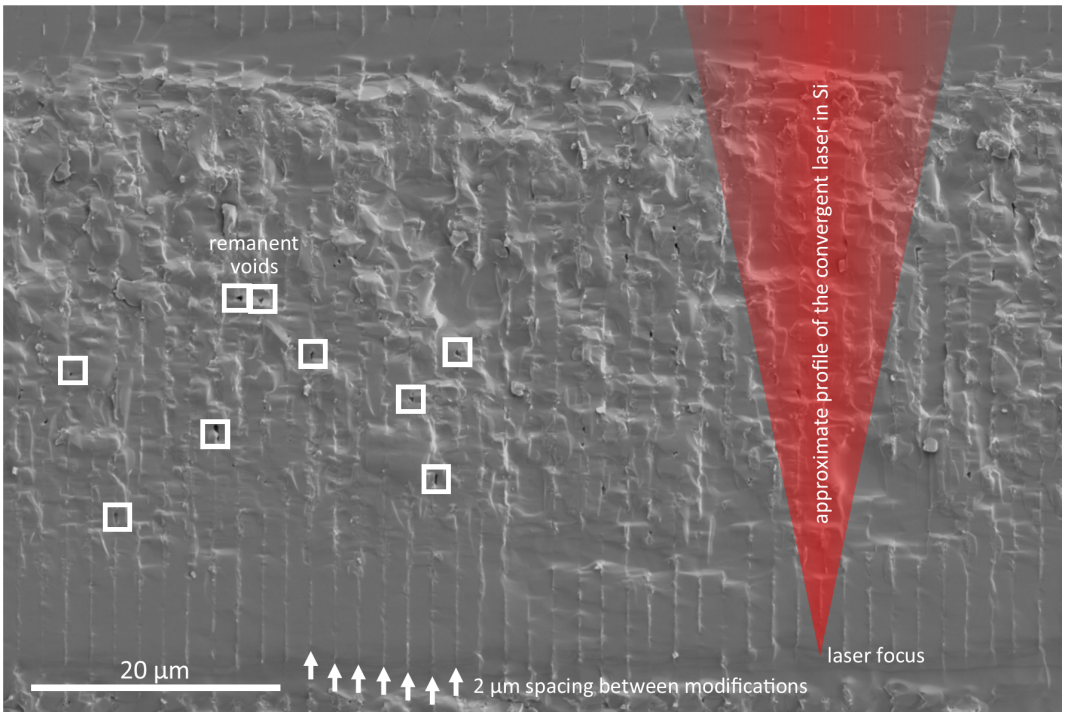

Figure 3.1: A SE SEM image of the middle of three layers of modifications exposed on the cleaved surface after dicing. Modifications run vertically with the focus end near the bottom where modifications are initially well defined. The surface is increasingly chaotic further from focus. Also visible are voids, several of which are outlined in squares.

length has been determined to be $53 \pm 6\ \mu m$. Each modification is separated by $2\ \mu m$, with the bottom, or focus end of the modification near the bottom of the image. In the bottom region each modification can be clearly delineated as indicated by the arrows. Further up, the surface becomes increasingly chaotic and individual modifications become more difficult to distinguish. The transition to a chaotic surface roughly aligns with the position that the convergent laser used to create the modifications begins to overlap the previous modification, as shown in the figure. One other key feature are the dark pits, several of which have been marked on the figure with white squares. These will be shown, as was previously suggested in the literature, to be voids.[49]

To understand these features requires a more detailed examination with Raman spectroscopy and TEM.

3.3 Information from Raman microspectroscopy mapping

Raman microspectroscopy was used in this work to examine strain around the modifications and to establish the presence of Si allotropes. These results were collected as maps that effectively examine the long axis of the modifications. In this section the spectral features will be presented first, followed by the mapping results.

3.3.1 Spectral features

The spectral features of a Raman spectrum are the product of the vibrational/rotational modes present in the sample. For the equilibrium phase of Si (dc-Si), this is dominated by the transverse

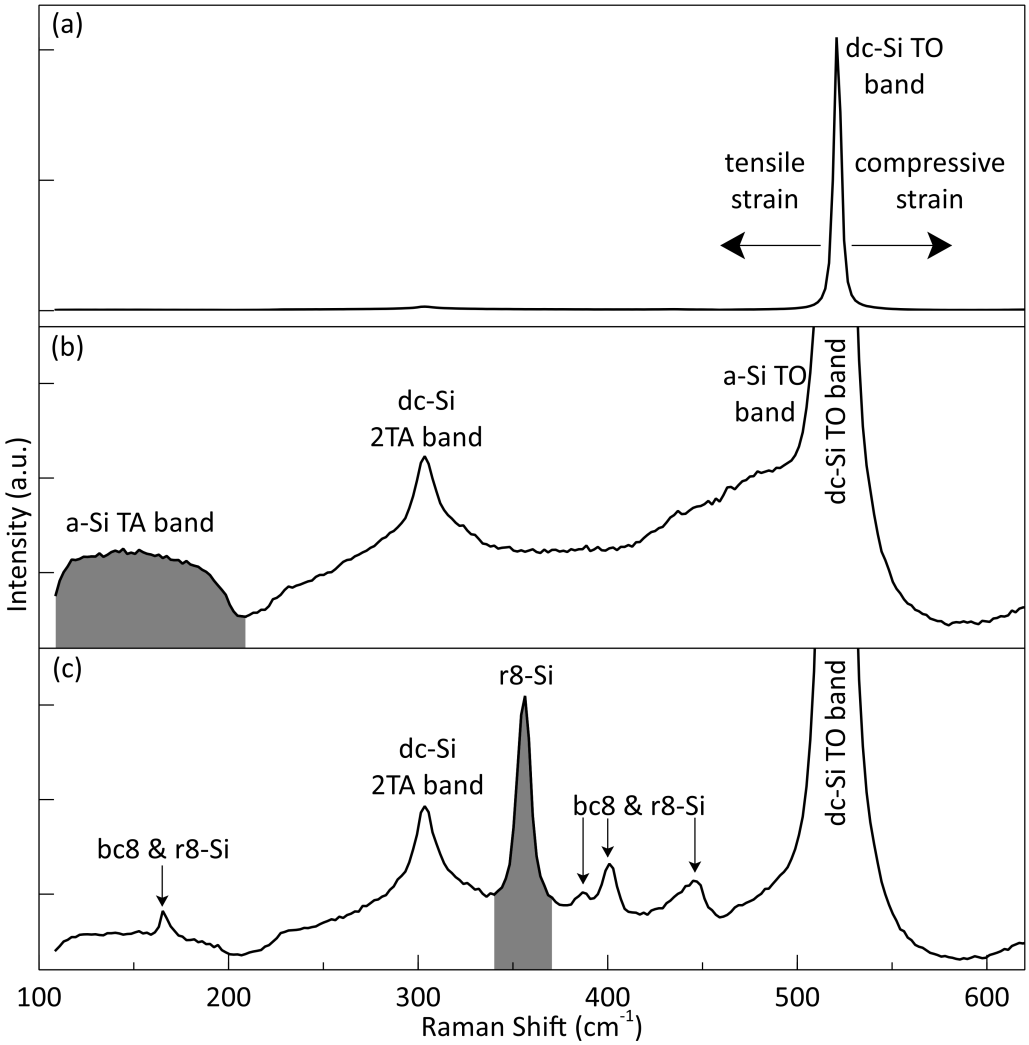

Figure 3.2: Raman spectra for (a) dc-Si with arrows indicating the shifts in the TO band due to strain, (b) a region containing both a-Si and dc-Si with two important a-Si bands labelled and (c) a spectrum additionally containing peaks associated with the closely related high density bc8-Si and r8-Si crystalline allotropes. The area under the a-Si TA band, shaded, is used to construct Raman map images of the a-Si while the dominant r8-Si peak, also shaded, is used for Raman map images of the crystalline allotropes.

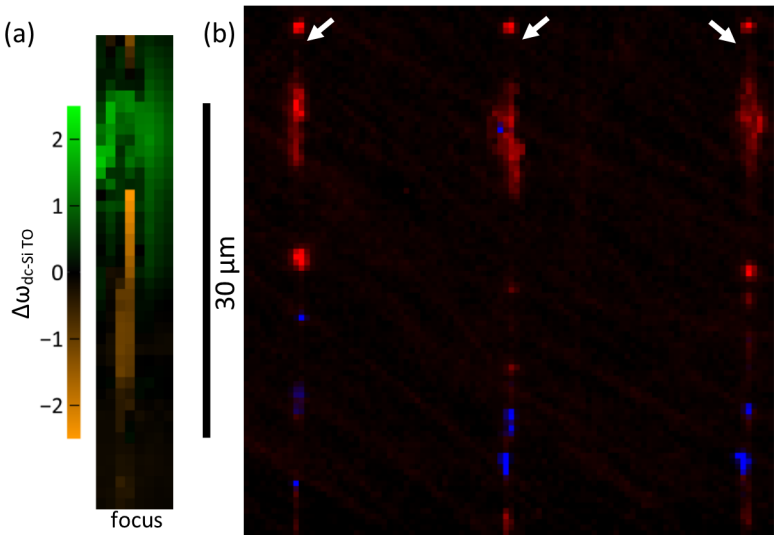

Figure 3.3: Raman map images, shown at the same scale, collected from isolated modifications which run vertically with the focus end of the modification near the bottom of the figure. (a) show strain around a single modification and (b) the presence of a-Si and bc8/r8-Si over three modifications. The strain measurements (a) were recorded with a 532 nm excitation wavelength and the figure shows compressive peak shifts in green and tensile shifts in orange. The latter may be influenced by the overlap with the a-Si TO band. The Si allotropes image (b) was recorded using a 633 nm excitation wavelength and uses red to show a-Si and blue to show bc8/r8-Si.

optical (TO) band at $\sim 520\ cm^{-1}$. A transverse acoustic (2TA) band is also present with the most prominent peak at $\sim 300\ cm^{-1}$. The vibration properties are sensitive to, among other things, strain. Strain can cause a shift to higher wave numbers under compression, and lower wave numbers under tension.[80,81] In Fig. 3.2 (a) the dc-Si spectrum is presented with the TO band clearly visible. The shift of this peak with compression and tension is also indicated.

The closely related bc8-Si and r8-Si crystal phases as well as a-Si are of interest in this work. These phases have their own characteristic peaks. Spectra containing evidence of these are shown in Fig. 3.2 (b) and (c). Figure 3.2 (b) contains peaks both from dc-Si as well as four broad peaks associated with a-Si,[82] of which the two dominant peaks are labelled. The intensity of these peaks increases with the amount of defective dc-Si and a-Si present. The spectrum in Fig. 3.2 (c) contains a number of additional peaks associated with the closely related bc8-Si and r8-Si phases.[83] The nature of these phases will be elaborated upon in Chapter 6. For now, it is sufficient to state that both are generally found together under ambient conditions. As such, although the dominant peak at $\sim 355\ cm^{-1}$ is associated with the more Raman active r8-Si phase,[83,84] it will be assumed that the presence of this peak implies that both bc8-Si are r8-Si are present.

3.3.2 Maps

The spectral features just outlined may be used to construct 'Raman map images' from the spatially mapped data. As the peak position of the dc-Si TO band shifts with strain, it may be used to create images of the strain around the modifications. Raman mapping for the purposes of strain measurement were performed using a 532 nm laser and modest (1.2 mW) laser power. This wavelength gives the best available spatial resolution, while the low laser power prevents significant sample heating and the associated thermal shift in peak position. An example of the

peak shift of the dc-Si TO band around an isolated modification is presented in Fig. 3.3 (a), where the modification runs vertically in the image, with the bottom/focus side near the bottom. In this figure, a compressive peak shift is displayed with green and can be seen to be concentrated near, but not at, the top of the modification. The tensile peak shift is shown in orange. It should be noted that, as the a-Si TO band overlaps the tensile side of the dc-Si TO band, the presence of a-Si can subtly increase the apparent tension within the sample.

Raman mapping to identify the Si polymorphs was conducted using a 633 nm laser and a higher laser power ($3-6\ mW$). The larger spot size and penetration depth of this laser proved to be beneficial in revealing the location of both a-Si and bc8/r8-Si in comparison with the 532 nm laser. The maps of the a-Si were created using the area under the TA band, between 100 and 210 cm^{-1}, as this peak is largely insensitive to the presence of other phases, this region is shaded in Fig. 3.2 (b). For the bc8/r8-Si the area under the $\sim 355\ cm^{-1}$ peak was used, which is shaded in (c). Note that the resulting maps are brighter where these signals are stronger, but these maps should only be interpreted qualitatively. A map image with three isolated modifications (marked with arrows) is presented in Fig. 3.3 (b), where the red colour corresponds to a-Si and the blue to bc8/r8-Si. The a-Si is notable as patches throughout each modification, including a small spot at the top of each modification. The bc8/r8-Si is also found in patches, although this time it is less extensive and is skewed towards the focus end. Many other Raman maps were collected which are broadly consistent with the results shown here.

3.4 Information from TEM

TEM is capable of resolving the complex morphology of the modifications in far greater detail than the previous techniques. Simultaneously, the differing operating modes, complicated contrast and cross-section orientation make interpretation of TEM results inherently less straightforward. To that end, a more in-depth discussion will be provided for this section of the chapter compared with the previous sections. The TEM overview will be split into two subsections; first results recorded from long axis cross-sections will be presented, then results from short axis cross-sections.

3.4.1 Results from long axis cross-sections

About ten long axis cross-sections of isolated modifications were prepared as part of this work, of which three will be referenced throughout this thesis. These three, presented and labelled in Fig. 3.4, contain the same structural features as other cross-sections, but are the most useful and easily interpretable of the long axis cross-sections prepared. In the first instance, only the structural features of the first modification will be introduced. Subsequently, the matter of image contrast will be discussed. For this it is necessary to know that the foil normal of the long axis cross-sections is closely aligned to the [011] crystal orientation. As such, unless otherwise noted, this is the ZA used for all on-ZA imaging of long axis cross-sections, while off-ZA imaging was performed with the sample tilted a few degrees away from this orientation.

Structural features observed

Many of the important structural features observed in a long axis cross-section have been marked for the first modification in Fig. 3.4 (a-d). As is shown on the figure, two of these results (a, c) are collected on-ZA, while the sample is deliberately tilted off-ZA for the other two (b, d). In the following sub-section, the influence that this has on image contrast will be discussed. For now, only the structural features revealed in these images are discussed.

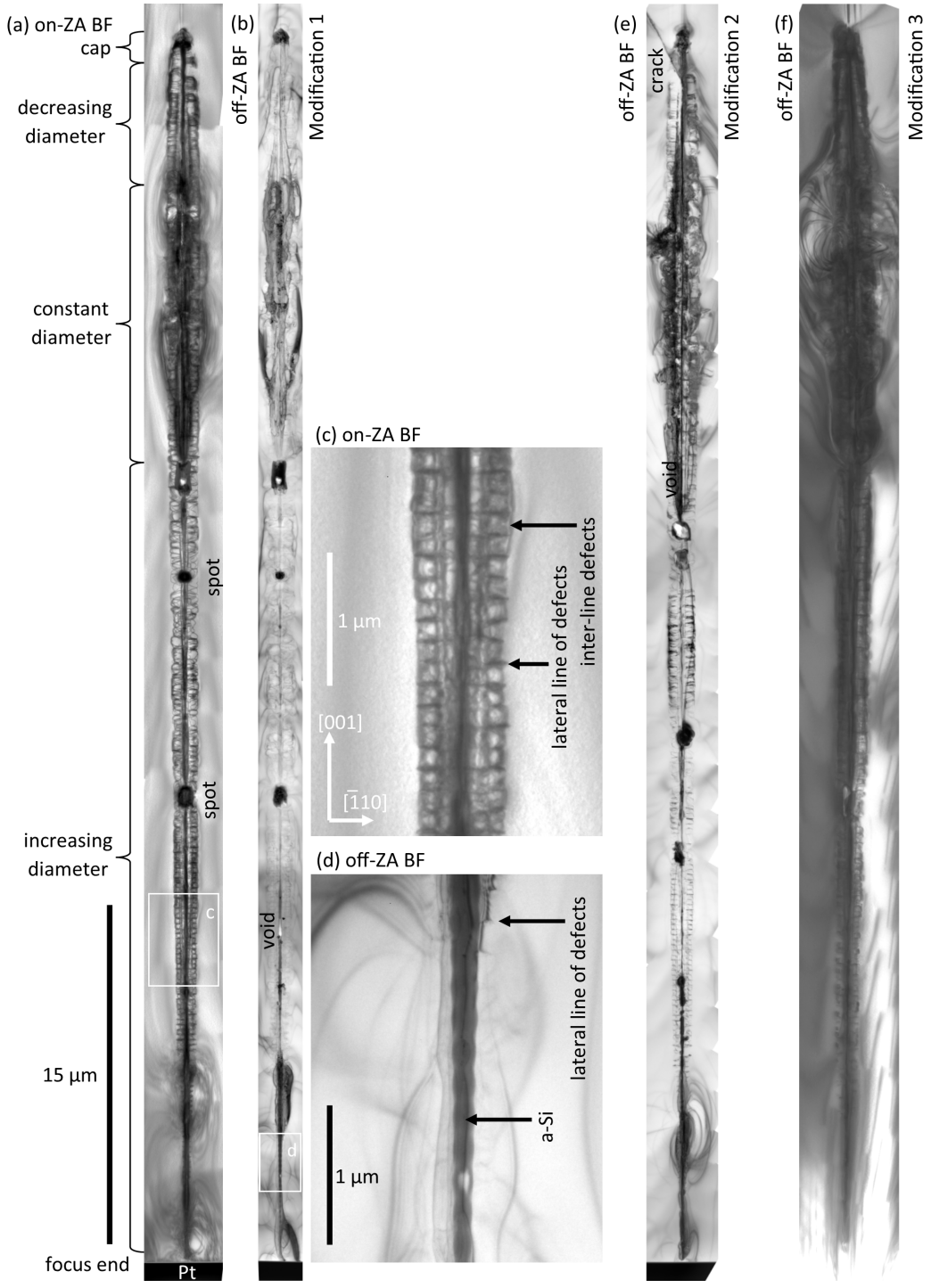

Figure 3.4: BF images of long axis cross-sections of three reference modifications (a-d, e and f), all at the same scale. These are numbered for the purposes of cross referencing. The results are recorded variously on the (011) ZA (a, c, e) and tilted slightly off-ZA (b, d, f) to minimise bend contrast, de-emphasising crystalline defects and revealing a-Si structures at the centre of the modification. Higher magnification images are presented for portions of the first modification (c, d) from the corresponding regions outlined in white (a, b). Annotations corrected.

Figure 3.4 (a) is now described beginning from the bottom of the image. Firstly, a dark bar of Pt is visible. This is deposited as part of the sample cross-sectioning process. Above this the modification can be found to consist of four major regions; the increasing diameter region, the constant diameter region, the decreasing diameter region and the cap. The diameter of the modification here is discernible from the width of the observable crystal defects, which are assumed to be a strong representation of the original radial extent of the melt. The morphology itself consists of crystalline defects, which are shown more clearly in Fig. 3.4 (c), a higher magnification image of a portion of Fig. 3.4 (a). The defects largely consist of lateral lines of defects, as well as more chaotic 'interline' defects, defects between the lateral lines. The centre of the modification will be shown to contain a number of structures. In Fig. 3.4 (d) the central structure is a-Si. Occasional perturbations at the centre of the modification are also visible in the form of voids and spots, as annotated in the figure. Another feature of these images is strong bend contrast, which is visible in all cases, but is particularly evident in the constant diameter region of Fig. 3.4 (a). It is noteworthy that this corresponds to the region of significant compressive strain as observed by Raman microspectroscopy, indicating that this extensive bend contrast and strain are related.

The modifications in Fig. 3.4 (e) and Fig. 3.4 (f) contain the same typical features. However, Fig. 3.4 (e) also contains a crack near the top of the modification which formed accidentally during the cross-sectioning process and is not representative of the normal morphology. Figure 3.4 (f) has poor contrast as a result of being relatively thick. Subsequent thinning of the cross-section has allowed for high quality imaging of sections of this modification, which will be presented later in this thesis. However, the constant diameter region also started to break apart, meaning no better image of the entire modification was available. It should also be noted that even after further thinning, long axis cross-sections tend to be thicker than short axis cross-sections.

At this point it is pertinent to note that the modifications are, by TEM standards, very large. To that end it was not possible to simultaneously image the entire modification and resolve the finer details of the modification. Instead, higher magnification images were recorded, then subsequently stitched together to create the complete images of these modifications. As such the images in Fig. 3.4 (a),(b),(e) and (f) are too small to resolve all the details; they have been reproduced at a larger scale in Appendix A. Throughout the thesis non-stitched images will be preferred when discussing particular features so as to avoid the prospect of stitching related artefacts. These pictures will always be presented with the nearer to focus end on the bottom of the image.

Bend contrast

With many of the important structural features now introduced, it is possible to discuss the differing image contrast between these conditions. For now, this will be restricted to the appearance of bend contrast. The appearance of a-Si will be discussed in the context of the short axis cross-sections below.

As was noted above, on-ZA BF imaging is very sensitive to bend contrast. The strong bend contrast around crystalline defects makes the defects highly visible in Fig. 3.4 (a), but not in Fig. 3.4 (b). This is even more evident in Fig. 3.4 (c) and (d) when examining the lateral lines of defects which are present in both figures, but only clearly visible in Fig. 3.4 (c). Tellingly, the difficulty in observing the defects in Fig. 3.4 (d) also demonstrates that these defects are in fact very thin, and that the apparent thickness when viewed on-ZA is an artefact of the bend contrast. Conversely, the structure at the centre of the modification is extremely difficult to

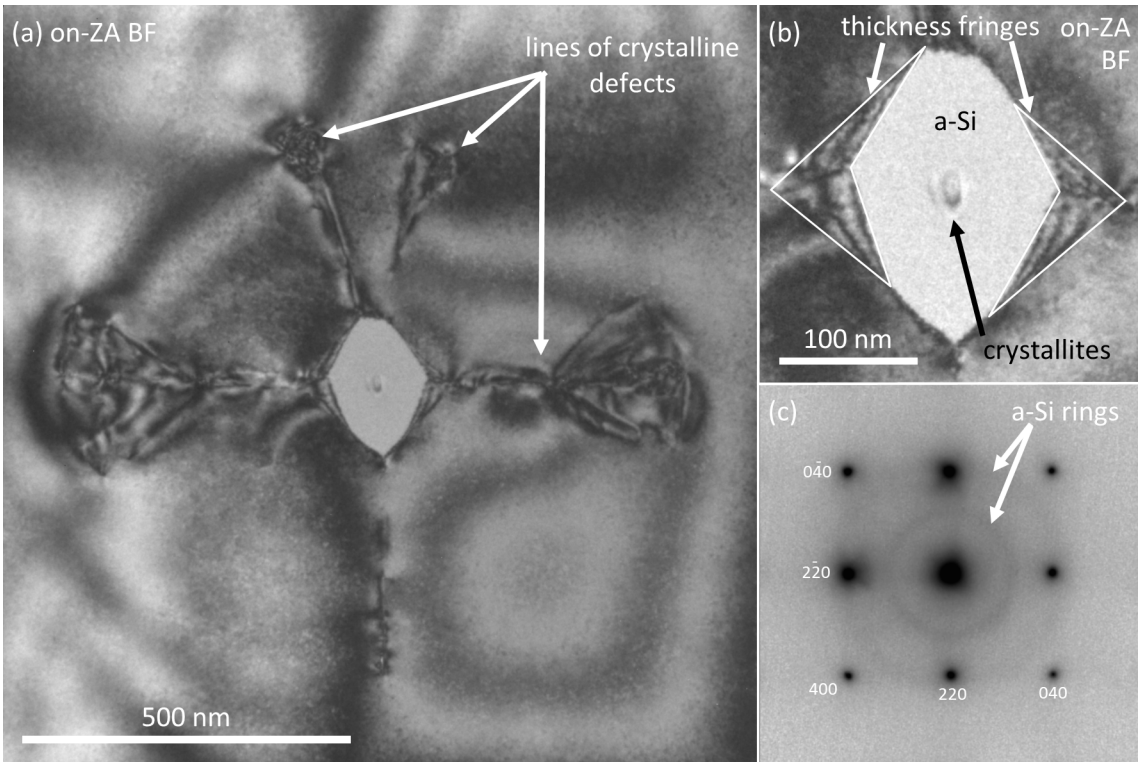

Figure 3.5: BF images of a short axis cross-section, (a), the centre of the cross-section at higher magnification, (b), and an SADP, (c). Collectively these reveal regions of perfect crystal, lines of crystalline defects, a-Si and crystallites. Additionally, two regions with thickness fringes, (b), are shown which result from an inclined interface between a-Si and dc-Si.

discern in the images recorded with the sample tilted onto ZA as they are obscured by bend contrast. When tilted off-ZA the spots and voids are far more visible, and in Fig. 3.4 (d), the structure of the a-Si core is visible. Note however, that bend contrast does not disappear completely, particularly in the highly strained constant diameter region where the bending of the cross-section is, evidently, still a major contribution to the image contrast. Clearly, both on-ZA and off-ZA imaging is beneficial depending on which aspect of the morphology is being considered.

3.4.2 Results from short axis cross-sections

Numerous short axis cross-sections have been prepared and will be presented throughout this work. Each of these is prepared from a different modification and at varying positions along the modification's length. However, these are always prepared with the same orientation, such that the foil normal approximately aligns with the [001] direction and the surface exposed to FIB milling and protected by Pt will be aligned with the top of the image. It follows that on-ZA-imaging is performed along the $[00\bar{1}]$ direction unless otherwise noted. In some instances, the Pt will not be visible as the modification is sufficiently deep from the surface. In other instances, the periphery of the modification has accidentally been removed during the mechanical polishing. There are also cases where the exposed surface was damaged by the ion beam before Pt protection. In these cases, there is a thin a-Si layer just below the Pt.

Structural features observed

An example of a short axis cross-section is shown in Fig. 3.5. Here, the entire cross-section of the modification is presented in Fig. 3.5 (a), a higher magnification image of the centre is presented in Fig. 3.5 (b) and a SADP is presented in Fig. 3.5 (c). This modification contains four distinct regions. Working from the centre outwards, the first region contains crystallites with an oval shaped periphery. Outside of this is a region of a-Si which is continuous throughout the thickness of the cross-section and has a roughly diamond shaped periphery. To the left and right of the diamond shaped amorphous region are two regions, outlined in white in Fig. 3.5 (b), featuring thickness fringes. These are a result of the existence of the overlapping of amorphous and crystalline material. As such, there is an inclined interface where the thickness of the crystalline region changes drastically, leading to thickness fringes. It follows that throughout the thickness of the cross-section, the periphery of the amorphous region ranges between being roughly square, and roughly diamond shaped. Notably, in both cases, the amorphous region has facetted sides. The fourth region is largely perfect crystal with the exception of five lines of crystalline defects which extend to the same radius from the centre of the modification. These lines of defects on the short axis are the same as both the lateral line defects and 'interline' defects observed on the long axis cross-sections. Again, the extent of these defect lines match the melt diameter and solidification will be shown to occur radially inwards. The SADP was recorded from an area overlapping both the near perfect crystal, which is responsible for the characteristic peaks, and the a-Si, which results in the rings in the SADP.

Relative contrast of a-Si and crystalline Si

At this stage crystalline Si has been shown to be both much brighter than the amorphous material in Fig. 3.4 (d) and much darker than the amorphous material in Fig. 3.5 (a). The relative appearance of these components warrants discussion. For amorphous material, the intensity can be expressed by the simple equation:

$$I_{BF} = I_0 exp\Big(- \frac{t}{\Lambda_{BF}} \Big) \tag{3.1}$$

where I_{BF} is the BF intensity, I_0 is the free space intensity, t is the sample thickness and Λ_{BF} is the a-Si BF mean free path. This equation implies that amorphous material should appear relatively featureless, with contrast due only to mass and thickness. The appearance of crystalline material, on the other hand, is dependent not just on mass and thickness, but also tilt, i.e. due to diffraction conditions and electron channelling. As such, when a sample is tilted onto a zone axis, as in Fig. 3.5, many planes satisfy Bragg conditions reducing the intensity of the crystalline region in a BF image, but not in the amorphous region. When tilted off-ZA, such as in Fig. 3.4 (d), the crystalline region is brighter, making the amorphous region appear darker. Other factors that may influence the relative brightness can relate to foil thickness influencing electron channelling, diffuse scattering and so on. Additionally, as has been demonstrated, bend contrast and thickness fringes occur in crystalline material. This change in appearance is of importance as more conventional methods for identifying a-Si, such as using SAD, are not always applicable for these thick samples where crystalline material may overlap amorphous material. So, by accounting for the influence of tilt on the relative contrast of these two components, it remains possible to identify amorphous material with a high degree of confidence.

3.4.3 Modification size

Finally, some comments on modification size are warranted. Modification diameter evidently varies with position along the modification, however the average modification diameter, measured across multiple cross-sections and multiple modifications, for the same laser irradiation conditions, was determined to be $1127 \pm 50\ nm$. Meanwhile, the average modification length was $53 \pm 6\ \mu m$ and so the average modification volume was $52.9 \pm 8.0\ \mu m^3$.

3.5 Summary of the structural features

In this chapter an overview of the modification morphology was presented as viewed from each of the key experimental techniques, SEM, Raman and TEM. All of these analysis methods resolved details about the long axis of the modification, while TEM was also used to reveal detail from cross-sections of the short axis. A basic framework to interpret these results was provided.

SEM of the cleaved sample showed evidence of individually discernible modifications at the focus end of the modifications, but the topology became increasingly chaotic along the length of the modifications. Spots which will be shown to be voids were also visible.

Raman microspectroscopy mapping showed small regions of dc-Si under tension along the modification's length, as well as highly compressed material near, but not at, the top of the sample. This compressed region overlaps with the constant diameter region as viewed in the long axis TEM cross-sections. Raman also showed evidence of a-Si patches along the length of the modifications and bc8/r8-Si patches mostly nearer to the focus end of the modifications.

TEM examination of the long axis cross-sections showed four regions where the radial limit of structural features is thought to represent the original melt periphery. Above focus is first the increasing diameter region, then further up is the constant diameter region which contained substantial bend contrast and evidence of strain, followed by the decreasing diameter region and finally the cap. Finer structures included lateral lines of crystalline defects, often with defects in-between, and a core which is at least partially a-Si. Also visible were perturbations in the form of dark spots and voids. Three modifications cross-sectioned along the long axis were presented, which will be referenced throughout the remainder of the thesis. TEM examination of a short axis cross-section revealed crystallites, a-Si and lines of crystalline defects. The outer limit of the defects is again thought to represent the original melt diameter. Also discussed were the various contributions to image contrast as a function of sample tilt, including thickness fringes, bend contrast and the relative contrast of crystalline and amorphous material.

All of the structural features introduced in this overview chapter are presumed to be contained within the solidified material from the original melt volume. These features will be explained in the following two chapters to be the result of rapid, inwardly propitiating solidification. The features will be shown to be dependent on position along the modification's length. The following chapter will develop a solidification based explanation (model) for the morphology from the perspective of the short axis. Chapter 5 will consider solidification from the perspective of the long axis, building upon the concepts established in Chapter 4. Chapter 6 will then discuss features that are also dependent on changes of density, including voids, high density crystalline allotropes and compressively strained dc-Si.

Chapter 4

The morphology of short axis cross-sections

This chapter will present and explain the range of morphologies visible in the TEM analysis of short axis cross-sections of the isolated sub-bandgap laser modifications. In doing so, a two-dimensional phenomenological solidification model will be developed. This model will, in part, be built upon the scientific basis underlying PLM and, more generally, one-dimensional liquid phase epitaxial solidification. As such, the chapter will begin with a short review of the relevant solidification literature. Next, this literature will be related to a single short axis cross-section that exhibits many of the key morphological features evident in short axis cross-sections more generally. A generalised phenomenological model is then proposed, before considering a spectrum of other short axis cross-sections to show how the morphological features fit with the model.

4.1 Solidification literature

In this section the literature necessary to understand the short axis morphology will be presented. This begins with some literature concerning PLM, which is essentially a one-dimensional melting and solidification process. Next, the literature concerning the melt-solid interfacial free energy and the epitaxial solidification interface kinetic coefficient is addressed. The crystallographic anisotropy of the interfacial free energy and the kinetic coefficient will be of relevance for generalising the PLM literature into two-dimensions in this chapter and three-dimensions in the following chapter.

4.1.1 Pulsed laser melting

PLM involves melting a thin (10s-100s of nanometres) surface layer of a wafer using a pulsed laser (typically long picosecond to nanosecond pulse length). Strong thermal gradients subsequently drive rapid epitaxial solidification off the underlying crystal.[54,55,85] The thermal gradients in this work are similar in magnitude to those in PLM and hence, the literature in this field is relevant to this thesis.

Cullis et al. investigated the solidification process on several Si wafer orientations across a range of thermal conditions.[55] This allowed transitions in solidification behaviour (from perfect epitaxy to defective epitaxy and then to amorphisation) and also the orientation anisotropy to be investigated. The work used a 347 nm wavelength laser with either a 0.7 ns or 2.5 ns pulse duration and various pulse energies on (001), (011), (111) and (112) oriented Si wafers. The combination of pulse duration and pulse energy allowed for control of the thermal gradients within the sample and hence the cooling and solidification rates. Computer modelling of the

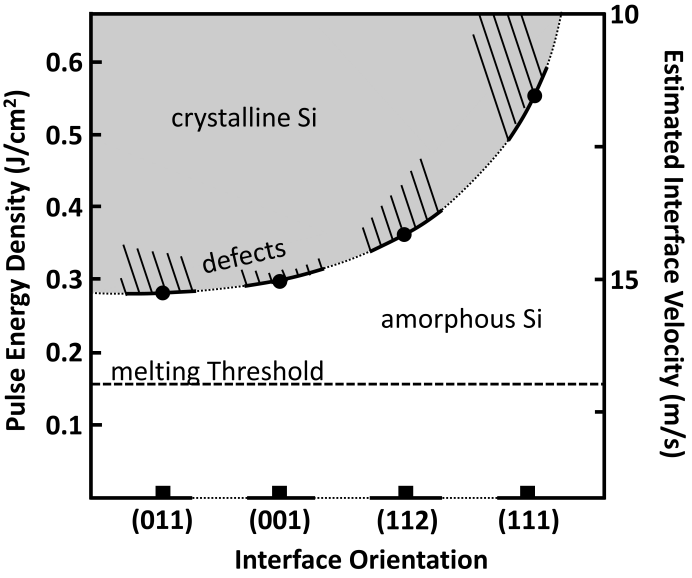

Figure 4.1: The morphology of the pulsed laser melted region after laser exposure at various pulse energy densities (using a 347 nm wavelength laser with a 2.5 ns pulse length) along four interface orientations fo Si. The estimated solidification interface velocity is also shown. Three regimes are of note: perfect epitaxy resulting in single crystal Si, defective epitaxy which is shown with hashes, and rapid solidification resulting in a-Si. Adapted from [55].

heat-flow allowed for the laser conditions to be linked with the solidification interface velocity. Thus, interface velocity-dependent solidification could be examined, as could the crystallographic anisotropy therein.

TEM showed that on all crystal orientations, smaller thermal gradients, and hence slower interface velocities, resulted in perfect epitaxial solidification. At higher thermal gradients and interface velocities a transition to defect-rich epitaxial solidification occurred. Higher velocities again resulted in solidification to an amorphous state. Significantly, this work found that the transitions between these solidification regimes differed on every orientation as is shown in Fig. 4.1. The interface velocity at the onset of defective epitaxy (v_{def}) followed the sequence v_{def} (001) > (011) > (112) > (111). The velocity at the onset of amorphisation (v_a) followed a sequence of v_a (011) > (001) > (112) > (111).

This figure does not cover all the intricacies that are of relevance to this thesis. Firstly, the defective epitaxy regime was not always observed. Using the slower 2.5 ns laser pulse on the (001) orientation resulted in a near direct transition from perfect epitaxy to amorphisation. Direct transitions are also observed in this thesis. It is worth discussing the amorphisation transition further. The transition was previously associated with an interface velocity, v_a. This transition can equivalently be associated with the undercooling of the melt, the depression of the melt temperature below the equilibrium melting temperature of crystalline Si (T_{mc}). Reported values for the equilibrium melting temperature of a-Si (T_{ma}) are on the order of 250 K below that of crystalline Si.[86–89] As such, should the undercooling exceed $\sim$ 250 K, amorphous solidification can occur instead of epitaxial solidification. A third matter concerns the crystalline defects observed after defective epitaxy. Cullis et al. noted twinning to be prominent, particularly along (111) oriented wafers.[55] Interestingly, when amorphisation also occurred, crystalline material in the vicinity of twins was noted to protrude beyond the otherwise flat interface between crystalline

and amorphous material. Defects such as twinning were suggested to impede amorphisation.

4.1.2 Epitaxial interfacial energetics and kinetic coefficients

As far as this thesis is concerned, a limitation of the PLM research was that it is effectively one-dimensional, whereas the explanations in this chapter require a two-dimensional perspective. In order that the higher dimensional influences can be understood, the literature concerning liquid phase epitaxy in more general terms will now be introduced.

Energetically, one critical parameter is the interfacial free energy, γ, the energy associated with the crystal-melt interface. This parameter is crystallographically anisotropic, with local minimums (per unit area) along low index crystal orientations. As such, minimisation of the interfacial free energy is a compromise between forming facets along low index orientations and the minimisation of total interfacial area. In Si, Apte et al. calculated the interfacial free energy values from molecular dynamics simulations using the cleaving wall method and found that; $\gamma_{001} = 0.42 \pm 0.02\ J \cdot m^{-2}$, $\gamma_{011} = 0.35 \pm 0.03\ J \cdot m^{-2}$, $\gamma_{111} = 0.34 \pm 0.02\ J \cdot m^{-2}$ and the rotational average was $\gamma_{solid-melt} = 0.37 \pm 0.03\ J \cdot m^{-2}$, which matches closely with experimental values.[90]

During rapid solidification kinetic factors are of great importance. In particular the interface kinetic coefficient, which is also crystallographically anisotropic, is of relevance to this work. The coefficient is defined by:

$$v = \beta \Delta T \tag{4.1}$$

where v is the interface velocity, β is the interface kinetic coefficient and ΔT is the undercooling below the equilibrium crystalline melting temperature. Values for interface kinetic coefficient are typically stated as the inverse, β^{-1}. One can see that at a given undercooling, an interface with a larger kinetic coefficient is expected to grow more quickly. Values for the interface kinetic coefficient in Si from the literature are shown in Table 4.1. Also shown are the interface kinetic coefficients inferred from the interface velocity at the onset of amorphisation, which will be elucidated upon below. Finally, the relative solidification rates based both on interface kinetic coefficients and other measures of solidification are shown. These results are not particularly consistent in absolute value, but the normalised sequence is very clearly $\beta_{001} \geq \beta_{011} > \beta_{111}$. It will be argued below that under equivalent conditions $\beta_{001} > \beta_{011}$.

A more in-depth discussion of these results will begin by considering the validity of Equation 4.1, which has a linear relationship between undercooling and interface velocity. While generally accepted in the literature, this is likely to be an over simplification. Indeed, solidification rates presented by Cullis et al. suggest that the coefficient itself may vary with driving force, for example the undercooling of the melt.[55] Furthermore, while most of the results presented in Table 4.1 pertain to PLM conditions, Buta et al. conducted molecular dynamic simulations of relatively slowly moving interfaces which might suggest why that result, at least, is lower than many of the other results.[91]

A more specific example as to why a linear relationship between interface velocity and undercooling may be an over simplification is that the interface kinetic coefficient would reasonably be expected to be dependent on the exact nature of the interface, which is known to change with interface velocity. In Si most interfaces are known to be atomically rough, that is they contain many vacancies and adatoms. One exception is the (111) interface which is generally atomically smooth, with crystal growth limited by the addition of adatoms (dangling bonds) from which lateral growth along the interface may occur.[92] However, at high solidification interface speeds, the (111) interface is thought to transition from atomically smooth to atomically rough.[93] This

process is mediated by the formation of crystalline twinning.[55,94] Recall that Cullis et al. found twinning to be prevalent on (111) oriented wafers during rapid solidification.[55] Thus, the interface kinetic coefficient likely varies depending on the exact nature of the crystal-melt interface due to it's smooth, rough or defective nature.

At this stage the validity of the parameters in Table 4.1 is suggested to be dependent on the nature of the interface and the similarity of thermal conditions. This may be further explored by comparing the interface velocity at the onset of amorphisation, the interface kinetic coefficient and the undercooling required for amorphisation. Adapting Equation 4.1 leads to:

$$v_a = \beta\Big(T_{mc} - T_{ma}\Big) \tag{4.2}$$

assuming that undercooling of the melt below T_{ma} does not occur. This assumption is likely to be approximately, but not strictly, true. Table 4.1 contains values from Cullis et al. based on this approach. However, recall that defect formation was previously suggested to suppress the transition to amorphous solidification, and that defect formation was more prevalent during (011) than during (001) epitaxial growth. Perhaps then, for a defect free interface, the correct sequence for the interface kinetic coefficient is $\beta_{001} > \beta_{011} > \beta_{111}$, which is in accordance with the solidification rate results of Cullis et al.[55]

Table 4.1: Literature results for the absolute and normalised values of interface kinetic coefficient along low index crystal orientations in Si. Also shown are values inferred from the interface velocity at the transition to amorphous solidification and from the ratio of solidification rates.

References	β_{001}^{-1}	β_{011}^{-1}	β_{111}^{-1}	$\frac{\beta_{011}}{\beta_{001}}$	$\frac{\beta_{111}}{\beta_{001}}$
		$K \cdot s \cdot m^{-1}$			
Measurements					
Thompson[85]	17 ± 3				
Galvin[95]	15 ± 5				
Tsao[96]	> 12				
Larson 1[97]	8.3 ± 4.5		18.3 ± 5		0.45
Larson 2[98]	5.6		11.4		0.49
Ivlev[99]	9.8	$\sim \beta_{001}^{-1}$	15.4	~ 1	0.64
Buta[91]	8.2 ± 0.2				
Extracted from amorphisation thresholds					
Cullis[55]	16.4	$\sim \beta_{001}^{-1}$	21.7	~ 1	0.76
Ratios from solidification rates					
Cillus[55]				0.82	0.6-0.7
Grabow[56]					0.605

Having discussed these details, the scientific basis for understanding crystallographic anisotropy in solidification behaviour and the relative prevalence of solidification along different crystal directions has been established. This knowledge will now be used to develop a basic phenomenological model to explain the morphology observed in the short axis cross-section results presented below.

4.2 Experimental

This chapter makes use of the standard, sub-bandgap regime modifications produced with the 1549 nm, 3.5 ns, 2 μJ laser pulse. The modifications are produced in isolation, with a sufficient gap (20 μm) so that adjacent modifications do not interact. Conventional TEM is used to

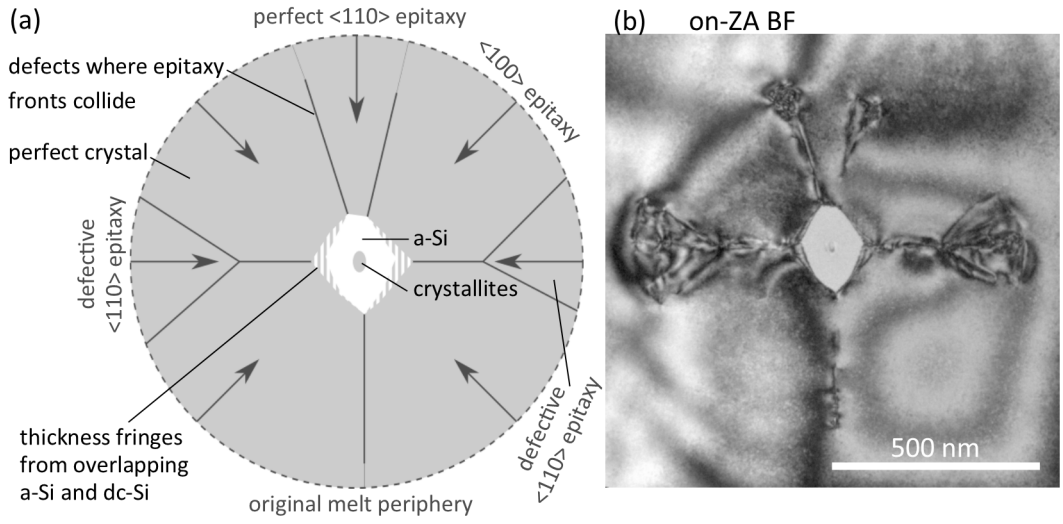

Figure 4.2: An annotated diagram, (a), that corresponds to the features visible in the TEM image, (b). This modification shows evidence of epitaxial solidification along ⟨100⟩ and ⟨110⟩ directions. Collisions of these epitaxial interfaces have resulted in lines of crystalline defects. Solidification to perfect crystal, defective crystal and a-Si have all occurred. Thermal insulation from the a-Si has slowed solidification, resulting in crystallites at the centre of the modification.

characterise short axis cross-sections prepared by FIB milling of ex-situ liftout samples. The cross-sections are all created from different modifications and at different positions along each modification's length.

4.3 Results and the development of a basic phenomenological model

In this section a single cross-section that illustrates a large portion of the structural features observed across all short axis cross-sections will be used to develop a basic, two-dimensional phenomenological model of solidification. This will be tested and expanded upon in the subsequent section.

Figure 4.2* consists of a schematic, (a), of the morphology visible in the TEM image, (b). This modification consists of a core of crystallites with an oval periphery at the centre of the modification, which is surrounded by a shell of a-Si with faceted sides and beyond this are five radial lines of crystalline defects.

To explain these results, consider first that the melt had a circular cross-section that was cooled radially, resulting in radially symmetric undercooling of the melt. This in turn drove inwardly propagating epitaxial solidification from the initial crystal-melt interface, specifically, along the ⟨100⟩ and ⟨110⟩ directions. Given the inward solidification, the epitaxy fronts inevitably intersect, leaving behind a trail of defects along their line of intersection. As solidification progressed it also accelerated, as is known to occur during PLM. However, because PLM is effectively one-dimensional, while the present work is effectively two-dimensional, the circular melt volume is expected to cool faster than the planar melt in PLM. Solidification is therefore expected to accelerate faster in the present work. On at least two of the ⟨110⟩ fronts, solidification was also sufficiently rapid for defective epitaxy to occur. Once the undercooling of

*This is the same modification shown in Fig. 3.5 from the previous chapter.

the melt reached T_{ma}, or equivalently the interface velocity passed v_a, solidification transitioned to amorphisation. The shape of the epitaxy front at this transition is preserved in the faceting on the periphery of the amorphous region. The remaining melt at the centre of the modification is now surrounded by a-Si, which has a thermal conductivity roughly two orders of magnitude less than that of dc-Si.[87,100–102] As such, the a-Si increasingly insulated the remaining melt until undercooling decreased sufficiently for crystal growth to again be preferred. Equivalently, the interface velocity decreased until it returned to a crystal growth regime. With no seed crystal on which to epitaxially solidify, several new crystals must have nucleated before growing through the remaining melt volume. As the crystal periphery is defined by the a-Si, which has an isotropic interfacial free energy, there are no facets.

It is noteworthy that this thermal-conductivity-induced transition back to crystalline Si solidification has not previously been reported in PLM literature. Presumably this is largely due to the thin, near-surface nature of PLM induced amorphous layers. That is, it was not possible to both induce amorphisation and then achieve sufficient insulation of the remaining melt to allow a return to a crystal growth regime.

There are two issues to address concerning the nature of the defective epitaxy in Fig. 4.2: why do only two of the three regions of ⟨110⟩ epitaxy contain defects, and why is there no significant defective region between the perfect epitaxy and the amorphous regions? In part, the presence and nature of different epitaxial fronts is a matter of stochastic variation. However, particularly in ⟨100⟩ directions, defective epitaxy was only possible over a narrow range of interface velocities. Thus, the interface is likely to pass through this regime very quickly, before any significant defects are formed. Recall that on ⟨100⟩ directions Cullis et al. could only clearly see the defects for very short, 0.7 *ns* laser pulses.[55] Given that rapid two-dimensional cooling occurs in these results, it seems plausible that in some cases epitaxy along both ⟨100⟩ and ⟨110⟩ directions transitioned through this defective regime fast enough to avoid significant defective crystal.

The asymmetry in the morphology also warrants discussion. Throughout this work it will be evident that short axis cross-sections of sub-bandgap regime modifications (which are always shown with the same orientation), will often exhibit behaviour consistent with higher speed of solidification on the image's horizontal axis, relative to the vertical axis. It is assumed that this is associated with some asymmetry in the spatial profile of the laser itself. The effect is small enough that it isn't thought to fundamentally change solidification behaviour. However, it becomes more evident in cross-sections that are best explained with more rapid solidification. Thus, in the case of Fig. 4.2, the slightly faster initial solidification on the horizontal ⟨110⟩ orientations relative to the vertical ⟨110⟩ orientation allowed for these interface fronts to enter a defective growth regime.

4.4 Additional results and the expansion of the phenomenological model

Having established the basis of the phenomenological model, a number of other modifications that represent the majority of features observed within short axis morphologies will be examined.[†] This will serve to validate and expand upon the explanation thus far provided. These differences will be associated with the initial magnitude of the thermal gradients, and thus, on the cooling and solidification rates. Modifications are presented and discussed with sequentially

[†]Several of these cross-sections have been over polished during sample preparation. As such a portion of the lines of defects is missing but the solidification process can nevertheless be unambiguously determined.

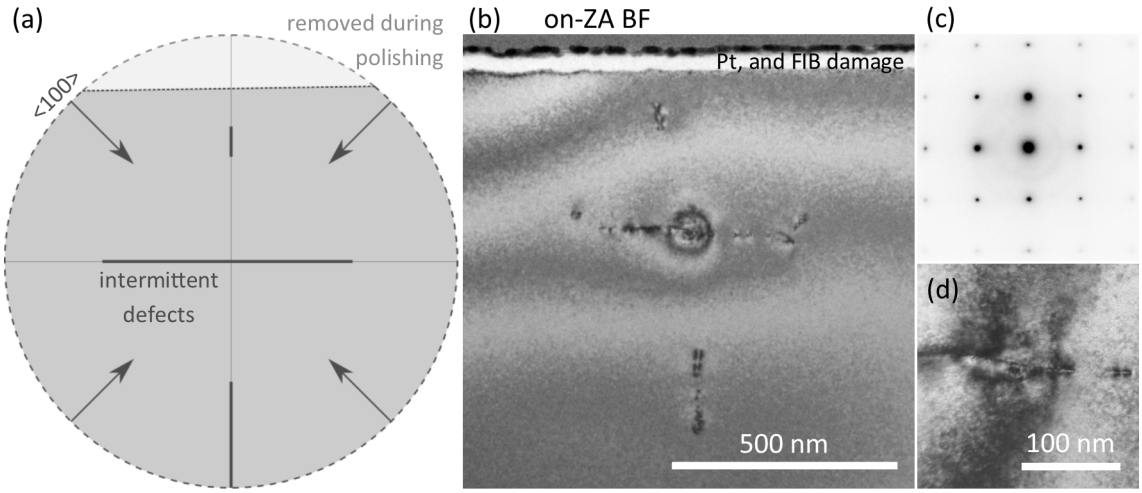

Figure 4.3: An annotated diagram, (a), of the features visible in the TEM image, (b), of a modification oriented on the [100] zone axis as shown by the SADP, (c), that has solidified under weak radial thermal gradient conditions. This modification has solidified only by slow ⟨100⟩ epitaxy. The solidification fronts intersected to mostly leave perfect crystal, but intermittently to leave a trail of defects. The centre of the modification, shown at higher magnification, (d), exhibits stress-induced bend contrast, but no change in solidification behaviour.

increasing initial thermal gradients. It should be noted that the initial thermal gradients are partially dependent on position along the length of the modification. However, a number of other factors also influence the morphology along the modification, as will be expanded upon in subsequent chapters. As such, no emphasis is placed on the specific position along the modification of cross-sections presented within this chapter.

The first additional modification, presented in Fig. 4.3, appears to have a much simpler morphology than the previous case. The lines of defects are not continuous, do not extend to the expected circular periphery of the melt, nor do they 'branch' as was previously associated with ⟨110⟩ epitaxy. The centre of the modification, shown more clearly in Fig. 4.3 (d), contains a continuation of the lines of defects. The remainder of the contrast in the image is associated with significant bend contrast, rather than structural features. An explanation for this morphology is that the melt was again circular. Epitaxial solidification from the periphery occurred only along ⟨100⟩ directions and propagated slowly. The intersection between neighbouring epitaxial fronts resulted in near-perfect solidification, with few crystalline defects. A second consequence of slow solidification was that a transition to defective epitaxy or amorphisation did not occur.

The second modification in this section, shown in Fig. 4.4, has continuous lines of defects. These have a shared radial limit and extend through to the centre of the modification. Additionally, the centre of the modification has a region of defective crystal with faceted sides. Clearly, this modification is again explained with only ⟨100⟩ epitaxy occurring from a circular melt. With stronger temperature gradients, solidification was sufficiently rapid that the epitaxy fronts could not intersect perfectly. It was also sufficient to cause a transition in epitaxy behaviour from perfect to defective epitaxy, indicated by the wavy texture on the schematic diagram, Fig. 4.4 (a).

The lines of defects in the third modification, Fig. 4.5, are again continuous and have a shared radial limit, but in two cases branch, providing evidence of ⟨110⟩ epitaxy. At the centre of the modification is a relatively small, facetted amorphous region due to rapid solidification.

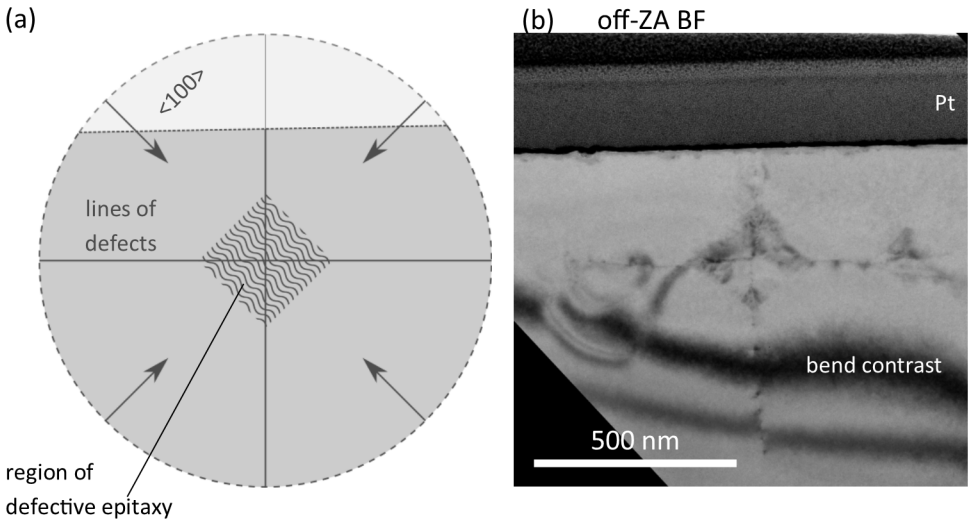

Figure 4.4: An annotated diagram, (a), of the features visible in the TEM image, (b), from a short axis cross-section of a modification that has solidified by ⟨100⟩ epitaxy as a result of modest radial thermal gradients. Lines of defects remain from the collision of epitaxial interfaces. An interface-velocity-induced transition from perfect epitaxy to defective epitaxy near the centre of the modification has resulted in a square shaped region of defects. The TEM image also contains significant bend contrast despite being tilted slightly off-ZA.

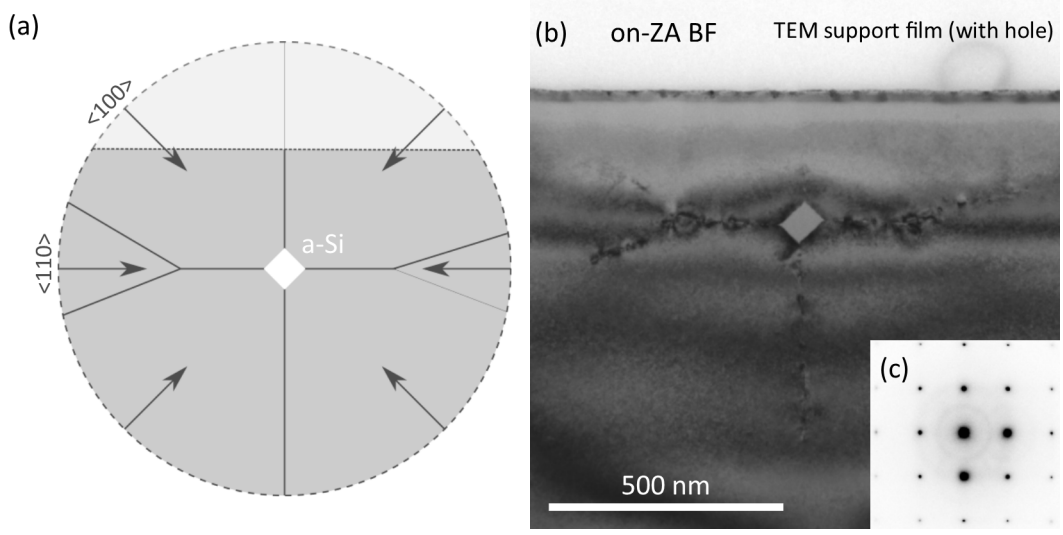

Figure 4.5: An annotated diagram, (a), of the features visible in the TEM image, (b). The modification has solidified by ⟨100⟩ epitaxy and ⟨110⟩ epitaxy as a result of moderate radial thermal gradients. Lines of defects from colliding epitaxy interfaces show signs of branching where ⟨110⟩ and ⟨100⟩ interfaces meet. The centre of the modification contains a roughly square shaped region of a-Si due to rapid solidification. The SADP, (c), recorded on the [001] ZA from a region containing the a-Si and dc-Si contains extremely weak amorphous rings.

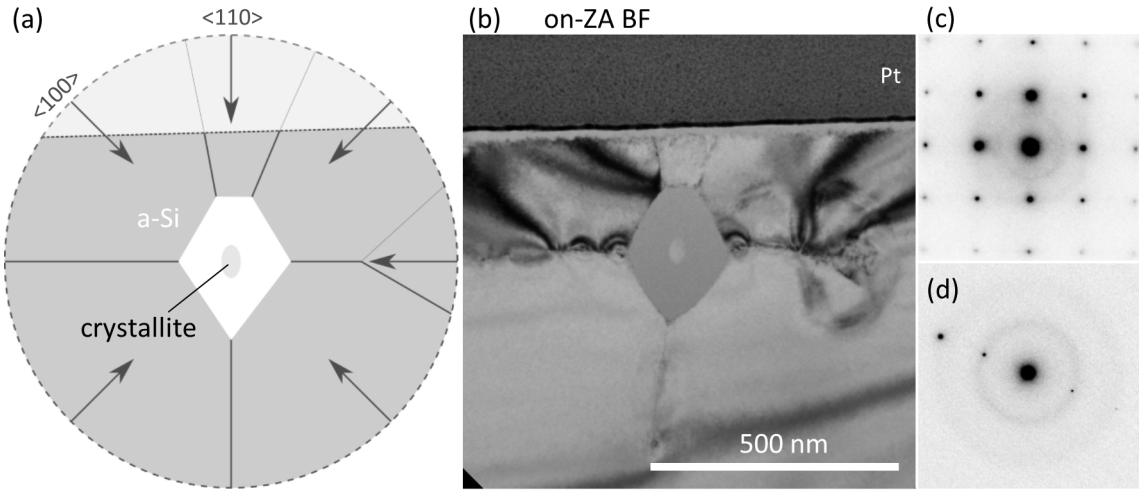

Figure 4.6: An annotated diagram, (a), of the features visible in the TEM image, (b), from a modification that has solidified by ⟨100⟩ and ⟨110⟩ epitaxy due to stronger radial thermal gradients. Rapid solidification has resulted in a transition to amorphous solidification, which in turn thermally insulated the remaining melt, slowing solidification such that a new crystallite could form at the centre. A SADP, (c), is shown from the a-Si and epitaxy region. Also shown is a SADP, (d), from the a-Si and crystallite region which shows both the a-Si rings more strongly, and the different orientation of the central single crystallite.

Faint rings associated with the a-Si are present in the SADP, Fig. 4.5, although the amorphous nature can also be confirmed by the characteristic appearance as was discussed in the previous chapter (in this case light uniform contrast).

The modification in Fig. 4.6 is essentially similar to that in Fig. 4.2, with a single crystallite encapsulated in a-Si. A notable difference in Fig. 4.6 is that epitaxy along ⟨110⟩ directions is evident only in two, rather than three cases. Additionally, no thickness fringes within the amorphous region are visible, implying some minor differences in the periphery of the amorphous region. A SADP from the amorphous and epitaxially solidified crystal is shown in Fig. 4.6 (c) and an SADP from the amorphous shell, crystallite core is shown in Fig. 4.6 (d). These SADPs reveal that the central single crystallite has a different orientation to the bulk crystal. Given the similarity with Fig. 4.2, this modification may be explained on exactly the same terms as previously. It is included here more to highlight stochastic variations rather than to illustrate different morphology.

Relatively drastic differences in morphology can be observed in the modification in Fig. 4.7. Only two or three lines of defects can be seen, although it is reasonable to assume that others were present, but polished off on the top of the modification. The centre of the modification contains an amorphous shell with a polycrystalline core structure. The periphery of the amorphous region appears smooth but is composed of multiple facets, some of which are separated by defect lines as had occurred previously. In other cases a smooth transition occurs between facets, and there is no accompanying defect line. Small cracks are also present. Cracking is a matter of concern in Chapter 7 but is not relevant here and, thus, will not be discussed further in this chapter. This structure may be explained by solidification additionally occurring along other, higher index, $\langle hk0 \rangle$ orientations. This has resulted in a semi-continuous crystal-melt interface that bends between facets. When the interface bends, rather than colliding with neighbouring facets, no trail of defects is produced. The amorphous shell and crystalline core structure is again explained on the same basis as previously. However, in this case solidification returned to

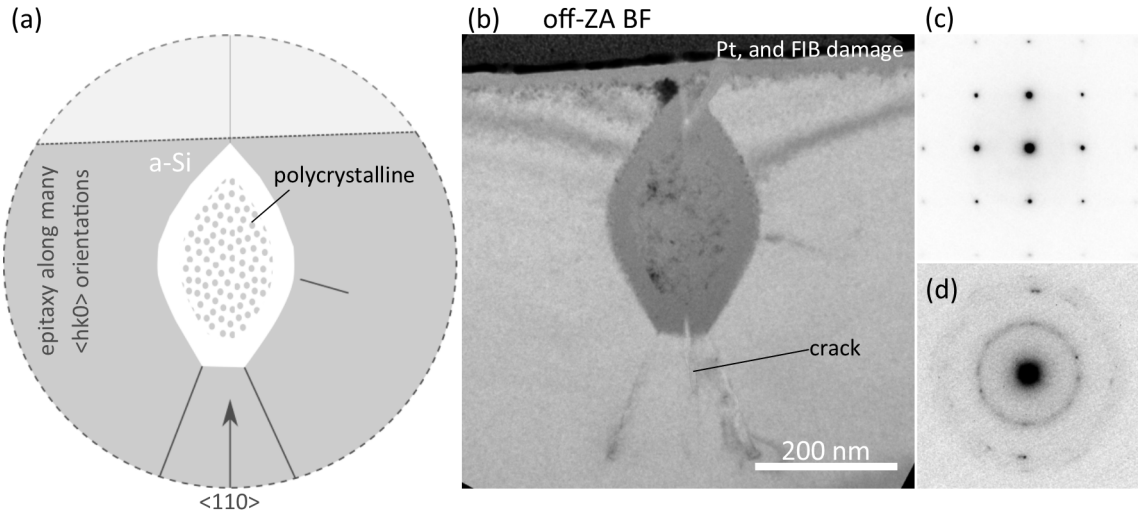

Figure 4.7: An annotated diagram, (a), of the features visible in the TEM image, (b), from a modification that has solidified under very strong radial thermal gradients. Epitaxy along many $\langle hk0 \rangle$ orientations has occurred resulting in a semi-continuous, but facetted solidification interface as is evident on the periphery of the a-Si. Within the a-Si shell is a core of polycrystallites. A SADP, (c), from the epitaxially solidified region shows a characteristic [001] ZA pattern. The SADP, (d), from the polycrystalline core and a-Si shell contains rings characteristic of a-Si as well as a number of randomly oriented diffraction spots from the crystallites. A small crack is also visible in (b), but is not of relevance to this chapter.

a crystal growth regime when the remaining melt volume was larger than previous examples. As such, multiple crystals were able to nucleate and grow through the remaining volume resulting in polycrystallinity, as revealed in the accompanying SADP, Fig. 4.7 (d).

In the final example, presented in Fig. 4.8, the cross-section consists of only two lines of defects and a fully amorphous structure at the centre. Note that the latter contains thickness fringes close to the periphery. It is also notably facetted, again suggesting that, as with the previous case, higher index $\langle hk0 \rangle$ epitaxy was present. The key difference with previous cross-section images, is that in this case solidification never returned to a crystal growth regime. Presumably in this case thermal gradients were so strong that the amorphisation continued to the centre of the modification despite the insulating properties of a-Si.

4.4.1 Discussion of the melt model

In this section the phenomenological model will be summarised and discussed with the aid of a schematic diagram in Fig. 4.9.

The transitions in solidification behaviour with increasing thermal gradient magnitude, Fig. 4.9 (a), are similar to those observed in one-dimensional PLM: perfect epitaxy (i), defective epitaxy (ii) and amorphisation (iii). Extending beyond the transitions reported in PLM literature was the return to a crystal growth regime due to the thermally insulating properties of a-Si (iv). Not shown in this diagram is that either a single crystal or polycrystalline core could result, depending on the melt volume. The strongest thermal gradients, however, prevent this transition, resulting in a relatively large volume of a-Si (v).

Macroscopically, the crystal-melt interface behaviour is simple. For weak radial thermal gradients, energetic considerations are dominant and the interface is faceted due to the interfacial free energy anisotropy, Fig. 4.9 (b)(i). With stronger radial thermal gradients, the interface

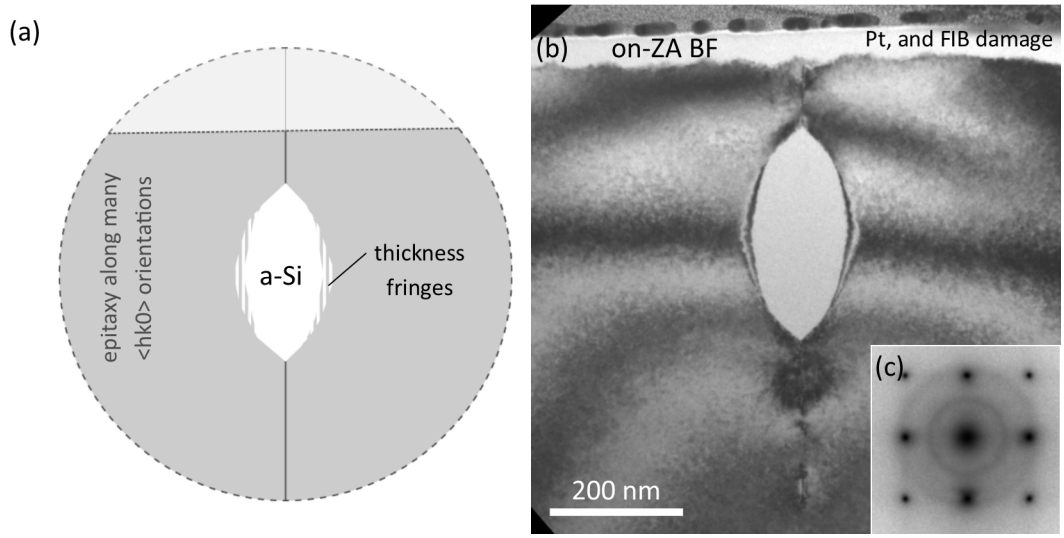

Figure 4.8: An annotated diagram, (a), of the features visible in the TEM image, (b), from a modification that has solidified under the strongest radial thermal gradients. Epitaxy along many $\langle hk0 \rangle$ orientations has occurred before solidification transitioned to amorphisation. No a-Si-insulation-induced transition back to crystal growth has occurred. The SADP, (c), from the [001] ZA shows a characteristic dc-Si pattern as well as a-Si rings.

becomes more circular as is thermally-favoured given the radial thermal symmetry. In practice the circular shape is approximated by the addition of higher index epitaxy and therefore, a large number of short facets on the crystal-melt interface, Fig. 4.9 (b)(ii). Laser anisotropy sometimes causes a discrepancy from the scenario depicted in the schematic. Results in this work are often consistent with stronger thermal gradients along the horizontal axis of short axis cross-sections, relative to the vertical axis, resulting in elliptical symmetry.

At a more local/microscopic level the simple picture of changing microstructure as a function of thermal gradients due to the interplay between energetic and thermal considerations is too simplistic. For example, why at lower thermal gradients is the less energetically favourable (001) facet dominant over the (011) facet? Similarly, why at large thermal gradients are the apparently slower $\langle hk0 \rangle$ orientations increasingly prevalent relative to the fastest $\langle 100 \rangle$ orientation? In both cases the answer can be found by considering the initial stages of solidification and the lateral growth rate of a facet. Solidification begins from a circular crystal-melt interface from which any $\langle hk0 \rangle$ orientation of an epitaxial front may propagate inwards. Simultaneously, the interface will propagate laterally to establish facets in order to minimise the interfacial free energy. Thus, many orientations may be overgrown by lateral growth of a neighbouring orientation, Fig. 4.9 (c)(i). Clearly the faster $\langle 001 \rangle$ orientations can overgrow all other orientations under conditions of weaker thermal gradients, as in Fig. 4.3 and Fig. 4.4. Effectively, the higher interfacial free energy of this facet relative to $\langle 011 \rangle$ is irrelevant. As the thermal gradients increase, energetic factors become less important which directly minimises the importance of forming long facets. Additionally, the relative rates of inward propagation and lateral propagation of a solidification interface are known to change, as illustrated with the magnitude of the arrows in Fig. 4.9 (c)(ii). Indeed, from the literature, the facet width of the fastest propagating interfaces has been known to decrease until extinction.[103] In other words, fast orientations shrink until they cease to exist. While this extreme is not reached in this work, this factor, combined with the reduced importance of the interfacial free energy, actually allow slower growth directions to become more prevalent under strong thermal gradients, as long as they are oriented to match the thermal gradients.

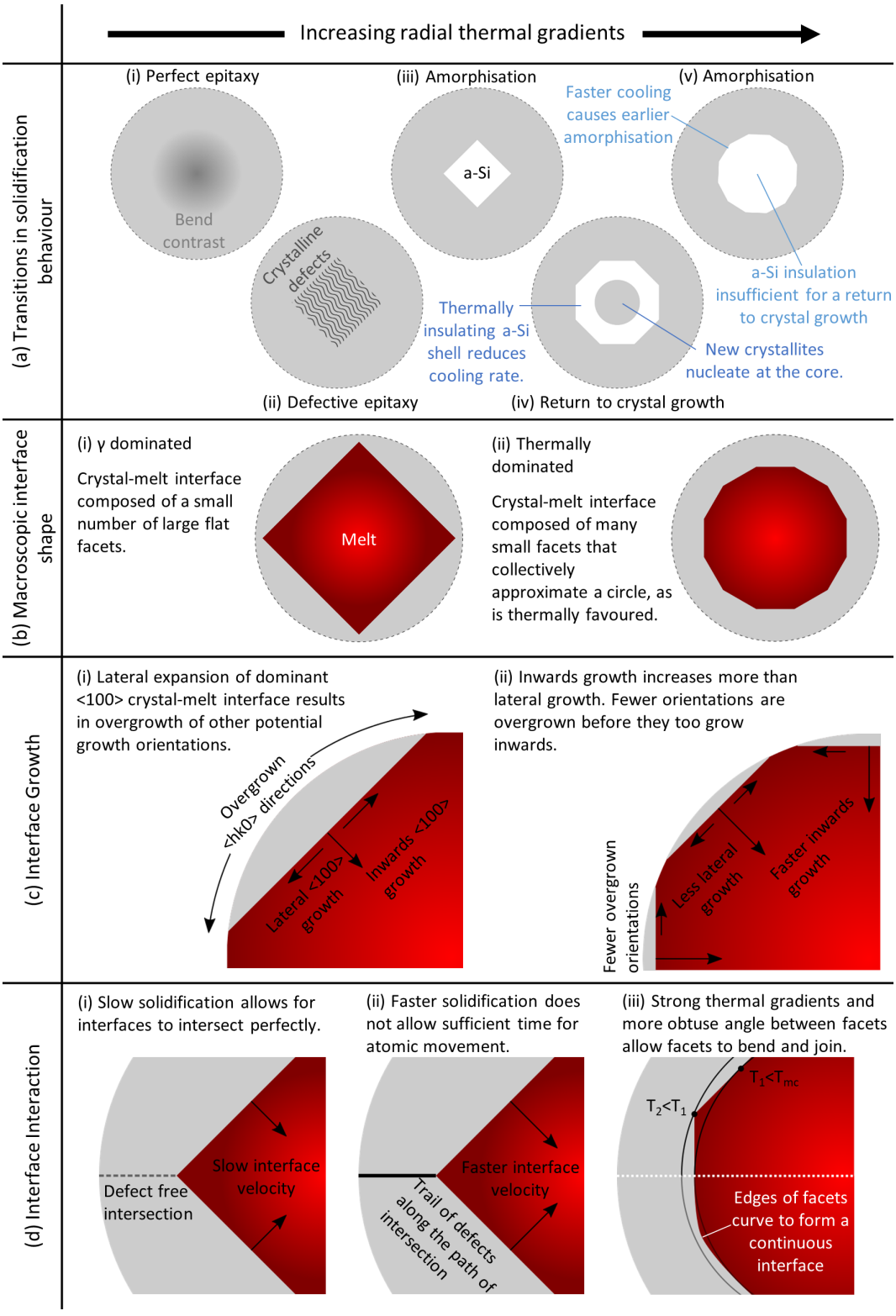

Figure 4.9: A schematic diagram summarising key features and how they vary with the initial magnitude of the radial thermal gradients. (a) The transition in solidification behaviour, (b) the macroscopic transition in interface shape, (c) Lateral growth of the crystal-melt interface resulting in overgrowth of $\langle hk0 \rangle$ orientations, and (d) The interaction of neighbouring facets on the crystal-melt interface.

The last intricacy for further discussion is the manner in which facets on the solidification interface interact, illustrated in Fig. 4.9 (d). As all the facets originate from the same crystal, it should be possible for each facet to intersect perfectly (i). Indeed, this does occur, but only intermittently and only for the smallest thermal gradients and slowest solidification, as in Fig. 4.3. More typically, a trail of defects is observed at the line of intersection Fig. 4.9 (d)(ii). It is assumed that a combination of the rapid propagation of the interfaces and spatial confinement at their intersection impedes the movement of atoms, potentially trapping them off lattice sites resulting in crystalline defects.

A third behaviour observed was another form of defect-free facet interaction. In this case of strong radial thermal gradients, the solidification process favours the rounding of the crystal-melt interface through high index epitaxy. The same is true locally/microscopically. Consider the top half of Fig. 4.9 (d)(iii) where two facets are shown, overlayed with isotherm lines. The inner line is at temperature T_1, which is below the equilibrium melting temperature of crystalline Si, T_{mc}, and it overlaps the centre of a facet. The second line is at temperature T_2, which is below that of T_1, and it overlaps the meeting points of two facets, demonstrating that the undercooling driving solidification is stronger at this point. Bending of the edges of the facets allows the variation in undercooling along the entire crystal-melt interface to be minimised, as is thermally-favoured. This is shown in the bottom half of Fig. 4.9 (d)(iii). Note that less bending is required as the angle between facets becomes more obtuse, such as when facets have formed on both low and high index $\langle hk0 \rangle$ orientations. The end result is a continuous crystal-melt interface with smooth connections between facets, a morphology which is not prone to leaving a trail of crystalline defects.

4.5 Attempts at numerical modelling

In addition to the two-dimensional phenomenological model of solidification on the short axis that has been presented in this chapter, there was also an attempt to develop a numerical model of the process as part of a collaborative effort.[‡] The numerical model was based upon a phase-field simulation of solidification.[104] This approach is distinct in that a specific phase-field variable is used to determine phase of the material (molten or solid) at every point on the simulation. This allows for a localised but smoothly transitioning interfacial region between the melt and solid regions. It is particularly suited to simulating the shape of a crystal-melt interface, making it useful, for example, to model dendritic growth.[105]

For this work the numerical model was intended to simulate the crystal-melt interface in two-dimensions from the perspective of a short axis cross-section. The model started with a circular melt with a constant undercooling below T_{mc}. It then used the anisotropic interfacial energy and the anisotropic interface kinetic coefficients, both discussed above to model the interface shape. The output was an crystal-melt interface that transitioned from a circle, to a rounded octagon.

A near octagonal crystal-melt interface shape does match several experimental results. However, as the numerical model only had inputs for the interfacial free energy and interface kinetic coefficient on the $\langle 100 \rangle$ and $\langle 110 \rangle$ orientations (within the relevant $\langle hk0 \rangle$ orientations), this near octagonal shape was inevitable. Solidification along higher index orientations could not be modelled as reliable data on these orientations is not available in the literature. The model, thus, proved to be of limited utility.

To provide useful results, the numerical model would require a more complex thermal model

[‡]A collaboration with L. Lai and A. Karma from the College of Science at Northeastern University

to be incorporated into it, including thermal gradients and thermal conductivity. It could potentially then explore the specific thermal conditions that cause the transitions between various solidification behaviours. Furthermore, by comparing it with experimental results, it should be possible to make estimates of the value of the interfacial free energy and interface kinetic coefficient along higher index orientations.

Although the numerical model did not directly provide any useful results, the discussions in developing the numerical model were critical in developing the phenomenological model.

4.6 Summary

To conclude this chapter, the phenomenological model will be summarised. For shallow thermal gradients, $\langle 100 \rangle$ epitaxy is dominant due to its high interface kinetic coefficient. However, macroscopically, energetics are dominant under such conditions, resulting in long facets that overgrow all other orientations. As thermal gradients increase, additional $\langle hk0 \rangle$ interfaces propagate before they can be overgrown, first on $\langle 110 \rangle$, then other indices. Inward epitaxy dictates that interfaces must interact with one another. For slow interface velocities the interfaces intersect perfectly (at least in part), without producing crystalline defects. In most cases velocities are higher, so less time is available for perfect atomic arrangement, and defects are produced. However, for the steepest thermal gradients, where epitaxy occurs along many directions, defects are again avoided. In this case the more obtuse angle between facets, and the significant undercooling at the meeting point create a smooth conjoining of facets. As with one-dimensional PLM, transitions in solidification behaviour are observed: from perfect epitaxy for shallow thermal gradients, to defective epitaxy with increasing thermal gradients, and then amorphisation. An additional feature of two-dimensional epitaxy, beyond that reported in the PLM literature, occurs when the amorphous layer is sufficiently thick so as to thermally insulate the remaining melt. Solidification then slows and returns to a crystal growth regime.

It remains unanswered as to why these thermal gradients differ along the length of the laser-induced modifications. This is where the three-dimensional nature of the modifications becomes important. The next chapter, examining the long axis of the modification, broadens the discussion to explore the morphology in three-dimensions.

Finally, it should be acknowledged that there is also a small number of features observed in the modified regions that do not fit the phenomenological model neatly. These are considered over the following two chapters.

Chapter 5

The morphology of long axis cross-sections

In this chapter the long axis morphology will be explored. This chapter will begin by reviewing the features observed in short axis cross-sections in the context of their presence and appearance on long axis cross-sections. Then, the solidification process will be considered at a macroscopic level, with reference to the long axis cross-sections presented in Chapter 3, Fig. 3.4, and Verburg's thermal modelling in Chapter 1, Fig. 1.6. Subsequently a more detailed examination of the features visible in the long axis cross-sections will be presented. This will sequentially consider the increasing diameter region, the constant diameter region, the decreasing diameter region and the cap. As with the previous chapter, the interplay between the thermally-favoured and energetically-favoured solidification interface shape will be a key factor for explaining the features observed. Also of importance will be the influence of features that form earlier during solidification on those that form later, not unlike the a-Si-induced slowing of solidification and return to crystal growth on the short axis cross-sections. Furthermore, more generally the sequence in which different regions solidify is important in understanding the final morphology. Finally, this chapter will begin to introduce the influence of density differences between the various Si phases on the solidification process, although full treatment of this topic will take place in the next chapter.

5.1 Experimental

This chapter makes use of the standard, sub-bandgap regime conditions (1549 nm, 3.5 ns, 2 μJ laser pulse) to produce modifications. The modifications are produced in isolation, with a sufficient gap so that adjacent modifications do not interact.

Conventional TEM is used to characterise morphology, primarily along the long axis. Some results from short axis cross-sections are also presented. Reference is also made to Raman microspectroscopy.

Sample preparation of the long axis cross-sections involved FIB milling of H-bar samples. The short axis cross-sections are prepared by FIB milling of ex-situ liftout samples.

5.1.1 The features contained within a long axis cross-section

The long axis cross-sections are not thick enough to contain the entire thickness of the modification. As such, it is possible for features that were observed in the short axis cross-sections to be missing in the long axis cross-sections. Furthermore, the features that are present in both do not always appear equivalently. In this subsection the presence and appearance of features that

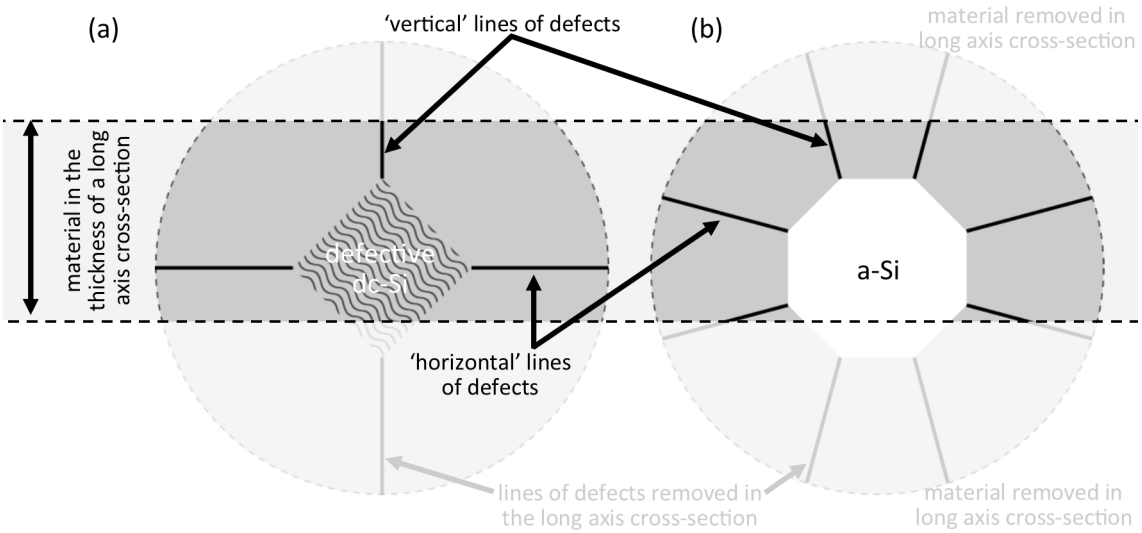

Figure 5.1: A schematic diagram of the morphology of modifications viewed from the perspective of the short axis, showing what features may be contained in a long axis cross-section(between the dashed lines) and those that may have been removed during thinning (low contrast). In (a) the morphology of a region that solidified by ⟨100⟩ epitaxy with a region of defective epitaxy is shown. In (b) the morphology of a region that solidified by ⟨100⟩ and ⟨110⟩ epitaxy with an a-Si core is shown. The long axis cross-sections are centred sufficiently to contain the core along their entire length. Portions of 'vertical' lines of defects may or may not be within the thickness of the cross-section. 'Horizontal' lines of defects should be within the long axis cross-section's thickness.

have already been discussed in the previous chapter will be briefly reviewed with regard to the long axis cross-sections.

In Fig. 5.1 the schematic diagrams of two different morphologies viewed from the perspective of the short axis are shown. In (a) the morphology of a region that has solidified by ⟨100⟩ epitaxy with a defective dc-Si core is shown. In (b) the morphology of a region that has solidified by ⟨100⟩ and ⟨110⟩ epitaxy with an a-Si core is shown. Both cases contain lines of defects due to the intersection of epitaxial interfaces of different orientations. Here it is useful to distinguish between the lines of defects that are approximately horizontal, and those that are approximately vertical. In a long axis cross-section the finite sample thickness (represented by the dotted lines in the schematic) means that the 'vertical' lines of defects may be missing. In the schematic the bottom vertical lines are missing while the top vertical lines are partially present. These vertical lines of defects are viewed end on in the long axis cross-sections, resulting in a dark line running roughly along the centre of the modification in the images presented below. The dark line may broaden and weaken in the case of inclined vertical lines of defects, such as those shown in Fig. 5.1 (b).

The 'horizontal' lines of defects, labelled in Fig. 5.1, are viewed side on in long axis cross-sections. This allows characteristics of the horizontal lines of defects to be resolved on the long axis cross-sections that can not be resolved on the short axis cross-sections. In particular, three defect morphologies that generally appear to be equivalent on the short axis cross-sections are shown below to be different from the perspective of the long axis cross-sections. These forms of defects are: lateral lines of defects, interline defects and arching defects. They will be shown and discussed below.

As for the core of the modification, this should always be contained in the long axis cross-sections, as it is in the schematic. The core may contain: strain, defects from defective epitaxy,

a-Si and crystallites. The polycrystallites and a-Si can generally be readily discerned when present. Indeed, the contrast of a-Si, including its appearance on the long axis cross-sections, was discussed in Chapter 3. However, from the perspective of the long axis, defects from defective epitaxy are only subtly different from the horizontal lines of defects.

5.2 A macroscopic picture of solidification on the long axis

In the previous chapter the morphology visible in short axis cross-sections was explained based on strong, but varying, radial thermal gradients which drove inwards solidification from the original melt periphery. On the long axis cross-sections this same basic process must also be occurring. In this section the factors that influence this inwards epitaxial solidification from the perspective of the long axis cross-sections at a macroscopic level will be introduced. This discussion will make reference to the TEM images of the entire length of long axis cross-sections, presented in Chapter 3, Fig. 3.4, and Verburg's thermal modelling from Chapter 1, Fig. 1.6.

Recall that in Chapter 3, the long axis cross-sections, Fig. 3.4, were divided into four sections. For most of the modification, starting from focus, the features initially increase in diameter. Then there is a region of near constant diameter, followed by a decreasing diameter region and finally a feature called the cap. The size of these features was previously suggested to reflect the initial melt shape. Indeed, the modelling in Chapter 1, of the peak temperature reached under similar laser conditions, Fig. 1.6 (a), is broadly consistent with this explanation. The modelling also shows strong radial thermal gradients, consistent with the explanation for the short axis cross-sections. Notably, the radial thermal gradients decrease along the length of the modification as distance from focus increases. The vertical thermal gradients are only comparable to the radial gradients at either end of the modification.

Based on these findings, macroscopically, the solidification process begins with the inwards propagation of the crystal-melt interface from it's initial limits. This inwards propagation is largely radial (and two-dimensional) in nature, with vertical cooling being relevant only at either end of the modification. This inherently means that the diameter of the melt volume varies along the modification's length. Regions where the remaining melt diameter is larger can be said to lag behind regions where the melt diameter is smaller. Solidification in the widest region, the constant diameter region, therefore, lags behind the rest of the of the modification. Indeed, the results below are consistent with the constant diameter region being the last to complete solidification.

The lag (or conversely, the lead) of solidification between different regions is additionally dependent on the relative strength of the radial thermal gradients. Near focus, where the thermal gradients are strongest, the solidification interface will propagate inwards quickly. In the decreasing diameter region, where the thermal gradients are weakest, the solidification interface will propagate slowly. As such, near focus solidification will lead solidification further from focus. This near focus lead in solidification increases due to the stronger thermal gradients near focus. In contrast, the decreasing diameter region initially leads the constant diameter region geometrically, but with weaker thermal gradients in the decreasing diameter region the lead is expected to decrease as solidification progresses.

This macroscopic picture and the important subtleties in melt geometry will be important for explaining the specific features shown in the following sections.

5.3 The increasing diameter region

From a macroscopic perspective, the increasing diameter region (above focus), is the most easily understood: as distance from focus increases the melt diameter increases and the thermal gradients decrease. The crystal-melt interface nearer to focus therefore begins with a lead relative to that further from focus, and this lead will increase until solidification is complete due to the stronger thermal gradients. However, at a more local (microscopic) level the increasing diameter region is complex and rich with features. Many of these features are periodic in nature and are related to the orientation mismatch between three factors: the energetically-favoured crystal-melt interface, the thermally-favoured crystal-melt interface and the crystal-melt interface at the onset of solidification. Note that this is similar to, but more complicated than the short axis cross-sections. On the short axis the initial crystal-melt interface was aligned with both the epitaxial orientations and the thermally-favoured interface crystal-melt interface geometry.

In this section the periodic features visible on the long axis will be explained on a similar basis to the short axis features. In doing so the general trends in the position-dependent morphology over the length of the increasing diameter region will be established. Subsequently, perturbations to the position-dependent morphology will be introduced and discussed.

5.3.1 Periodic features in the increasing diameter region - results

Throughout the increasing diameter region are a set of periodic features, the exact nature of which is position-dependent (and also subject to the perturbations discussed below). The various forms are visible in Fig. 5.2. Here Fig. 5.2 (a) and (b) are, respectively, on and off-ZA BF images from the same location near to the focus end of the modification. Figure 5.2 (c) and (d) are likewise on and off-ZA BF images of a position midway up the increasing diameter region. Figure 5.2 (e) is an off-ZA BF image from a position further from focus than the previous two positions. The features within these images will now be detailed, starting from the position nearest to focus.

The features in Fig. 5.2 (a) consist of a difficult to discern core and five pairs of defects extending laterally, marked by arrows, that are visible only in the top half of the image. In Fig. 5.2 (b) the lateral lines of defects are now difficult to discern, but the core is more evident and is characteristically a-Si, with the exception of one region that may be a void. The a-Si has a subtly oscillating width, which is emphasised by the adjacent, slightly exaggerated guide line. The local maxima in width of the a-Si coincide with the position of the lateral lines of defects visible in Fig. 5.2 (a).

At an intermediate distance along the increasing diameter region, where the melt and feature diameter is wider, Fig. 5.2 (c) and (d) also have highly evident lateral lines of defects. Three examples are marked with longer black arrows in Fig. 5.2 (d). In between the lateral lines of defects are more chaotic ‘interline’ defects, one example of which is marked with a short black arrow. Also labelled is a continuous line of defects running vertically along the centre of the image. This is a vertical line of defect viewed end on, as discussed with regard to Fig. 5.1. As for the core, this region is difficult to discern but most probably consists of defective crystalline material.

The last position, furthest from focus and shown in Fig. 5.2 (e), features a small number of lateral lines of defects, a large amount of arching defects, and a core consisting of a-Si and crystallites. Notice that, in this case, the a-Si has no obviously oscillating width, unlike that in Fig. 5.2 (b).

Interestingly, the lateral lines of defects and the oscillating width of the a-Si core have been

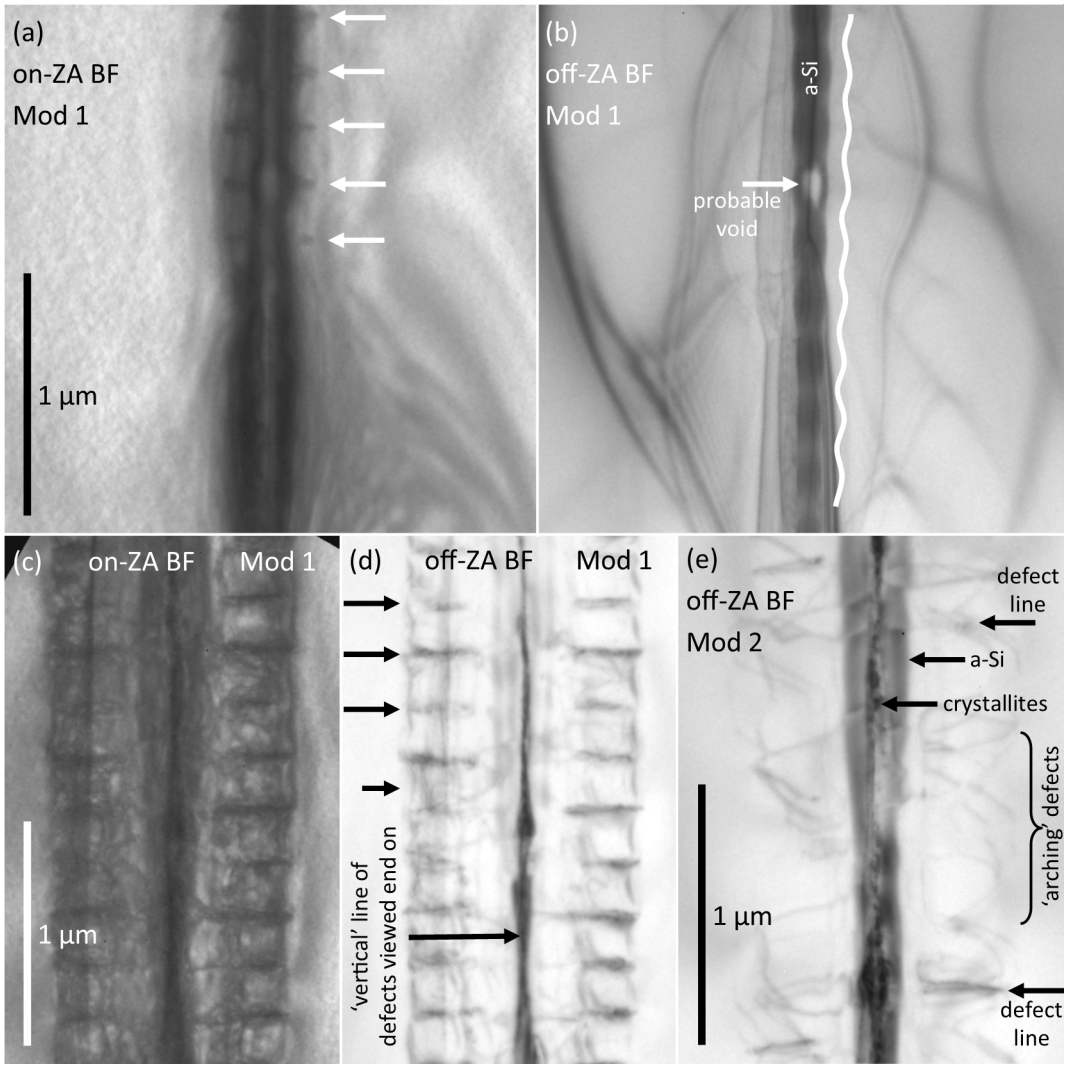

Figure 5.2: TEM images of the increasing diameter region, showing various periodic features visible in the morphology of long axis cross-sections. The results from a region close to focus, when viewed on-ZA, (a), show lateral lines of defects marked with white arrows only in the top half of the image. The same region viewed off-ZA at the same scale, (b), reveals an a-Si core with an oscillating width, emphasised by the white guide line. The lateral lines of defects align with local maxima in the a-Si's width. Midway along the increasing diameter region, images at the same scale collected on-ZA, (c), and off-ZA, (d), again show lateral lines of defects, examples of which are marked by the mid length arrows. In between the lateral lines of defects are 'interline' defects, an example of which is marked by the small arrow. Running vertically along the centre of the image is a continuous line of defects. The morphology furthest from focus, while still within the increasing diameter region, is shown in (e). Most defects in this region are arching 'interline' defects, although some lateral lines of defects are also present and labelled. The centre of this region contains a-Si and crystallites.

measured across multiple long axis cross-sections to have a constant period of 226 ± 30 nm within the increasing diameter region. Furthermore, further from focus the periodic features are mostly absent, as in Fig. 5.2 (e), but when the lateral lines do occur their spacing is at integer multiples of the 226 ± 30 nm period.

5.3.2 Periodic features in the increasing diameter region - discussion

In this subsection the periodic features will first be discussed with reference to the shape of the crystal melt interface, and how the interface varies over the length of the increasing diameter region. The nature of the crystalline defects also varies over the length of the increasing diameter region, and this matter will also be discussed.

The crystal-melt interface

The periodic features are largely a product of an orientation mismatch between the three factors mentioned previously: the energetically-favoured crystal-melt interface (facets), the thermally-favoured crystal-melt interface and the crystal-melt interface at the onset of solidification. This is shown schematically, in two-dimensions, in Fig. 5.3. In (a), the facets observed on the short axis cross-sections (mainly {100} or {110}), are vertical from the perspective of the long axis cross-sections. The original melt periphery, also shown, is inclined to the vertical facets. Furthermore, the thermally-favoured interface shape, represented here by the isotherm curve, is even more inclined due to the presence of stronger thermal gradients closer to focus. In order to accommodate this orientation mismatch, the actual solidification interface will approximate the thermally-favoured interface with a series of facets separated by steps. Figure 5.3 (a) is a highly simplified schematic of this morphology.

The exact nature of the faceted and stepped interface varies along the length of the increasing diameter region. Nearest to focus, strong radial thermal gradients favour a solidification interface that more closely approximates of the thermally-favoured crystal-melt interface, rather than the preferred facet orientations. In Fig. 5.3 (b)(i) this closer adherence to the isotherm is shown to take the form of smoothly curved steps between the facets. Note that this is similar to the rounding of the crystal-melt interface on the short axis under conditions of strong radial thermal gradients. This condition creates a smoothly undulating solidification interface, as shown in the schematic. Given the isotherm curve shown, and that the original crystal-melt interface could also constitute a cooler isotherm curve, it is evident that the undercooling along the solidification interface must also be undulating. It follows that should undercooling-induced amorphisation occur, it will do so at an oscillating distance from the centre of a modification. The end result is illustrated in Fig. 5.3 (a)(ii) which corresponds to the experimental results in Fig. 5.2 (a) and (b).

The thermal gradients midway along the increasing diameter region are weaker than those near focus. As such, the crystal-melt interface is more strongly defined by the preferred facet orientations. This is shown schematically in Fig. 5.3 (c). Notice that the facets are flatter and the steps between facets are much more abrupt. The abrupt steps cause an increase in defect density along their path as the interface propagates inwards, denoted by the black lines in the schematic. This is the cause of the lateral lines of defects in the top half of Fig. 5.2 (a), throughout (c) and (d) and in some portions of (e). The nature of these defects will be expanded upon below.

Further from focus the thermal gradients vary slowly along the vertical direction and the inclination of the thermally-favoured interface (isotherm) to the facet orientation is minimal. This condition is illustrated in Fig. 5.3 (d). Notice that this implies a much smaller step is

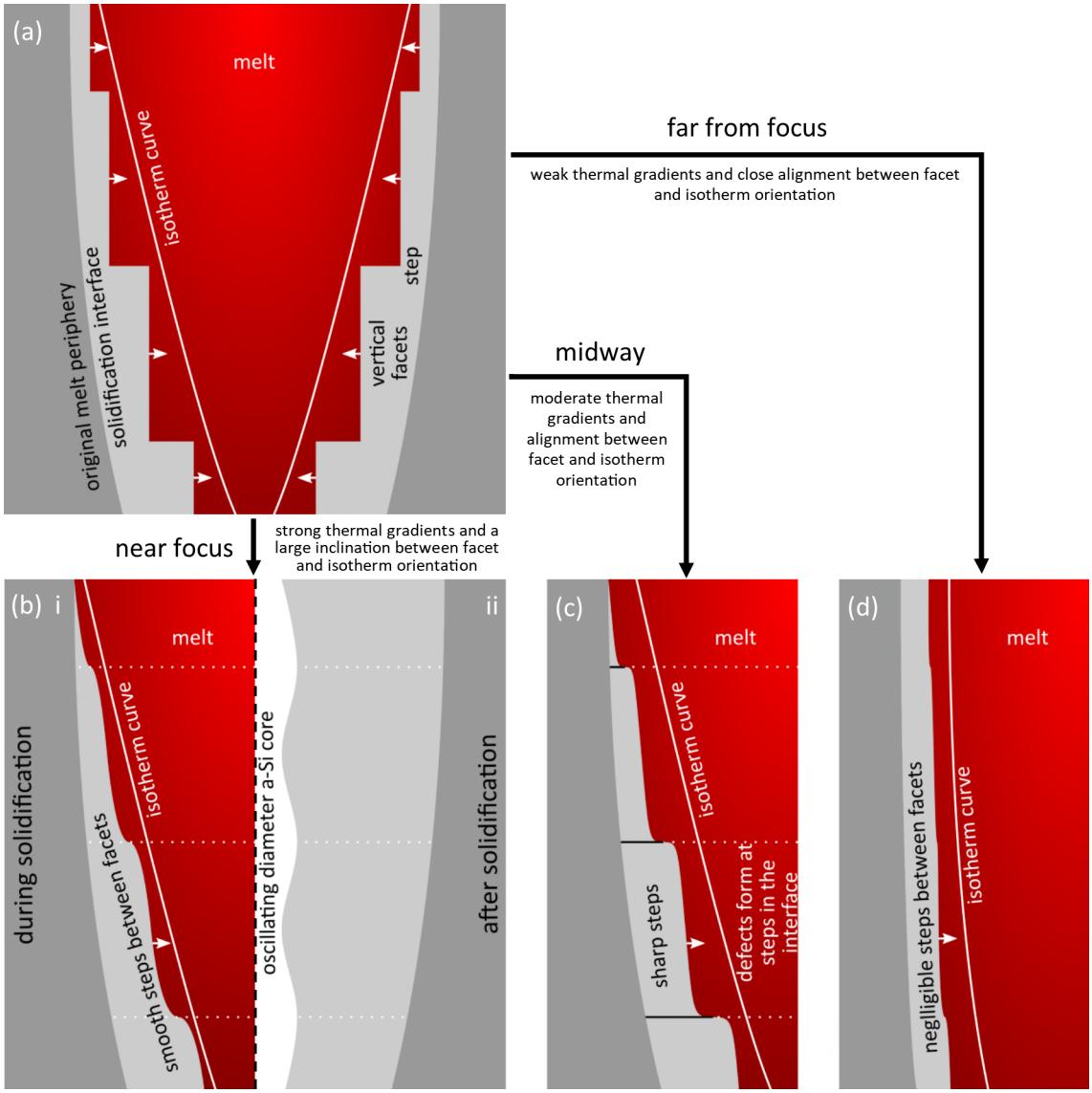

Figure 5.3: Schematic diagrams of the solidification process in the increasing diameter region from the perspective of the long axis. Highly simplified in (a) the crystal-melt interface approximates the thermally-favoured interface (represented by the isotherm line) by forming a series vertical facets (which are energetically-favoured), separated by steps. Less simplified schematics of the faceted and stepped interface are shown under different conditions along the length of the increasing diameter region in (b-d). Nearest to focus, (b), the strong radial thermal gradients allow for highly curved steps between facets, (i). Undercooling along the crystal-melt interface oscillates, as can be inferred from its departure from the isotherm curve. Provided sufficient undercooling is reached, this effect allows for the transition to amorphisation to occur at an oscillating distance from the centre of the modification, (ii). Midway along the increasing diameter region, (c), the steps are more abrupt as the thermal gradients are weaker. The abrupt steps cause an increase in defect density as represented by the black lateral lines. Near the top of the increasing diameter region, (d), the thermally-favoured crystal-melt interface nearly aligns with the facet orientation allowing for a small step amplitude and no increase in defect density.

required between facets. As such, curving of the interface between facets becomes plausible. This behaviour reduces the propensity to form lateral lines of defects and Fig. 5.2 (e) is mostly with in this regime, which explains why very few lateral lines of defects are present. It is worth reinforcing here that when the lateral lines of defects are present far focus, such as those examples in Fig. 5.2 (e), they appear at integer multiples of the 226 ± 30 nm periodic distance. This suggests that it not the distance between steps that is changing, only the step amplitude.

Crystalline defects

At this stage the exact nature of the lines of crystalline defects should be discussed. Previously it was stated that three forms of defects observed in long axis cross-sections: 'lateral lines' of defects, 'interline' defects and 'arching' defects, all appear equivalent from the perspective of short axis cross-sections. This is because they all have the same basic origin, colliding epitaxial interfaces as explained in the previous chapter from the perspective of short axis cross-sections. They differ on the long axis because of differences in the conditions under which this collision occurs.

Generally the colliding epitaxial interfaces result in the 'interline' defects from the perspective of the long axis, like those indicated by the small arrow in Fig. 5.2 (d). When abrupt steps between long axis facets simultaneously occurs, the density of the defects between colliding epitaxial interfaces increases. This explains the lateral lines of defects in Fig. 5.3 (c) and (d).

In the conditions far from focus, as in Fig. 5.2 (e) the thermal gradients are weaker and the step size between facets is limited. As such, the lateral lines of defects are largely absent and defects from colliding epitaxial interfaces form only intermittently. When the defects do form they may propagate laterally along the inwardly progressing interface. For this reason, the defects appear more like 'arches'. The equivalent morphology on the short axis would correspond to Fig. 4.3 from the previous chapter.

In conditions of stronger radial thermal gradients, the crystal-melt interface tends to be highly curved and defects generally aren't produced. However, when a step on the long axis occurs then defects may form between the epitaxial interfaces. This explains the presence of lateral lines of defects without 'interline' defects in the top of Fig. 5.2 (a) and (b). In the bottom of these figures the thermal gradients are sufficient that even the presence of steps does not induce defect formation.

5.3.3 Periodic features in the increasing diameter region - origin of the period

Another matter to address in this section is why the steps between facets appears to be a constant 226 ± 30 nm within the increasing diameter region. This isn't known, although some relevant statements can be made.

As the periodic features are visible from the melt periphery, their length can not be an emergent property of the solidification process. Nor can the length of the periodicity be related directly to any of the key parameters raised when discussing the morphology: the thermal gradients, the inclination or the crystal-melt interface (relative to the facet orientation) or the curvature of the crystal-melt interface, as all vary over the length of the increasing diameter region. However, it is possible that some combination of these factors defines a constant period. What this combination is, or what other parameters might be relevant, has not been established.

A second possibility is a wavelength-dependent origin. The free space laser wavelength, 1549 nm, is 444 nm in Si (accounting for the refractive index). The periodicity of the absolute amplitude of the light is therefore 222 nm, which is within uncertainty of the 226 ± 30 nm periodicity of the features. It follows that should there be some sort of wavelength-dependent

periodicity in the thermal conditions and/or melt shape, this could give rise to the periodicity. This must be subtle enough that it is not directly visible after solidification, but sufficient to define the vertical facet length. A potential mechanism has, again, not been established.

5.3.4 Periodic features - summary and trends

To conclude this section the key findings will be reiterated and expected trends over the increasing diameter region stated. On the long axis, the solidification interface takes the form of facets separated by steps. Nearest to focus, where the thermal gradients are strongest, defect formation is suppressed due to the solidification interface bending between facets. As thermal gradients weaken, the defects initially form only along the path of the steps between adjacent facets. Further from focus they also formed in between the steps as a consequence of colliding interfaces, from the perspective of the short axis. However, the defect density still increases when vertical steps simultaneously occur. Finally, far from focus where the facet orientation nearly matches the thermally-favoured interface shape (isotherm), the steps become negligible and only the lower density defects occur from colliding interfaces of different orientations.

At the centre of the modification, nearest to focus, rapid solidification results in a-Si. This has an oscillating width due to the undulations on the solidification interface that arise from steps and a varying degree of undercooling along the interface. Initially the average width of the a-Si is expected to increase as the overall melt diameter increases. However, as thermal gradients decrease further from focus the average a-Si width should eventually also decrease, resulting in a transition to defective epitaxy. Again, the width of the defective region will decrease further from focus as the thermal gradients decrease and eventually the centre of the modification may be defect-free.

In practice these trends are often perturbed, which is the topic for the following subsection.

5.3.5 Perturbations in the increasing diameter region

The general solidification process is subject to various perturbing influences. In this section examples of perturbing influences will be demonstrated in the increasing diameter region. The coverage of this topic will be limited to two cases with an a-Si core, as these examples are more easily demonstrated and explained. However, it should be appreciated that similar perturbations may occur both outside of the increasing diameter region and without an a-Si core. These other cases are excluded for brevity and because the change in morphology and underlying physical processes are often more subtle.

Based on the previous section the expectation within the increasing diameter region is for the average width of the a-Si at the centre of the modification to decrease as distance from focus increases. This is because the strength of the radial thermal gradients decreases further from focus. Indeed, this has been observed. More typically though, the a-Si is suddenly interrupted while relatively thick. Two examples of this behaviour are presented in Fig. 5.4.

The first example, in Fig. 5.4 (a), features typical defects on the periphery of the modification. The dark feature at the centre of the image is largely a-Si. The top of this dark feature is wider and encapsulates what is likely a crystallite core. Above this a-Si is a short region of defective crystalline material followed by a void, highlighted in white and indicated with an arrow. A full discussion of the voids follows in the next chapter, in this section only their influence on the a-Si will be considered.

The second example, in Fig. 5.4 (b), also has typical defects on the periphery of the modification, although with the sample tilted off-ZA, their visibility is reduced. In the bottom portion of the image the core is composed of a-Si with oscillating width. Midway up the image, crystallites

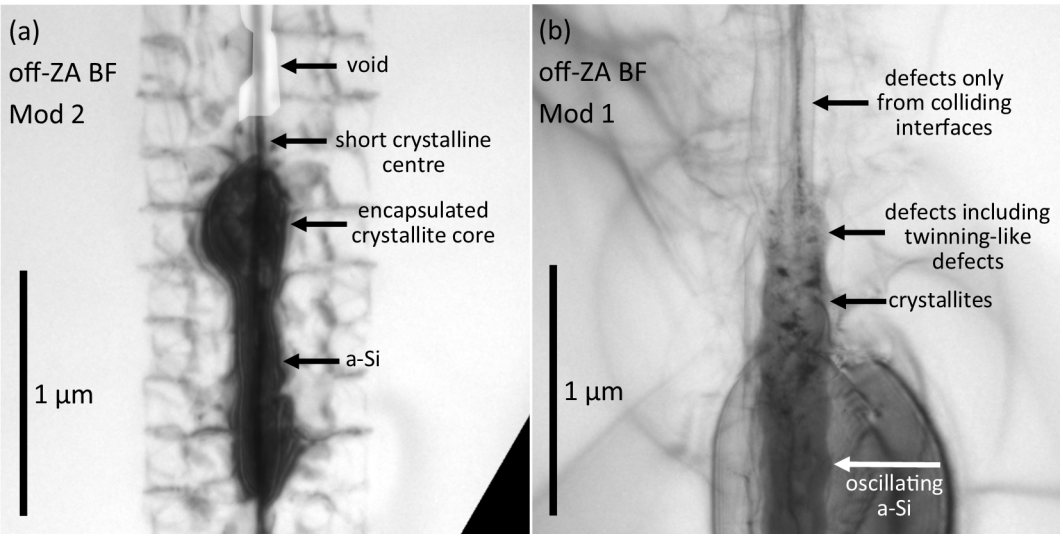

Figure 5.4: Perturbations to the solidification process can be observed by the abrupt end of a-Si cores when viewed in long axis cross-sections. In (a) the top of the a-Si encapsulates a crystallite core above which is a short section of defective crystal and then a void. In (b) the oscillating diameter a-Si core transitions to an increasingly polycrystalline filled structure, before becoming highly defective single crystal. Above this is a region conventional solidification with defects from colliding facets only.

are present, sometimes visible as darker spots and these are most likely encapsulated within a-Si. Higher up the core of the modification then transitions to highly defective single crystal, including twinning-like defects, before the defect density decreases further up the image.

In both cases above, the sudden interruption of the a-Si can be associated with morphological features that, once formed, influence the remaining solidification process. Here, these features are divided into three interrelated categories. The first category is perturbations due to dramatic changes in the density of the material, for example the existence of a void. This will obviously affect local solidification. For example, solidification within the vicinity of a void is heavily influenced by the movement of molten material during solidification, as discussed in the next chapter, and also because the void constitutes a significant interruption to the thermal conditions driving solidification. Indeed, interruptions to thermal conditions away from the norm is the second form of perturbation. For example, cooling can be slowed by a reduction in thermal conductivity as was already demonstrated for a-Si in the short axis results. On the long axis, vertical thermal gradients may also be decreased due to the presence of a-Si or a void. Of course, vertical cooling is small in comparison with radial cooling, but it may still have a tangible influence. In addition, the heat energy that must be extracted for solidification can also change the thermal conditions. For example, the latent heat of solidification is higher for dc-Si compared with a-Si.[106–109] Finally, the presence of strain is known to influence solidification.[110,111] Indeed, it will be shown to have a strong influence in the constant diameter region, discussed below.

Collectively all the perturbations discussed here are of relevance to one or both of the structures shown in Fig. 5.4 (a) and (b). However, this discussion does not constitute a comprehensive list of possible contributing factors. It does however serve to illustrate the role that local morphology may have on the solidification of an a-Si core. It follows that these, and similar factors may influence other aspects of the morphology during the solidification process.

5.4 The constant diameter region

The constant diameter region, above the increasing diameter region, is characterised by a near constant melt diameter and relatively weak radial thermal gradients. It differs greatly from the remainder of the modification in that the isotherm curves are basically aligned with the preferred facets during solidification. Consequently, steps between facets are not of significance in explaining the resultant morphology. However, as the region with the widest initial melt diameter and relative weak radial thermal gradients, solidification in the constant diameter region is expected to lag behind solidification through the remainder of the modification. This will be shown to be of great importance to the morphology of this region.

5.4.1 The constant diameter region - results

Two examples of the constant diameter region on long axis cross-sections are presented in Fig. 5.5. With the exception of the lower contrast in (a) and the void in (b), both have the same basic features. Beyond the melt diameter are bands due to bend contrast. Indeed, this region has the most intense bend contrast of any throughout the modification. Recall that in Chapter 3, Fig. 3.3, Raman mapping revealed strong compressive stresses that is presumably the underlying cause of this bend contrast. The bend contrast continues within the modification itself, where it overlaps with a region of highly defective Si with a roughly oval shape as marked on the figure. The tapered ends of this compressively strained, highly defective Si actually extent beyond the constant diameter region into the increasing and decreasing diameter regions adjoining it.

5.4.2 The constant diameter region - discussion

Clearly the morphology of the constant diameter region is strongly dependent on the presence of compressive strain. This sections seeks to briefly explain the origin of the strain, and how it gives rise to the morphology visible in Fig. 5.5.

The main cause of the strain is associated with density changes and redistribution of material via the molten volume. This topic is covered in depth in the following chapter and so only a brief and partial description is provided here. In short, an increase in density upon melting drives the formation of voids (the melt is $\sim 10\%$ more dense than dc-Si[112,113]). Voids are not completely removed during solidification, dictating that the displaced material must be accommodated in a higher density solid region elsewhere in the modification. Since Si largely returns to dc-Si during solidification (particularly in the constant diameter region), the displaced material is expected to be increasingly concentrated in the remaining melt volume and therefore the constant diameter region. The excess material must be contained within the solid and the mechanism by which dc-Si can accommodate the excess is compressive strain. This then explains the compressive strain in the Raman results and the bend contrast in the TEM.

The high density of crystalline defects is easily explained in the context of compressive strain as strain is known to lower the quality of subsequent epitaxial solidification.[110,111] The roughly oval shape of this region would somewhat reflect the crystal-melt interface shape as the strain-induced effects on epitaxy quality gradually increased.

5.5 The decreasing diameter region

The decreasing diameter region again involves a mismatch between the isotherm curves and the favoured facet orientations as a result of changing thermal gradients along the modification.

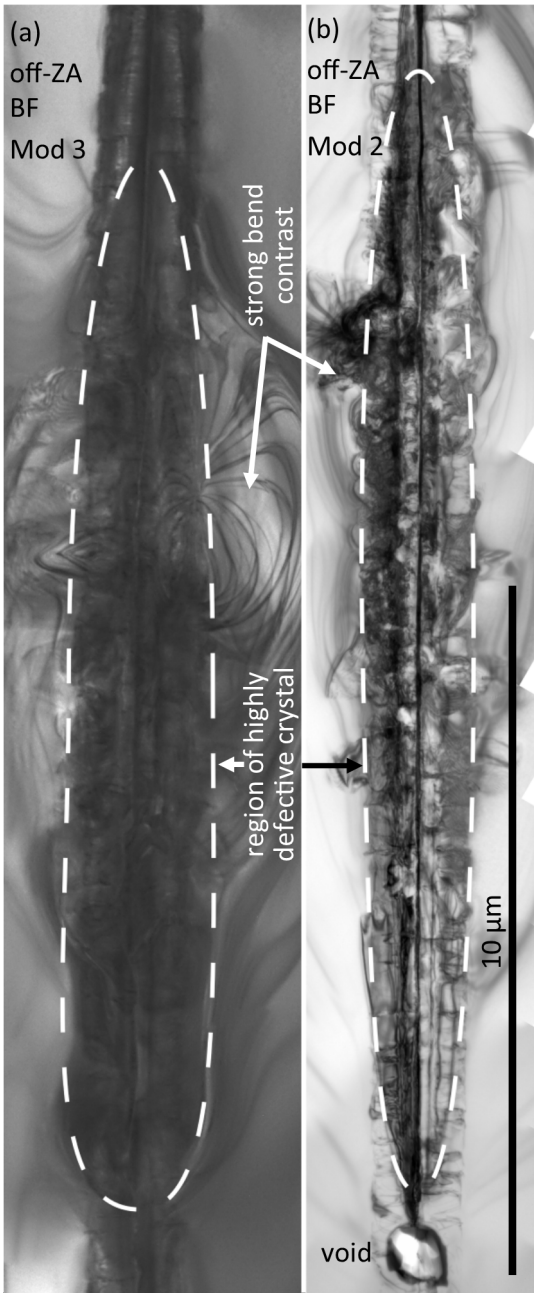

Figure 5.5: TEM images from long axis cross-sections in the constant diameter regions of two modifications. They contain substantial strain-induced bend contrast both within the modification, and beyond the melt diameter. The defect density is also notably high within a roughly oval shaped region outlined. They differ only in that the contrast in (a) is lower and a void is visible in (b).

The initial melt periphery is, of course, narrowing further from focus. So too is the crystal-melt interface during solidification. However, with weakening radial thermal gradients further from focus, the mismatch between isotherm curves and preferred interface facets is expected to decrease.

5.5.1 Decreasing diameter region - results

Figure 5.6 (a) shows both the decreasing diameter region and the cap. Consideration of the cap will be left to the following section. For the purposes of comparison, the morphology far from focus in the increasing diameter region, Fig. 5.6 (b), and the middle of the increasing diameter region, Fig. 5.6 (c), are also shown. All images are collected under the same imaging conditions and are presented at the same scale.

Most of the crystalline defects visible in Fig. 5.6 (a) resemble the 'interline' defects (resulting from the collision of facets on the radially solidifying interface), which are also observed midway up the increasing diameter region, Fig. 5.6 (c). Lateral lines of defects (due to steps between vertical facets) are also present, some of which are marked with arrows. However, compared with the equivalent features in the increasing diameter region, Fig. 5.6 (c), they are less pronounced. They also appear to have no well-defined periodicity in Fig. 5.6 (a). There is also evidence of defects with a more 'arching' appearance. These somewhat resemble those in the increasing diameter region far from focus, Fig. 5.6 (b), although, the defect density is clearly higher in (a) than in (b).

5.5.2 Decreasing diameter region - discussion

The most pertinent feature of these results is that the defect density in the increasing diameter region is relatively high. This is inconsistent with the weak radial thermal gradients expected in this region, which should result in a low defect density. For comparison, stronger thermal gradients are expected in Fig. 5.6 (b), but the defect density is lower than in Fig. 5.6 (a). This suggests that, like the constant diameter region, but to a lesser extent, excess material has led to a strain-induced reduction in the quality of the epitaxy, and therefore more defects. The geometry and weak thermal gradients within the decreasing diameter region is expected to result in a decreasing lead over the constant diameter region. Additionally, the solidification interface is expected to become better oriented with the preferred vertical facets. Collectively, this suggests that the rejection of excess material into the constant diameter region within the remaining melt will become less favourable as solidification progresses. This will result in the high defect density observed in Fig. 5.6 (a) as the solid accommodates excess material.

The decreasing inclination of the solidification interface from vertical also provides an explanation for the nature of the defects. A less inclined interface has already been explained to allow for more subtle steps between facets, in this case causing less pronounced lateral lines of defects. This is also the condition that appears to give rise to the 'arching' defects in the far from focus portion of the increasing diameter region, such as in Fig. 5.6 (b).

5.6 The cap

The cap is a unique and relatively complex region of the modification. In addition to strong radial thermal gradients, the cap also has a strong vertical thermal gradient. This should allow for faster cooling compared with the decreasing diameter region. Indeed, the morphology shown below is more consistent with the morphology near focus in the increasing diameter region. The

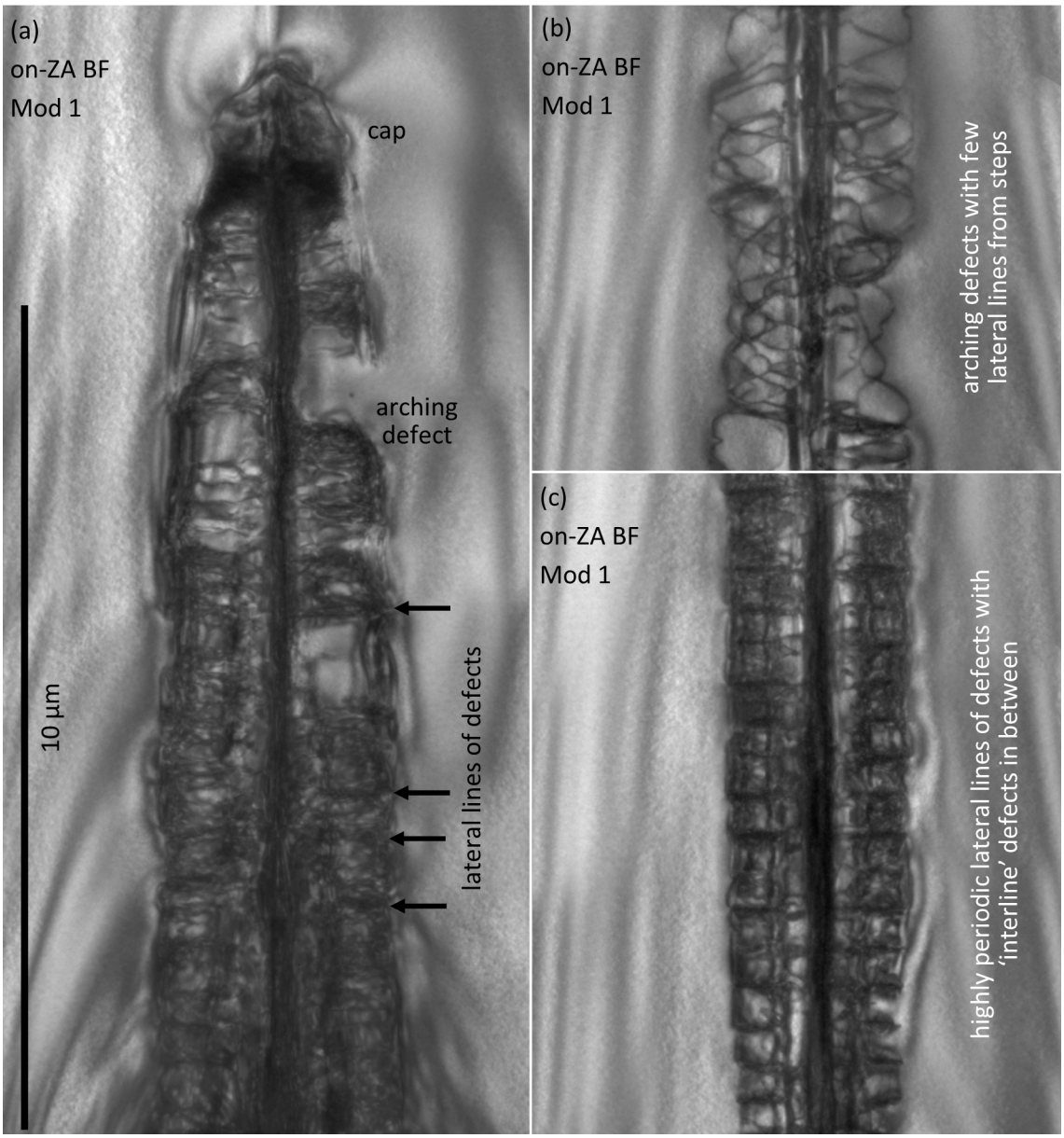

Figure 5.6: A TEM image of the decreasing diameter region, (a), reveals arching defects, similar to but more dense than the arching defects in the increasing diameter region far from focus, (b). Aperiodic lateral lines of defects are also visible in (a) which resemble the periodic lateral lines of defects midway along the increasing diameter region, (c). All are at the same scale.

vertical thermal gradient also raises the possibility of epitaxy along orientations with a vertical component. The results demonstrate that inwards and downwards solidification results in some unique features within the cap. Elevated density is also of relevance to the cap, although this matter will be considered only in the next chapter.

5.6.1 The Cap - results

The following discussion of the cap will require results from both long axis cross-sections and short axis cross-sections.

Figure 5.7 consists of results from all three long axis cross-sections used in this work, including both images and diffraction patterns. In all three modifications the periphery of structural features is faceted and at the very top of the modifications these facets are inclined to the vertical. Clearly this is suggestive of inclined epitaxy. Furthermore, there are inclined lines of defects, most visible and labelled in Fig. 5.7 (a). These are assumed to be the result of the downwardly propagating epitaxy intersecting with the radially propagating epitaxy below. Figure 5.7 (a) also features a band of dark contrast. This is present, but less visible in the other long axis cross-sections.

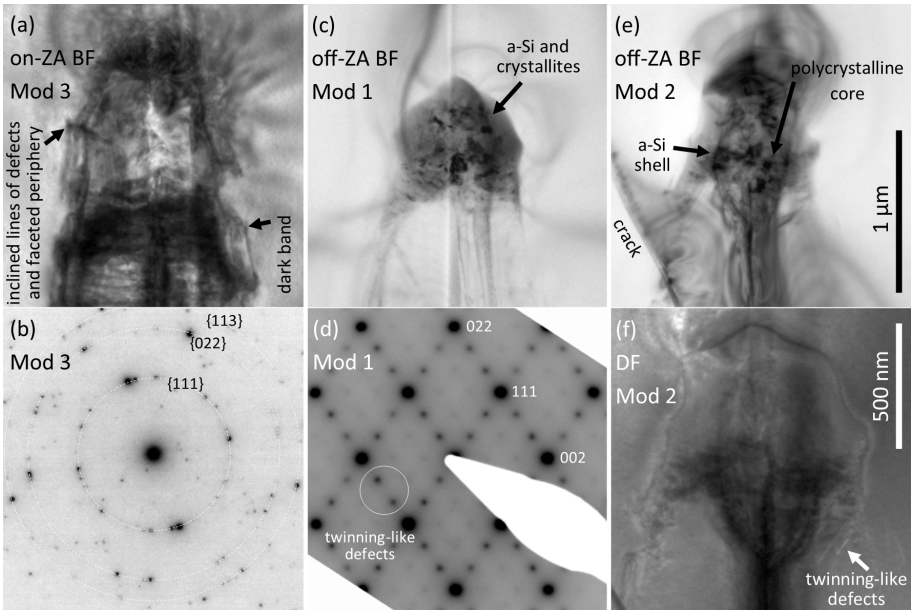

Figure 5.7: TEM results from long axis cross-sections of the cap region of three different modifications. The image, (a), and SADP, (b), from one cap reveals inclined facets on the periphery, with inclined lines of defects and polycrystallinity within the cap. A second cap viewed off-ZA, (c), shows polycrystallites and reveals that a-Si is also present. A SADP from the same region, (d), reveals additional spots which are characteristic of twinning-like defects. The third cap reveals a core-shell structure, with a polycrystalline core and a-Si shell, (e). A DF image from twinning-like spots, (f), shows that twinning-like defects are present in many areas, but most obviously on the bottom right of the image. (a,c,e) are the same scale. Annotations corrected.

A diffraction pattern from the cap in Fig. 5.7 (a) is shown in Fig. 5.7 (b). This consists of a multitude of diffraction spots indicating that the cap is polycrystalline. Furthermore, many of these spots are not at appropriate spacings for dc-Si, which is the result of the presence of both defects and other Si allotropes. When the cap is viewed off-ZA, as in Fig. 5.8 (c), the crystallites become visible in the images. The contrast is also consistent with the presence of

a-Si. In fact, the cap is an a-Si shell and polycrystalline core structure. The core is more distinct in Fig. 5.7 (e).

Many regions of the cap are rich with twinning-like defects. This is evident from the SADP in Fig. 5.7 (d), recorded from the cap in (c), and from the DF image, (f), of the cap shown in the BF image in (e). The SADP in Fig. 5.7 (d) contains additional spots at one third increments of the normal dc-Si spots, which is characteristic of twinning-like defects. Using these spots to create a DF image, as in (f), results in brighter regions corresponding to the location of the twinning-like defects. The most obvious of these in the image are labelled on the bottom right. However, they are also present through a large portion of the cap, including within the polycrystalline core.

On the short axis, results from cross-sections of the caps of two modifications are presented in Fig. 5.8. The first modification is shown on-ZA, (a) and off-ZA, (b), while a SADP is shown in (c). The second modification is shown both on the usual [001] ZA, (d) and on the $[\bar{1}\bar{1}4]$ ZA (e). The SADP, (f), is also of the $[\bar{1}\bar{1}4]$ ZA. All the images, but particularly Fig. 5.8 (a), show evidence of strong bend contrast which is suggestive of compressive strain around the cap. The morphology consists of short lines of defects, a region of defective Si surrounding an a-Si shell which in turn surrounds a polycrystalline core. The lines of defects are again the result of colliding solidification interfaces. The short length is noteworthy as it implies that a transition to amorphisation occurred much earlier than in the comparably sized core-shell structures shown in the previous chapter. The defects decorating the periphery of the a-Si are suggestive of a regime of defective epitaxy, which again differs from otherwise comparable cross-sections in the previous chapter. For example in the increasing diameter region defects around the a-Si were either absent, or minimal.

The a-Si shell is more evident when viewed off-ZA, as in Fig. 5.8 (b). The shell is clearly relatively thin. Indeed, the shell appears to be incomplete with defective crystallites extending from the periphery of the bulk into the polycrystalline core. The core itself appears streaky, with the streaks roughly oriented along the solidification direction, based on the facetted periphery of the a-Si. In part, the streaks are the result of elongated crystallites. The diffraction pattern for the core of the first cross-section, Fig. 5.8 (c), clearly inidicates polycrystalline Si, but these crystallites seem to have some bias towards the bulk orientation. A second potential cause of the streaky contrast in the core is the presence of defects, including twining-like defects. All the images contain evidence of this, but it is most obvious when viewed off the [001] ZA, Fig. 5.8 (e). This image contains bands which are believed to be due to twinning-like defects and are labelled as such. Corresponding streaks are visible on the SADP, Fig. 5.8 (f), which is recorded on the $[\bar{1}\bar{1}4]$ ZA of the bulk, but within the polycrystalline core.

5.6.2 The cap - discussion

The long axis cross-sections of the cap contain inclined facets on the periphery and inclined lines of defects. These features indicate that epitaxy with a vertical component is occurring near the cap, as would be expected given the presence of vertical thermal gradients. This is interesting as it potentially opens up epitaxy along ⟨111⟩ orientations. This has already been noted to be prone to defective epitaxy and the formation of twinning-like defects, both of which were quite evident in the cap. However, even without ⟨111⟩ epitaxy, the intersection of an inclined solidification interface with neighbouring facets is inherently more chaotic and therefore more likely to cause defects to form.

The vertical thermal gradients have also clearly allowed for sufficiently rapid cooling such that amorphisation occurs. However, a transition back to crystal growth occurs soon after when

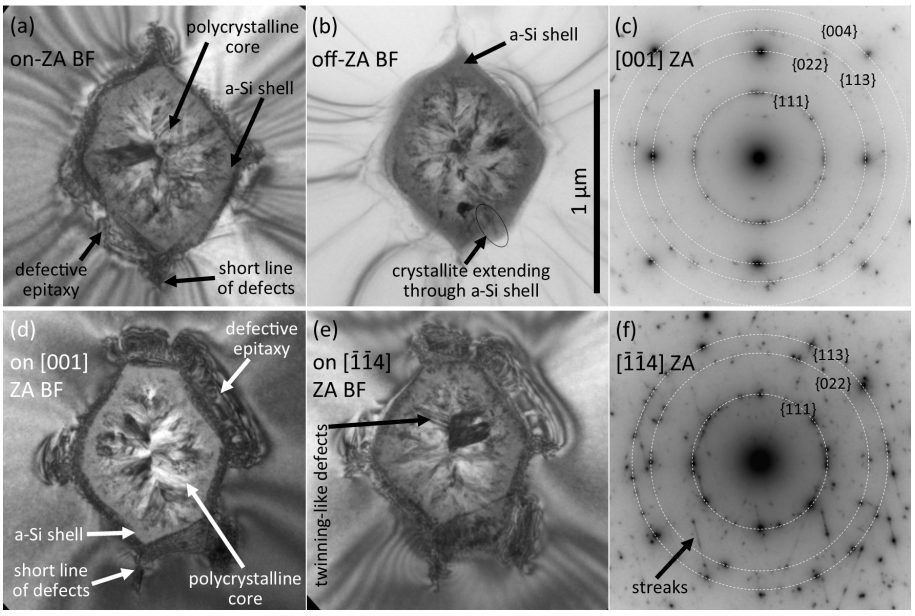

Figure 5.8: TEM results from short axis cross-sections of the cap region of two different modifications. The first modification, (a-c), is show on-ZA in (a) and off-ZA in (b) and includes a SADP, (c). These results reveal: short lines of defects, regions of defective epitaxy, a facetted thin a-Si shell and polycrystalline core. The a-Si shell appears to be sometimes punctuated by crystallites. The second modification, (d-f), is shown on the [001] ZA in (d) and on the [1̄1̄4] ZA in (e), which better reveals the presence of defects within the core, such as the labelled twinning-like defects region. A SADP, (f), recorded under the same tilt conditions as (e) reveals streaks on the diffraction pattern. All images are at the same scale. Annotations corrected.

the remaining melt volume is still relatively large. Presumably, crystallites form on the inner periphery of the a-Si, then grow inwards. This potentially explains the elongated appearance of the crystallites in the core. However, there is a second potential contribution to the presence of crystalline defects and crystallites extending through the a-Si shell. It is likely that in some cases small portions of defective crystal may extend through the amorphous shell. These crystallites then provide a defective seed from which crystallites may nucleate and grow, thus closely matching the orientation of the bulk. This implies that many crystallites will remain well aligned for efficient inwards growth. Of course, the defective seed crystals provide ample opportunity for crystallites to form on other orientations, and for defective growth to propagate throughout the polycrystalline core.

Thus far, the presence of Si polymorphs and the dark band on the long axis cross-sections have not been discussed. Both are thought to be density-related and as such will be discussed in the next chapter.

5.7 Summary

In this chapter the morphology visible on long axis cross-sections was largely explained on the basis of radial inwardly-propagating epitaxy. The energetically-favoured facet orientation is therefore vertical, but the initial melt shape and isotherm curves are inclined to the vertical in most regions of the modification. As such, the isotherm is approximated with a series of energetically aligned facets, separated by steps. The amplitude and curvature of these steps varies over the modification's length depending upon the local conditions.

In the increasing diameter region, the diameter of the melt increases, while the strength of the radial thermal gradients decrease further from focus. Nearest focus, where thermal gradients are strongest, the steps between facets on the solidification interface are highly curved which allows for defect-free solidification. The degree of undercooling along the solidification interface oscillates as a result of vertical variations in the melt front separation from the T_{ma} isotherm, leading to a periodic oscillation in the width of the a-Si at the centre of the modification. As distance from focus increases, the thermal gradients decrease, first causing defects to form when steps between long axis facets occur. Subsequently, defects form continuously during the inward solidification, but defect density increases further when steps occur. Nearing the top of the increasing diameter region, the step amplitude decreases, again allowing for curvature of the solidification interface between facets and generally a decrease in defect density where the steps occur. However, 'interline' defects still form from the colliding facets during the radial solidification process.

In the constant diameter region, the crystal-melt interface is vertical leading to few steps between facets. However, solidification in the constant diameter region lags behind the rest of the modification. Combined with redistribution of mass (due to the presence of voids), the constant diameter region contains a local excess of material that is accommodated by compressive strain. The compressive strain causes a dramatic decrease in epitaxy quality, leaving behind a highly defective region.

The decreasing diameter region accommodates a more modest excess in material, causing a modest decrease in crystal quality. It also features steps between facets which cause local increases in defect density. However, the position of these steps is more random when compared with the increasing diameter region.

The cap, at the top of the modification, is a special case where the vertical thermal gradients are comparable to the radial thermal gradients. This allows for rapid cooling, more comparable to the focus end of the increasing diameter region. It also allows for epitaxy with a vertical component. The solidification process is initially very defective, it subsequently briefly transitions to an amorphisation regime, before returning to a crystal growth regime. Portions of defective crystal appear to permeate the a-Si shell and provide a flawed seed for crystal nucleation growth in the core. The end result is a highly defective a-Si shell and polycrystalline core structure. The cap also accommodates an excess of material, but this will be considered in depth in the following chapter.

All of the features are prone to perturbations, which were demonstrated in the increasing diameter region. Interruptions in material density (e.g. a void), sudden changes in thermal conditions or solidification conditions can all cause strong, local deviations from the solidification behaviour expected at any given position along the length of the modification.

Chapter 6

The role of density

The morphology of the laser-induced modifications is dependent not only on the solidification process, but also upon changes in density and the associated movement of material brought upon by phase transformations within the Si. These density changes originate from the fact that the sub-surface Si melts and that the density of molten Si is around 10% greater than dc-Si. The conservation of mass dictates that there will be regions where the density is both greater and less than that of dc-Si. Relative to dc-Si, the modifications have already been noted to contain regions of low density (voids) and regions of high density (high density Si allotropes and compressed dc-Si). Additionally, a-Si has been observed, which can have either an elevated or depressed density compared with dc-Si.

In this chapter, the role of density on the modification morphology will be considered. It will begin with a short review of the literature concerning relevant Si allotropes of differing density to dc-Si. The experimental approach to examining density-related features in the modifications will then be presented. A macroscopic picture of density changes within the modification will follow. The experimental results and discussion will begin by considering the origin of the voids and their evolution during the solidification process. Next, the density of the a-Si will be considered, along with the high density Si allotropes. Finally, the role of density within the cap region will be investigated.

6.1 Literature concerning Si allotropes

In this section some of the literature concerning Si allotropes of relevance to the current work will be presented. In particular, the density and formation of resolidified dc-Si, molten Si, several high-density Si allotropes (β-Sn-Si, r8-Si and bc8-Si) and a-Si will be considered. However, much of the literature concerning the density of Si is the product of experiments under near equilibrium experiments, that is from near static loading. Specifically, the literature is the product of experiments where pressure is applied in a diamond anvil cell, or during nanoindentation. The conditions in those experiments differ greatly to the high temperature, highly nonequilibrium subsurface laser-induced melting of the current work. As such, caution is required when considering the equivalence of both the transformation pathways and the properties of materials following laser melting and those associated with near static pressure conditions.

From a thermal perspective, the starting state of the sample is dc-Si, with a density of 2.33 $g \cdot cm^{-3}$.[114] Heating causes thermal expansion[115] until melting is induced at 1687 K.[114] Melting is known to cause Si to shrink by about 10% compared with room temperature dc-Si to 2.57 $g \cdot cm^{-3}$.[112,113]

From a density perspective, diamond anvil cell and nanoindentation experiments show that the application of pressure to bulk dc-Si at room temperature can cause approximately 9%

of compression to the dc-Si phase before a phase transformation to the metallic β-Sn-Si occurs.[116,117] This transition occurs at about 11 GPa and results in a $20-22\%$ increase in density (from 2.55 $g \cdot cm^{-3}$ to 3.27 $g \cdot cm^{-3}$).[116–118] Relative to dc-Si at ambient, the density of β-Sn-Si is about 30% higher. Further application of pressure results in a series of reversible metal to metal phase transitions that are not of relevance to this work.[119–122]

The dc-Si to β-Sn-Si phase transformation is not generally thought to be reversible upon unloading. Rapid unloading of pressure results in pressure-induced a-Si, while slow unloading results in the formation of r8-Si, with a density of 2.8 $g \cdot cm^{-3}$, from about 9 GPa.[123,124] The density of the r8-Si continues to decrease upon further unloading until approximately 2 GPa where a transition to bc8-Si begins.[123] This is associated with a small ($\sim$ 2%) decrease in density to 2.6 $g \cdot cm^{-3}$.[123] In the case of nanoindentation, some r8-Si is typically preserved after complete unloading due to remanent stress in the material.[84,124] Importantly, however, r8-Si is rarely reported in TEM experiments, presumably cross-sectioning of the sample reduces the remanent stress and allows the r8-Si to transform to bc8-Si. Conversely, r8-Si is more visible to Raman spectroscopy as it has a larger indirect bandgap, (0.24 eV)[125] when compared with bc8-Si (0.03 eV)[126].

As for a-Si, being a disordered network the properties of a-Si are variable and dependent on the pathway by which it is created. Three pathways have already been mentioned in this work, ion implantation (self implantation can be used to create highly pure a-Si), pressure-induced a-Si and rapid solidification-induced a-Si. All of these forms should be highly pure, but may differ in their density and bond angle distortion (which in turn is related to coordination defects within the continuous random network).[82]

Studies of the pressure-induced behaviour of a-Si usually focus on self-ion implantation-induced a-Si due to its purity and consistent properties. It has been measured to have a slightly lower density than dc-Si[127], by 1.8%.[128] As implanted the material can be described as unrelaxed (large bond angle distortion or, equivalently, number of coordination defects). Suitable thermal annealing results in structural relaxation (a reduction in bond angle distortion).[82,129] The application of pressure to relaxed a-Si also results in a transformation to β-Sn-Si.[130–132] However, the pressure and conditions at which the transition occurs presumably differ between dc-Si and relaxed a-Si.

Pressure-induced a-Si, as was just mentioned, forms from β-Sn-Si after the rapid unloading of pressure, or decompression of Si at low temperatures.[133–135] It has been shown to have a similar or higher density than dc-Si.[128] It should be noted that some simulations of a-Si also suggest a higher density than dc-Si.[108,136] Interestingly, the reapplication of pressure to pressure-induced a-Si has been shown to result in a direct transformation to r8-Si at pressures below that required for β-Sn-Si to form, a point of relevance to this work.[137]

The a-Si formed during rapid solidification is less studied compared with either ion implantation-induced a-Si or pressure-induced a-Si. However, it is known that the degree of relaxation of a-Si that forms in PLM experiments depends upon the laser pulse length. Long pulse lengths (10s of nanoseconds) result in fully relaxed a-Si, while short pulse lengths (10s of picoseconds) result in unrelaxed a-Si.[54,109]

At this stage it should be emphasised that a-Si is a complicated material with highly variable properties. Further details are available in the literature.[138–141]

6.2 Experimental

This chapter mostly makes use of the standard, sub-bandgap regime modifications produced with the 1549 nm, 3.5 ns, 2 μJ laser pulses. Most of the modifications were produced in isolation,

with a sufficient gap so that adjacent modifications did not interact.

The samples were prepared for TEM by cross-sectioning using FIB milling of either H-bar samples or ex-situ liftout samples.* EELS samples were further thinned by Ar ion milling to limit the depth of the ion beam damage.

Both conventional TEM and STEM were used to characterise cross-sections. STEM is used to collect BF images, HAADF images and perform EELS, considered further below. Additionally, SEM is used to examine voids on the cleaved surface of modifications produced in close proximity (2 μm spacing).

6.2.1 EELS

EELS is used to measure the energy lost by electrons in the direct beam due the interactions with the sample. In this work the density of a-Si is determined from the measured energy loss of incident electrons as they interact with plasmons in the sample as was detailed in Chapter 1.

The measurements were conducted using an aberration corrected, cold FEG, Jeol ARM200F STEM operating at 200 keV with a Gatan EELS system. The samples used were multiple short axis cross-sections of the increasing diameter region (region closer to focus) which had an a-Si core, or an a-Si shell and crystalline core. The samples were deliberately left thicker than is ideal for EELS as it is conceivable that the lack of confinement on any high-density a-Si might allow it to expand. Repeat measurements with further thinned samples was planned, but never conducted due to a lack of time, instrument access and because high density a-Si was not found in thicker specimens.

Measurements were recorded either as spectrum images (two-dimensional maps) or line scans. In most cases multiple sets of measurements were recorded on each sample for each of the three regions of interest; the a-Si core, the dc-Si just before the onset of amorphisation and dc-Si beyond the melt periphery which is assumed to be negligibly strained.

As the samples were thick, the resultant spectra are the result of plural scattering and therefore feature multiple plasmon peaks. A Fourier-log deconvolution was used to remove the additional peaks. However, the results within the unmelted dc-Si consistently and unrealistically exceeded that of the known density of dc-Si from the literature. This suggests a systematic error remains after the Fourier-log deconvolution. As such, the results below are expressed relative to the unmelted dc-Si so as to mitigate this error.

6.3 A macroscopic picture of density

Before laser irradiation the sample is in a dc-Si state. The laser irradiation process results in Si melting, which is accompanied by an increase in density. However, because the melt volume is confined subsurface, the overall modification volume must be conserved. As such, the increased melt density must be accompanied by a low density region, specifically a void. In fact, as shown below, multiple voids are routinely observed along the length of each modification.

After melting, cooling drives rapid solidification which previous chapters have shown to be fastest near focus. Much of this solidification is to a dc-Si state and is therefore accompanied by expansion of the Si back to its original density. As will be shown below, this causes the voids to change shape and shrink. Nevertheless, portions of the voids remain after solidification, dictating that the displaced material must be accommodated in a high density region elsewhere

*It should be noted that redeposition of material sputtered during FIB milling can occur within the voids examined in this chapter. However, the amount of redeposited material is generally so minimal that it cannot be observed under the exposure conditions used in this work.

in the modification. As has previously been stated, much of the displaced material is expected to be concentrated in the last regions to solidify, particularly the constant diameter region. Indeed, the constant diameter region, decreasing diameter region and the cap all have evidence of compressive strain which is associated with accommodating excess material. Specifically, the excess material was suggested in the previous chapter to cause compressive strain and therefore, an increase in defect density during the epitaxial solidification process. The accommodation of excess material by compressive strain will not be expanded upon further in this chapter.

An additional mechanism by which to accommodate a local excess of material is through high density Si allotropes. Indeed, the presence of higher density r8-Si and bc8-Si has already been noted in Raman spectroscopy results in Chapter 3. There is also a possibility of high density a-Si which will be discussed below.

6.4 Voids

In this section the nature of voids in the laser-induced modifications will be considered. First the void formation process will be considered with reference to their position on a cleaved surface examined by SEM. Next, the evolution of the voids during solidification, as well as their final form, will be considered by examining the morphology of the remanent voids as examined by TEM. Typically, the remanent voids appear to be distinctly different depending upon their location on the long axis cross-section. As such, voids near-focus will be considered separately to those far-from-focus. Finally, smaller features that appear to be fully refilled voids will be considered.

6.4.1 Void formation

As was recently stated, the formation of voids is driven by the densification of Si as it melts. The driving force for void formation must therefore increase as the amount of molten Si increases over the duration of the laser pulse. However, this does entail the formation of a new melt-vacuum interface, which presents an energetic barrier to void formation. This firstly implies that there may be a delay before sufficient melt exists to 'nucleate' the void. It secondly implies that minimisation of the interfacial free energy will favour the growth of a singular void. However, the expansion of a singular void may be kinetically limited if the growth of the molten region is fast in comparison with the movement of material within the melt. In such cases multiple voids would instead be expected to form.

To investigate the influence of these energetic and kinetic factors, the position, shape and frequency of voids will be examined. There are insufficient TEM results to stochastically investigate these factors, except to say that each long axis cross-section does contain multiple voids. Instead, SEM results of a cleaved sample will be used to estimate the number and distribution of voids. For a cleaved sample, the modifications are closely spaced, unlike most results so far in this work. As will be shown in the following chapter, the closely spaced modifications do differ from isolated modifications. However, there is no basis for them to differ appreciably from a void formation perspective. As such, for the purposes of this investigation the cleaved results are considered to be equivalent to isolated modifications. A second caveat is that this approach requires that the voids be visible on the cleaved surface. It is possible that some voids are too small to discern from the other topographic features of a cleaved surface. It is also possible that in some cases the voids exist subsurface. It should therefore be assumed that some voids will be missed. However, the visible voids can be identified on both sides of the cleaved interface, it can therefore be concluded that voids will not be erroneously identified from inconsistencies in

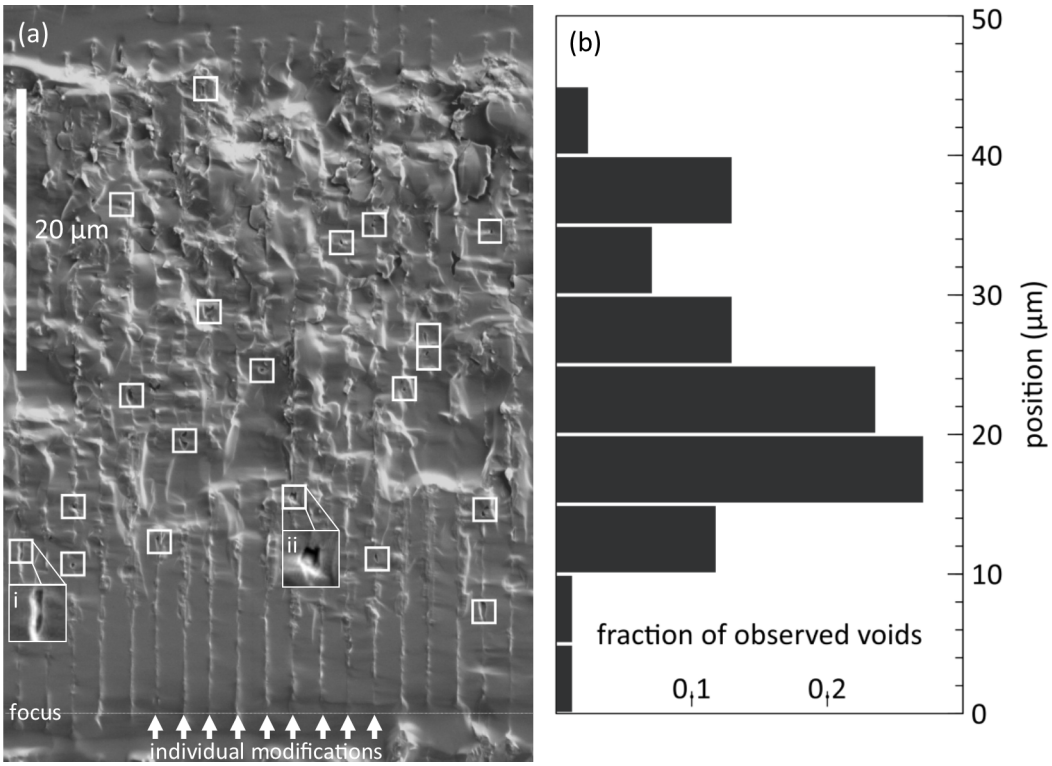

Figure 6.1: Remanent voids (outlined in squares) can be identified during SEM examination of closely spaced modifications exposed on a cleaved surface, (a). Modifications routinely contain multiple visible voids, although the smallest voids may not be discernable or may reside subsurface. The void distribution is visible skewed in the histogram, (b), but voids are rare immediately above focus.

cleaving path.

An example of a cleaved surface is shown in Fig. 6.1 (a). The image contains 19 modifications which run vertically with the focus end of the modifications near the bottom of the image (where the cleavage path is less chaotic). Outlined in squares are each of the voids visible on the cleaved surface. Two examples (i) and (ii) are shown at larger scale. Void (i) is very highly elongated despite clearly having a width below the melt diameter. The width of void (ii) could plausibly match the melt diameter and the void's length is comparable with the width. The image also reveals that many modifications have multiple voids, with three voids visible in one modification on the right side of the image.

Measuring the visible void position on over 100 modifications results in the histogram, shown to scale, in Fig. 6.1 (b). This shows that void distribution is skewed, with more voids in the bottom half, although voids are rare within the first 10 μm from focus. The average void position is just below the midpoint, 23.1 ± 0.9 μm from focus.

From these results several insights can be made into the void formation process. The rarity of voids near focus is suggestive that energetic barriers do delay void formation until a sufficiently large melt volume is created. Between 10 and 25 μm from focus voids are particularly common, which can be interpreted as being the result of voids forming once the melt volume is larger. In the top half of the modification, voids are less concentrated. Given that multiple voids per modification are common, voids in the top half of a modification are presumably generally not the first form. As such, the position and size of far-from-focus voids will be highly dependent on the position, growth and coalescence of the nearer-to-focus voids. Nevertheless, it is clear that kinetic limitations do prevent the growth or coalesce to a single void over the entire length of

the modification. As for the observed void shape, the elongation of the void in Fig. 6.1 (a)(i) does show that minimisation of interfacial free energy isn't always a defining parameter of the remanent void shape. This matter was investigated further by TEM examination.

6.4.2 Remanent voids near focus

In this subsection the voids nearer to focus will be considered. The results that follow are all from long axis cross-sections as no equivalent voids were observed within short axis cross-sections.

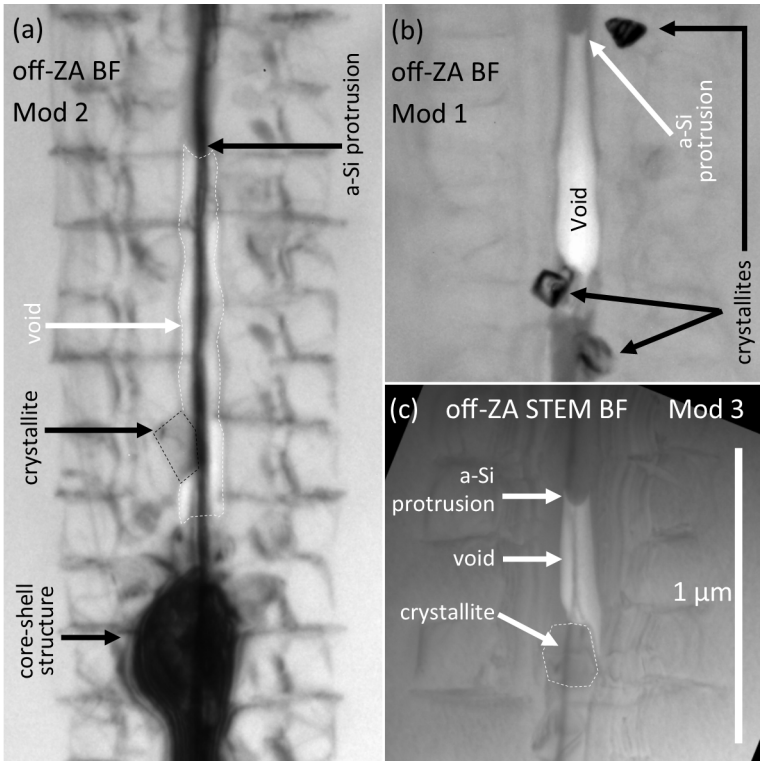

Figure 6.2: TEM images, (a-c), of the remanent voids closer to focus in each of the three modifications cross-sectioned along their long axis. In each case the remanent void diameter matches the diameter of the a-Si immediately above, and often below, the void. Characteristic protrusions are visible at the top of the voids, and crystallites exist at the base of the voids. All images are at the same scale.

In Fig. 6.2 the nearer to focus remanent void for each of the long axis cross-sections is shown, all at the same scale. The remanent void from modification 2, (a), is highly elongated with a similar diameter to the a-Si core above it at the top of the image. The a-Si protrudes characteristically into the void, a feature observed in all the near focus voids. Below the void is a short region with a crystalline core, below which is a larger a-Si shell and crystalline core structure. The crystal in the solidified region around the periphery of the void is entirely conventional with the exception of the labelled crystallite.

The near-focus remanent void from modification 1, (b), is also elongated and of a similar diameter to the a-Si core that exists in the regions above and below it. The side walls of the void appear to have a very thin layer of a-Si. The modification also contains an a-Si protrusion, crystallites and conventional defects in the crystalline region around its radial periphery.

Finally, the near-focus remanent void from modification 3, (c), is the smallest of the three. It is otherwise very similar, with an elongated shape that is of a similar diameter to the core structures above and below it, conventional defects around its radial periphery, an a-Si protrusion

at its top and a crystallite at its base.

The results will be explained by first addressing the elongation of the voids. This elongation is unlikely to reflect melt shape (since interfacial free energy would favour a spherical shape) and hence the elongation shape most probably results during the solidification process. Three processes are thought to potentially contribute: the expansion of Si that occurs when the high density melt solidifies, capillary action on the melt-void interface, and the Gibbs-Marangoni effect (in particular, thermocapillary convection which is explained below).[142–145] Two scenarios will be considered, one with the Gibbs-Marangoni effect, one without. In Fig. 6.3 these two scenarios are illustrated. In both cases the void begins as a sphere (or capsule) as shown in (a). Radial inwards solidification is accompanied by expansion of the Si, effectively refilling the sides of the void and thus, changing the void's aspect ratio. Additionally, as the width of the melt decreases, the solidification interface remains wetted presumably due to capillary action. Consequentially, the void elongates. Both the expansion and wetting driven by capillary action are illustrated at an early stage of solidification in (b). At this stage the two scenarios begin to differ. In (c), only capillary action is considered, while in (d) both capillary action and the Gibbs-Marangoni effect is considered.

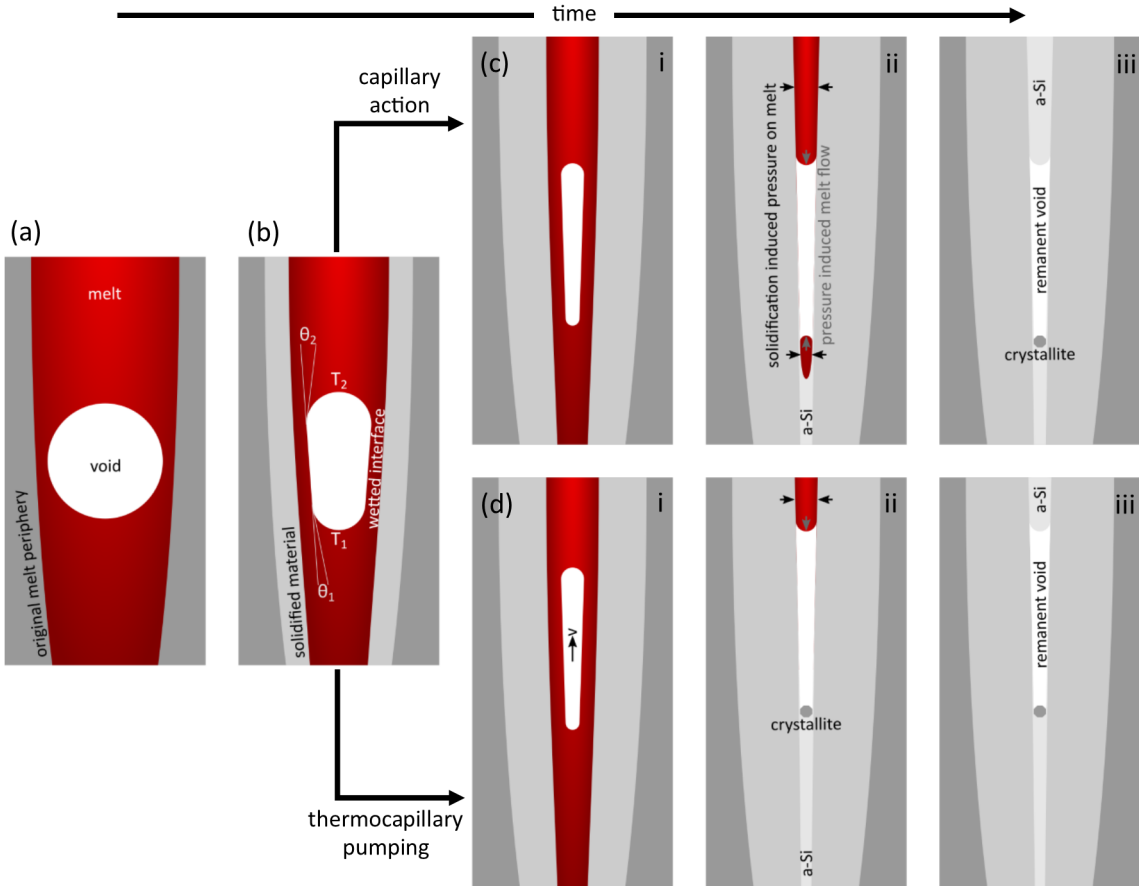

Figure 6.3: A schematic showing the evolution of a void (a) during solidification (b), showing the influence of changes in density and capillary action (c) and additionally the Gibbs-Maragoni effect (d).

In the first scenario, (c), as solidification progresses capillary action will cause further elongation of the void, (c)(i). This thinning and elongation process cannot continue indefinitely and at some point, the side walls of the void must solidify. It is assumed that this slowing or stopping of elongation is dependent on the surface tension. Perhaps, for example, given that the

remanent void diameter matches that of the a-Si above it (and often below it), the surface tension changes dramatically once amorphisation on the periphery of the void begins. This stage of solidification is shown in (c)(ii). However, at this stage the top and bottom of the void remains molten. The continuation of the inwards solidification and accompanying expansion of the Si will apply pressure on the remaining melt along the centre line of the modification. As these molten regions are adjacent to the void, this pressure is can be relieved by the melt flowing into the void. This process is also shown in (c)(ii). Note that the refilling component of this process has already been suggested in the literature.[49] At the top of the void strong thermal gradients are expected to remain throughout the melt, particularly given that subsequent solidification results in a-Si, and so it is likely already in an amorphous solidification regime, and so the refill also amorphises. In contrast, the thermal gradients at the bottom of the voids appear to be slightly weaker, allowing for a return to a crystal growth regime . It is thought that, typically, since no crystalline material is adjacent to the refill at the bottom of the void, a completely new crystallite nucleates. The final state of the remanent void after the refill has solidified is illustrated in (c)(iii).

The second scenario, (d), involves both capillary action and the Gibbs-Marangoni effect. The Gibbs-Marangoni effect is the transport of material driven by variation in the surface tension around a fluid.[145] In this work the surface tension around the void is believed to vary primarily, but not exclusively, due to thermal differences between the top and bottom of the void. This special case is called thermocapillary pumping.[142–144] Although not entirely accurate for the geometry in the current work, thermocapillary pumping can be described in a constant diameter channel. The capillary pressure, P_c, is defined by a form of the Young-Laplace equation[142,143]:

$$P_c = P_v - P_m = \frac{G\sigma\cos(\theta)}{d} \tag{6.1}$$

where P_v is the interface pressure on the void side, P_m is the interface pressure on the melt side, G is a geometry-dependent constant, σ is the surface tension, θ is the contact angle between melt and the void and d is channel diameter. As surface tension has a temperature-dependence[146], a temperature difference at either end of the void will induce a pressure difference across the void, ΔP_c, and therefore a net force, F_c on the void[144]:

$$F_c = \Delta P_c A = (P_{c2} - P_{c1})A = GA\left[\left(\frac{\sigma\cos(\theta)}{d}\right)_2 - \left(\frac{\sigma\cos(\theta)}{d}\right)_1\right] \tag{6.2}$$

where P_{c2} is the capillary pressure on the top of the void, P_{c1} is the pressure at the bottom of the void and A is the interfacial area. This force will induce vertical motion of the void. Since, Equation 6.2 is for a constant diameter channel it is not entirely accurate for this work. The interfacial area, channel diameter and contact angle are expected to differ on either end of the void because of the void geometry. Nevertheless, the thermocapillary pumping process can be qualitatively understood to drive movement of the void up the length of the modification.

Applying thermocapillary pumping to Fig. 6.3, based on the parameters shown in (b) results in the process illustrated in (d). Initially, the void not only shrinks and elongates, but also rises up the modification's length into a region with a wider melt diameter, (d)(i). If the void's velocity is slow, relative to the solidification interface velocity, then solidification around the void probably occurs in a very similar manner to the capillary action scenario in (c). However, if the void velocity is fast enough then some other mechanism would be required to trap the void, after which solidification would again occur in a similar manner to (c). The trapping mechanism is not known, but the common presence of a crystallite at the base on the void is suggestive of the crystallite being relevant to the trapping mechanism.

One interesting aspect of the thermocapillary pumping scenario is that it provides an additional explanation as to why voids are rare within the first 10 μm from focus. Any voids that do form in this region may rise out of the region during solidification. Nevertheless, while thermocapillary pumping of the near-focus voids seems highly plausible within these modifications, the features observed in Fig. 6.2 can be qualitatively explained without it.

6.4.3 Remanent voids further from focus

The remanent voids far-from-focus appear, superficially, quite different to those near-focus. In this section the remanent void morphology will be explained, making reference to both results recorded from long axis cross-sections and short axis cross-sections. In part, the differences in morphology will be related to the differences in the initial conditions between the far-from-focus and near-focus voids.

Two far-from-focus voids are shown in Fig. 6.4, one from a long axis cross-sections (a-b) and one from a short axis cross-section (c-d). From the perspective of the long axis (a-b), the remanent void is observed within an unusual structure primarily consisting of a-Si, but also containing polycrystallites and crystalline defects, including twinning-like defects, on the top and bottom. Radially beyond this structure are features consistent with conventional solidification, namely crystalline defects, which are most visible in (a). On the short axis cross-section conventional solidification defects are again visible on the periphery (c). The unusual structure at the centre contains the remanent void, a-Si and defective dc-Si. Notably, the periphery of this unusual structure is roughly oval shaped, and distinct from any features shown to date in this work. Close examination of the periphery of the unusual structure, viewed out of focus and off-ZA in (d), reveals small regions of Fresnel fringing which are indicated with arrows. This is suggestive of small open volumes between the unusual structure at the centre, and the conventional crystalline periphery.

It is suggested that this unusual structure closely corresponds to the shape of the void when the sample was molten. Its shape is essentially a capsule, as might be expected from the minimisation of interfacial free energy. Interestingly, surface tension driven wetting of the unmelted side walls appears to define the capsule shape.

During solidification, the initial conditions around the far-from-focus voids differ to the near-focus voids in that the melt diameter is wider, the thermal gradients are more modest, and the solidification interface is closer to vertical (from the perspective of the long axis). All these factors are expected to reduce the influence of capillary-related phenomena. As such, movement and elongation of the voids by capillary action and thermocapillary pumping are not strongly defining processes of the far-from-focus voids. Instead, refilling of the voids due to the flow of melt from above and below, driven by pressure applied by the expansion of Si during solidification, is the defining process that gives rise to the final morphology.

In detail, since a void can carry no heat energy that needs to be dispersed, the material surrounding it radially is expected to solidify relatively quickly. In contrast, the regions above and below do have to transfer heat from the molten core, and solidify more slowly as a consequence. The expansion arising from solidification again applies pressure to the melt along the centreline of the modification, forcing melt into the void. Qualitatively this refill process differs little from the near-focus voids. However, both the volumes and thermal conditions involved are different. Indeed, the upward and downward components of refill clearly meet, leaving only a small remanent void compared with the original void volume.

The refill material must subsequently solidify, and can do so epitaxially if crystalline material is adjacent to the void. However, strong, potentially non-radial thermal gradients may exist

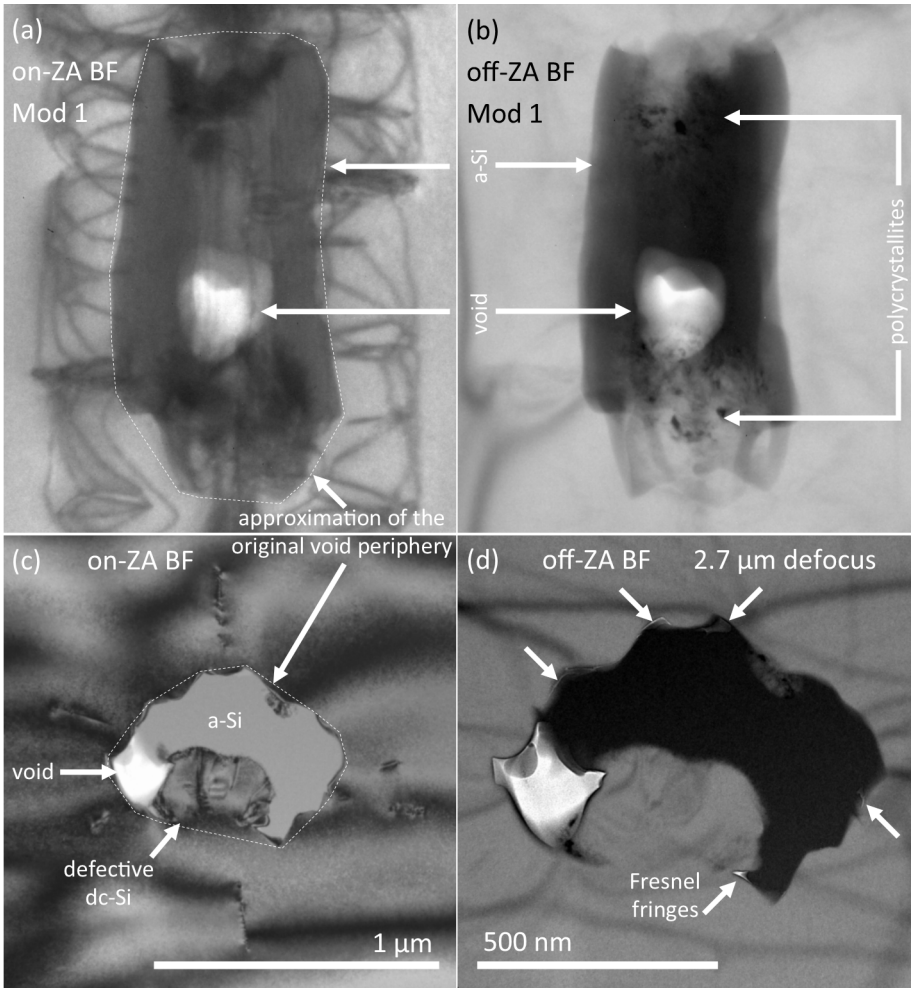

Figure 6.4: TEM images of far-from-focus voids in a long axis cross-section, (a-b), and a short axis cross-section, (c-d), at the same scale with the exception of (d). The remanent void constitutes a small part of a larger void structure consisting primarily of a-Si, but also containing Si defects and in (b) polycrystallites are also visible. Fresnel fringes visible on close examination of the short axis, tilted off ZA and defocussed, (d), indicate that open volumes exists between the principally a-Si structure and the surrounding, conventional, dc-Si.

between the refill and the void periphery. Additionally, the void periphery may not align with low index crystal facets. Unsurprisingly, this results in many defects, as were noted in Fig. 6.4, particularly at the top and bottom of the structure. More generally though, the refill material is coming in contact with the already cooled original void periphery, creating strong thermal gradients and inducing amorphisation. For this reason a-Si is prevalent throughout the refilled portion of the void. A transition region where crystallites encapsulated in a-Si is also notable in (a-b).

To reinforce the solidification process of the refill material, consider Fig. 6.4 (c-d) again. The refill material is suggested to have initially made contact with the bottom surface of the original void, resulting in a region of defective epitaxy. Thereafter, solidification accelerated and the remaining, crescent shaped region of refill, amorphised. However, the refilling process was imperfect, hence leaving both the remanent void, and the open volumes around the periphery.

6.4.4 Refilled voids

In addition to the remanent voids were a series of features that will be argued to be smaller voids that have been fully refilled.

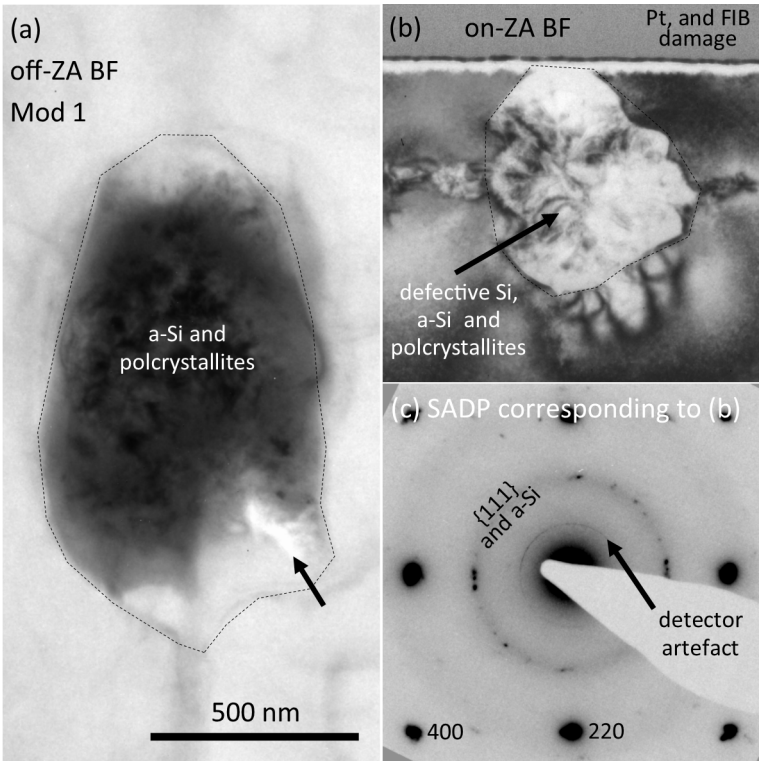

Figure 6.5: TEM results from both long, (a), and short axis, (b-c), cross-sections of refilled voids with all images presented at the same scale. Refilled voids are smaller than remanent voids, and contain less (a-Si) and more dc-Si. The dc-Si is often defective. Annotations modified.

Two different modifications are shown in Fig. 6.5. Figure 6.5 (a) is a long axis cross-section of a refilled void. Its periphery, which is marked with a dashed line, has a roughly capsule shape like some of the previous void examples, although in this case it is smaller. The crystalline material beyond the periphery of the refilled void is consistent with radial solidification. The material within the refilled void is largely a mixture of a-Si and polycrystallites. Additionally, there is a feature that appears as a bright region on the image, marked with an arrow. This

feature is likely to be an open volume region as a result of imperfect filling of the void, akin to the open volumes in Fig. 6.4 (d). From the short axis cross-sections, the closest equivalent to Fig. 6.5 (a) is shown in (b), with a corresponding SADP shown in (c). The periphery of the cross-section is, again, consistent with radial solidification. The refilled region, again marked with a dashed line, consists of defective dc-Si, a-Si and polycrystallites. The polycrystallites are more evident in the SADP.

These refilled features can be explained by comparison with the remanent voids discussed above. While the Si is molten, refilled voids differ only in that they are smaller than the remanent voids. The expansion of Si as it solidifies from the high density melt should first radially shrink the void, then refill it from above and below in a similar manner to the previous cases. Being smaller, the voids are more likely to be fully refilled.

A second implication of the smaller size is that the thermal gradients between the refill material and the periphery of the void are smaller. For this reason a-Si becomes less prevalent with smaller refilled voids. In contrast, defective dc-Si becomes more prevalent. Indeed, although not shown for brevity, refilled voids that appear to be entirely defective dc-Si are present.

6.4.5 Accounting for the melt volume of the voids

Having examined near-focus, far-from-focus and refilled voids, it is interesting to consider whether the expected volume of the voids while the modification is molten, estimated to be $5.3 \pm 0.8\ \mu m^3$ (10% of total modification volume), can be accounted for based on the volume of the remanent void-related features. Using the long axis cross-sections, and assuming features were spherical, ellipsoidal or cylindrical, depending on which shape was the closest match, the remanent features were measured. From this only $23 \pm 13\%$ of the melt volume of the voids could be accounted for.

The discrepancy between the expected melt volume of the void and the observable volume of void-related features can be explained in part by the fact that any estimate of the volume of void-related features is almost certainly a considerable underestimate. This underestimate is impossible to account for due to voids that shrink during surrounding solidification and also those where refilling and epitaxial solidification leaves no trace of the original void shape.

A second potential explanation for the discrepancy is that there are additional voids in the melt that leave no easily recognisable remanent features. For example, although larger remanent voids are surrounded mostly by a-Si, smaller refilled voids are largely defective dc-Si. It follows that voids that are smaller again (in the melt) might solidify entirely as dc-Si with minimal remanent features. It is also possible that near-focus voids could be fully refilled with a-Si, in which case they would again have minimal remanent features by which to identify them.

6.5 High density a-Si

As the a-Si in these samples forms due to the rapid solidification of a melt with a higher density than the solid dc-Si, it is sensible to consider whether the a-Si maintains an elevated density relative to dc-Si. If so, this would provide an additional mechanism by which the modification would accommodate the material displaced by the remanent voids.

To investigate this matter EELS was conducted on multiple cross-sections, all from the increasing diameter region of isolated modifications. The results of these measurements were consistent and are presented in Table 6.1, expressed relative to a measurement of dc-Si in the same cross-section, but beyond the melt radius. The unmelted dc-Si is assumed to be negligibly

Table 6.1: EELS results for the density of a-Si in the core and dc-Si just before the onset of amorphisation relative to dc-Si beyond the melt radius. Also shown are the literature values for ion-beam-induced a-Si after thermal relaxation and as-implanted pressure-induced a-Si.

Specimen	$\rho_0/\rho_{\text{dc-Si}}$
a-Si core	0.986 ± 0.013
Compressed dc-Si near a-Si core	1.006 ± 0.013
Relaxed implanted a-Si[128]	0.984 ± 0.005
As-indented pressure-induced a-Si[128]	1.000 ± 0.004

strained. Also shown are measurements of dc-Si adjacent to the a-Si as well as results for a-Si from the literature.

These results show that the density of the dc-Si near the centre of the cross-sections is likely slightly elevated, but that the a-Si is less dense than unstrained dc-Si. In fact, the a-Si measured here has a similar density to relaxed, ion implantation-induced a-Si measured in the literature. This is well below the literature result for high density a-Si measured by EELS after the indentation of pressure-induced a-Si.

The significance of this result is unclear and warrants discussion. Does this result reflect the a-Si before cross-sectioning? Does this result reflect all of the a-Si, or only that near focus? Does the match with relaxed ion implanted a-Si imply that this solidification-induced a-Si is also relaxed?

The cross-sectioning process requires thinning the sample, which would be expected to relieve any residual pressure that might preserve a high density state in the a-Si. It is for this reason that the samples were deliberately produced thicker than is ideal for EELS. Nevertheless, it is entirely possible that the density of the a-Si decreased during cross-sectioning. Furthermore, as the cross-sectioning was performed with Ga and Ar ion beam milling, which is accompanied by dynamic annealing, the sample preparation conditions have parallels with those that lead to the relaxed, ion implantation-induced a-Si in the literature. Therefore, it is unclear whether the experimental results from this work are representative of the solidification-induced a-Si in the bulk.

Whether the results from a-Si near focus are representative of a-Si elsewhere in the modification is also questionable. The potential for high density a-Si is presumably highly dependent on the confinement imparted by the surrounding material. As material displaced by the voids is preferentially displaced to the last regions to solidify, it seems that the region near focus is the least likely to have high density a-Si. As discussed below, the cap region contains a-Si which is considered more likely to be higher density a-Si.

Finally, the matter of relaxation of the a-Si was never specifically examined. The laser pulse duration used in this work is between the limits in the literature which resulted in unrelaxed a-Si (10s of picoseconds) and relaxed a-Si (10s of nanoseconds).[54,109] Thus, both possibilities are plausible.

Evidently, the properties of solidification-induced a-Si in a confined volume warrant further investigation in future work.

6.6 High density crystalline allotropes

In this section the nature of the high density crystalline allotropes (which have already been shown with Raman spectroscopy) will be investigated using TEM. These phases have been observed to form at the core of core-shell structures, where the crystallites are encapsulated by

a-Si, or as crystallites between colliding solidification interfaces. In both cases expansion during solidification of small pockets of melt is constrained by the surrounding solid, instead resulting in high density allotropes.

6.6.1 Si allotropes - results

Examples of each of the two scenarios in which high density crystalline allotropes have been observed by TEM in short axis cross-sections are shown in Fig. 6.6. The example of high density crystallites forming the core of a core-shell structure is shown in Fig. 6.6 (a-b), noting that this is the same cross-section as shown earlier in Fig. 3.5 and Fig. 4.2. The SADP, (b), recorded on the [001] ZA of the bulk dc-Si, contains spots from the dc-Si, rings from a-Si, as well as additional spots which are outlined in circles, squares and triangles, which index to two crystals of bc8-Si. Specifically, the spots outlined in squares correspond to one crystallite, those in triangles to the second crystallite, and those in circles are shared between both crystallites. Clearly, the shared spots indicate that one crystal must have grown off the other.

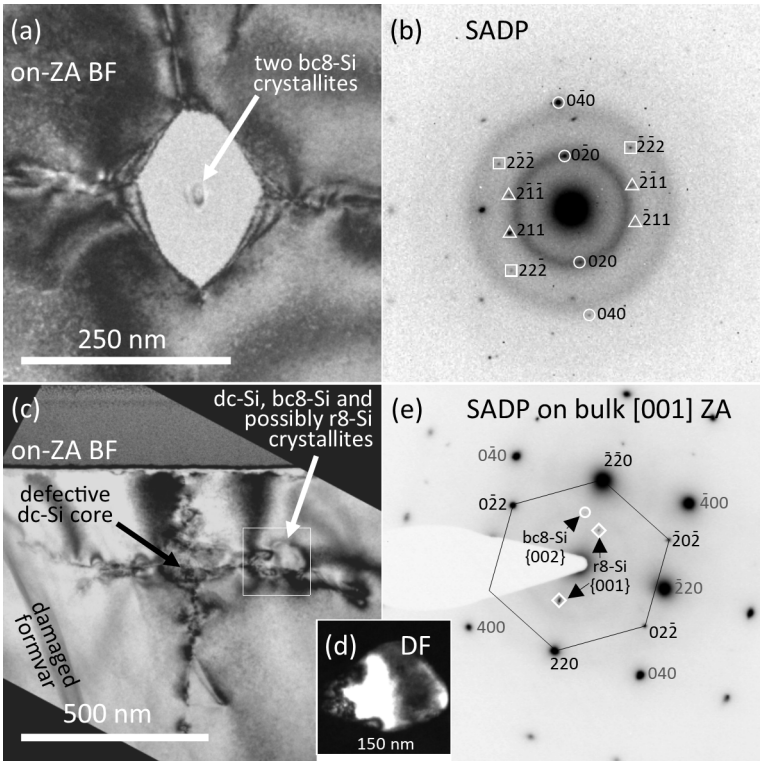

Figure 6.6: TEM results from two scenarios in which the high density crystalline allotropes have been observed in short axis cross-sections. The crystallites at the centre of the modification shown in (a) are bc8-Si as determined from the corresponding SADP, (b). The SADP is labelled with triangles for one bc8-Si crystallite, squares for the other crystallite and circles for diffraction spots shared by both crystallites. In (c) a region, outlined in a square, on one of the lines of defects consists of several crystallites. A DF image, (d), from the largest crystal, which is dc-Si, shows this region more clearly. The corresponding SADP, (e), contains diffraction spots from the bulk (grey), the dc-Si crystallite (black) and at least two crystallites of high density allotropes. The dc-Si crystallite shares diffraction spots with the bulk. The diffraction spots from the high density crystallites match best with bc8-Si and r8-Si as labelled, however there is insufficient information for an unambiguous indexing.

The second scenario in which high density crystalline allotropes have been observed is shown

in Fig. 6.6 (c-e). This particular cross-section sits on a slightly damaged TEM grid, hence the contrast from the damaged formvar on the lower left of the BF image, (c). The morphology of the modification itself consists of a defective dc-Si core, as well as lines of crystalline defects from colliding epitaxial interfaces. Significantly, on one of these lines of defects is a region of crystallites, outlined with a square in (c). A DF image, (d), from the largest crystallite (which is dc-Si) depicts this region more clearly. The SADP, (e), consists of diffractions spots from several components. One component is the bulk dc-Si, which is aligned with the [001] ZA, several spots are labelled in grey. A second component is the dc-Si crystallite which is approximately aligned on a [111] ZA orientation. Diffraction spots corresponding to the dc-Si crystallite are joined by lines and are labelled in black. Note that two diffraction spots are shared between the bulk dc-Si and the dc-Si crystallite. The crystallite must therefore have grown in a well-defined orientation off the bulk dc-Si. The final components are the diffraction spots outlined in white diamonds and circles, which are from (at least) two additional crystallites. They are most likely bc8-Si, or perhaps r8-Si, and are labelled according to their closest matches for these phases. However, this assignment should not be considered definitive given how few diffraction spots are available to refine the indexing.

6.6.2 Si allotropes - discussion

In both cases the pathway by which the high density crystalline allotropes formed is suggested to begin with a small volume of trapped melt. In the first case, Fig. 6.6 (a-b), the melt is trapped simply because the centre of a modification is the last portion to solidify. Presumably in this case the melt volume is also constrained along the long axis of the modification. In the second case, Fig. 6.6 (c-e), the chaotic collision of neighbouring epitaxial solidification interfaces as they progress towards the centre of the modification bypassed a small volume of melt. These molten regions will subsequently solidify, but as they are surrounded by already solidified material, the ability of the melt to expand upon solidification is constrained. Instead, at least a portion of the molten Si is likely to transform to r8-Si which in turn transforms to bc8-Si.

The exact pathway for this molten Si to r8/bc8-Si transformation is not clear. Three possibilities warrant further discussion; r8-Si forms from β-Sn-Si, r8-Si forms from high density a-Si, or r8-Si forms directly from the melt.

The first possibility, r8-Si forming from β-Sn-Si during unloading, is the typical pathway in conventional, near static and near equilibrium conditions (diamond anvil cell and nanoindentation). However, this pathway would first require a drastic increase in density as the molten Si ($2.57\ g \cdot cm^{-3}$) solidifies to β-Sn-Si ($3.27\ g \cdot cm^{-3}$), followed by a drastic decrease in density ($2.8\ g \cdot cm^{-3}$), as the r8-Si forms. Such a pathway appears implausible, in part as there is a lack of driving force for this additional densification during the molten Si to β-Sn-Si transformation.

The second possibility is that r8-Si forms from high density a-Si. This pathway has been demonstrated in near equilibrium, near static conditions[137], and given that high density a-Si is entirely plausible in this work, r8-Si from high density a-Si should also be considered plausible. In such a case, the molten Si must transform to a transitory high density a-Si state, which subsequently transforms to the r8-Si. Presumably the high density a-Si reaches densities similar to r8-Si, in which case no drastic changes in density are required at any stage of this potential formation pathway.

The final possibility is that r8-Si forms directly from the melt when expansion during solidification is constrained by the surrounding material. This pathway has not been demonstrated in the literature, but should be considered plausible given that molten Si has roughly the same density as r8-Si.

6.7 High density in the cap

The cap, far from focus at the top of the modification, also contains features consistent with an elevated density. In this section these features are considered separately due to the atypical nature of the cap.

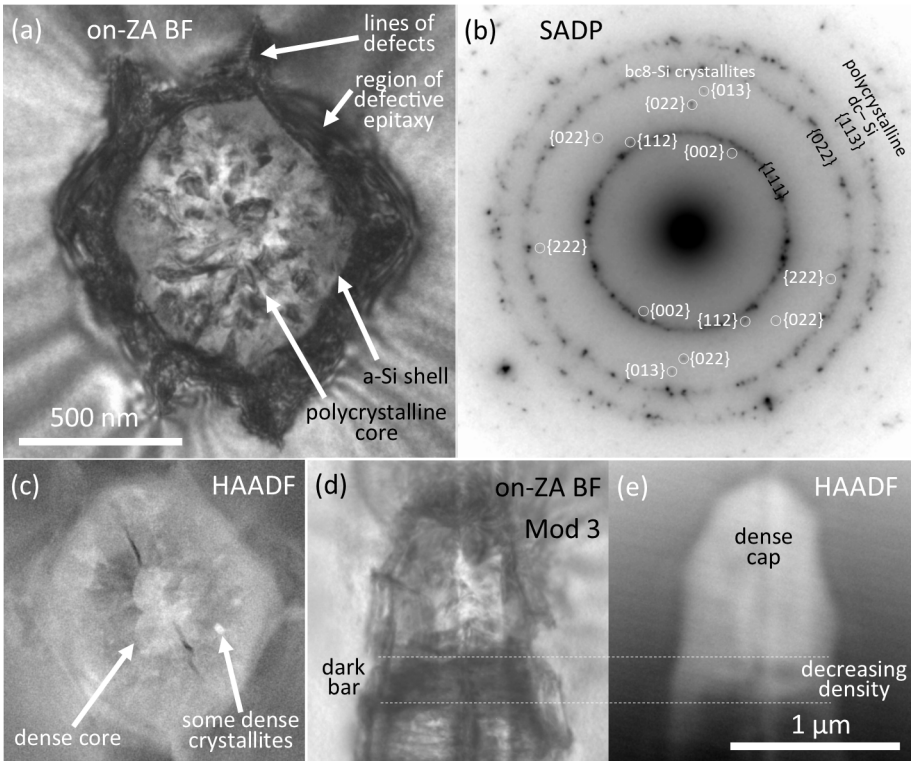

Figure 6.7: TEM results showing density-related features of the cap in short axis cross-sections, (a-c) to scale, and long axis cross-sections, (d-e) to scale. In (a) substantial bend contrast exist beyond a region of defective epitaxy which surrounds an incomplete a-Si shell which in turn encapsulates a polycrystalline core. In the accompanying SADP, (b), some of these crystallites are bc8-Si. The HAADF image, (c) shows some particularly dense crystallites, although the entire core-shell structure appears more dense than the surrounding dc-Si. On the long axis a dark bar is visible in the conventional BF image, (d), that corresponds to a region of decreasing density in the HAADF image, (e). The entire cap appears to have an elevated density here.

6.7.1 High density in the cap – results

In Fig. 6.7 TEM results from both a short axis cross-section (a-c) and a long axis cross-section (d-e) of the cap region are presented. The morphology here is consistent with morphology shown in the cap region in the previous chapter. On the short axis cross-section the modification is surrounded with strong bend contrast which is presumed to be the product of compressive strain. The modification itself consists of short lines of defects, a region of defective epitaxy surrounding a thin a-Si shell which in turn encapsulates a region of crystallites, many of which are also defective. In this case the SADP, (b), reveals additional diffraction spots from multiple bc8-Si crystallites. These are labelled in white with circles around the relevant diffraction spot. Imaging the same cross-section under HAADF conditions, shown in (c) at the same scale as (a), reveals that the entire a-Si shell and polycrystalline core is brighter than the surrounding dc-Si,

but with some regions, particularly near the centre and particular crystallites, brighter again. Given that this is a HAADF image, the higher brightness is suggestive of higher density.

From the perspective of the long axis cross-section, the conventional TEM BF result, (d), is again as described previously. One feature of note here is that a dark bar is present at the bottom of the cap, as labelled in the figure. Imaged under HAADF conditions, (e), with an atypical 80 keV accelerating voltage, results in the entire cap being brighter, which is again suggestive of an elevated density. It must be emphasised that similar contrast was not achieved with a 200 keV accelerating voltage, suggesting that the density difference between the cap and the surrounding material is modest. Note that the dark bar in (d) overlaps the bottom of the brighter region in the HAADF image, (e). Presumably the dark bar is strain-induced bend contrast due to the density difference between the cap and the decreasing diameter region.

6.7.2 High density in the cap - discussion

Evidently the cap region exists in a state of elevated density in comparison with the bulk dc-Si. This is noteworthy because the cap is not the last region to solidify. The elevated density must therefore be preserved for some other reason. The most plausible explanation is related to the non-negligible vertical thermal gradients. These have already been explained to lead to rapid solidification within the cap, which could additionally trap much of the local excess material from the molten Si. As such, the cap exists at elevated densities on a scale larger than the isolated crystallites from trapped melt, but also at higher densities than the constant diameter region.

At this stage it is worth considering that, given the prevalence of morphological features related to high density, the a-Si within the cap is the most likely to also be at an elevated denisty compared with a-Si formed elsewhere in the modification. Unfortunately the investigation of a-Si density was conducted before any cross-sections of the cap were created, and so no EELS measurements of the a-Si in the cap were ever recorded.

6.8 Summary

In this chapter the density of the modification morphology was investigated. Both voids, and regions of elevated density exist.

Void formation is driven by the densification of Si as it melts. Multiple voids remain after solidification indicating that the growth of a single void, or coalescence of multiple voids is kinetically limited. During solidification there are position-dependent changes to the size and shape of the voids. These changes are due to surface-tension-driven wetting of the solidification interface, potentially thermocapillary pumping and the expansion of the surrounding Si as it solidifies. The latter also results in the refilling of voids from the top and bottom. Larger voids appear less likely to be fully refilled, and the molten material that is injected into voids encounters strong thermal gradients and largely amorphises. As void size decreases the likelyhood of complete refilling increases, and the temperature gradients through the refilled material decreases. As such, intermediate sized voids principally contain polycrystallites encapsulated in a-Si after solidification. Smaller voids are principally defective dc-Si after solidification.

As the voids are not fully refilled after solidification, the material displaced by the voids must be accommodated in high density regions elsewhere in the modification. Much of the higher density remains associated with the melt until the last regions solidify. In the previous chapter this was seen to lead to compressed dc-Si, particularly in the constant diameter region which solidifies last.

A second mechanism to accommodate the displaced mass is in high density crystalline allotropes. These form when small pockets of high density melt are trapped during solidification, generally at the centre of the modification or between colliding solidification interfaces. With insufficient volume to expand to dc-Si upon solidification, the r8-Si phase instead forms. This subsequently (partially) transforms to the bc8-Si phase. The conventional pathway by which r8-Si forms is via β-Sn-Si, an even higher density allotrope. The volume changes implied by this pathway are unrealistic in this work, suggesting an alternative pathway. One possibility is that r8-Si forms from a transient high density a-Si phase. A second possibility is that r8-Si forms directly from the melt.

The third and final potential mechanism by which the displaced mass may be accommodated is in high density a-Si. EELS investigation of a-Si near focus yielded a density lower than that of dc-Si. The legitimacy of this result is questionable as it is possible that the density of the a-Si decreased during cross-sectioning as the confinement from the surrounding material was removed. Additionally, the a-Si near focus may not be representative of a-Si throughout the entire modification. In particular, high density a-Si is probable in the cap. Indeed the cap also shows ample evidence of high density in the form of compressive strain, bc8-Si crystallites and strong HAADF contrast. Thus, the investigation of the a-Si density is inconclusive and it remains plausible that high density a-Si exists within the sample.

Chapter 7

Closely spaced modifications

The topic of this chapter are the closely spaced modifications ($\sim$ 2 μm spacing) as used for dicing. The chapter will begin with a short experimental section, followed by an investigation of the morphology of closely spaced modifications. This will show that all of the key features observed in isolated modifications are also present in closely spaced modifications. However, there are also differences between two experimental situations and the underlying causes of these differences will be discussed.

Next, the dicing process will be investigated from the perspective of the morphology visible in short axis cross-sections. It will show that many small cracks either form during solidification or are easily nucleated subsequently. During dicing many of these cracks propagate simultaneously before joining together to complete the cleaving path. Portions of many of these cracks are bypassed by the final cleaving path, which presumably makes the cleaved surface somewhat fragile.

7.1 Experimental

The modifications are produced using 1549 nm, 3.5 ns, 2 μJ laser pulses under two closely-spaced geometries. The majority of the chapter considers closely spaced modifications created in a segmented row; 25 modifications each separated by 2 μm over a distance of 50 μm, with a separation of 150 μm between each set of modifications. This is sufficient to replicate the morphology of closely spaced modifications intended for dicing, while allowing the sample to retain sufficient strength for handling, polishing and cross-sectioning. After polishing to expose the modifications, they were examined for evidence of phase transformations using Raman spectroscopy with a 633 nm excitation wavelength. Short axis cross-sections were examined with TEM after preparation by FIB milling using the H-bar geometry. In the closely spaced samples the adjacent modifications are to the left and right from the perspective of the TEM images. Due to the fragility of the closely spaced modification samples (i.e. their tendency to easily crack during handling or thinning), long axis cross-sections were not realistic and were not attempted.

The second geometry examined were cleaved samples, where the modifications were produced in a continuous row with a 2 μm separation, then cleaved. For these samples, short axis cross-sections from one side of the cleaved sample were prepared using the ex-situ liftout technique. As such, only a portion of each modification is visible within any given TEM cross-section. For this reason, these samples are most easily interpreted with reference to the non-cleaved samples.

7.2 The morphology of closely spaced modifications

In this section the morphology of the closely spaced modifications will be investigated. The initial emphasis will be placed on demonstrating that all the key features observed in isolated modifications are also present in closely spaced modifications. As such, the presence and morphology of density-related features will be shown to be similar. The variation in morphology and solidification behaviour as a function of thermal gradient strength will also be shown. Next, the differences between closely space and isolated modifications will be considered and the underlying cause for these differences discussed.

7.2.1 Morphology - results

From a density perspective, the morphology of the modifications is first contingent on the formation of voids due to the densification of Si as it melts. These have already been demonstrated in cleaved samples in Chapter 6, Fig. 6.1. For completeness the short axis cross-section of a void from a closely spaced modification is shown in Fig. 7.1. Adjacent modifications are to the left and right from the perspective of this, and the following, TEM images. This void is essentially equivalent to the voids observed in isolated modifications; it contains regions which have solidified to dc-Si by normal epitaxial solidification, but with lines of defects from the imperfect collision of solidification interfaces. The remanent void is surrounded mostly by a-Si which is assumed to have been molten material that refilled the void from above or below due to the application of pressure on the melt by the surrounding material as it solidified and expanded. As this refilling melt will encounter strong thermal gradients with the colder side walls of the void, it solidifies rapidly into an amorphous state. There is also a small region of defective dc-Si which is likely the first point of contact between the surrounding material and the refilled material. As such, the temperature differences were less extreme and the solidification was initially by defective epitaxy, rather than amorphisation.

The presence of remanent voids requires that displaced material be found in high density regions elsewhere in the modifications. Compressively strained Si, high density crystalline allotropes and potentially high density a-Si would therefore be expected. Raman spectroscopy maps from a set of closely spaced modifications show that a-Si and bc8/r8-Si are present, Fig. 7.2 (a) and (b) respectively. There is also some surface damage from sample preparation marked in (a) which is not representative of the original morphology. Nevertheless, the potential for high density a-Si is as valid as it is in the isolated modifications. The high density crystalline allotropes are not only present, but are more prevalent in the closely spaced modifications compared with isolated modifications.

The morphology surrounding the high density allotropes appears to be similar between closely spaced and isolated modifications. An example of bc8-Si in the cross-section of a closely spaced modification is shown in Fig. 7.3. The BF image, (a), contains a crack, lines of defects, a region of defective epitaxy (which also features strong bend contrast) surrounding an a-Si shell with a facetted periphery and a polycrystalline core. A noteworthy difference that is common in closely spaced modifications, regardless of their position along the modification's length, is the reduced symmetry. No line of defects is visible on the right side of this image. The SADP, (c), from the core-shell region contains diffraction spots from at least two bc8-Si crystallites (marked with triangles) and two dc-Si crystallites (marked with squares and hexagons). The latter share the diffraction spots marked with circles, suggesting that one crystallite grew off the other. A DF image of one of the bc8-Si crystallites is shown in (b). Evidently, just as for isolated modifications, this is a case where molten Si trapped at the core has insufficient room to fully expand

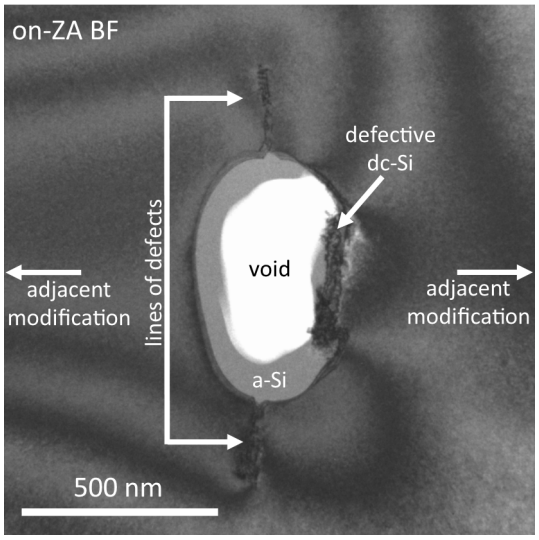

Figure 7.1: A TEM image from a short axis cross-section of a void in a closely spaced modification. Adjacent modifications are to the left and right from the perspective of the image. The features of the void are entirely consistent with voids in isolated modifications, with a remanent void surrounded by a-Si and defective dc-Si, which in turn is surrounded by normal dc-Si and lines of crystalline defects.

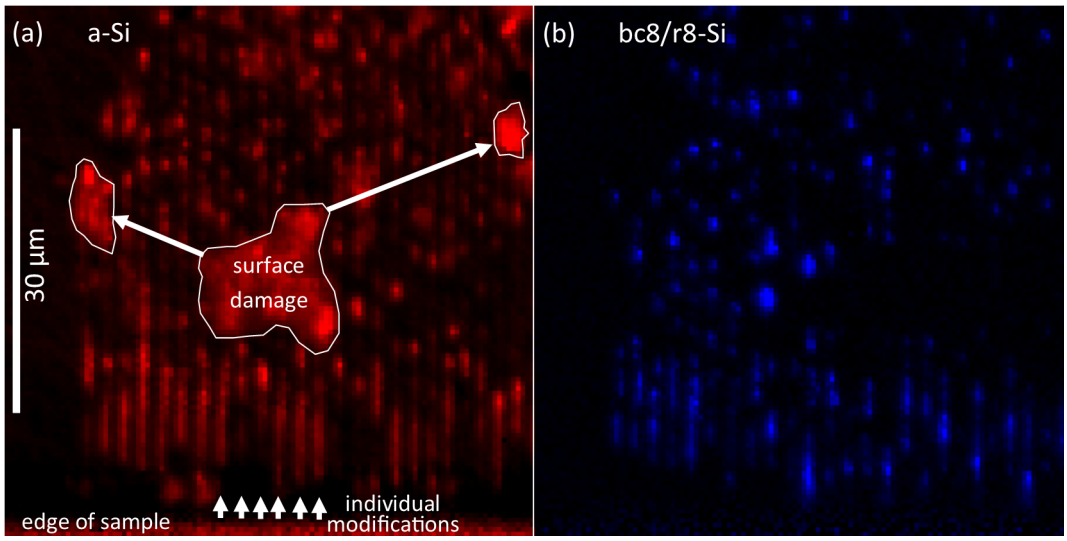

Figure 7.2: Raman map images of the a-Si, (a), and the bc8/r8-Si, (b), from a set of closely spaced modifications. The bc8/r8-Si is notably more prevalent than in isolated modifications. Some amorphous surface and sample edge damage from sample preparation is also observed.

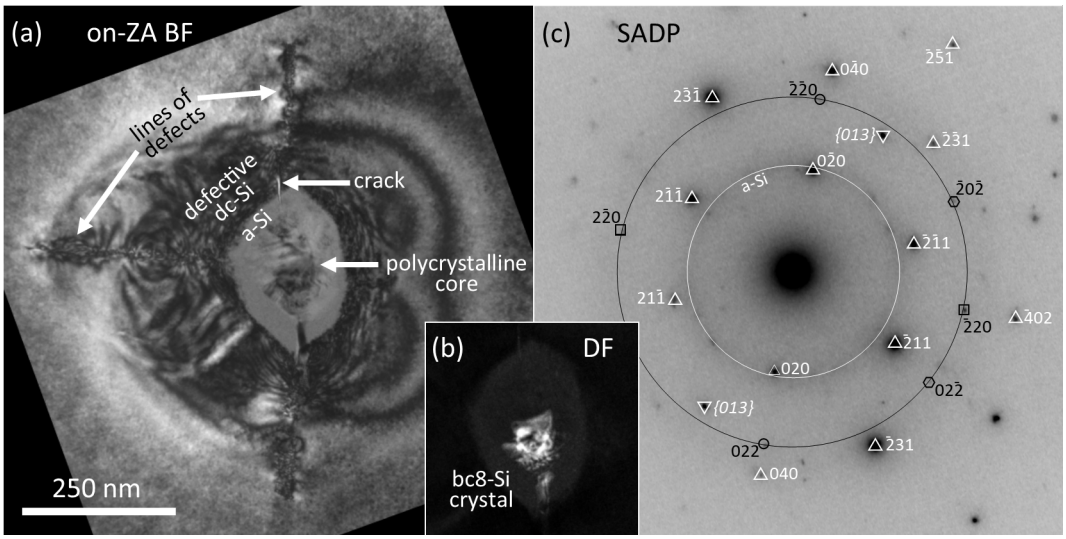

Figure 7.3: TEM results from the short axis cross-section of a closely spaced modification that contains bc8-Si in its core. A BF image is shown in (a), which reveals relatively conventional morphology, although extensive defective Si exists beyond the a-Si shell. A DF image created from the $(\bar{2}11)$ bc8-Si diffraction spot is shown in (b). It is produced at the same scale as (a). The SADP, (c), contains diffraction spots from at least two bc8-Si crystallites (marked in white with triangles at different orientations for each crystal). At least two dc-Si crystallites (black with squares and hexagons) are also present. The diffraction spots marked with circles belong to both dc-Si crystallites, indicating that one crystallite must have nucleated off the other.

to dc-Si during solidification, and so some of it has transformed to bc8/r8-Si, with a density closer to that of the melt. High density crystallites were also observed in isolated modifications after melt was trapped between colliding solidification interfaces. Similar crystallites have been observed in closely spaced modifications but have not been included for brevity.

Next, results pertaining to the variation in morphology due to the solidification process and its thermal-gradient-dependence will be presented. Figure 7.3 has already demonstrated a high thermal gradient extreme, where strong undercooling in the melt has induced amorphisation, but the thermal insulation of the a-Si has resulted in a return to crystal growth and thus, a polycrystalline core. In Fig. 7.4 several examples of closely spaced modifications with a range of thermal-gradient-dependent structures, first discussed in isolated modifications in Chapter 4, are shown. The morphology in Fig. 7.4 (a) appears to have formed under slightly weaker thermal gradients than Fig. 7.3 and contains an a-Si shell, single crystal core. It is also noteworthy that it contains cracks and a reduced symmetry.

In Fig. 7.4 (b) weaker thermal gradients again have delayed the onset of amorphisation. As such, the amorphous region is smaller and the thickness was never sufficient to insulate the remaining melt and induce a return to crystal growth. A point of difference compared with isolated modifications is that the a-Si is surrounded not by lines of defects, but broader regions of defective dc-Si. Substantial, presumably strain-related, bend contrast is also present within the defective regions. The modification lacks a broad line of defects on the right-hand side.

With weaker thermal gradients again, Fig. 7.4 (c), undercooling is insufficient to induce amorphisation and so the core of this modification is instead a roughly diamond shaped region of defective dc-Si due to defective epitaxy. Two sharp lines of defects are present, which overlap with long cracks. Also present are two very broad regions of defects where sharp lines of defects would be expected in isolated modifications.

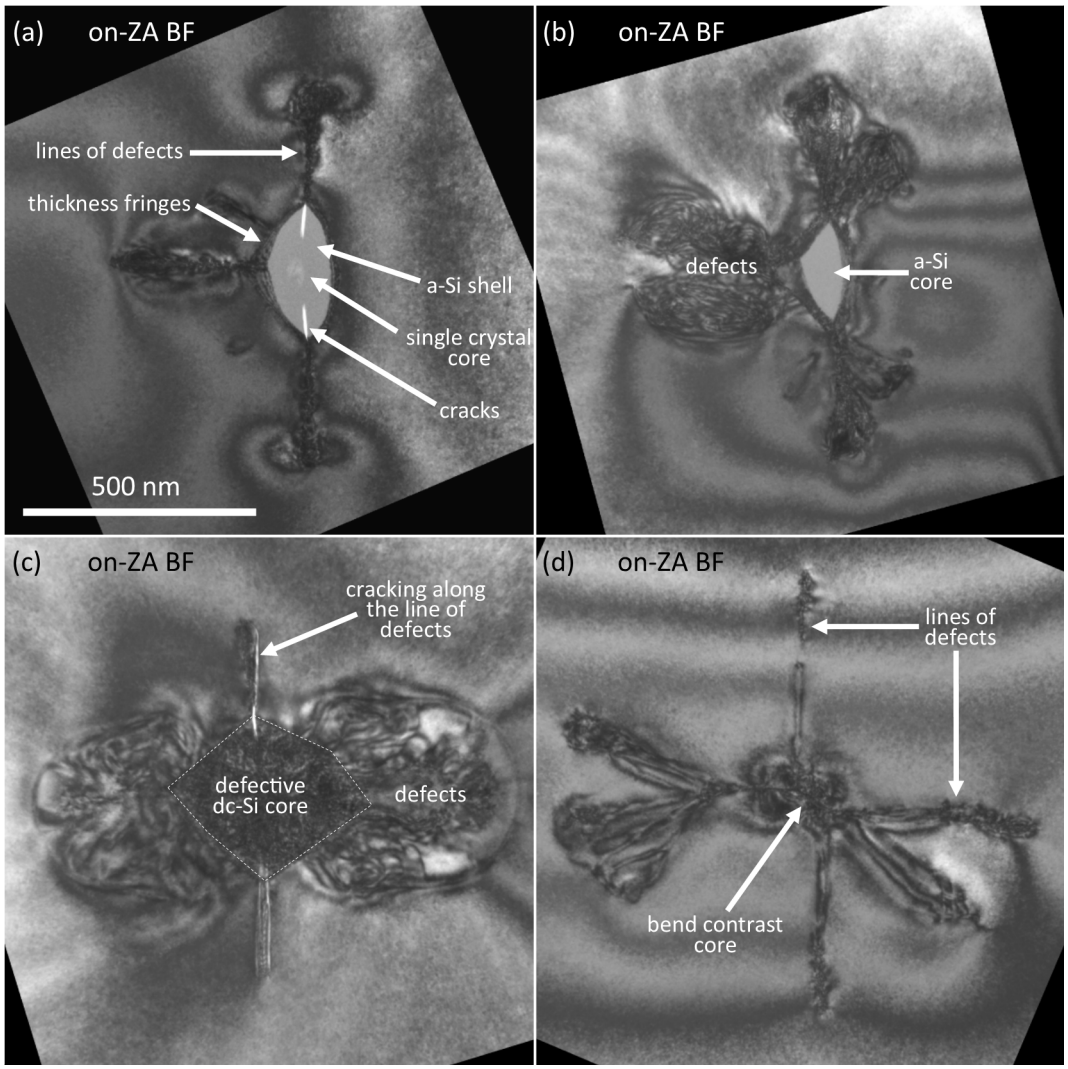

Figure 7.4: TEM images from short axis cross-sections of four closely spaced modifications, all produced at the same scale, that reveal most of the same range of features observed in isolated modifications. In (a) is an example of a single crystal core, a-Si shell morphology. Notably the line of defects that would typically be found on the right side is missing. In (b) is an example of an a-Si core, again no line of defects is present on the right side. An example with a defective Si core is shown in (c), which also has extensive defects and bend contrast on the horizontal lines of defects and cracks on the vertical lines of defects. The morphology in (d) is entirely lines of defects due to the collision of competing epitaxial solidification interfaces.

Nearer to the lower limit of thermal-gradient-dependent morphology is the structure in Fig. 7.4 (d). In this case no transition in solidification behaviour has occurred and the core of the modification is dc-Si with broad lines of defects only from the collision of epitaxial solidification interfaces.

Collectively, these cross-sections of closely spaced modifications demonstrate most of the range of thermal-gradient-dependent features shown in isolated modifications in Chapter 4. While there are some differences, it is clear that the underlying solidification process is fundamentally equivalent.

7.2.2 Morphology - discussion

From the results section it is clear that most general aspects of the closely spaced modifications are similar to those in isolated modifications. However, several differences are noteworthy. In comparison with isolated modifications, it appears that cracking is more prevalent, defects from defective epitaxy are more prevalent, defects from the collision of solidification interfaces are typically broader, and the morphology is often less symmetric. It should also be noted that in general, bend contrast is more prevalent in closely spaced modifications. Presumably much of this bend contrast is the result of substantial strain within the modifications.

The underlying cause of the differences between closely spaced and isolated modifications is thought to primarily be a result of strain. Due to the existence of previous modifications to one side of a new modification, and more importantly their strain field, epitaxial solidification will occur off strained crystal. As such, the solidification interface is presumably macroscopically rougher, directly resulting in more defects. Furthermore, the collision of different solidification interfaces would also be expected to be more chaotic, leading to more defects again. This explanation would then explain much of the asymmetry and increased prevalence of defects within Figs. 7.1-7.4.

A secondary consequence of a chaotic collision of rough solidifications interfaces is that it becomes more likely that molten Si is trapped between them. This has been shown to lead to the formation of bc8/r8-Si and this presumably explains the greater prevalence of these high density allotropes in the Raman results, Fig. 7.2 (b). Additionally, the redistribution of mass through the length of the modification is likely impeded by the trapping of volumes of melt. Consequently, material will be less concentrated in the final portions of the modification to solidify, the constant diameter region. As such, strain is expected to be more homogenous over the length of the modification.

Another difference in closely spaced modifications is that the convergent laser will overlap the upper portions of previous modifications. This would be expected to lead to the partial absorption of one side of the laser pulse and therefore a less symmetric deposition of energy in the new modification. The portions of the laser pulse that irradiates the previous modification will lead to heating. This heating must be modest as there are no morphological features that can be explained by annealing or remelting. It is plausible that the heating induces thermal stresses which may exacerbate cracking, a point that will be expanded upon in the following section.

Finally, it should be noted that the direction of the pulse train used to create the modifications was not recorded. This would have been useful when considering the asymmetry in the modifications. It should also be stated that the repetition rate of the laser, 100 Hz, is sufficiently slow that each modification would be expected to have cooled by the time a new modification is created.

7.3 The dicing of closely spaced modifications

In this section the morphology visible in short axis cross-sections of closely spaced modifications will be used to investigate the dicing process. Three topics will be covered; the formation of cracks, the propagation of cracks within thin cross-sections and the propagation of cracks in the bulk. Samples that are cleaved in the bulk result in the modifications being split on either side of the dicing path. As such, the cross-sections examined in TEM contain only a portion of the modification making them more difficult to analyse. Conversely, cracks that propagate after the modifications are cross-sectioned are not always representative of the cracking behaviour in the bulk. However, the modification morphology is fully visible and crack initiation and propagation are easily analysed. In the results and discussion that follows, only cases with equivalence between cracking in thin cross-sections and cracking within the bulk will be considered. These two conditions are therefore complimentary to one another.

A note concerning the orientation of cracks is warranted before continuing. In the bulk, the cracks nucleate and propagate in three-dimensions, with the cracks extending along the long axis of the modification. The cracks observed in the TEM cross-sections are effectively two-dimensional traces. The nature of these cracks along the long axis of the modification can not be investigated.

7.3.1 Dicing - results

Crack formation may be investigated by examining instances in which small cracks are visible in the short axis cross-sections of the modifications. One example is presented in Fig. 7.5. The BF image recorded with the sample tilted on-ZA, (a), appears relatively conventional for a modification that has solidified under modest thermal gradients. With the sample tilted off-ZA and slightly defocussed, (b), two cracks become evident sitting at the ends of the lines of defects that run near vertical on the image. Such cracks are common in closely spaced modifications, with Fig. 7.4 (c) being a second example. Equivalent cracks have also been observed in isolated modifications, although less commonly and less preferentially along the near vertical lines of defects. Furthermore, similar, but smaller cracks have been observed within highly defective cores of some modifications, both closely spaced and isolated.

An additional situation in which small cracks are often observed is at the interface between dc-Si and a-Si. This was visible in Fig. 7.3 (a) and Fig. 7.4 (a). This too is observed in isolated modifications, such as in Chapter 4, Fig. 4.7. It notable that these cracks are vertical, from the perspective of the short axis cross-section images, even when no vertical line of defects are present.

Examples of cracks that have propagated in thin cross-sections are presented in Fig. 7.6. Similar features will be shown in samples that were cleaved before cross-sectioning in Fig. 7.7. In Fig. 7.6 (a) two TEM images, recorded on-ZA, are overlayed to examine the cracks around two adjacent modifications. Six cracks, marked by arrows, are visible in the images. The left most crack runs vertically (from the image's perspective) and appears not to have propagated at all. The remaining cracks have propagated after the sample was thinned due to the stresses of handling TEM samples. Each of these runs roughly horizontally (again, from the perspective of the image), but none have successfully connected with the neighbouring cracks.

A second example of crack propagation after cross-sectioning is shown in Fig. 7.6 (b). It contains four modifications and three large cracks along a single well defined path that is parallel to the cleaving direction. More detailed images of the left most and right most modifications are shown in (c) and (d) respectively. This example is noteworthy, first, because the core of all

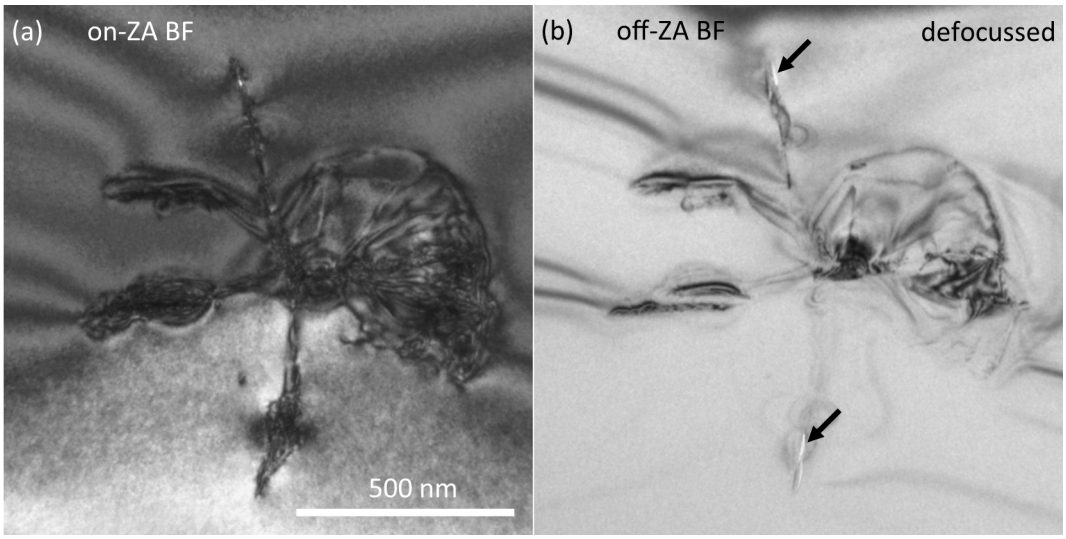

Figure 7.5: An on-ZA BF TEM image, (a), and off-ZA defocussed BF, (b), from a closely spaced modification that reveals the presence of cracks (indicated by arrows) at the ends of the vertical lines of defects. Images are at the same scale. Annotation corrected.

these modifications remains connected. For the two left most examples the core remains the only section not to cleave, suggesting that the core is tougher than the surrounding modification. In (c) it is also shown that there are additionally two cracks running vertically (in the image) that align with the lines of defects. These are also marked with arrows. The core of the right most modification, (d), also remains intact, but three cracks exist within its vicinity. It appears that the path of the larger crack has deviated so as to connect with a smaller crack. The remaining modification in (b) has largely been bypassed by the crack.

Further cleaving of the samples in Fig. 7.6 could conceivably lead to the results in Fig. 7.7, which are from samples that were cleaved before cross-sectioning. Figure 7.7 (a) contains a modification with a small a-Si core. The cleavage path appears consistent on either side of the core, but has deviated through the core. Presumably this represents a situation similar to that in Fig. 7.6 (c), where the core was tougher, and failed only after the surrounding area had already cracked.

The second image, Fig. 7.7 (b), contains a modification that shows no signs of interacting with the crack and has largely been bypassed. This is very similar to one of the modifications in Fig. 7.6 (b).

The modification in Fig. 7.7 (c) is largely missing, with the exception of a vertical line of defects. At the expected location of the core is a noticeable step that connects the paths of what presumably were originally two separate cracks. This would be similar to the expected situation in Fig. 7.6 (a) and (d) if they were further cleaved. Interestingly, there is also a crack in Fig. 7.7 (c) that has been bypassed by the main cleaving path. Again, this is to be expected in some cases in Fig. 7.6 and is even clearly present in Fig. 7.6 (d).

The final example from a cleaved sample, Fig. 7.7 (d), is fairly similar to (c) except that the step between cracks on the cleaving path is smaller and even less of the modification is visible on this side of the cleaved path.

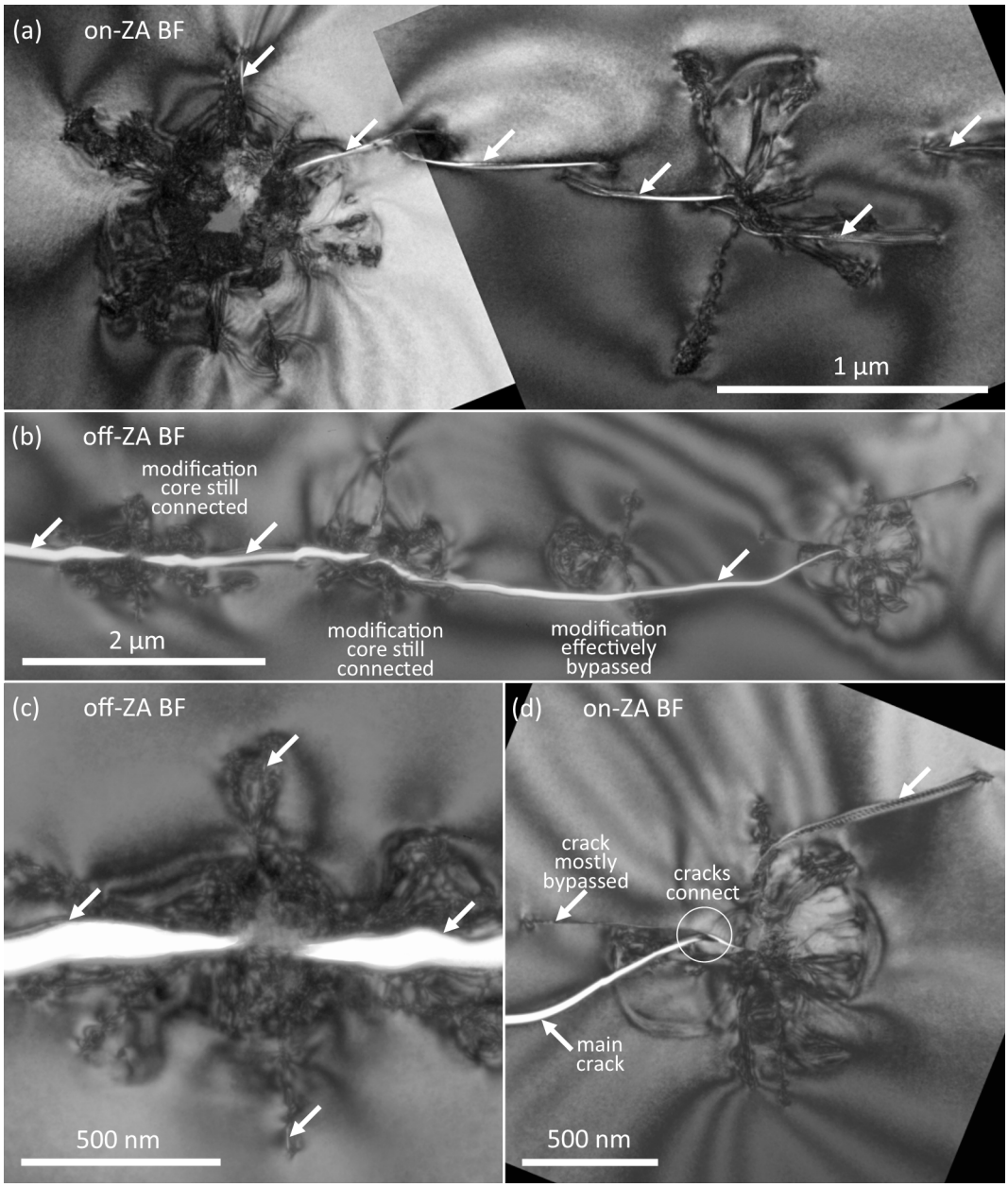

Figure 7.6: TEM images from closely spaced modifications in which cracks propagated after the samples were cross-sectioned due to the ordinary stresses involved in handling a TEM sample. In (a) two images are overlayed showing adjacent modifications and six cracks within their vicinity. The cracks are largely parallel, but are not in line, with one another. In (b) a set of four modifications are shown in a single image with three large cracks forming a single well defined cleaving path. The centre of all the modifications remains largely intact. More detailed images of the left most modification, (c), and right most modification, (d), reveal more detail on the cracks that are present. Arrows mark the cracks.

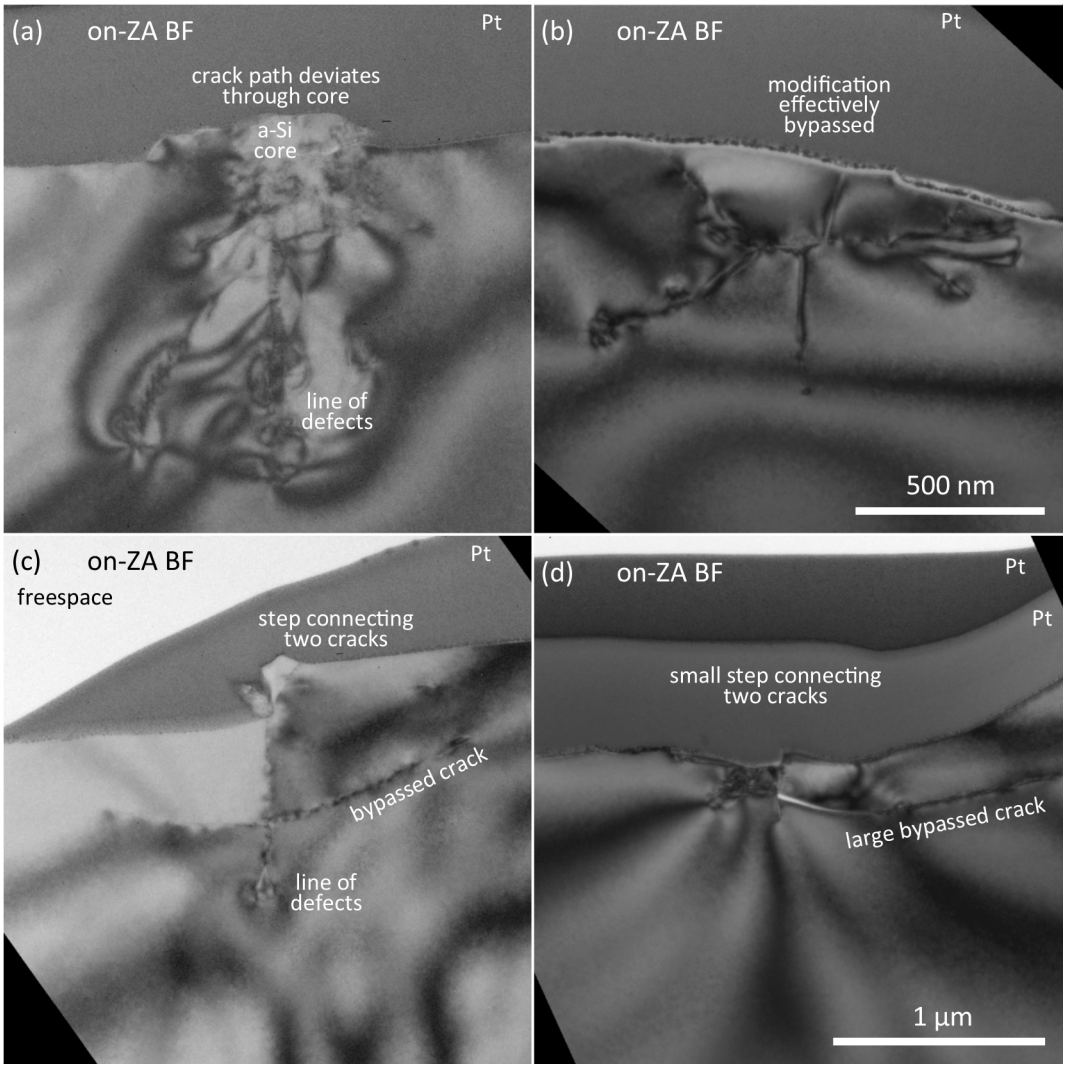

Figure 7.7: TEM images from short axis cross-sections prepared from a cleaved sample. Collectively these show equivalence in the crack propagation behaviour of bulk samples when compared with the examples of crack propagation in cross-sections shown previously. In (a) the core appears to have fractured separately to the surrounding Si. In (b) the modification has largely been bypassed and shows no sign of interacting with the crack. In (c) a step exists to connect two parallel, but not in line crack paths. A crack that was bypassed by the cleaving path is also present. In (d) a step and a bypassed crack is again present. In this case very little of the modification is visible, suggesting most of the modification exists on the other side of the cleaved surface. (a-c) are at the same scale.

7.3.2 Dicing - discussion

The regularity of cracks at certain positions within modifications is clear evidence that there are natural crack formation sites within the modifications. The core itself is thought to often be compressively strained, making it resistant to crack formation. But this compression presumably leads to a tensile force beyond the core that encourages crack formation, particular at the edge of an a-Si core as was noted in Fig. 7.3 and Fig. 7.4 (a) for example. Crack formation also appears to be common along many of the lines of defects, as in Fig. 7.4 (c) and Fig. 7.5.

At what stage the cracks actually form is unclear as they may form directly from internal stresses, or from the external stresses involved in cross-sectioning (or cleaving) the modifications. However, the heightened prevalence of cracks in closely spaced modifications does suggest an underlying difference to isolated modifications. The prevalence of strain due to the adjacent modifications is an obvious factor in closely spaced modifications. A second potential factor is thermally-induced stresses. Recall that the convergent laser will overlap much of the previous modification, although not the region nearest focus. The SEM image of the cleaved surface in Chapter 3, Fig. 3.1, shows that a transition is notable between a chaotic area above focus, and the well defined area near focus. This transition coincides with the height above focus in which the laser begins to overlap the previous modification. This suggests that the chaotic cleavage further from focus is related to the presence of more cracks, induced by thermal stresses from the overlapping laser. Regardless of when the cracks form, crack formation is clearly not a large obstacle for cleaving the sample.

Interestingly, crack formation before cleaving did appear to be biased towards the vertical axis of the short axis cross-sections. This is thought to be partly the result of the asymmetry in the laser used to create the modifications. It is also probable that the strain from adjacent modifications enhances this orientation bias. Nevertheless, this raises the prospect of deliberately inducing asymmetry in the laser and orienting this asymmetry in the desired dicing direction. As such, cracks should preferentially be aligned with the dicing direction, improving dicing performance.

As for the process of crack propagation, this does preferentially occur in the direction of adjacent modifications, as is desired for the dicing application. It is noteworthy that this occurs even as the formation of cracks is biased perpendicular to the propagation direction. Crack propagation also occurs simultaneously with many parallel cracks, as can be inferred from Fig. 7.6 and Fig. 7.7. However, presumably because the initial cracks are often vertical, the cracks do not always propagate in line with one another. As such, a step is required to connect each of the parallel cracks. This can lead to portions of cracks being bypassed, which is undesirable from an application perspective. The residual cracks will serve to weaken the side walls of the chip and raises the possibility of debris if fragments subsequently break off.

Crack propagation is also influenced by compressive strain at the centre of the modification. In Fig. 7.6 this resulted in a higher fracture toughness in the core, a behaviour confirmed in the bulk with Fig. 7.7 (a). It is possible that this will sometimes cause the crack to propagate around a core, rather than through it. This may even be the case in Fig. 7.7 (d), which is why so little of the modification is visible in the cross-section. On the other hand, if no strong stress concentrations, compression or weaknesses exist within the modification then it may not influence crack propagation at all, as in Fig. 7.7 (b).

Given these results, the main shortcoming with crack propagation from an application perspective is the presence of bypassed (i.e. redundant) cracks on the diced sample. As suggested above, this could be reduced by modifying the laser process to try and align the initial cracks with the cleaving direction. A second avenue is to slightly increase the modification separation,

which will have several consequences. First, this will reduce the overlap of the laser with the previous modification and hence the thermal stresses. Given the cleaving path is superior in the non-overlapped region, perhaps this will improve chip wall strength with minimal loss in dicing performance. Secondly, this will reduce the influence of strain from previous modifications on the solidification of new modifications. Given that this strain appeared to cause crack formation perpendicular to the dicing orientation, greater spacing should also help keep the cracks that do form and propagate in line with one another. Third, greater spacing will directly result in a low concentration of cracks along the cleaving path. As such, the stress concentration on the cracks that do exist should be larger and should reduce the likelihood of cracks being bypassed. These changes will come at the cost of requiring a higher cleaving force to induce dicing, and eventually the reduction in crack density will also compromise how well the cracks are guided. Nevertheless, it seems unlikely that the current spacing of 2 μm is the ideal compromise between ease of dicing and chip wall strength, and so further testing would be warranted.

7.4 Summary

This chapter has shown that the morphology of closely spaced modifications is largely consistent with that of isolated modifications. The modifications differ mostly due to the overlapping strain field from adjacent modifications, which influences the solidification process. The strain appears to result in a rougher solidification interface, which leads to an increased prevalence of defective Si both from defective epitaxy and the imperfect collision of competing solidification interfaces. It is noteworthy that this effect is asymmetric, as modifications only exists on one side of a new modification.

A second consequence of a rough solidification interface and a chaotic collision of competing interfaces is that the trapping of molten Si by the passing interfaces becomes more likely. This is thought to lead to an increased prevalence of high density crystalline allotropes in the closely spaced modifications when compared with isolated modifications. It is speculated that this also influences the redistribution of mass through the length of the modification. As such, compressive strains are expected to be slightly less concentrated to the constant diameter region.

The closely spaced modifications also differ in that cracks are more prevalent, particularly cracks oriented perpendicular to the row of closely spaced modifications. This orientation is likely partly the result of an asymmetry in the laser, and partly the result of the stress from adjacent modifications. The increased prevalence is also related to the adjacent modifications but may also be the result of thermal stresses induced by reheating due to the overlap of the convergent laser with previous modifications when inducing a new modification.

The cracks can initially be found along the lines of defects that result from solidification interfaces colliding, as well as smaller cracks from similar circumstances at the core of modifications. Modifications with a-Si cores also often feature small cracks on the outer periphery where it meets the dc-Si.

Crack propagation occurs simultaneously, in parallel, for many cracks initiated around the modifications, which then subsequently join together. The joining of cracks often requires steps in the cracks path as the cracks are not always in line with one another. This step often results in portions of the cracks being bypassed by the cleaving path. Bypassed cracks are undesirable from an application perspective, as they may weaken the side walls of a chip. Increasing the spacing between modifications, and deliberately inducing and directing an asymmetry in the laser may allow for better control of crack formation and propagation. As such, the dicing performance could be improved.

Chapter 8

Low energy modifications

Over the previous chapters all the significant aspects of the standard modification morphology have been explored. It is now opportune to contrast those results with modifications produced under different laser conditions. This will allow for the validation of many of the conclusions that had previously been reached; indeed, in several cases the evidence will be stronger for the low energy modifications. However, as the laser conditions are different, the manifestation of some processes that occur during melting and solidification do also differ.

This chapter will investigate modifications produced after the filtering of the beam to reduce the laser power. This leads to a lower on-sample pulse energy, 0.6 μJ rather than 2 μJ, which is just above the threshold for observable modification of the material when examined by IR microscopy. All other experimental conditions are otherwise identical to the standard isolated modifications.

As will be shown, the resultant modifications are significantly smaller with a length of 15.5 ± 0.8 μm. Given the laser pulse duration remains the same as for the standard sub-bandgap regime modifications, the low energy modifications must melt slower, but presumably solidify faster.

This chapter will begin with a short experimental section, followed by the results and the discussion, which will separately consider solidification and the influence of density.

8.1 Experimental

This chapter examines isolated low energy modifications created in the sub-bandgap regime, specifically with the 1549 nm, 3.5 ns, 0.6 μJ laser pulse. These conditions differ from the standard isolated modifications in that the on-sample laser energy has been reduced by filtering of the laser beam.*

The modifications were exposed for Raman spectroscopy by polishing such that the modifications were just subsurface. In this particular case the modifications appear to be slightly deeper than the previous examples of standard isolated modifications and closely spaced modifications.

TEM cross-sections were prepared in the FIB along both the long and short axis using the H-bar geometry.

8.2 Results

In this section the results from Raman spectroscopy will be shown first, followed by TEM results from long axis cross-sections, then short axis cross-sections and finally density-related features

*The low energy modifications are focussed further from the back edge of the wafer than previous modifications. This should not influence the modification morphology.

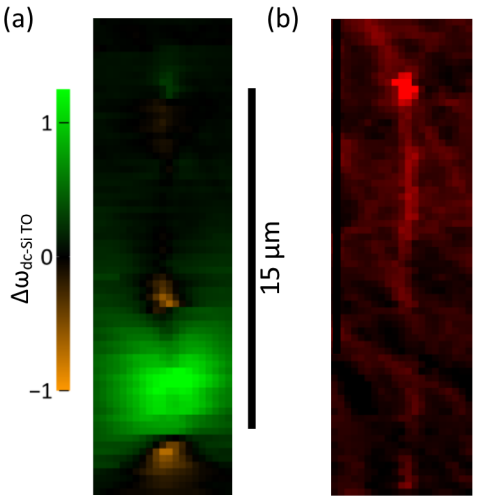

Figure 8.1: Raman map images recorded with a 532 nm excitation wavelength shown at the same scale and collected from isolated low energy modifications which run vertically with the focus end of the modification near the bottom of the figures. These show strain around a single modification, (a), and the presence of a-Si, (b). The strain measurement shows compressive peak shifts in green and tensile shifts in orange. The a-Si measurement is also sensitive to scratches from the polishing process.

will be shown.

Results from Raman spectroscopy mapping of a low energy modification are shown in Fig. 8.1. The modification runs vertically with the focus end at the bottom of the image. The first Raman map image, (a), shows the shift in the dc-Si TO band peak and is negative (orange) under tension and positive (green) under compression. The sample is notably compressed near, but above, focus.

The second Raman map image, (b), shows in red the area under the a-Si TA band and therefore the presence of a-Si. Amorphous material is present along much of the modification's length but is particularly prominent in the cap. Streaks outside the modification are surface scratches from sample polishing. These scratches are more prevalent here than in previous Raman results only because the modification is further subsurface.

No Raman map image is shown of the bc8/r8-Si phases in the low energy modifications as they were not observed in Raman. However, they are known to be present, as will be shown in the TEM results below. Presumably Raman was unable to resolve these phases because the modifications were further subsurface than was ideal and because a 532 *nm* excitation wavelength was used. The 532 *nm* wavelength is less suitable for locating subsurface allotropes compared with the 633 nm wavelength, but the latter was not available at the time of the measurement.

TEM examination of the long axis cross-section of a low energy modification yielded the results shown in Fig. 8.2. The full length of the modification is shown under two different imaging conditions in (a) and (b), with the focus end of the modification on the bottom of the image, and the cap on the top of the image. Portions of the modification are shown in more detail in (c-g), and all are at the same scale.

A notable absence in these images, compared with standard isolated modifications, is the lateral lines of defects. This absence is a product of the previously mentioned laser asymmetry, a topic that will be discussed further below. Without the lateral lines of defects it is more difficult to evaluate the shape of the original melt periphery. However, the aggregate of short axis cross-section results reveals that the cross-sectional area is smallest at focus, and increases

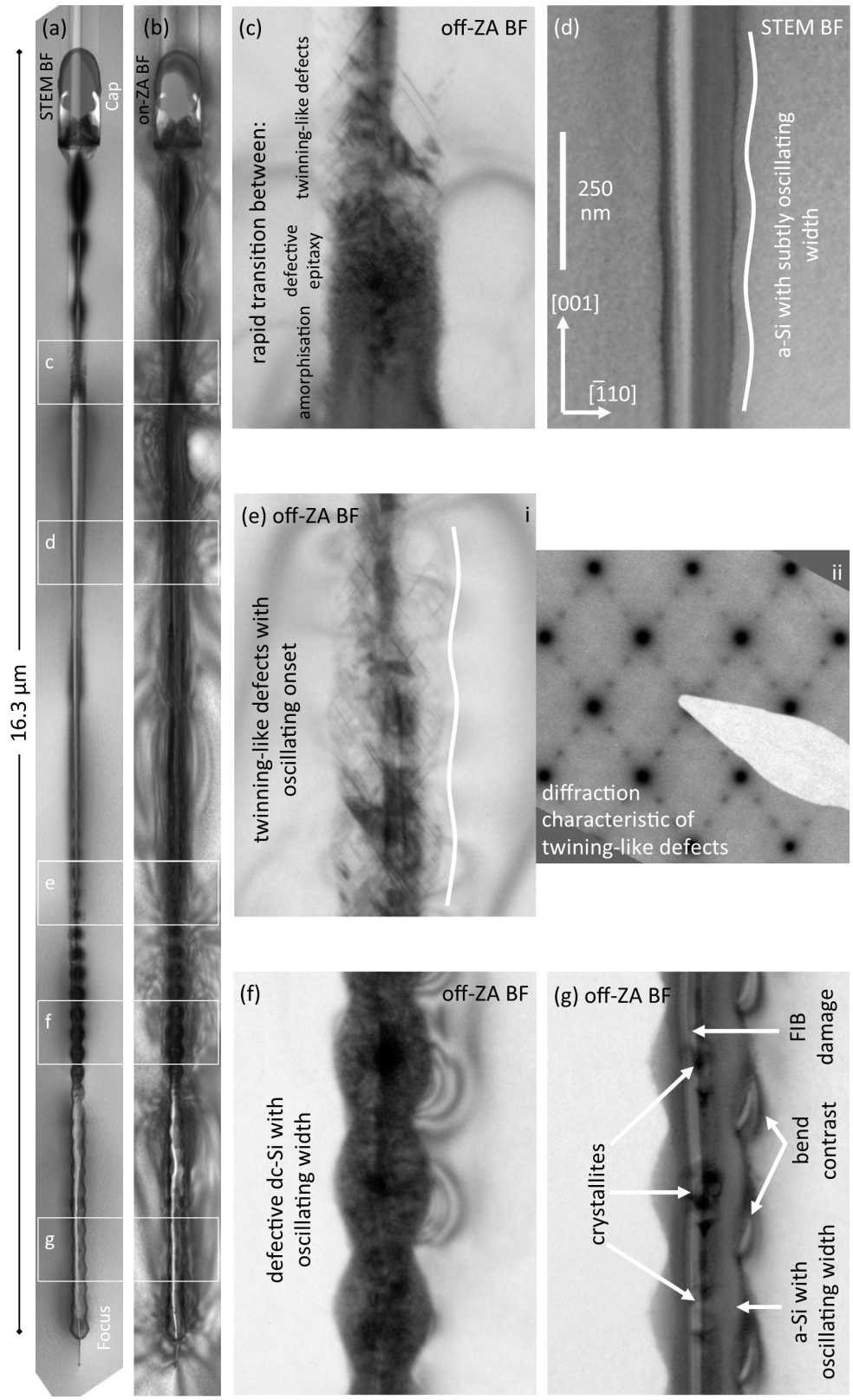

Figure 8.2: TEM results from a long axis cross-section of a low energy modification. The entire modification is shown in a STEM BF image, (a), and a conventional BF, (b), where the focus end is at the bottom and the cap is at the top of the images. The labelled regions in (a-b) are shown in greater detail, (c-g), at the scale shown in (d). Annotation corrected.

along the entire modification's length until the cap, which is the widest point. This is a notable difference to standard isolated modifications where the constant diameter region, below the cap, was the widest region.

Considering the features in greater depth now, starting from focus, oscillations in the width of the core are evident. These have a measured period of $247 \pm 24\ nm$, which is within uncertainty of the $226 \pm 30\ nm$ period in standard isolated modifications. The oscillation amplitude is, however, notably more pronounced. In (g) the oscillating core is largely a-Si, but with crystallites at the centre of the modifications, mostly where the a-Si width is largest. Further up the modification the oscillations continue, but the core is now highly defective, as shown in (f). This corresponds to the region of compressive strain in the Raman map image, Fig. 8.1 (a). Further up the modification, the defective region transitions into a region of twinning-like defects, shown in Fig. 8.2 (e)(i) with the corresponding SADP in (e)(ii). Interestingly, even the onset of the twinning-like region appears to have an oscillating width. Furthermore, the oscillation amplitude appears to be near constant through all these sections. Although, because the width of the original molten region is increasing, the onset of the oscillating core is occurring later during solidification further up the modification. Nearest to focus the maximum extent of the a-Si is thought to be approximately equal to the melt width.

The initial set of oscillations shown in (e-g) transition above (e) to a second set of oscillations (d). This second set initially also consists of an a-Si core but with a much smaller width and less pronounced oscillations. The width of the a-Si increases further along the modification and by the position of (d) is comparable to the width near focus. At the top of this set of oscillations solidification by amorphisation rapidly transitions to defective epitaxy and then to twinning-like defects as shown in (c).

Beyond these two sets of oscillations in the core only a line of defects (the product of colliding solidification interfaces, rather than transitions in solidification behaviour) and bend contrast can be found until reaching the cap. The cap contains a remanent void(s) and a-Si among other features and will be considered further below.

The range of morphologies (below the cap) observed in the long axis can also be found in the short axis cross-sections and are presented in Fig. 8.3. The cross-section shown in (a) consists of lines of defects from colliding solidification interfaces, defects from defective epitaxy and an a-Si shell encapsulating a polycrystalline core. This is the expected structure near focus under conditions of strong radial thermal gradients. Weaker thermal gradients allow for an a-Si core, as shown in (b). In (c) many defects are present due to rapid, low quality epitaxy. Interestingly the defective epitaxy is not restricted to the core of the modification. Under conditions of weaker thermal gradients, such as the region just below the cap, the morphology consists only of a line of defects as is shown in (d).

As the lateral lines of defects in long axis cross-sections correspond to the horizontal lines of defects in short axis cross-sections, it is to be expected that no horizontal lines are present in Fig. 8.3. Nevertheless, from the available results it is possible to state that the short axis melt shape is approximately oval shaped, with a height roughly twice that of the width. It is for this reason that the morphology is notably less symmetric compared with standard isolated modifications.

One further point of interest in the short axis morphology can be found when considering the next example, Fig. 8.4, which is of particular interest for density-related reasons. The morphology consists of an a-Si shell that encapsulates a bc8-Si core. Notably, the a-Si periphery has better defined facets than Fig. 8.3 (a) or (b). This demonstrates that the orientation of epitaxial solidification is comparable to standard isolated modifications, with the exception of solidification not occurring along the [220] and $[\overline{2}\overline{2}0]$ directions.

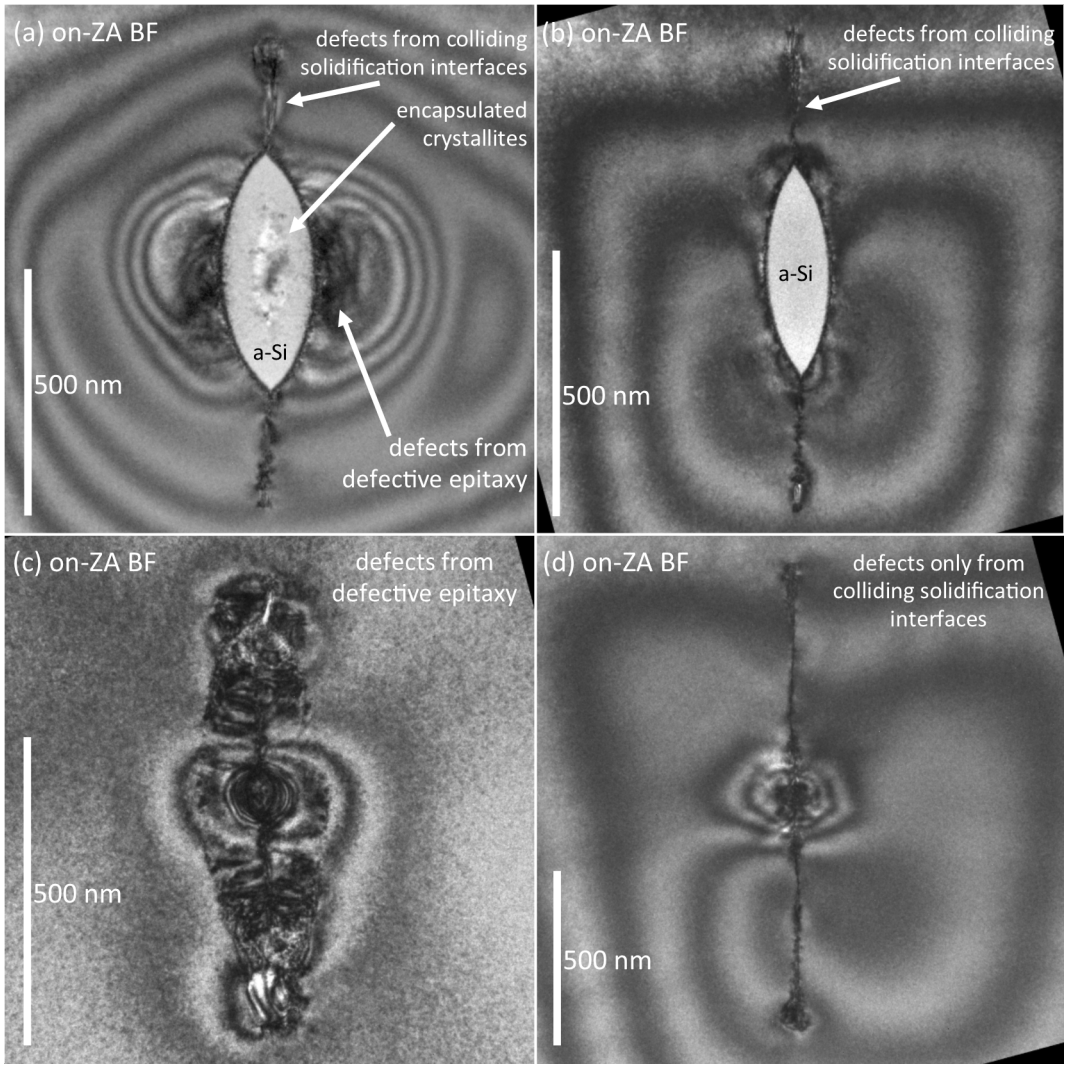

Figure 8.3: TEM images from short axis cross-sections of low energy modifications showing a range of thermal-gradient-dependent morphologies. Strong thermal gradients result in (a), an a-Si shell, polycrystalline core structure. Weaker thermal gradients result in an a-Si core as in (b). Weaker thermal gradients again result in a defective Si structure, (c). The weakest thermal gradients observed result in a line of defects, as in (d), due to colliding solidification interfaces.

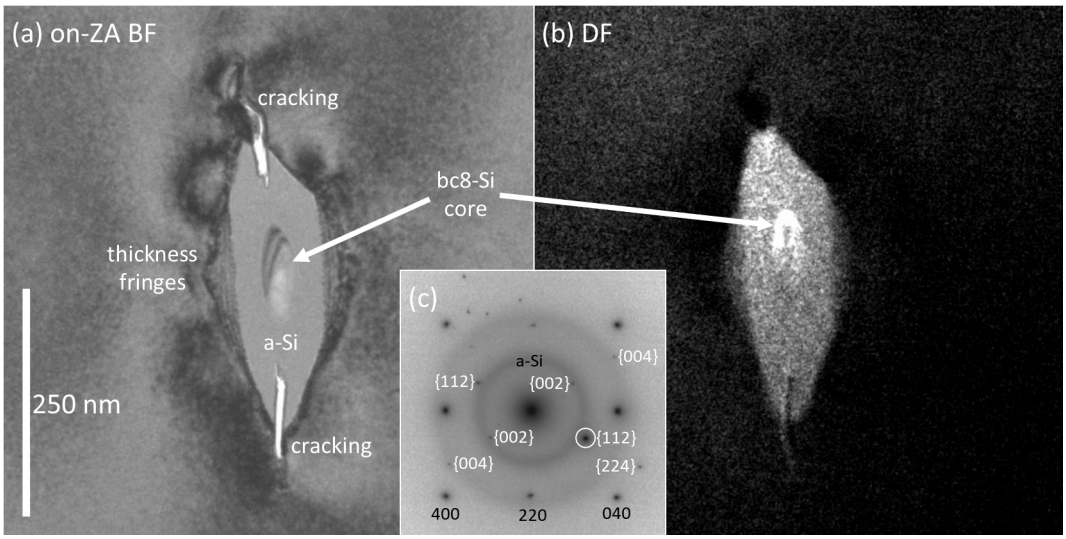

Figure 8.4: TEM results from the short axis cross-section of a low energy modification that features an a-Si shell encapsulating a high density crystalline allotrope (bc8-Si) at the core. In (a) the BF image is shown, which is additionally notable for the faceted periphery of the a-Si. A DF image of one of the bc8-Si crystals is shown, to scale, in (b) and was recorded using the circled diffraction spot in the SADP, (c). The white labels in (c) correspond to bc8-Si, while the black labels correspond to a-Si and dc-Si.

A DF image of one of the bc8-Si crystals in the core is shown in Fig. 8.4 (b) which is created using the {112} bc8-Si diffraction spot circled in the SADP, (c). As this spot essentially overlaps the a-Si ring, the a-Si is also bright in the DF image. The SADP also contains several other bc8-Si diffraction spots, some of which are labelled in white, while some of the dc-Si diffraction spots are labelled in black.

The cap is also of interest for density-related reasons. Results from a long axis cross-section are shown in Fig. 8.5. The entire cap is shown in (a). The top of the cap is largely a-Si, although thickness fringes are also visible in the image. Midway down the cap residual voids can be seen on either side. The bottom of the cap has a roughly diamond shaped region which contains polycrystalline material, twinning-like defects as well as other crystalline defects. It is shown under different imaging conditions in (c) which make some of these defects more visible. The SADP (b) is collected near the top of the diamond region and shows rings from a-Si as well as spots from polycrystallites. The SADP (d) is collected nearer the bottom and contains spots consistent with twinning-like defects.

The cap has also been examined in short axis cross-sections, of which several results are shown in Fig. 8.6. The first image and corresponding SADP, (a-b) respectively, are from higher in the cap where the morphology consists only of a-Si and the remanent void. Slightly further down the SADP and image, (c-d) respectively, additionally show evidence of polycrystallinity.

Within the highly defective region the morphology is drastically more chaotic as shown in Fig. 8.7. The first image, (a), is recorded on the [001] ZA and shows open volumes between the original melt periphery and the material within the cap. This material, other than a small amount of a-Si, is highly defective and also appears to feature lines of defects from colliding solidification interfaces. The corresponding SADP, (b), likely has diffraction spots related to twinning-like defects and double diffraction. Tilting to the [101] ZA, (c), results in a more easily interpretable SADP with spots characteristic of twinning-like defects. The circled spots were used to create the DF image, (d), where several bright twinning-like defect streaks are visible.

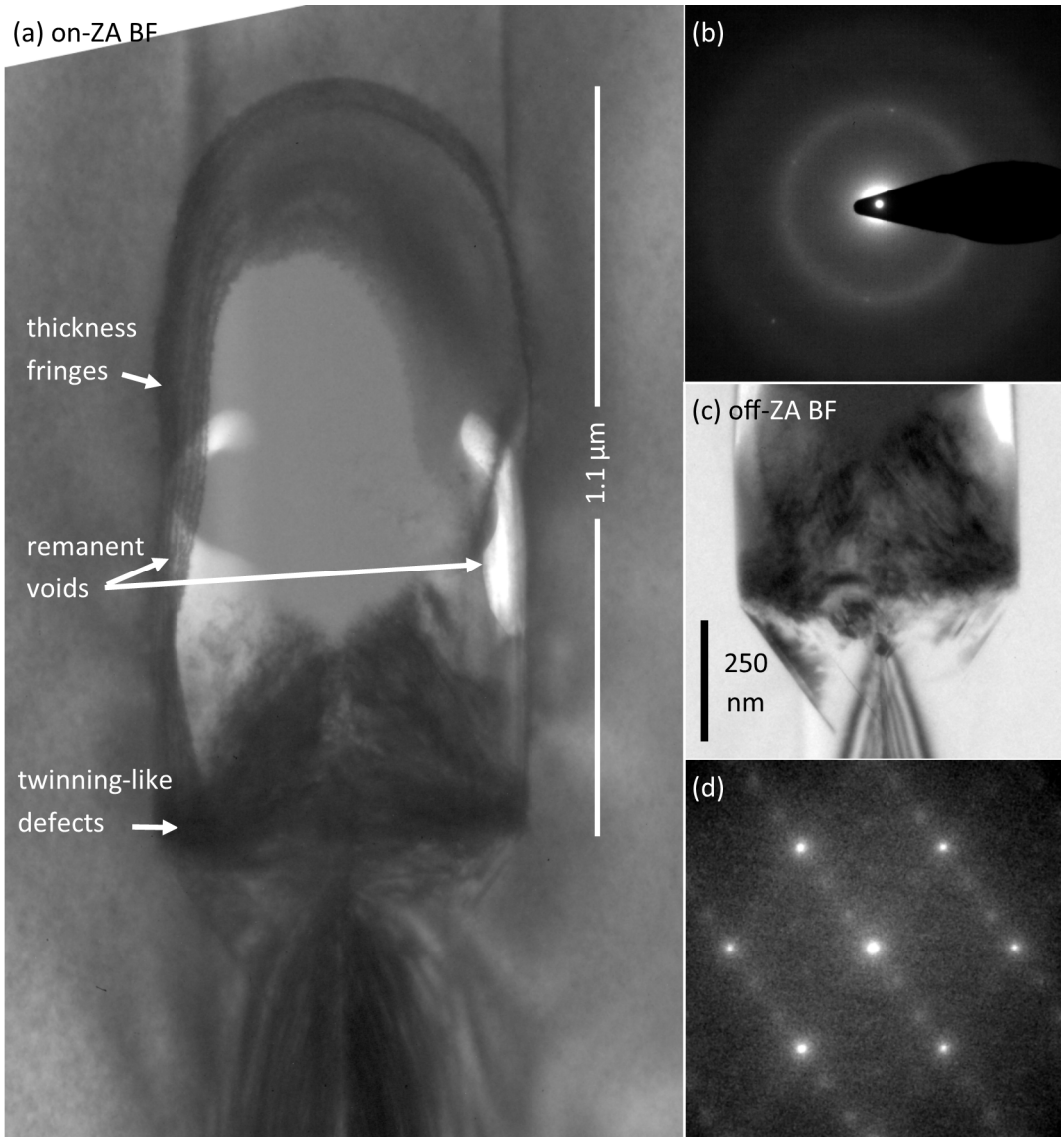

Figure 8.5: TEM results of the cap region of a long axis cross-section of a low energy modification. In (a) the entire cap is shown to principally consist of a-Si, but that remanent voids are also present, as is a region of defects, including twinning-like defects, at the base at of the cap. An SADP recorded from a region primarily consisting of a-Si, but also containing crystallites is shown in (b). In (c) the defective region is shown under different imaging conditions where some of the twinning-like defects are more obvious. The corresponding SADP, (d), contains diffraction spots characteristic of twinning-like defects.

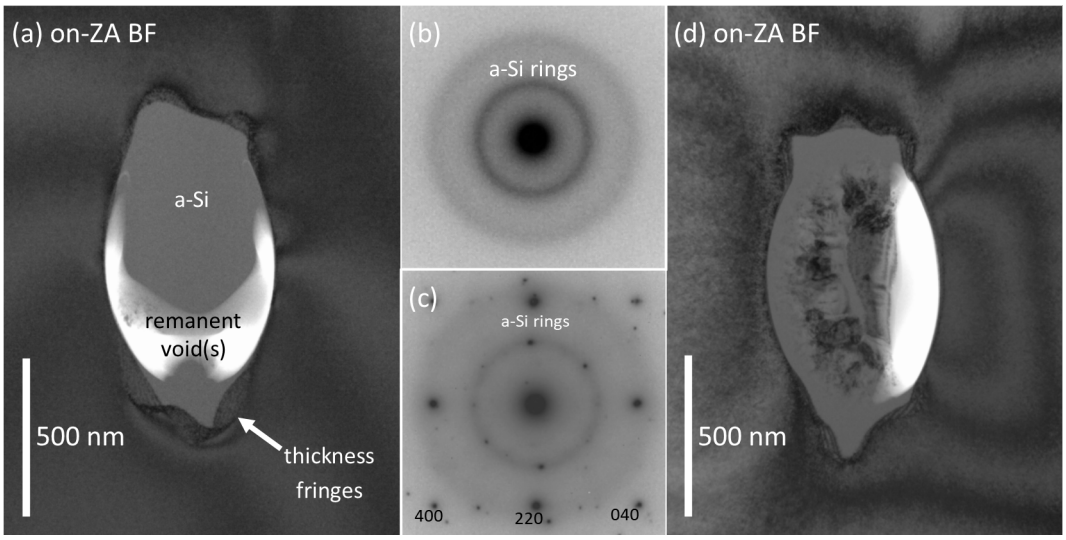

Figure 8.6: TEM results from short axis cross-sections of the cap in different low energy modifications. A cross-section of the upper portion of a cap contains only a-Si and the remanent void as shown in the image and corresponding SADP, (a-b). A cross-section from further down in another cap additionally contains polycrystallites as shown in the SADP and image, (c-d).

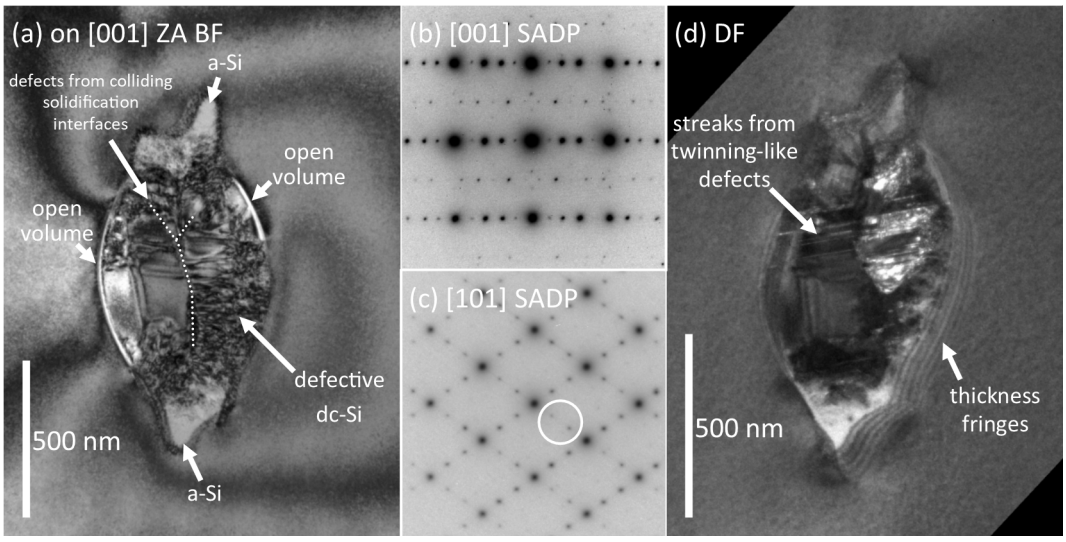

Figure 8.7: TEM results from a short axis cross-section of the region of twinning-like defects in the cap in a low energy modification. In (a) the general features are shown, but the twinning-like defects are not obvious on this zone axis. The corresponding SADP, (b), features double diffraction effects. Tilting the sample to a different zone axis results in a SADP that is characteristic of twinning-like defects, (c). The circled diffraction spots were used to create the corresponding DF in (d), where twinning-like defect streaks are visible.

8.3 Discussion

The discussion of these results will follow a similar order to that of the standard isolated modifications; solidification from the perspective of the short axis, solidification from the perspective of the long axis, the formation and evolution of the void and the mechanisms by which the displaced mass is accommodated in high density regions.

8.3.1 Solidification from the perspective of the short axis

From the perspective of short axis cross-sections of low energy modification's, solidification is largely equivalent to that of standard modifications. Solidification was observed to be clearly occurring along multiple crystal orientations simultaneously and thermal-gradient-dependent transitions in solidification behaviour were occurring. However, the morphology suggests that the melt shape is oval, rather than circular as in the standard isolated modifications. This is thought to be caused by the same asymmetry in the laser that was suggested to lead to much more subtle asymmetry in the standard isolated modifications. Several potential factors may explain the stronger influence of the asymmetry in the low energy modifications, as discussed below.

One factor that may explain the stronger asymmetry is that the laser asymmetry itself may be stronger. The laser power was controlled by a cross polarisation based filtering method. It is conceivable that such a method could induce or lead to inhomogeneity in the spatial distribution of the laser energy and thus, on the shape of the laser-induced melt. Since greater filtering was applied when creating the low energy modifications, it is conceivable that more asymmetry in the laser was also induced.

The second factor concerns the energy of the laser pulse. Being less powerful, but having the same pulse duration, the rate at which material melted in the low energy modifications must have been slower than for standard isolated modifications. Simultaneously, the smaller sizes dictates faster solidification times. Collectively, this allows for less time for the temperature around the molten region to equilibrate, thus rounding out the melt profile. This explanation is reinforced by the fact that the asymmetry in standard isolated modifications was stronger near focus, where solidification was fastest and thus, this was also a condition where less time was available for temperatures to equilibrate.

8.3.2 Solidification from the perspective of the long axis

As with the short axis cross-sections, the long axis cross-sections of low energy modifications share many features with standard isolated modifications. However, the manifestation of some of these features does at times notably differ.

One of the features that is present in both low energy and standard modifications, but differs slightly in manifestation is the oscillations in core width of the modifications. The oscillations were previously explained by the thermally-favoured solidification interface shape being approximated by energetically-favoured facets, separated by steps. It follows that the stronger oscillations near focus in low energy modifications must be the result of a greater step amplitude. Indeed, although difficult to examine in low energy modifications, the melt width does appear to increase $\sim$ 15 % faster in the low energy modifications compared with standard isolated modifications. This would then require larger steps between the facets and hence, stronger oscillations. Further from focus, in the second set of oscillations in the low energy modifications the oscillations are weaker, suggesting the energetically-favoured interface and thermally-favoured interface are more closely aligned.

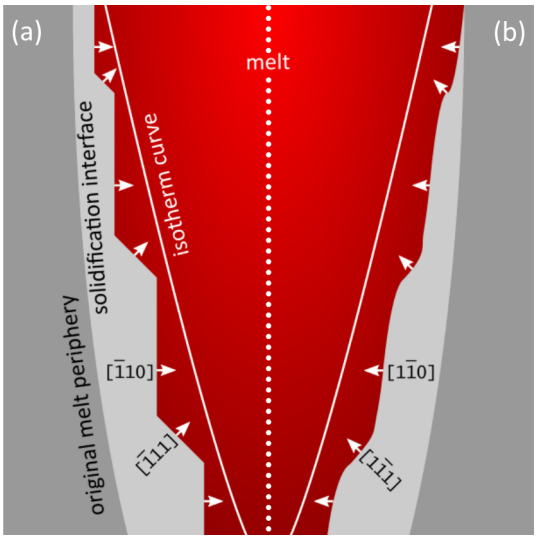

Figure 8.8: A schematic of the solidification interface from the perspective of the long axis in a low energy modification. A large step amplitude between {110} facets likely allows for small {111} facets to form, which in turn allow twinning-like defects to form. A simplified example is shown on the left in (a), and a more realistic curved interface is shown on the right in (b).

An additional second order effect may also contribute to the stronger oscillations in the low energy modifications. This concerns the thermal conductivity of a-Si, which has already been established to be significantly less than that of dc-Si. It follows that during solidification, the onset of amorphisation in one portion of the solidification interface will slow cooling in the neighbouring, still crystallising regions. This further delays the transition to amorphisation in the neighbouring regions. Furthermore, the latent heat of solidification is also less for a-Si compared with dc-Si. Thus, this too will slow the cooling rate along a crystallising portion of the solidification interface, relative to an amorphising portion. Given this explanation, it is interesting to compare Fig. 8.2 (g) with (e)(i). The oscillating core of the former is principally a-Si, while the latter is principally twinning-like defects. Notice that the oscillations are weaker in the twinning-like defects region, presumably because the second order, a-Si-dependent effects are not relevant to twinning-like defects. Although, being further from focus, the step amplitude is likely also smaller in the twinning-like defects region.

The nature of this twinning-like defects region warrants further discussion. Twinning-like defects in standard isolated modifications were observed in conditions of atypical solidification, likely solidification along ⟨111⟩ directions. The same fundamental explanation is likely valid in low energy modifications. However, in Fig. 8.2 (e) the cause of the ⟨111⟩ epitaxy is thought to be the presence of smooth, high amplitude steps between the {110} facets on the solidification interface. Inevitably, a portion of each step will be aligned with the {111} facet orientation. This is shown schematically in Fig. 8.8, where (a) is a simplified case and (b) is a case with more realistic rounding between the facets. With non-negligible {111} facets, it is plausible that ⟨111⟩ epitaxy will occur, creating the twinning-like defects that can be seen in the sample. This also explains the oscillating width at the onset of the twinning-like defects.

The transition between the first and second sets of oscillating features at the core is accompanied by a significant decrease in both the width of the features (a-Si) and the oscillation amplitude. Nevertheless, the average width in the a-Si of the second region of oscillating features increases as the distance from focus also increases. This suggests that the transition between the two sets was a product of a solidification perturbation, rather than because the radial ther-

mal gradients had weakened near the transition. It also suggests that the energetically and thermally-favoured solidification interface are more closely aligned in the second set, hence the smaller oscillations.

8.3.3 The cap and voids in low energy modifications

In low energy modifications only the cap contains evidence of a void(s), suggesting either that only one void forms, or that multiple voids coalesce. It further suggests that the cap is a favourable position for the void. That a singular void is present after melting is arguably consistent with standard isolated modifications given the smaller size of the low energy modifications (with a 15.5 ± 0.8 μm length). In standard isolated modifications only one, if any, voids would be expected within a distance of 15 μm from focus and the distance between voids would typically exceed this length. Furthermore, the melt volume is 6.0 ± 0.1 μm^{-3} in low energy modifications which is smaller than that for a similar length of the standard isolated modifications. Thus, collectively, only a single void would be expected in a low energy modification based on size considerations.

Timing considerations in a low energy modification are also more favourable towards a singular void. Given equal laser pulse durations, the rate at which a given volume melts in the low energy modifications must be slower. It follows that more time is available within a given volume for movement of material to respond to densification upon melting. In other words, it is easy for either one void to form, or for multiple voids to coalesce in a low energy modification.

The position of the void(s) is also an interesting topic. It seems implausible that the cap, furthest from focus where melting is initiated, would be the location that a void would first form. It follows that regardless of where the void forms, it must be beneficial for the void to move to the cap. A likely explanation is the minimisation of interfacial free energy. As the cap is the widest region, the aspect ratio (and therefore the interfacial area and energy) of the void can be minimised if it is in the cap. Indeed, this explanation can be reinforced by considering the void volume quantitatively. Given the total modification volume, the void volume (while the Si is molten) is expected to be $\sim 0.60 \pm 0.01$ μm^{-3}. Taking the average (short axis) cross-sectional area of the cap this would result in a void length of 1.15 ± 0.11 μm, which matches excellently with the actual length of the cap in Fig. 8.5 (a). Thus, assuming all the material in the cap flows in during solidification, as will be argued below, the entire volume of the void while the Si is molten can be accounted for in a morphology that minimises the interfacial free energy.

As for the cap morphology, the large quantities of a-Si are suggestive of rapid cooling and amorphisation during solidification. However, based on the modelling, Chapter 1 Fig. 1.6 (a), and excluding the influence of vertical thermal gradients, the top of the modification is expected to have the weakest thermal gradients. Instead, the thermal gradients in the cap are suggested to be the result of molten Si entering a void from below and contacting the already significantly cooled periphery of the void. In detail, the expansion of Si below the void as it solidifies applies pressure to the remaining melt at the centre of the modification. This pressure can be relieved by flow of the molten Si into the void, where it comes in contact with the already cooled periphery of the void. The injected material therefore cools rapidly resulting is amorphisation during solidification, which principally occurs from the top of the cap downwards. As the volume of a-Si increases, it increasingly insulates the remaining melt below it, allowing for a return to crystal growth and thus, the formation of the crystals encapsulated in a-Si observed in Fig. 8.6 (d). Slightly further down the cap the thermal gradients are more modest, and the radial and vertical thermal gradients are likely comparable. As such, defective epitaxy may occur, very likely along atypical directions including along $\langle 111 \rangle$ orientations given the presence

of twinning-like defects at the bottom of the cap.

It is noteworthy that the underlying processes invoked in explaining the cap morphology of the low energy modifications are largely equivalent to those used to explain the voids in the standard isolated modifications. The only principal difference is that the voids exist at the top of the low energy modifications where the void's interfacial free energy can be minimised. As standard isolated modifications consist of multiple smaller voids (relative to the melt diameter) the voids are less subject to the influence of interfacial free energy minimisation. Rather, their position was likely a result of kinetic factors when they formed. It is, however, interesting to consider the capillary-related influence, which is also a result of interfacial free energy, and results in elongation of voids near focus in standard isolated modifications.

8.3.4 Elevated density in low energy modifications

As with standard isolated modifications, remanent voids remained in the low energy modifications after solidification. In this case the remanent void volume is estimated to be $0.03 \pm 0.01\ \mu m^{-3}$. Again, this displaced material must be accommodated in high density regions elsewhere in the modification and the same mechanisms are of relevance, compressed dc-Si, high density crystalline allotropes and high density a-Si.

Compressed dc-Si was observed with Raman spectroscopy, Fig. 8.1 (a), in a region near, but above focus. The corresponding region in the TEM images of the long axis cross-section, Fig. 8.2 (f), consists of a highly defective core, with an oscillating periphery. Clearly the displaced material in this region has resulted in compressive strain which has led to defective epitaxy, not unlike the constant diameter region of standard isolated modifications.

The second mechanism listed, high density crystalline allotropes was also observed, but only in TEM, Fig. 8.4, where bc8-Si was found. These crystallites encapsulated in a-Si appear to only be present near focus, largely below the region of compressed dc-Si, based upon the long axis cross-section, Fig. 8.2. It is notable that no bc8-Si was observed in low energy modifications that was caused by the trapping of melt between colliding solidification interfaces. Presumably such an occurrence is less likely in low energy modifications because solidification interface collisions are less prevalent due to the melt asymmetry. Nevertheless, the occurrence of bc8-Si in low energy modifications is similar to standard isolated modifications.

The final mechanism, high density a-Si, is difficult to directly address as no further EELS measurements were performed on low energy modifications. Nevertheless, given that a large amount of a-Si is present in low energy modifications, this mechanism should be considered to be just as plausible as it is in standard isolated modifications.

Considering these features macroscopically, all are present near focus. The a-Si is also present along much of the modification's length and even in the cap. However, because of the void in the cap, the ability for Si to expand during solidification is greatest near the top of the modification. This suggests that the material displaced by the remanent void is essentially trapped nearer to focus due to rapid solidification and the inability to transport the excess material back to the void at the other end of the modification. This is an interesting contrast to standard isolated modifications where density-related features are scattered throughout the modification. Only compressive strain in the constant diameter region is consistently positioned, specifically in the constant diameter region. This difference is merely a consequence of the specific conditions relevant to each modification, rather than a reflection of fundamental differences in the underlying processes.

It is also worth considering whether the material displaced by the remanent void can be accounted for quantitatively. However, two-dimensional TEM images only allow for estimates

of the volume of the various high density regions of the low energy modifications. Similarly, it isn't known what the density of any given region is. Instead, a series of scenarios will be forwarded that test both the realistic densities for various high density components, and the maximum density these high density components could be. The outcome of these scenario's will allow for some limits to be placed on the contribution each high density component has towards accommodating the mass displaced by the remanent void.

The first scenario will consider whether the displaced mass can be accommodated without invoking high density a-Si. All the crystallites near focus in Fig. 8.2 will be assumed to be bc8-Si with a density ~ 10 % higher than dc-Si. The region of compressed dc-Si, Fig. 8.1 (a), will be assumed to be uniformly compressively strained by ~ 1 % out to the maximum melt limits in this region. Note that both these assumptions are extreme. Nevertheless, this scenario can only account for 0.016 ± 0.005 μm^{-3} of the 0.03 ± 0.01 μm^{-3} remanent void volume. While technically within uncertainty of each other, the need to invoke such extreme assumptions suggests that some high density a-Si is needed to account for the remanent voids volume.

For the next scenario a more realistic one third of crystallites near focus will be assumed to be bc8-Si, but the a-Si in the first set of oscillations, near focus, will be unrealistically assumed to be ~ 10 % higher density than dc-Si. The compressed dc-Si will be as it was in the last scenario. This scenario can account for 0.015 ± 0.005 μm^{-3} of the remanent void volume. Again, technically within uncertainty of the measured volume, but it again required extreme assumptions.

For the final scenario the density of the a-Si near focus will be reduced to be more realistic, ~ 2 % higher density than dc-Si. The a-Si in the second set of oscillations will be set to be ~ 1 % more dense than dc-Si. This scenario can account for 0.014 ± 0.006 μm^{-3} of the remanent void volume which is just within uncertainty of the measured volume. This is a more realistic condition than the above scenarios and suggests that high density crystalline allotropes and compressed dc-Si account for most of the extra mass but a-Si at a modestly elevated density must also be present.

8.4 Summary

In this chapter the morphology of modifications produced with a reduced energy, 0.6 μJ, were presented, explained and contrasted with standard modifications produced with a 2 μJ pulse energy. Most underlying processes that lead to the final morphology were similar between the two conditions, but some aspects differed significantly. These differences can mostly be related to the smaller size of the low energy modifications. As the pulse duration of the laser used to create the modifications remains the same, the smaller modification size implies that the growth of the molten volume is slow in the low energy modifications.

The combined influence of smaller modification volume and slower melt growth ensure that in low energy modifications only a single void is present after the modification melts. This single void is large relative to the cross-sectional area of the melt, meaning that minimisation of interfacial free energy is of greater importance, relative to the voids in standard isolated modifications. The void therefore moves to the widest region of the modification, the cap, where the void's aspect ratio can be minimised. It is noteworthy that the cap volume matches well with the expected volume of the void while the Si is molten.

During solidification the expansion of the Si below the void drives molten Si from the centre of the modification upwards, refilling the void from below. This molten Si contacts the outer periphery of the void where it encounters strong thermal gradients and consequently amorphises during solidification, largely from the top down. However, near the bottom of the cap the ther-

mal insulation provided by the a-Si results in shallower thermal gradients allowing crystallites to form. Subsequently, more modest cooling both radially and vertically allows for atypical solidification to occur. This results in many defects, including twinning-like defects which are suggestive of ⟨111⟩ epitaxy. The refilling process is, however, partial, and a remanent void remains, indicating that the displaced mass must be accommodated in a high density region elsewhere in the modification. This entire process is very similar to the refilling of voids in standard isolated modifications. The differences, where they exist, are easily explained by the particulars of the low energy modifications.

The displaced mass does not appear near the void at the top of the modification as the refilling process provides a mechanism for the molten Si to expand during solidification. Instead, features consistent with an elevated density are found close to focus, trapped by rapid solidification. The same three mechanisms raised when considering standard isolated modifications are relevant to low energy modifications; bc8/r8-Si, high density a-Si and compressed dc-Si. Interestingly, the simpler morphology of the low energy modifications allows for some limited attempts to quantise these components. These attempts suggest that bc8/r8-Si and compressed dc-Si are the dominant mechanisms by which the displaced mass is accommodated. However, a-Si must also exist with a modest density elevation relative to uncompressed dc-Si.

TEM examination of the short axis cross-sections of low energy modifications show similar morphology to standard isolated modifications, with the exception that the melt periphery appears to highly asymmetric. This is thought to originate in an asymmetry in the spacial distribution of the laser energy. Otherwise, solidification is equivalent, with epitaxy occurring mostly along ⟨100⟩ and ⟨110⟩ orientations. Neighbouring interfaces often intersect smoothly, but sometimes collide, resulting in a line of defects. The same transitions in solidification behaviour are also observed; perfect epitaxy, defective epitaxy, amorphisation and insulation-induced return to crystal growth. In some cases bc8-Si is observed at the centre of the modification, encapsulated in a-Si as was observed in standard isolated modifications

TEM examination of the long axis cross-sections shows equivalent features to those observed on the short axis. Additional interesting features include stronger oscillations in the width of the core of the modifications when compared with standard isolated modifications. This is thought to be the result of larger steps between the facets that collectively approximate the thermally-favoured solidification interface shape. The larger steps are required as the cross-sectional area of the melt appears to grow faster in low energy modifications than for standard isolated modifications. However, the oscillations may well be reinforced by second order effects relating to the differing thermal conductivity and latent heat of a-Si relative to dc-Si.

The larger steps also seem to lead to non-negligible portions of the step aligning with ⟨111⟩ crystal orientations. This may allow for epitaxial solidification along this orientation, resulting in substantial twinning-like defects which is far more prevalent than the instances of twinning-like defects in standard isolated modifications.

Compressively strained dc-Si was observed to lead to defective epitaxial solidification, similar to the constant diameter region in standard isolated modifications. In low energy modifications this defective epitaxy occurred nearer to focus as faster solidification traps excess mass before it is concentrated to the same extent as in standard modifications.

Chapter 9

Near-bandgap modifications

As with the previous chapter, this chapter will examine modifications created under different laser conditions to the standard sub-bandgap regime modifications. More specifically, this chapter will examine modifications produced in the near-bandgap regime, which makes use of a laser with a higher pulse energy, shorter wavelength and much longer pulse durations. It will be shown that the resultant modifications are smaller than the standard sub-bandgap regime modifications, indicating this process is less efficient both from the perspective of the volume melted per unit energy, and per unit time. This has important implications for the results that follow.

Modifications in this regime were produced with a 2 μm separation in samples that have been cleaved. This is not ideal as it does not allow the cleaved results to be compared with isolated modifications and uncleaved but closely spaced modifications produced in the same near-bandgap regime. Furthermore, although presented last, these samples were the first examined in this work at a time when the experimental methodology was less refined. As such there are several important features that were not investigated thoroughly and are not understood to the same depth as equivalent features in the sub-bandgap regime. Nevertheless, many features can be understood and related to the sub-bandgap regime modifications.

The chapter will begin with a short experimental section, followed by the results and then the discussion. The discussion will first consider the role of density in these modifications, then the solidification-related morphology will be discussed, followed by the cracking and dicing behaviour. The last section of the discussion will relate the modifications in this work to modifications in the literature that were produced in the same regime, but with slightly different laser conditions.

9.1 Experimental

This chapter examines cleaved, closely spaced modifications created in the near-bandgap regime, specifically with 1064 nm, 220 ns, 4 μJ laser pulses. These conditions differ significantly to the modifications shown previously in this work, but are substantially closer to those in the literature.

The cleaved surface was imaged with SEM to examine the surface topography. Raman spectroscopy was also performed directly on the cleaved surface. Due to the surface roughness, useful Raman map images could not be collected and only point measurements will be considered here.

Short axis TEM cross-sections were prepared from the cleaved surface using FIB milling in the ex-situ liftout geometry. As the modifications are closely spaced and the samples are cleaved, no long axis cross-sections were successfully prepared.

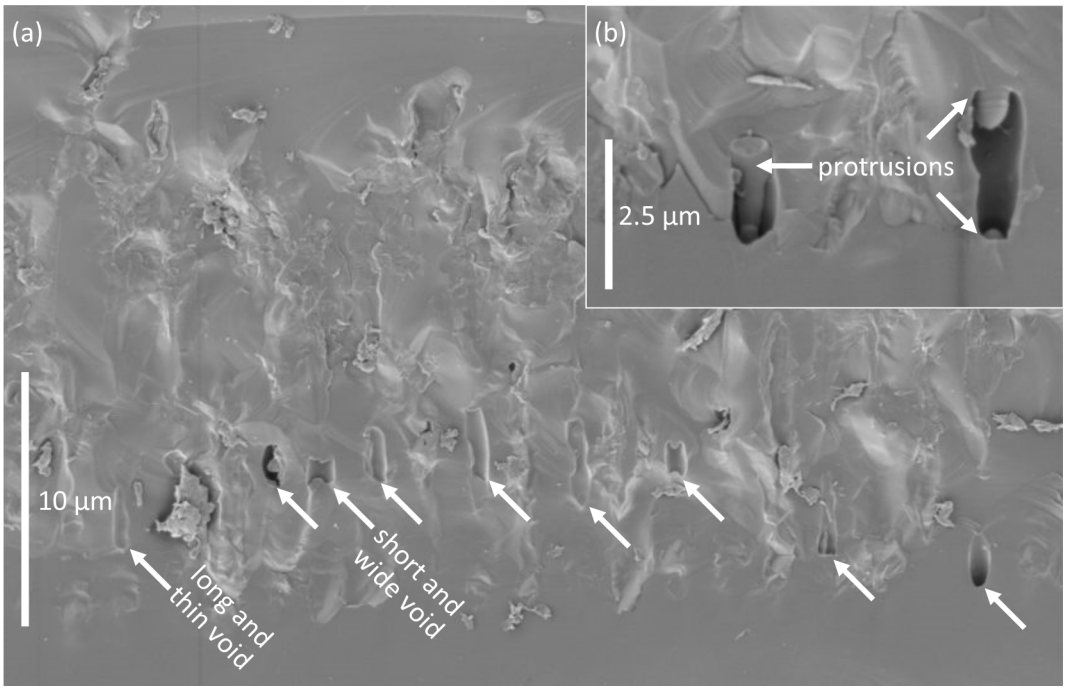

Figure 9.1: SEM images of the near-bandgap modifications on the cleaved surface. In (a) the full length of the modification is shown with focus on the bottom. Remanent voids, marked with arrows, are visible in most modifications. Closer examination of the voids, (b), reveals that many voids contain protrusions.

9.2 Results

Examining the surface exposed by cleaving near-bandgap modifications with SEM yields the results shown in Fig. 9.1. In this image the focus end of the modifications are shown on the bottom and individual modifications can mostly be delineated due to the presence of a single remanent void, marked with arrows, for each modification. The remanent void's position typically seems to shift gradually, modification to modification, within the first third of the modification's length. The modified area is otherwise chaotic and is rougher than the cleaved surface in the sub-bandgap regime modifications. The near-bandgap modifications are also notably shorter, with an estimated length of $18.9 \pm 0.6\ \mu m$. In conjunction with measurements from short axis cross-sections, the modification's total volume is estimated to be $18.2 \pm 3.1\ \mu m^3$. In addition, the cross-sectional area near focus is smaller than that far from focus. However, it does appear that the modification's diameter varies less over the length of the modification compared with any of the sub-bandgap regime modifications.

Considering the remanent voids more closely, several features are noteworthy. The remanent void volume is large. It is estimated to be $0.6 \pm 0.3\ \mu m^3$ which is one third of the melt volume of the void ($1.8 \pm 0.3\ \mu m^3$) and much larger than the remanent voids in the sub-bandgap regime. From a shape perspective the remanent voids vary between being long and thin, and being short and wide. In fact, the widest remanent voids are of comparable width to the estimated average melt diameter, $1.1 \pm 0.2\ \mu m$. The longest remanent voids are of comparable length to the expected void length in the melt, $1.9 \pm 0.5\ \mu m$, assuming the void's diameter in the melt matches the average melt diameter. Within the remanent voids, protrusions from the top and bottom are visible, as shown in Fig. 9.1 (b). In some instances the protrusions appear to meet midway along the length of the remanent void.

The remanent voids can also be examined with TEM of short axis cross-sections, the first

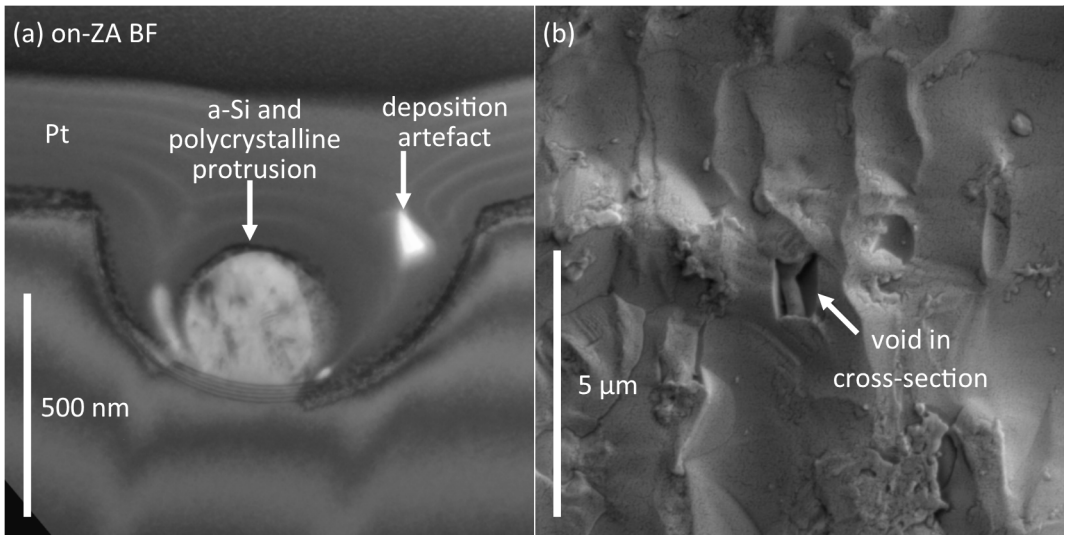

Figure 9.2: TEM, (a), and SEM, (b), of a remanent void containing a protrusion which is largely a-Si, but also contains small crystallites.

result of which is shown in Fig. 9.2 (a), from the void indicated in the SEM image, (b). The SEM image shows the presence of protrusions from both the top and bottom of the void, which have met midway. The TEM results reveal the protrusion to be a mixture of a-Si and polycrystalline Si. No defects are visible outside the periphery of the void. A second result is an example of a long and skinny void and is shown in Fig. 9.3 (a), which is the void indicated in the SEM image (b). In this case the SEM image was recorded with the sample tilted and after some Pt had already been deposited. The void, however, was not fully filled by Pt during the FIB sample preparation process, hence an unfilled region is visible in the TEM image. Within the original periphery of the void is a mixture of a-Si and polycrystalline Si. There are a few visible defect outside the void periphery. These defects are presumably the result of colliding epitaxial solidification interfaces.

In addition to low density features, elevated density regions were observed in the near-bandgap regime modifications. Figure 9.4 (a) is a Raman spectrum recorded from the cleaved surface which contains the peaks associated with bc8-Si and r8-Si. Several TEM cross-sections also contain evidence of non-dc-Si crystallites. A BF image of one such case is shown in (b), with a corresponding DF image in (c) which contains at least two non-dc-Si crystals. The morphology otherwise consists of a dc-Si core surrounded by a largely a-Si shell that has a rounded outer periphery. Defect lines surround this shell. Bend contrast is also evident in many cross-sections which is suggestive of compressive strain.

Considering the cross-section morphology more generally now, Fig. 9.5 contains images of three different structures. The modification in (a) features an a-Si core with a faceted periphery surrounded by highly defective dc-Si which also appears to have a subtle facets on its periphery. Aligned with the intersection of several facets are what appear to be cracks overlapping lines of defects. It is likely that these cracks extend beyond the original melt periphery of the modification. The modification in (b) consists of a highly defective dc-Si core, again with subtle facets to its periphery, as well as lines of defects. At least one of the lines of defects overlaps a crack which in this case definitely extends beyond the melt periphery. It is also notable that the cleaving path has bypassed the core of this modification. The last example, (c), has an ill-defined core surrounded by defective dc-Si with a rounded periphery. It is not clear if any distinct lines of defects are present. Below the modification is contrast from a long crack that

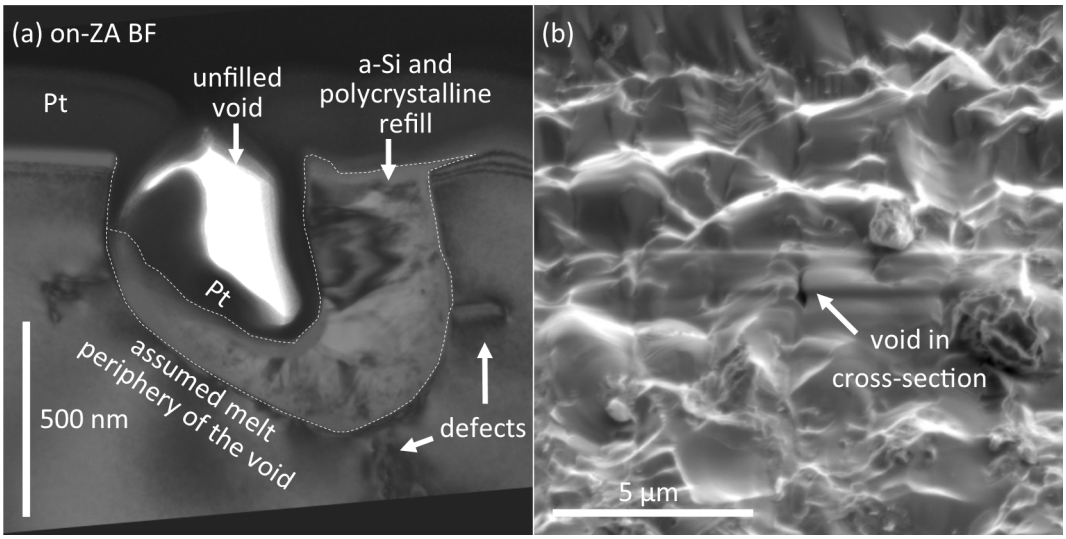

Figure 9.3: TEM, (a), and SEM, (b), of a long and thin remanent void. The TEM cross-section contains short lines of defects outside the void's melt periphery, and refill containing a-Si and polycrystallites within the melt periphery. The remanent void is partially, but incompletely refilled by Pt during the FIB sample preparation process. The SEM image was recorded with the sample tilted and after some Pt had already been deposited.

has been bypassed by the main cleaving path.

Several more results pertinent to the crack propagation behaviour are shown in Fig. 9.6. Two modifications are present in Fig. 9.6 (a). Between these are substantial interacting strain fields, as can be inferred from the bend contrast. The cleaving path contains evidence of several steps that presumably facilitated cracks, that had been propagating in parallel, to connect together. The modification in Fig. 9.6 (b) is composed largely of defective, epitaxially solidified dc-Si. Aligned with several of the defect lines are cracks that have not contributed to the cleaving process. The final cross-section, Fig. 9.6 (c), contains very little of the modification on this side of the cleaved surface. What is present is a small amount of defective Si and a crack. The cleaved path is composed of several steps suggesting multiple cracks have connected together over a short distance.

9.3 Discussion

The following discussion is presented in two sections. The first section seeks to understand the near-bandgap regime modifications using both the results presented above, and the knowledge gained from the sub-bandgap regime modifications. In the second section the discussion will relate the near-bandgap regime modifications to comparable modifications in the literature.

Before considering the individual features that make up the near-bandgap modifications, it is worth considering how the modifications might be expected to differ macroscopically because of the differences in the laser conditions. As stated above, the near-bandgap regime is less efficient than the sub-bandgap regime both with regard to the volume melted per unit energy and per unit time. This provides more modest, and because there is more time for thermal equilibration, more consistent radial thermal gradients along the length of the near-bandgap modifications. This explains why the melt diameter is also more consistent along the modification's length. This feature will be useful when discussing the specific features.

From a density perspective the first feature of note is void formation. The formation of a

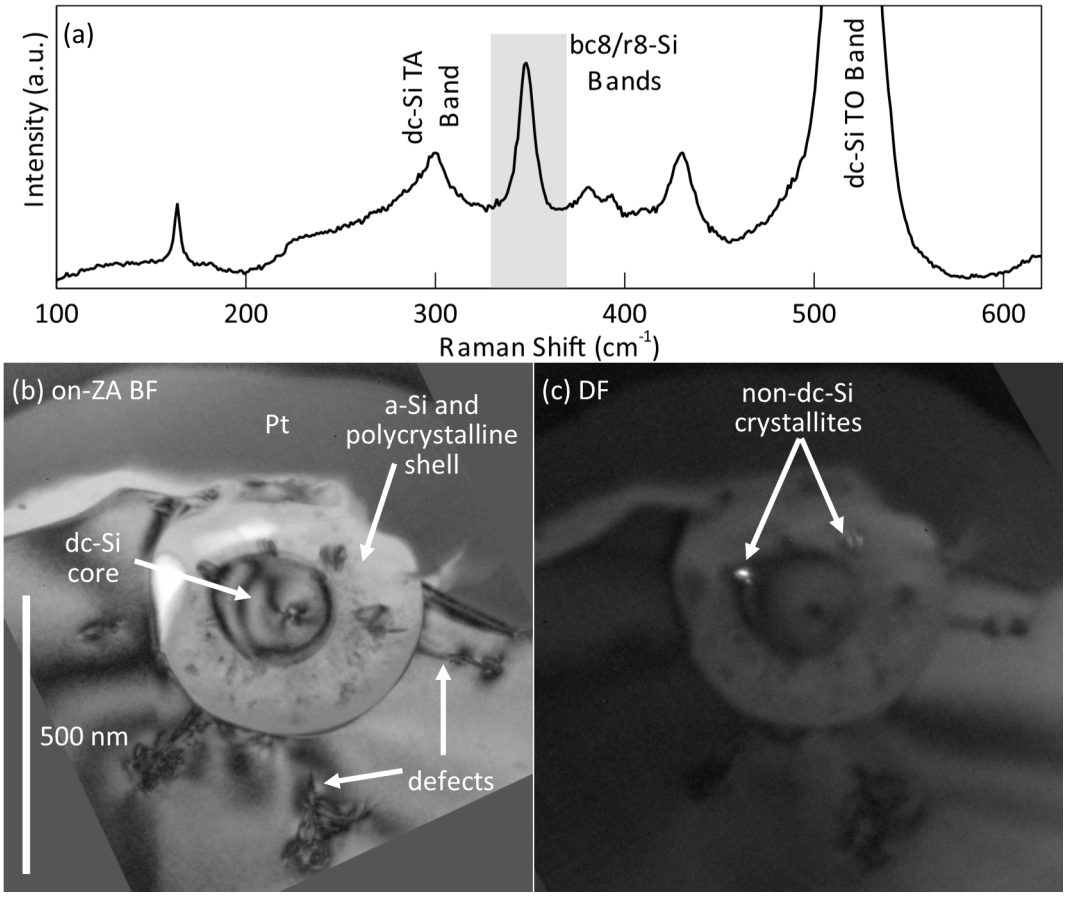

Figure 9.4: Raman, (a), and TEM, (b-c), evidence of high density allotropes in near-bandgap modifications. The Raman spectrum contains peaks associated with the bc8-Si and r8-Si phases, the strongest r8-Si peak is outlined with the grey box. The TEM cross-section, (b), features lines of defects on the periphery surrounding a largely a-Si shell which in turn encapsulates a dc-Si core. The shell region also contains crystallites, some of which do not appear to be dc-Si. The to scale DF image, (c), highlights a pair of non-dc-Si crystallites. This cross-section is thought to be in the vicinity of a void, which defines the near circular periphery of the principally a-Si shell.

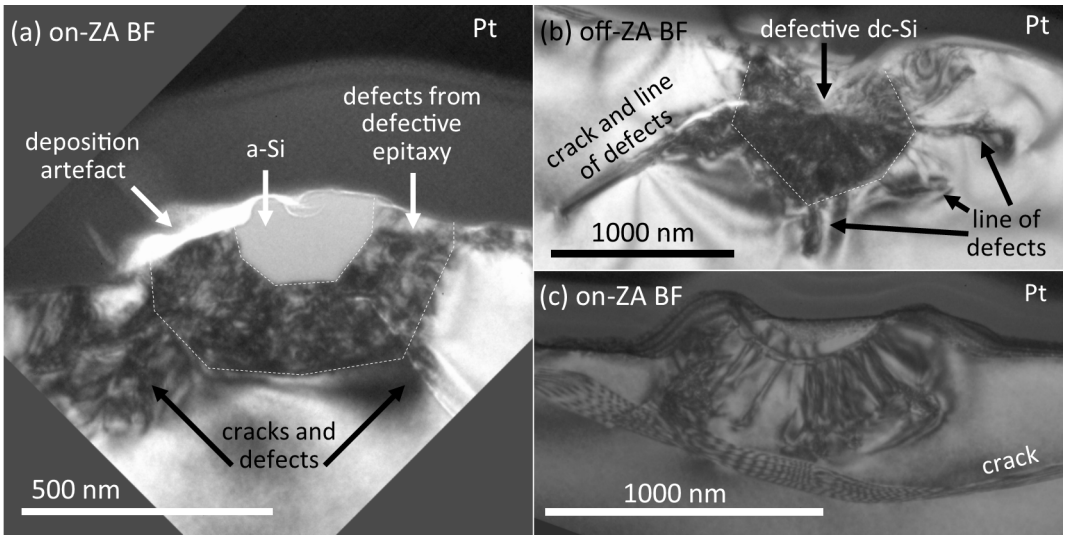

Figure 9.5: TEM images of near-bandgap modifications. The modification in (a) consists of an a-Si core with a faceted periphery, marked with a dashed line, surrounded by a region that has solidified by defective epitaxial solidification which also has a somewhat faceted periphery. Cracks overlap several of the lines of defects from colliding solidification interfaces. The modification in (b) has a somewhat faceted core of defective dc-Si with short lines of defects from colliding solidification interfaces. One line of defects overlaps a crack that extends well beyond the original melt periphery. The modification in (c) is composed of defects with no well defined facets on its periphery or lines of defects from colliding epitaxial solidification interfaces. A crack, bypassed by the cleaving path, exists below the modification.

void must inherently occur near focus for temporal reasons, the longer pulse duration implies that the void will form when the volume near focus has melted. Thereafter, as the melt volume increases, so too must the void volume. Geometrically, the growth is expected to be limited by the melt diameter meaning that the void will elongate into a capsule shape. It follows that movement of the void may be induced either to minimise its surface area (interfacial free energy) or due to thermocapillary pumping. Both effects are likely weak in this regime, but if they do occur it may explain why the voids are often above focus.

During solidification much of the Si expands, partially refilling the void as was observed in the sub-bandgap regime modifications. Macroscopically, two limits were noted. The molten Si may adhere to the periphery of the void and refill along the entire void's length, resulting in a thin but long remanent void. Alternatively, the Si may enter from the top and bottom uniformly, resulting in a wide but short remanent void. Intermediate cases also occur. Given that a-Si is present in both Fig. 9.3 and Fig. 9.4 it appears that amorphisation of the refill material is common. More microscopically, the radial inwards solidification and expansion above and below the void can push melt along the centre of the modification into the void from above and below, causing the protrusions noted in the figures. Strong thermal gradients between the periphery and protrusion appear to cause partial amorphisation, however, as the protrusions are relatively large in this regime, thermal insulation effects are also of relevance. As such, the a-Si often encapsulates small crystallites, as in Fig. 9.2.

The relatively high remanent void volume dictates that the displaced mass must be accommodated more densely over the remainder of the modification compared with the sub-bandgap regime modifications. In both laser regimes bc8/r8-Si formation is one mechanism by which the displaced mass is accommodated. Amorphous material is also present in both regimes, although it may be of less relevance in the near-bandgap regime. This is because the radial thermal

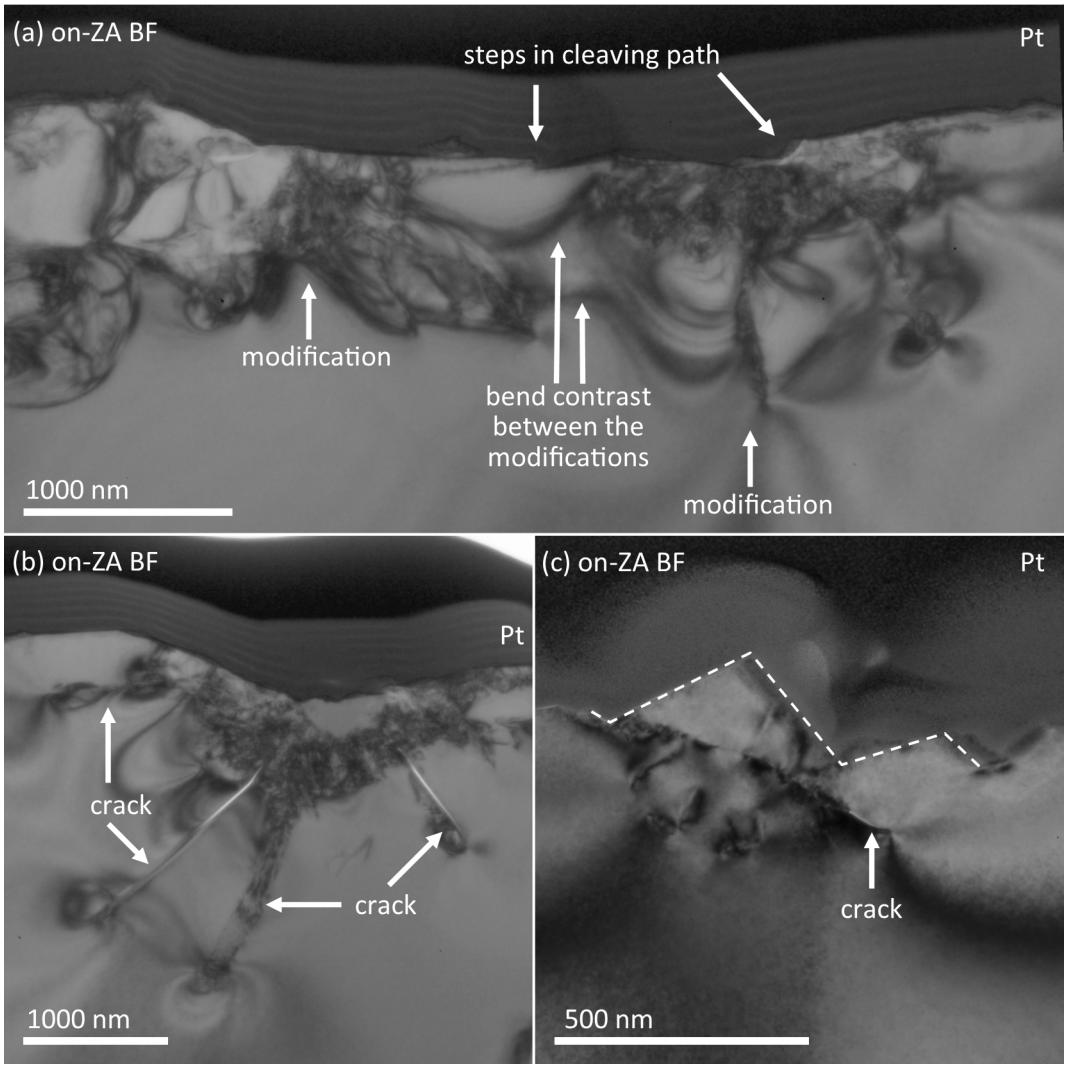

Figure 9.6: TEM images pertinent to cracking and cleaving in near-bandgap modifications. (a) contains two modifications with strain-induced bend contrast extending between them. The cleaving path contains small steps indicative of seperate cracks joining together. The modification in (b) appears to have cracks overlapping all of the visible lines of defects that formed due to colliding epitaxial solidification interfaces. The modification in (c) has largely been bypassed with only a bypassed crack and several small regions of defects in this cross-section. The cleaving path is composed of several steps suggesting multiple cracks have connected together in this region.

gradients are thought to generally be more modest in the near-bandgap regime, meaning that a smaller proportion of the modification will solidify as a-Si. Certainly, very little a-Si was observed away from voids, while the a-Si near voids is unlikely to have an elevated density given that the void provides a mechanism by which the Si can expand. The final mechanism by which the displaced mass may be accommodated is by compressed dc-Si. This is suspected to be of greater significance to the near-bandgap regime modifications. The increased prevalence of defective epitaxial solidification is assumed to be the product of compressive strains and is therefore evidence of compressed dc-Si being more common. Some of the cracking behaviour discussed below is also consistent with greater compression in the dc-Si.

As for the solidification process more generally, TEM results from the short axis cross-sections show that the process is largely similar between the two laser regimes. The same transitions in solidification behaviour were noted; perfect epitaxy, defective epitaxy, amorphisation and an insulation-induced return to crystal growth. The proportions of each behaviour do, however, differ. Defective epitaxy appears to be more common because, as mentioned above, compressive strain is more significant. Amorphisation, in contrast, appears to be less common because of the more modest radial thermal gradients. A transition from amorphisation back to crystal growth was only observed in cross-sections in, or near, a void. For this reason it is not known whether comparable structure to those in the sub-bandgap regime occur away from voids in the near-bandgap regime.

The orientations of the epitaxial solidification also appear to be similar between the two regimes, for which Fig. 9.5 is the most relevant result. In this case the solidification interface would appear to have multiple facets that would correspond to $\langle 100 \rangle$ and $\langle 110 \rangle$ epitaxy. Higher index $\langle hk0 \rangle$ epitaxy was not observed. Presumably the lack of higher index epitaxy is evidence of more modest radial thermal gradients. It is noteworthy that the lines of defects from colliding interfaces are less well defined and less consistent in this regime. Obscuration by other features in the modification appears to a partial explanation for this. A second factor is that strain from adjacent modifications likely roughens the solidification interfaces, making their collision path less well defined.

Solidification from the perspective of the long axis can only be speculated upon given the lack of any long axis cross-sections. Given though that both the radial thermal gradients and melt diameter are expected to be more homogenous over the length of the modification, compared with sub-bandgap regime modifications, steps between vertical facets are probably rather less important in this regime.

Cracking and dicing related features are also largely consistent between the near-bandgap and sub-bandgap regime modifications, although there are again a few notable differences. Crack formation in the near-bandgap regime is inferred from the TEM cross-section results to occur mostly or entirely along the lines of defects from colliding epitaxial solidification interfaces. This was a mode of crack formation in the sub-bandgap regime as well, but cracks were also common closer to the core in regions of chaotic solidification or near a-Si. Equivalent cracks are not observed in the near-bandgap regime and are unlikely to occur if, as is suspected, substantial compressive strain is present in the core of the modification. The compressive strain will effectively increase the fracture toughness of the modification and suppress crack formation and growth. However, compressive strain at the core of the modification may cause tensile strain on the periphery of the modification which would in fact promote crack development from the cracks overlapping the lines of defects.

Crack propagation may be also occur due to thermal stresses induced by subsequent laser pulses. Indeed, the shorter wavelength of the near-bandgap regime laser presumably makes absorption by defective regions around a crack more likely, and therefore more extensive heating

occurs. The presence of bypassed cracks and steps between cracks again provides evidence that cracks propagate in parallel before joining together. Interestingly, the steps in the near-bandgap regime appear smaller than the sub-bandgap regime, but the overall roughness of the cleaved surface is larger. These seemingly contradictory facts are worthy of comment. In the sub-bandgap regime, the laser asymmetry caused the initial cracks, which formed perpendicular to the cleaving direction, to require large steps to propagate in the cleaving direction and hence the cleavage often bypassed the centre of the modifications. In contrast, the more symmetric near-bandgap modification are more likely to have cracks already aligned with the cleaving orientation and, thus, the step required between neighbouring cracks is typically smaller. Another relevant factor is the compressive strain within the modification, which appears to be more prevalent in the near-bandgap regime. As mentioned above, this will impede crack development and so the cleaving path is therefore more likely to propagate around the periphery of the modifications, rather than through the centre. This is likely the reason that the surface roughness is higher.

Having explained the near-bandgap regime modifications produced in this work, it is worth comparing them to very similar modifications that have been reported in the literature.[39,48–51] Specifically, the literature modifications were produced with 1064 nm, 150 ns, $4 - 6.5$ μJ laser pulses with a 3.75 μm gap between modifications. This represents a more powerful laser pulse and larger modification separation, but it is otherwise very similar to the modifications in this work.

The literature modifications are slightly larger (nearly 30 μm long) than those in this work (18.9 ± 0.6 μm) and contain voids with protrusions which reportedly always appear at focus based on imaging of the modifications on a cleaved surface. This is an interesting contrast to the near-bandgap modifications in this work where the voids are near, but not always at focus. Above the void the surface topography is, as with the modifications in this work, chaotic and rough. The morphology was explained to be the consequence of rapid heating inducing not just melting, but also a thermal shockwave. The thermal shockwave component of this explanation is not consistent with the observations in this thesis. Indeed, the standard sub-bandgap regime modifications in this thesis are created with a substantially more powerful laser pulse and yet they could be fully explained without reference to any shockwave-related phenomena. Furthermore, PLM experiments are of comparable laser powers and, in that field too, the observations can be fully explained by rapid melting and solidification behaviour, again without invoking shockwave phenomena.[52–54,147]

A more detailed examination of the voids in the literature modifications[49] concluded that multiple voids formed, driven by densification during melting, but subsequently coalesced and expansion on solidification formed a protrusion. Thus, the explanation for the voids in the literature was broadly consistent with the explanation of the voids in this work. It must be noted, however, that the more nuanced understanding established in this thesis leads to different interpretations of many of the intricacies compared with those in the literature.

Another detailed examination in the literature concerned crack development and propagation.[50,51] That work suggested that cracks formed from shockwave-induced defects due to the presence of thermal stresses during subsequent laser pulses. This explanation is again broadly consistent with explanations forwarded in this work. However, the defects are clearly solidification-induced, rather than shockwave-induced. Furthermore, inhomogeneous stress distributions, inhomogeneous material density and imperfect epitaxial solidification are also clearly of relevance to crack formation. Indeed, the presence of small cracks in standard isolated sub-bandgap regime modifications show that crack nucleation is not contingent on thermal stresses from subsequent laser pulses at all. The thermal stresses may, of course, nucleate more cracks in addition to thermally propagating the cracks. Indeed, the greater laser power of the literature

modifications may make thermal-stress-induced cracking more significant in those modifications.

9.4 Summary

In this chapter the morphology of the near-bandgap modifications was explained using the same underlying physical processes that were used to explain the sub-bandgap regime modifications. In both regimes the laser induces melting which in turns results in void formation because of the higher melt density of Si. The regimes do differ in that a single voids evolves at or near focus in the near-bandgap regime because of the slower growth of the melt volume. The longer pulse duration of the near-bandgap regime also allows for greater equilibration of the melt shape and radial thermal gradients along the length of the modification.

In both regimes expansion during solidification results in the partial refilling of the void(s). The remanent void volume is larger in the near-bandgap regime though, meaning that the displaced mass must be accommodated more densely throughout the remainder of the modification. The same three mechanisms to accommodate this displaced mass are valid for both regimes, high density crystalline allotropes, high density a-Si and compressed dc-Si. Of these, the a-Si component is suspected to be less significant in the near-bandgap regime because modest thermal gradients mean that there is less a-Si. Compressed dc-Si, however, appears to be more common, resulting in more defective epitaxy and slightly different crack propagation behaviour.

The solidification process largely occurs through epitaxial solidification in both regimes. The weaker radial thermal gradients mean that high index $\langle hk0 \rangle$ epitaxy is either less common, or absent in the near-bandgap regime. Lines of defects from colliding epitaxial solidification interfaces occur in both regimes, but are less evident and less consistent in the near-bandgap regime.

In both regimes the presence of cracks is often correlated with the presence of defects from colliding epitaxial solidification interfaces. The near-bandgap regime modifications lack cracks equivalent to those at the centre of the modifications in the sub-bandgap regime modifications. This is likely due more to substantially compressed material that suppresses crack formation in the core of the near-bandgap regime modifications.

Crack propagation appears to occur in parallel for many cracks in both regimes, after which the cracks connect together, often leaving a characteristic step on the cleaving path. This allows the bypassing of some cracks as the sample is cleaved, which is not desirable from an application perspective. The near-bandgap regime does differ in that the cleaved surface is rougher than for the sub-bandgap regime. This is thought to be the result of cracks propagating around, rather than through, the core of modifications due to the strong compressive stresses in the near-bandgap regime modifications.

Chapter 10

Summary, conclusions and future work

Prior to the work in this thesis, the laser irradiation process used to create the subsurface modifications had been successfully implemented. The laser conditions, including spacing of modifications, had also been empirically optimised for dicing. The morphology, however, was almost entirely unknown. Characterisation in previous studies had largely been limited to the observation of features visible on the cleaved surface. This had only revealed the presence of a void and the approximate length of the modifications. A range of mechanisms by which the modifications formed had been put forward based on heating-induced melting, boiling and thermal shockwaves. Thus, knowledge of the nature and origin of the modification morphology was highly deficient. This thesis provides a detailed and nuanced explanation of all significant aspects of the modification morphology. It also provides some insight into the dicing process.

This work shows that, consistent with Verburg's modelling[30,31,44], the observed morphology can be explained entirely with a melting and solidification model. During the laser irradiation process, the melt volume grows from focus up the path of the laser. The shape of the melt, and the strength of the thermal gradients driving solidification differ between the different laser conditions examined.

Standard sub-bandgap irradiation produces the largest melt volume which is roughly circular in cross-section and increases in diameter from focus over most of the modification's length. There is then a region of near constant melt diameter after which the melt diameter decreases. The thermal gradients are strongest at focus and weakest near the top of the modification. However, there is some asymmetry in the thermal gradients due to an asymmetry in the laser itself, which is most noticeable near focus.

The low energy modifications are smaller and the cross-sectional area increases over the entire length of the modification, with the cap at the top being the widest section of the modification. As with standard higher energy modifications, the thermal gradients weaken further from focus, but on average they appear to be stronger than in the standard sub-bandgap modifications. The melt cross-section was not circular due to the asymmetry in the laser.

The near-bandgap modifications are of an intermediate size despite making use of a drastically more energetic laser pulse. This demonstrates that the slower near-bandgap laser regime has lower melting efficiency. These conditions result in a greater degree of thermal equilibration along the length of the modification. As such, the melt diameter and thermal gradients appear to change less over the length of the modification.

In all cases, as Si melts, it shrinks, driving the formation of voids. The manifestation of the voids differs for each laser condition. In the standard sub-bandgap regime modifications, the melt volume grows so quickly that the energetically-favoured growth of a single void is kinetically limited. Instead, multiple voids seem to form along the length of the modification. In the low

energy sub-bandgap regime void growth is not kinetically limited and a single void is found. This void is at the top of the modification where its surface area (and interfacial free energy) can be minimised. In the near-bandgap regime, void growth is not kinetically limited and only a single void is found, this time within the bottom third of the modification, partially dictated by where it formed early in the relatively long pulse length.

The voids are generally expected to take a capsule shape in the melt, but this is subject to change during the solidification process. In all laser conditions the expansion of Si during solidification appears to drive the partial refilling of the voids from above, below, or both. The molten refill material often encounters strong thermal gradients upon contact with the much colder walls of the void. As such, the refill material often solidifies rapidly and atypically, resulting in defective dc-Si and a-Si. In the standard sub-bandgap regime modifications, the voids nearer to focus are also highly subject to elongation driven by capillary effects. Thermocapillary pumping may also result in void movement along the modification's length. It appears that some smaller voids in the standard sub-bandgap regime modifications can be fully refilled.

As the voids normally only partially refill, the displaced material must be accommodated in high density regions elsewhere in the modification's volume. To some extent the displaced material is accommodated by compressive strain of dc-Si. This was observed in regions that solidified very quickly where time prevented the transport of excess material in the melt towards voids. It was also observed in the last regions of the modification to solidify. This mechanism appears to be of greater importance in the near-bandgap regime modifications which have the largest remanent void volume.

The excess material is likely to also be partially accommodated in a-Si with an elevated density. This explanation was not validated experimentally. However, at least for the low energy sub-bandgap regime modifications estimates of the excess mass that must be accommodated in the modification based on remanent void volume resulted in the conclusion that high density a-Si must be present. Because of the more modest radial thermal gradients in the near-bandgap regime, high density a-Si is considered to be less important for those modifications.

The final mechanism by which the displaced material was accommodated is in the high density crystalline allotropes bc8-Si and r8-Si. These were observed in all the modifications, where they formed after small volumes of the high density melt were trapped by the surrounding solid. As such, the trapped melt had insufficient volume in which to expand to dc-Si and instead transformed to r8-Si and ultimately bc8-Si. Based on density change arguments the initial transformation to r8-Si must have occurred either directly from the melt or via a transitory high density a-Si state. Neither pathway has been reported under high temperature conditions. Thus, this work has revealed a new pathway by which r8-Si may form.

TEM examination of short axis cross-sections of the modifications revealed that because the thermal gradients are predominantly radial, solidification in the cross-sections can largely be explained in two-dimensions. This solidification is dependent on the undercooling in the melt, which is, in turn, dependent on the strength of the thermal gradients driving cooling.

On the periphery of the cross-section, where undercooling is more modest, solidification generally occurs by two-dimensional defect free epitaxial solidification. During solidification undercooling at the centre of the modification increases, which can result in a transition to imperfect, defective epitaxial solidification. Defective epitaxy is also more prevalent under compressive strain. It is therefore particularly prominent in near-bandgap modifications which are highly compressively strained. It is also more prominent in closely spaced modifications due to the presence of strain induced by previous modifications. Alternatively, with stronger undercooling again, solidification may instead transition to amorphisation. This is common in the sub-bandgap regime modifications, particularly for the low energy modifications. These regimes

have been reported in the literature concerning the quasi one-dimensional surface PLM experiments. An additional regime beyond that observed in the literature was also observed. As the thermal conductivity of a-Si is drastically lower than that of dc-Si, a thick amorphous layer can reduce cooling rates in the remaining melt. As such, undercooling in the melt decreases, allowing for a return to a crystal growth regime. This results in a crystalline core, a-Si shell morphology.

The actual shape of the solidification interface is the product of the interplay between the thermal and energetic factors. The thermally-favoured shape is circular (ignoring laser asymmetry), a reflection of the original melt periphery and subsequent radial cooling. The energetically-favoured shape is facetted in accordance with the crystallography. Under conditions of strong radial thermal gradients the thermal factors dominate. Epitaxial solidification occurs along many $\langle hk0 \rangle$ orientations so as to approximate a circular shape. In such a case the angle between facets can be obtuse enough that the interface bends between the facets, creating a more continuous solidification interface. As the radial thermal gradients weaken epitaxial solidification occurs only on lower index $\langle hk0 \rangle$ orientations. Under these conditions the angle between neighbouring facets is more acute and the interfaces collide imperfectly. This results in a trail of defects along the collision path. With the weakest radial thermal gradients $\langle 100 \rangle$ epitaxy is dominant. Here neighbouring epitaxial solidification interfaces sometimes collide perfectly simply because more time is available during their intersection.

From the perspective of long axis cross-sections there is again a mismatch between the thermally and energetically-favoured interface shape. In this case, the thermally-favoured interface is approximated by energetically-favoured facets separated by steps.

Under conditions of strong thermal gradients, the steps between the facets are relatively smooth and the interface can be considered to be undulating along the modification's length. The discrepancy between the smoothly varying thermal gradients and undulating interface results in oscillations in the undercooling. This can result in an oscillating periphery to the core of the modification. This is because the undercooling-dependent transitions in solidification behaviour will occur at different distances from the centre of the modification over the length of each undulation. These conditions are evident in the sub-bandgap regime modifications, particularly near focus.

Under conditions of modest thermal gradients, the steps between facets are more abrupt. The abrupt steps tend to cause the defect density to increase and these are evident over most of the length of the standard sub-bandgap regime modifications, with the exception of the region nearest to focus.

When the energetically-favoured facets align well with the thermally-favoured interface the steps are either absent or negligible. It is assumed that the near-bandgap regime modifications are mostly in this condition.

The long axis cross-sections also revealed that the general two-dimensional solidification process that was just summarised is also subject to various perturbations. The dominant forms of perturbation have density and thermal origins, for example the presence of voids and thermally insulating a-Si.

On the topic of dicing, many of the details of the process are now understood. In all three laser conditions small cracks are often found in modifications along the lines of defects that result from colliding solidification interfaces. Additional cracks were also observed near the centre of the modifications in the sub-bandgap regime, but not in the near-bandgap regime because they are more compressively strained at the core. Cracking appears to be more common in closely spaced modifications. This could be the result of lower quality solidification, due to the stresses imparted by previous modifications. It may also be the result of thermal stresses induced by

reheating of previous modifications when a new modification is created.

During cleaving crack propagation appears to occur simultaneously for many cracks, which subsequently join together to complete the cleaving path. This often requires steps between cracks that are propagating parallel to, but displaced from, one another. The cleaving path often bypasses portions of cracks, leaving an undesirable weakness in the side walls of the diced sample. This raises the first potential practical benefit of this work for wafer dicing, the weakness can probably be minimised by slightly increasing the distance between modifications. Additionally, in the sub-bandgap regime modifications, crack formation preferentially occurred perpendicular to the cleaving direction because of the laser asymmetry. As such, dicing performance could be improved by either eliminating the laser asymmetry, or orientating it to be parallel to the desired cleaving path. This is a second potential practical benefit, although one that requires further work to validate.

Comparing the sub-bandgap regime to the near-bandgap regime, the larger size of the sub-bandgap regime is preferential as it covers more of the cleaving plane. Furthermore, the cleaving path is smoother in the sub-bandgap regime, despite the laser asymmetry, because the cracks often propagate around the compressed core of the near-bandgap regime modifications. This finding is particularly noteworthy as equipment using the near-bandgap process is commercially available, while the technically superior sub-bandgap process is not used commercially.

Thus, it should be evident that this thesis has investigated and explained every significant aspect of the previously largely unknown morphology of these modifications. In extrapolating the previous one-dimensional solidification model related to surface pulsed laser melting to two-dimensions for sub-surface melting, new features and phenomena were revealed. In particular, when thermally insulating a-Si was formed during solidification, it resulted in a return to the crystallisation regime. This work also provided a more nuanced understanding to the transitions in solidification behaviour and interactions between solidification along competing and differing crystal orientations. The thesis also found evidence of a new pathway by which the high density crystalline allotrope of Si, r8-Si, may form. This new pathway either involves a direct transition from the melt, or a transition through a transitory high density a-Si state.

Several topics do warrant further investigation in future work. First, the near-bandgap regime modifications were never examined in isolation, in a closely spaced but uncleaved geometry, or in long axis cross-sections. Doing so would allow many of the hypothesises provided in this work concerning these modifications to be investigated.

A second topic of future work concerns the potential for high density a-Si, which likely exists but was not experimentally confirmed. In part this may be because not all the a-Si is at elevated density, and so cross-sections prepared from different regions of the modifications would be beneficial. It is also possible that different cross-sectioning techniques would be required to prevent the expansion of a-Si as the cross-section is thinned.

These modifications provide a unique way in which to compare and investigate the crystal orientation-dependent and undercooling-dependent solidification behaviour. They may thus serve as a useful tool for further investigation of these factors, particularly if performed quantitatively. A further extension of this work could be to perform similar experiments on Si wafers of different orientations.

Finally, the knowledge gained in this thesis could be used to guide the iterative refinement of the modifications for improved dicing performance. In particular, as mentioned above, it would be beneficial to test the hypothesis that a larger spacing between modifications may increase chip wall strength without a significant penalty to dicing performance. It would also be interesting to deliberately introduce a laser asymmetry in the desired dicing direction to preferentially orient the induced cracks.

Bibliography

[1] A. Misra and I. Fininie. On the scribing and subsequent fracturing of silicon semiconductor wafers. *Journal of Materials Science*, 14(11):2567–2574, 1979.

[2] M. Birkholz, K. E. Ehwald, M. Kaynak, T. Semperowitsch, B. Holz, and S. Nordhoff. Separation of extremely miniaturized medical sensors by IR laser dicing. *Journal of Optoelectronics and Aadvanced Materials*, 12(3):479, 2010.

[3] J. R. Chelikowsky and M. L. Cohen. Electronic structure of silicon. *Physical Review B*, 10(12):5095, 1974.

[4] B. N. Brockhouse. Lattice vibrations in silicon and germanium. *Physical Review Letters*, 2(6):256, 1959.

[5] F. A. Johnson. Lattice absorption bands in silicon. *Proceedings of the Physical Society*, 73(2):265–272, feb 1959.

[6] D. L. Stierwalt and R. F. Potter. Lattice absorption bands observed in silicon by means of spectral emissivity measurements. *Journal of Physics and Chemistry of Solids*, 23(1-2):99–102, 1962.

[7] S. K. Sundaram and E. Mazur. Inducing and probing non-thermal transitions in semiconductors using femtosecond laser pulses. *Nature materials*, 1(4):217, 2002.

[8] E. G. Gamaly. The physics of ultra-short laser interaction with solids at non-relativistic intensities. *Physics Reports*, 508(4-5):91–243, 2011.

[9] E. G. Gamaly and A. V. Rode. Physics of ultra-short laser interaction with matter: From phonon excitation to ultimate transformations. *Progress in Quantum Electronics*, 37(5):215–323, 2013.

[10] L. Rapp, B. Haberl, J. E. Bradby, E. G. Gamaly, J. S. Williams, and A. V. Rode. Confined micro-explosion induced by ultrashort laser pulse at SiO_2/Si interface. *Applied Physics A*, 114(1):33–43, 2014.

[11] L. Rapp, B. Haberl, C.J. Pickard, J.E. Bradby, E.G. Gamaly, J.S. Williams, and A.V. Rode. Experimental evidence of new tetragonal polymorphs of silicon formed through ultrafast laser-induced confined microexplosion. *Nature Communications*, 6:7555, 2015.

[12] B. C. Stuart, M. D. Feit, S. Herman, A. M. Rubenchik, B. W. Shore, and M. D. Perry. Nanosecond-to-femtosecond laser-induced breakdown in dielectrics. *Physical Review B*, 53(4):1749, 1996.

[13] C. B. Schaffer, A. Brodeur, and E. Mazur. Laser-induced breakdown and damage in bulk transparent materials induced by tightly focused femtosecond laser pulses. *Measurement Science and Technology*, 12(11):1784, 2001.

[14] R. R. Gattass and E. Mazur. Femtosecond laser micromachining in transparent materials. *Nature photonics*, 2(4):219, 2008.

[15] E. N. Glezer, M. Milosavljevic, L. Huang, R. J. Finlay, T.-H. Her, J. P. Callan, and E. Mazur. Three-dimensional optical storage inside transparent materials. *Optics letters*, 21(24):2023–2025, 1996.

[16] K. Miura, J. Qiu, H. Inouye, T. Mitsuyu, and K. Hirao. Photowritten optical waveguides in various glasses with ultrashort pulse laser. *Applied Physics Letters*, 71(23):3329–3331, 1997.

[17] Y. Kondo, K. Nouchi, T. Mitsuyu, M. Watanabe, P. G. Kazansky, and K. Hirao. Fabrication of long-period fiber gratings by focused irradiation of infrared femtosecond laser pulses. *Optics letters*, 24(10):646–648, 1999.

[18] Y. Cheng, H.-L. Tsai, K. Sugioka, and K. Midorikawa. Fabrication of 3D microoptical lenses in photosensitive glass using femtosecond laser micromachining. *Applied Physics A*, 85(1):11–14, 2006.

[19] W. Steen and J. Mazumder. *Laser material processing*. Springer Science & Business Media, 2010.

[20] M. Mirkhalaf, A. K. Dastjerdi, and F. Barthelat. Overcoming the brittleness of glass through bio-inspiration and micro-architecture. *Nature communications*, 5:3166, 2014.

[21] S. Juodkazis, K. Nishimura, S. Tanaka, H. Misawa, E. G. Gamaly, B. Luther-Davies, L. Hallo, P. Nicolai, and V. T. Tikhonchuk. Laser-induced microexplosion confined in the bulk of a sapphire crystal: evidence of multimegabar pressures. *Physical Review Letters*, 96(16):166101, 2006.

[22] E. N. Glezer and E. Mazur. Ultrafast-laser driven micro-explosions in transparent materials. *Applied Physics Letters*, 71(7):882–884, 1997.

[23] E. G. Gamaly, S. Juodkazis, K. Nishimura, H. Misawa, B. Luther-Davies, L. Hallo, P. Nicolai, and V. T. Tikhonchuk. Laser-matter interaction in the bulk of a transparent solid: Confined microexplosion and void formation. *Physical Review B*, 73(21):214101, 2006.

[24] R. A. Soref and B. R. Bennett. Electrooptical effects in silicon. *IEEE Journal of Quantum Electronics*, 23(1):123–129, 1987.

[25] A. D. Bristow, N. Rotenberg, and Henry M. Van D. Two-photon absorption and Kerr coefficients of silicon for 850–2200 nm. *Applied Physics Letters*, 90(19):191104, 2007.

[26] H. H. Li. Refractive index of silicon and germanium and its wavelength and temperature derivatives. *Journal of Physical and Chemical Reference Data*, 9(3):561–658, 1980.

[27] A. Singh. Free charge carrier induced refractive index modulation of crystalline silicon. In *7th IEEE International Conference on Group IV Photonics*, pages 102–104. IEEE, 2010.

[28] A. Couairon and A. Mysyrowicz. Femtosecond filamentation in transparent media. *Physics reports*, 441(2-4):47–189, 2007.

[29] B. E. A. Saleh and M. C. Teich. *Fundamentals of Photonics*. John Wiley & Sons, 2019.

[30] P. C. Verburg, GRBE Römer, and A. J. Huis. Two-photon–induced internal modification of silicon by erbium-doped fiber laser. *Optics express*, 22(18):21958–21971, 2014.

[31] P. C. Verburg. *Laser-induced subsurface modification of silicon wafers*. PhD thesis, University of Twente, 2015.

[32] V. V. Kononenko, V. V. Konov, and E. M. Dianov. Delocalization of femtosecond radiation in silicon. *Optics letters*, 37(16):3369–3371, 2012.

[33] S. Leyder, D. Grojo, P. Delaporte, W. Marine, M. Sentis, and O. Utéza. Multiphoton absorption of 1.3 μm wavelength femtosecond laser pulses focused inside Si and SiO_2. In *17th International School on Quantum Electronics: Laser Physics and Applications*, volume 8770, page 877004. International Society for Optics and Photonics, 2013.

[34] P. C. Verburg, GMH Knippels, and J. Betz. Experimental validation of model for pulsed laser-induced subsurface modifications in Si. In *13th International Symposium on Laser Precision Microfabrication, LPM 2012*. JLMN, 2012.

[35] V. V. Parsi Sreenivas, M. Bülters, and R. B. Bergmann. Microsized subsurface modification of mono-crystalline silicon via non-linear absorption. *Journal of the European Optical Society-Rapid publications*, 7, 2012.

[36] A. Lietoila and J. F. Gibbons. Computer modeling of the temperature rise and carrier concentration induced in silicon by nanosecond laser pulses. *Journal of Applied Physics*, 53(4):3207–3213, 1982.

[37] A. L. Smirl, I. W. Boyd, T. F. Boggess, S. C. Moss, and H. M. van Driel. Structural changes produced in silicon by intense 1-μm ps pulses. *Journal of applied physics*, 60(3):1169–1182, 1986.

[38] H. M. Van Driel. Kinetics of high-density plasmas generated in Si by 1.06-and 0.53-μm picosecond laser pulses. *Physical Review B*, 35(15):8166, 1987.

[39] E. Ohmura, F. Fukuyo, K. Fukumitsu, and H. Morita. Internal modified-layer formation mechanism into silicon with nanosecond laser. *Journal of Achievements in Materials and Manufacturing Engineering*, 17(1-2):381–384, 2006.

[40] M. Kumagai, N. Uchiyama, E. Ohmura, R. Sugiura, K. Atsumi, and K. Fukumitsu. Advanced dicing technology for semiconductor wafer—stealth dicing. *IEEE Transactions on Semiconductor Manufacturing*, 20(3):259–265, 2007.

[41] E. Ohmura, M. Kumagai, M. Nakano, K. Kuno, K. Fukumitsu, and H. Morita. Analysis of processing mechanism in stealth dicing of ultra thin silicon wafer. *Journal of Advanced Mechanical Design, Systems, and Manufacturing*, 2(4):540–549, 2008.

[42] E. Ohmura. Temperature rise of silicon due to absorption of permeable pulse laser. In *Heat Transfer-Engineering Applications*. IntechOpen, 2011.

[43] Y. Izawa, Y. Tsurumi, N. Miyanaga, S. Tanaka, H. Kikuchi, M. Esashi, and M. Fujita. Debris-free in-air laser dicing for multi-layer MEMS by perforated internal transformation and thermally-induced crack propagation. In *2008 IEEE 21st International Conference on Micro Electro Mechanical Systems*, pages 822–827. IEEE, 2008.

[44] P. C. Verburg, GRBE Römer, and A. J. Huis. Two-temperature model for pulsed-laser-induced subsurface modifications in Si. *Applied Physics A*, 114(4):1135–1143, 2014.

[45] P. C. Verburg, L. A. Smillie, GRBE Römer, B. Haberl, J. E. Bradby, J. S. Williams, and A. J. Huis. Crystal structure of laser-induced subsurface modifications in Si. *Applied Physics A*, 120(2):683–691, 2015.

[46] V. Alex, S. Finkbeiner, and J. Weber. Temperature dependence of the indirect energy gap in crystalline silicon. *Journal of Applied Physics*, 79(9):6943–6946, 1996.

[47] ALSI. private communication, 2013-2014.

[48] T. Monodane. Thermo-elastic-plastic analysis on internal processing phenomena of single-crystal silicon by nanosecond laser. *Proceedings of LAMP 2006, Kyoto, May 16-19*, 2006.

[49] K. Shimamura, J. Okuma, S. Ohmura, and F. Shimojo. Molecular-dynamics study of void-formation inside silicon wafers in stealth dicing. *Journal of Physics: Conference Series*, 402:12044, 2012.

[50] E. Ohmura, K. Ogawa, M. Kumagai, M. Nakano, K. Fukumitsu, and H. Morita. Analysis of crack propagation in stealth dicing using stress intensity factor. *Transactions of the Japan Society of Mechanical Engineers, Part A*, 76(764):446–448, 2010.

[51] E. Ohmura, Y. Kawahito, K. Fukumitsu, J. Okuma, and H. Morita. Analysis of internal crack propagation in silicon due to permeable pulse laser irradiation: study on processing mechanism of stealth dicing. In *Fundamentals of Laser-Assisted Micro-and Nanotechnologies 2010*, volume 7996, page 799603. International Society for Optics and Photonics, 2011.

[52] A. G. Cullis. Transient annealing of semiconductors by laser, electron beam and radiant heating techniques. *Reports on Progress in Physics*, 48(8):1155, 1985.

[53] J. M. Poate. High speed crystal growth and solidification using laser heating. *Journal of Crystal Growth*, 79(1-3):549–561, 1986.

[54] P. Baeri and E. Rimini. Laser annealing of silicon. *Materials Chemistry and Physics*, 46(2):169 – 177, 1996.

[55] A. G. Cullis, N. G. Chew, H. C. Webber, and David J. Smith. Orientation dependence of high speed silicon crystal growth from the melt. *Journal of Crystal Growth*, 68(2):624–638, 1984.

[56] M. H. Grabow, G. H. Gilmer, and A. F. Bakker. Molecular dynamics studies of silicon solidification and melting. *MRS Proceedings*, 141:349, 1988.

[57] C. H. Crouch, J. E. Carey, M. Shen, E. Mazur, and F. Y. Genin. Infrared absorption by sulfur-doped silicon formed by femtosecond laser irradiation. *Applied Physics A*, 79(7):1635–1641, 2004.

[58] J. E. Carey, C. H. Crouch, M. Shen, and E. Mazur. Visible and near-infrared responsivity of femtosecond-laser microstructured silicon photodiodes. *Optics letters*, 30(14):1773–1775, 2005.

[59] M. A. Sheehy, B. R. Tull, C. M. Friend, and E. Mazur. Chalcogen doping of silicon via intense femtosecond-laser irradiation. *Materials Science and Engineering: B*, 137(1-3):289–294, 2007.

[60] J. Bonse, S. Baudach, J. Krüger, W. Kautek, and M. Lenzner. Femtosecond laser ablation of silicon–modification thresholds and morphology. *Applied Physics A*, 74(1):19–25, 2002.

[61] J. Bonse and J. Krüger. Pulse number dependence of laser-induced periodic surface structures for femtosecond laser irradiation of silicon. *Journal of Applied Physics*, 108(3):034903, 2010.

[62] M. J. Smith, M. Winkler, M.-J. Sher, Y.-T. Lin, E. Mazur, and S. Gradečak. The effects of a thin film dopant precursor on the structure and properties of femtosecond-laser irradiated silicon. *Applied Physics A*, 105(4):795–800, 2011.

[63] M. J. Smith, Y.-T. Lin, M.-J. Sher, M. T. Winkler, E. Mazur, and S. Gradečak. Pressure-induced phase transformations during femtosecond-laser doping of silicon. *Journal of Applied Physics*, 110(5):053524, 2011.

[64] M. J. Smith, M.-J. Sher, B. Franta, Y.-T. Lin, E. Mazur, and S. Gradečak. The origins of pressure-induced phase transformations during the surface texturing of silicon using femtosecond laser irradiation. *Journal of Applied Physics*, 112(8):083518, 2012.

[65] C. B. Carter and D. B. Williams. *Transmission electron microscopy: Diffraction, imaging, and spectrometry*. Springer, 2016.

[66] L. A. Giannuzzi. *Introduction to focused ion beams: instrumentation, theory, techniques and practice*. Springer Science & Business Media, 2004.

[67] J. W. Edington and K. T. Russell. *Practical electron microscopy in materials science*. Macmillan International Higher Education, 1977.

[68] R. F. Egerton. *Physical principles of electron microscopy*. Springer, 2005.

[69] Microscopy Australia. My Scope TEM introduction. `https://myscope.training/legacy/tem/introduction/`, 2013. [Online; accessed 2019-07-23].

[70] R. H. Finch, H. J. Queisser, G. Thomas, and J. Washburn. Structure and origin of stacking faults in epitaxial silicon. *Journal of Applied Physics*, 34(2):406–415, 1963.

[71] J. A. Kohn. Twinning in diamond-type structures: a proposed boundary-structure model. *American Mineralogist: Journal of Earth and Planetary Materials*, 43(3-4):263–284, 1958.

[72] F. J. Lopez, E. R. Hemesath, and L. J. Lauhon. Ordered stacking fault arrays in silicon nanowires. *Nano letters*, 9(7):2774–2779, 2009.

[73] R. F. Egerton. Electron-energy-loss spectroscopy in the TEM. *Reports on Progress in Physics*, 72:016502/1–25, 2009.

[74] R. F. Egerton. *Electron energy-loss spectroscopy in the electron microscope*. Springer Science & Business Media, 2011.

[75] S. M. Sze. *Physics of Semiconductor Devices*. Wiley-Interscience, 2nd edition, 1981.

[76] S. Kivelson and C. D. Gellat, Jr. Effective-mass theory in noncrystalline solids. *Physical Review B*, 10:5160–5177, 1979.

[77] A. C. Ferrari, A. Libassi, B. K. Tanner, V. Stolojan, J. Yuan, L. M. Brown, S. E. Rodil, B. Kleinsorge, and J. Robertson. Density, sp^3 fraction, and cross-sectional structure of amorphous carbon films determined by X-ray reflectivity and electron energy-loss spectroscopy. *Physical Review B*, 62(16):11089–11103, 2000-II.

[78] H. A. Szymanski, editor. *Raman Spectroscopy - Theory and Practice*. Plenum Press, New York, 1967.

[79] D. A. Lang, editor. *Raman Spectroscopy*. McGraw-Hill International Book Company, London, 1977.

[80] T. P. Mernagh and L.-G. Liu. Pressure dependence of Raman phonons of some group IVA (C, Si, and Ge) elements. *Journal of Physics and Chemistry of Solids*, 52(3):507–512, 1991.

[81] V. Paillard, P. Puech, M. A. Laguna, P. Temple-Boyer, B. Caussat, J. P. Couderc, and B. de Mauduit. Resonant Raman scattering in polycrystalline silicon thin films. *Applied Physics Letters*, 73(12):1718–1720, sep 1998.

[82] S. Roorda, W. C. Sinke, J. M. Poate, D. C. Jacobson, S. Dierker, B. S. Dennis, D. J. Eaglesham, F. Spaepen, and P. Fuoss. Structural relaxation and defect annihilation in pure amorphous silion. *Physical Review B*, 44(8):3702–3725, 1991.

[83] B. C. Johnson, B. Haberl, J. E. Bradby, J. C. McCallum, and J. S. Williams. Temperature dependence of Raman scattering from the high-pressure phases of Si induced by indentation. *Physical Review B*, 83(23):235205, jun 2011.

[84] S. Wong, B. Haberl, B. C. Johnson, A. Mujica, M. Guthrie, J. C. McCallum, J. S. Williams, and J. E. Bradby. Formation of an r8-dominant Si material. *Phys. Rev. Lett.*, 122:105701, Mar 2019.

[85] M. O. Thompson, P. H. Bucksbaum, and J. Bokor. Relation between temperature and solidification velocity in rapidly cooled liquid silicon. *MRS Proceedings*, 35:181, 1984.

[86] E. P. Donovan, F. Spaepen, D. Turnbull, J. M. Poate, and D. C. Jacobson. Heat of crystallization and melting point of amorphous silicon. *Applied Physics Letters*, 42(8):698–700, 1983.

[87] H. C. Webber, A. G. Cullis, and N. G. Chew. Computer simulation of high speed melting of amorphous silicon. *Applied Physics Letters*, 43(7):669–671, 1983.

[88] M. O. Thompson, G. J. Galvin, J. W. Mayer, P. S. Peercy, J. M. Poate, D. C. Jacobson, A. G. Cullis, and N. G. Chew. Melting temperature and explosive crystallization of amorphous silicon during pulsed laser irradiation. *Physical Review Letters*, 52(26):2360–2363, 1984.

[89] W. D. Luedtke and U. Landman. Preparation and melting of amorphous silicon by molecular-dynamics simulations. *Physical Review B*, 37(9):4656–4663, 1988.

[90] P. A. Apte and X. C. Zeng. Anisotropy of crystal-melt interfacial free energy of silicon by simulation. *Applied Physics Letters*, 92(22):2–5, 2008.

[91] D. Buta, M. Asta, and J. J. Hoyt. Kinetic coefficient of steps at the Si(111) crystal-melt interface from molecular dynamics simulations. *Journal of Chemical Physics*, 127(7), 2007.

[92] K. M. Beatty and K. A. Jackson. Monte Carlo modeling of silicon crystal growth. *Journal of Crystal Growth*, 211(1):13–17, 2000.

[93] K. A. Jackson. The Interface Kinetics of Crystal Growth Processes. *Interface Science*, 10(2):159–169, 2002.

[94] R. Drosd and J. Washburn. Some observations on the amorphous to crystalline transformation in silicon. *Journal of Applied Physics*, 53(1):397–403, jan 1982.

[95] G. J. Galvin, J. W. Mayer, and P. S. Peercy. Solidification kinetics of pulsed laser melted silicon based on thermodynamic considerations. *Applied Physics Letters*, 46(7):644–646, 1985.

[96] J.Y. Tsao, M. J. Aziz, M. O. Thompson, and P. S. Peercy. Asymmetric melting and freezing kinetics in silicon. *Physical Review Letters*, 56(25):2712–2715, jun 1986.

[97] B. C. Larson, J. Z. Tischler, and D. M. Mills. Nanosecond resolution time-resolved x-ray study of silicon during pulsed-laser irradiation. *Journal of Materials Research*, 1(1):144–154, 1986.

[98] B. C. Larson, J. Z. Tischler, and D. M. Mills. Interface temperatures and temperature gradients in silicon during pulsed laser irradiation. *MRS Proceedings*, 100:513, 1988.

[99] G. D. Ivlev and E. I. Gatskevich. Solidification temperature of silicon surface layer melted by pulsed laser irradiation. *Applied Surface Science*, 143(1):265–271, 1999.

[100] H. J. Goldsmid, M. M. Kaila, and G. L. Paul. Thermal conductivity of amorphous silicon. *physica status solidi (a)*, 76(1):K31–K33, mar 1983.

[101] D. H. Lowndes and R. F. Wood. Studies of pulsed laser melting and rapid solidification using amorphous silicon. *Journal of Luminescence*, 30(1):395–408, 1985.

[102] J. L. Feldman, M. D. Kluge, P. B. Allen, and F. Wooten. Thermal conductivity and localization in glasses: Numerical study of a model of amorphous silicon. *Physical Review B*, 48(17):12589–12602, 1993.

[103] A Van Der Drift. Evolutionary selection, a principle governing growth orientation in vapour-deposited layers. *Philips Res. Repts*, 22:267–288, 1967.

[104] W. J. Boettinger, J. A. Warren, C. Beckermann, and A. Karma. Phase-field simulation of solidification. *Annual Review of Materials Research*, 32(1):163–194, 2002.

[105] A. Karma and W.-J. Rappel. Quantitative phase-field modeling of dendritic growth in two and three dimensions. *Phys. Rev. E*, 57:4323–4349, Apr 1998.

[106] P. Baeri, G. Foti, J. M. Poate, and A. G. Cullis. Phase transitions in amorphous Si produced by rapid heating. *Physical Review Letters*, 45(25):2036, 1980.

[107] E. P. Donovan, F. Spaepen, D. Turnbull, J. M. Poate, and D. C. Jacobson. Calorimetric studies of crystallization and relaxation of amorphous Si and Ge prepared by ion implantation. *Journal of Applied Physics*, 57(6):1795–1804, 1985.

[108] W. D. Luedtke and U. Landman. Preparation, structure, dynamics, and energetics of amorphous silicon: A molecular-dynamics study. *Physical Review B*, 40(2):1164–1174, 1989.

[109] M. G. Grimaldi, P. Baeri, M. A. Malvezzi, and C. Sirtori. Thermodynamic properties of amorphous silicon investigated by pulsed laser heating. *International Journal of Thermophysics*, 13(1):141–151, Jan 1992.

[110] A. G. Cullis and G. R. Booker. The epitaxial growth of silicon and germanium films on (111) silicon surfaces using UHV sublimation and evaporation techniques. *Journal of Crystal Growth*, 9:132–138, 1971.

[111] J. Narayan and F. W. Young Jr. Growth of dislocations during laser melting and solidification. *Applied Physics Letters*, 35(4):330–332, 1979.

[112] R. A. Logan and W. L. Bond. Density change in silicon upon melting. *Journal of Applied Physics*, 30(3):322–322, 1959.

[113] H. Sasaki, E. Tokizaki, K. Terashima, and S. Kimura. Density variation of molten silicon measured by an improved archimedian method. *Japanese Journal of Applied Physics*, 33(Part 1, No. 7A):3803–3807, jul 1994.

[114] D. R. Lide. *CRC handbook of chemistry and physics*, volume 85. CRC press, 2005.

[115] Y. Okada and Y. Tokumaru. Precise determination of lattice parameter and thermal expansion coefficient of silicon between 300 and 1500 K. *Journal of applied physics*, 56(2):314–320, 1984.

[116] J. Z. Hu and I. L. Spain. Phases of silicon at high pressure. *Solid state communications*, 51(5):263–266, 1984.

[117] A. Mujica, A. Rubio, A. Munõz, and R. J. Needs. High-pressure phases of group-IV, III-V, and II-VI compounds. *Reviews of Modern Physics*, 75(3):863–912, 2003.

[118] B. Haberl, T. A. Strobel, and J. E. Bradby. Pathways to exotic metastable silicon allotropes. *Applied Physics Reviews*, 3(4):040808, 2016.

[119] M. I. McMahon and R. J. Nelmes. New high-pressure phase of Si. *Physical Review B*, 47(13):8337–8340, 1993.

[120] M. Hanfland, U. Schwarz, K. Syassen, and K. Takemura. Crystal structure of the high-pressure phase silicon VI. *Physical Review Letters*, 82:1197–1200, 1999.

[121] H. Olijnyk, S. K. Sikka, and W. B. Holzapfel. Structural phase transitions in Si and Ge under pressures up to 50 GPa. *Physics Letters*, 103A(3):137–140, 1984.

[122] S. J. Duclos, Y. K. Vohra, and A. L. Ruoff. hcp to fcc transition in silicon at 78 GPa and studies to 100 GPa. *Phys. Rev. Lett.*, 58:775–777, Feb 1987.

[123] R. O. Piltz, J. R. Maclean, S. J. Clark, G. J. Ackland, P. D. Hatton, and J. Crain. Structure and properties of silicon XII: A complex tetrahedrally bonded phase. *Physical Review B*, 52(6):4072–4085, 1995.

[124] J. Crain, G. J. Ackland, J. R. Maclean, R. O. Piltz, P. D. Hatton, and G. S. Pawley. Reversible pressure-induced structural transition between metastable phases of silicon. *Physical Review B*, 50(17):13043–13046, 1994.

[125] B. D. Malone, J. D. Sau, and M. L. Cohen. Ab initio survey of the electronic structure of tetrahedrally bonded phases of silicon. *Physical Review B*, 78:035210, 2008.

[126] H. Zhang, H. Liu, K. Wei, O. O. Kurakevych, Y. L. Godec, Z. Liu, J. Martin, M. Guerrette, G. S. Nolas, and T. A. Strobel. BC8 silicon (Si-III) is a narrow-gap semiconductor. *Phys. Rev. Lett.*, 118:146601, Apr 2017.

[127] J. S. Custer, M. O. Thompson, D. C. Jacobson, J. M. Poate, S. Roorda, and W. C. Sinke. Density of amorphous Si. *Applied Physics Letters*, 64(4):437–439, 1994.

[128] E. Holmström, B. Haberl, O.H. Pakarinen, K. Nordlund, F. Djurabekova, R. Arenal, J.S. Williams, J.E. Bradby, T.C. Petersen, and A.C.Y. Liu. Dependence of short and intermediate-range order on preparation in experimental and modeled pure a-Si. *Journal of Non-Crystalline Solids*, 438:26 – 36, 2016.

[129] D. L. Williamson, S. Roorda, M. Chicoine, R. Tabti, P. A. Stolk, S. Acco, and F. W. Saris. On the nanostructure of pure amorphous silicon. *Applied Physics Letters*, 67(2):226–228, 1995.

[130] N. Garg, K. K. Pandey, K. V. Shanavas, C. A. Betty, and S. M. Sharma. Memory effect in low-density amorphous silicon under pressure. *Physical Review B*, 83:115202, 2011.

[131] K. K. Pandey, N. Garg, K. V. Shanavas, S. M. Sharma, and S. K. Sikka. Pressure induced crystallization in amorphous silicon. *Journal of Applied Physics*, 109:113511, 2011.

[132] B. Haberl, M. Guthrie, D. J. Sprouster, J. S. Williams, and J. E. Bradby. New insight into pressure-induced phase transitions of amorphous silicon: the role of impurities. *Journal of Applied Crystallography*, 46(3):758–768, Jun 2013.

[133] M. Imai, T. Mitamura, K. Yaoita, and K. Tsuji. Pressure-induced phase transitions of crystalline and amorphous silicon and germanium at low temperatures. *High Pressure Research*, 15:167–189, 1996.

[134] V. Domnich, Y. Gogotsi, and S. Dub. Effect of phase transformations on the shape of the unloading curve in the nanoindentation of silicon. *Applied Physics Letters*, 76(16):2214–2216, 2000.

[135] J. E. Bradby, J. S. Williams, J. Wong-Leung, M. V. Swain, and P. Munroe. Mechanical deformation in silicon by micro-indentation. *Journal of Materials Research*, 16(5):1500–1507, 2001.

[136] F. Wooten, K. Winer, and D. Weaire. Computer generation of structural models of amorphous Si and Ge. *Physical Review Letters*, 54(13):1392–1395, 1985.

[137] B. Haberl, M. Guthrie, J. J. Molaison, T. B. Shiell, G. Shen, J. S. Williams, and J. E. Bradby. Phase behaviour of pure amorphous silicon and germanium under pressure. In *International Conference on High Pressure Science and Technology*, Madrid, Spain, 2015.

[138] B. Haberl, A. C. Y. Liu, J. E. Bradby, S. Ruffell, J. S. Williams, and P. Munroe. Structural characterization of pressure-induced amorphous silicon. *Physical Review B*, 79:155209, 2009.

[139] B. Haberl. *Structural Characterization of Amorphous Silicon.* PhD thesis, Australian National University, December 2010.

[140] B. Haberl, S. N. Bogle, T. Li, I. McKerracher, S. Ruffell, P. Munroe, J. S. Williams, J. R. Abelson, and J. E. Bradby. Unexpected short- and medium-range atomic structure of sputtered amorphous silicon upon thermal annealing. *Journal of Applied Physics*, 110:096104, 2011.

[141] L. B. B. Aji. *Structural relaxation process in pure amorphous silicon.* PhD thesis, Australian National University, 2014.

[142] T. S. Sammarco and M. A. Burns. Thermocapillary pumping of discrete drops in microfabricated analysis devices. *AIChE Journal*, 45(2):350–366, 1999.

[143] T. S. Sammarco and M. A. Burns. Heat-transfer analysis of microfabricated thermocapillary pumping and reaction devices. *Journal of Micromechanics and Microengineering*, 10(1):42, 2000.

[144] P. S. Glockner and G. F. Naterer. Surface tension and frictional resistance of thermocapillary pumping in a closed microchannel. *International journal of heat and mass transfer*, 49(23-24):4424–4436, 2006.

[145] B. E. Rapp. Chapter 20 - surface tension. In B. E. Rapp, editor, *Microfluidics: Modelling, Mechanics and Mathematics*, Micro and Nano Technologies, pages 421 – 444. Elsevier, Oxford, 2017.

[146] J. J. Jasper. The surface tension of pure liquid compounds. *Journal of Physical and Chemical Reference Data*, 1(4):841–1010, 1972.

[147] P. S. Peercy, M. O. Thompson, and J. Y. Tsao. Dynamics of rapid solidification in silicon. *MRS Online Proceedings Library Archive*, 80, 1986.

Appendix A

Large scale long axis cross-sections

In this appendix the long axis cross-sections shown in Chapter 3, Fig. 3.4 are reproduced at a larger scale. In Fig. A.1 the first modification is shown in an on-ZA BF image, (a), in an on-ZA BF image recorded using a larger objective aperture such that several diffracted beams also contribute to the final image, (b), and in an off-ZA BF image (c). In Fig. A.2 (a) the second modification is shown in BF images both on-ZA, (i), and off-ZA, (ii). In Fig. A.2 (b) the third modification is shown in an on-ZA BF image while the sample is still thick, (i), and after further thinning (in which the constant diameter region has fractured) also in an on-ZA BF image (ii) and in a STEM BF image (iii).

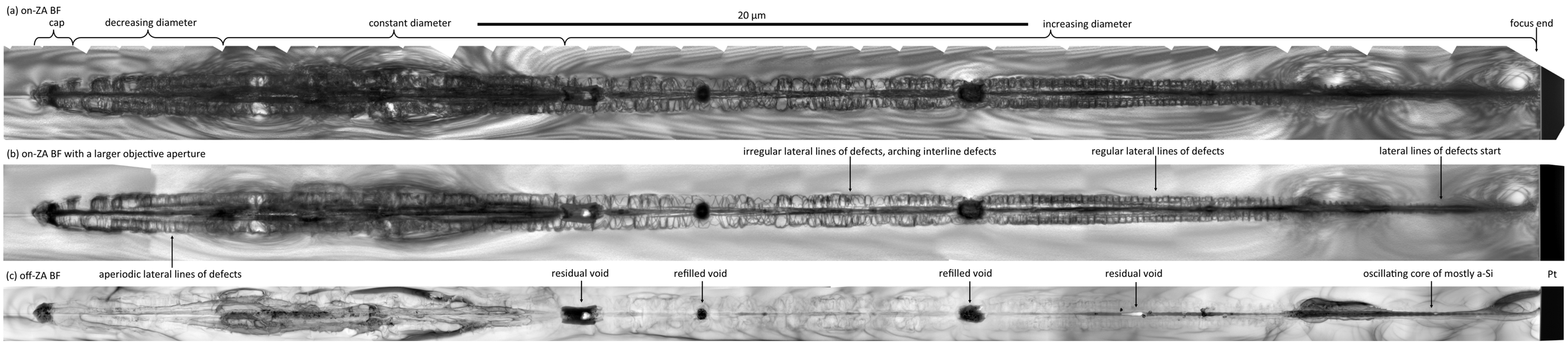

Figure A.1: Long axis cross-section images under different imaging conditions of Modification 1.

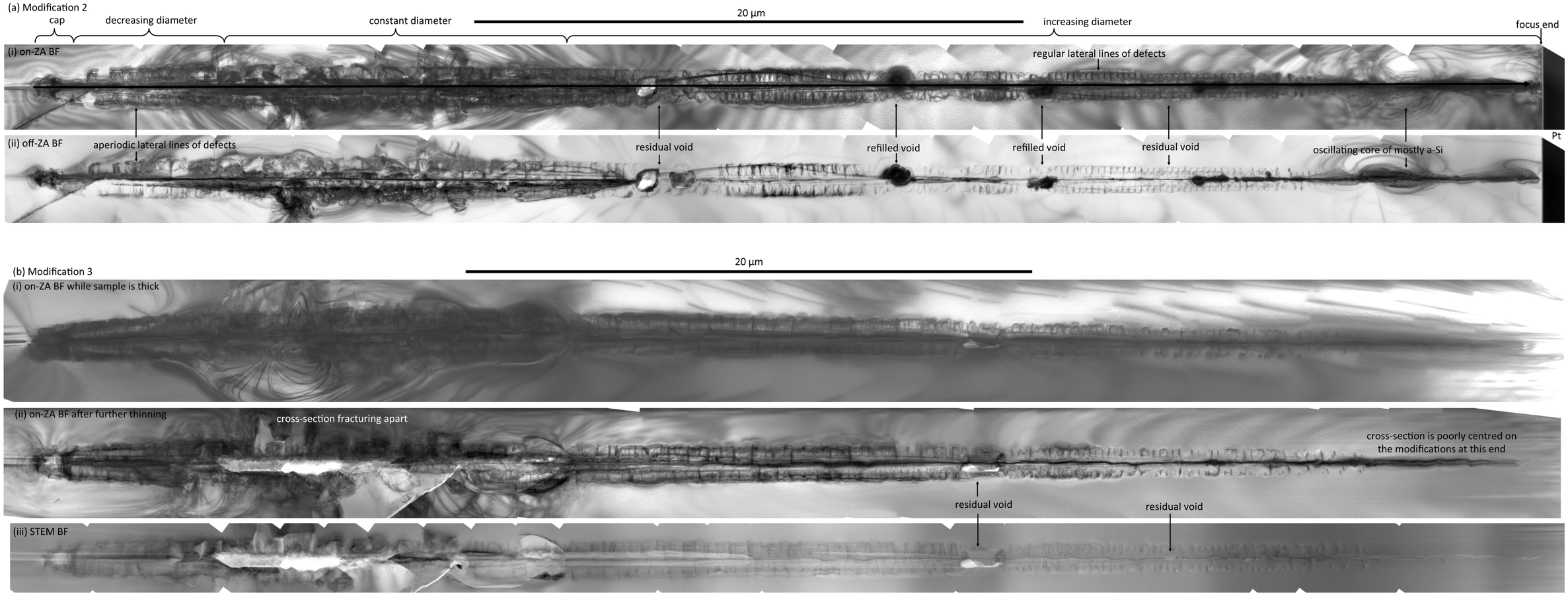

Figure A.2: Long axis cross-section images under different imaging conditions of Modification 2 and 3.